Aline de Oliveira Ferreira

Contributions to Array Signal Processing: Space and Space-Time Reduced-Rank Processing and Radar-Embedded Communications

PUC-Rio - Certificação Digital Nº 1321805/CA

Tese de Doutorado

Thesis presented to the Programa de Pós-graduação em Engenharia Elétrica of PUC–Rio in partial fulfillment of the requirements for the degree of Doutor em Ciências – Engenharia Elétrica.

Advisor   : Prof. Raimundo Sampaio Neto
Co–Advisor: Prof. José Mauro Pedro Fortes

Rio de Janeiro
February 2017

PONTIFÍCIA UNIVERSIDADE CATÓLICA
DO RIO DE JANEIRO

Aline de Oliveira Ferreira

Contributions to Array Signal Processing: Space and Space-Time Reduced-Rank Processing and Radar-Embedded Communications

Thesis presented to the Programa de Pós-Graduação em Engenharia Elétrica of the Departamento de Engenharia Elétrica do Centro Técnico Científico of PUC–Rio as partial fulfillment of the requirements for the degree of Doutor em Engenharia Elétrica. Approved by the undersigned Examination Committee.

Prof. Raimundo Sampaio Neto
Advisor
Centro de Estudos em Telecomunicações — PUC–Rio

Prof. Jose Mauro Pedro Fortes
Co–Advisor
Centro de Estudos em Telecomunicações — PUC–Rio

Prof. Marcello Luiz Rodrigues de Campos
UFRJ

Prof. José Antonio Apolinário Junior
Exército Brasileiro

Prof. Ernesto Leite Pinto
IME

Fabian David Backx
Instituto de Pesquisas da Marinha

Cesar Augusto Medina Sotomayor
IME

Prof. Márcio da Silveira Carvalho
Coordinator of the Centro Técnico
Científico da PUC–Rio

Rio de Janeiro, February 17th, 2017

Aline de Oliveira Ferreira

Aline de Oliveira Ferreira received her undergraduation Diploma in Engenharia de Telecomunicações from the Universidade Federal Fluminense (UFF), Niterói, in 2009. She earned her Master diploma in Engenharia Elétrica from the Pontifícia Universidade Católica do Rio de Janeiro (PUC–Rio) in 2011. She has been with the Instituto de Pesquisas da Marinha (IPqM) as a researcher since 2010.

To my children, Mateus and Julieta.

Acknowledgments

Abstract

Ferreira, Aline de Oliveira; Sampaio Neto, Raimundo (Advisor); Fortes, José Mauro Pedro (Co-Advisor). **Contributions to Array Signal Processing: Space and Space-Time Reduced-Rank Processing and Radar-Embedded Communications**. Rio de Janeiro, 2017. 204p. Tese de Doutorado — Departamento de Engenharia Elétrica, Pontifícia Universidade Católica do Rio de Janeiro.

Array processing is an area with many civilian and military applications, e.g. sonar, radar, seismology and wireless communications. By means of space and space-time processing it is possible to enhance their features and explore new possibilities. This area has been attracting increasingly more attention and gathering more efforts of the science community, especially now, that phased array antennas are established as a commercial and mature technology. Within this context, we address the problem of reduced rank processing in space and space-time radar signal processing and the new area of dual-function radar-communications (DFRC), which may be summarized as embedding communication messages into radar emissions as a secondary task for the radar. In this thesis, we investigate the application of a new joint interpolation and decimation rank reducing scheme in two different areas: beamforming and space-time radar processing. This rank reducing algorithm was never tested within these contexts before and shows impressive results. We also propose simplifications for decreasing the computational complexity of the algorithm in beamforming. In the topic of DFRC, we propose two original robust radar-embedded sidelobe phase/amplitude modulation methods which have simple closed form equations. The proposed methods are much simpler than the state of the art and have superior performance in terms of robustness and real-time applicability.

Keywords

Beamforming; Space-time adaptive processing (STAP); Joint interpolation and decimation rank reducing scheme; Dual function radar; Sidelobe modulation.

Resumo

Ferreira, Aline de Oliveira; Sampaio Neto, Raimundo; Fortes, José Mauro Pedro. **Contribuições ao Processamento em Arranjos de Sensores: Processamento Espacial e Espácio-Temporal com Posto Reduzido e Radares com Comunicações Incorporadas**. Rio de Janeiro, 2017. 204p. Tese de Doutorado — Departamento de Engenharia Elétrica, Pontifícia Universidade Católica do Rio de Janeiro.

Processamento em arranjos de sensores é uma área com vasta aplicação, tanto civil quanto militar, por exemplo em sonar, radar, sismologia e comunicações sem fio. Por meio de processamento espacial e espácio-temporal é possível melhorar suas funcionalidades e explorar novas possibilidades. Esta área vem atraindo cada vez mais a atenção e os esforços da comunidade científica, especialmente agora, em que antenas phased-array se estabeleceram como uma tecnologia comercial e madura. Neste contexto, nós tratamos o problema de processamento com posto reduzido em processamento espacial (*beamforming*) e espácio-temporal de sinais radar e a nova área de radares com função dual de radar e comunicações (*dual-function radar-communications*, DFRC), que pode ser resumida na incorporação de mensagens de comunicações nas transmissões radar como uma tarefa secundária. Nesta tese, nós investigamos a aplicação de um novo esquema de redução de posto baseado em interpolação e decimação em duas áreas distintas: processamento espacial e processamento espácio-temporal de sinais radar. Este algoritmo para redução de posto nunca havia sido testado nestes ambientes antes e apresentou resultados bastante expressivos. Nós também propomos simplificações para reduzir a complexidade computacional do algoritmo em bemforming. Quanto ao tópico de DFRC, nós propomos dois métodos originais para incorporar modulação de amplitude/fase aos lóbulos laterais do diagrama de irradiação do radar de forma robusta. Os métodos propostos são muito mais simples do que o estado-da-arte e apresentam desempenho superior em termos de robustez e aplicabilidade em operações de tempo-real. Nós ainda provemos várias outras análises, comparações e contribuições a esta nova área.

Palavras-chave

Processamento espacial; Processamento espácio-temporal; Esquema de redução de posto baseado em interpolação e decimação conjunta; Radares de função dual; Modulação dos lóbulos laterais.

Contents

List of Figures

List of Tables

1
Introduction

This thesis is divided into two main topics related to the area of array signal processing. The first topic addresses the problem of reduced rank processing in space and space-time radar signal processing. The second topic addresses the dual-function radar-communications (DFRC) problem, which may be summarized as embedding communication messages into radar emissions as a secondary task for the radar.

As both topics deal with space and/or space-time processing, we make an introduction to space processing, commonly known as beamforming and to space-time processing, commonly named space-time adaptive processing (STAP). Chapter 2 gives the fundamentals of beamforming. We present the general radio frequency (RF) signal model and derive the beamforming signal model that is used throughout this thesis. We define important concepts in beamforming like snapshot and beampattern for example. Chapter 3 makes an introduction to space-time processing specialized for radar applications. From the general radar model we derive the system model used in STAP and explain the most important figures of merit and metrics used to evaluate the performance of space-time filters. These two chapters compose the base for understanding the rest of this thesis.

Chapter 4 introduces the reduced rank array processing topic. We give the motivation for reducing the rank in array signal processing, for both space only and radar (space-time) applications. We review the most relevant rank reducing techniques existent in the literature and we introduce the rank reduction technique based on an interpolation and decimation scheme, which is the object of our study in this rank reducing topic. We name this method the JIDS (joint interpolation and decimation scheme) and we present its development history.

In Chapter 5, we **specialize** the JIDS for **beamforming** applications. Considering this new scenario, we propose **simplifications** of the method, which lead to a significantly **reduction** of its overall **complexity**. The new specialized and simplified JIDS for beamforming is named here **JIDSB**. In Section 5.4 we compare the JIDSB performance results with other renowned rank reducing techniques. Results of this technique in a beamforming environment

are **new** in the literature and they reveal excellent SINR loss performance with superior robustness with a low computational complexity. The conclusions of the rank reduced beamforming topic is presented in Section 5.5. The study on this topic, carried out during this thesis, resulted in a paper that was submitted to the IEEE TAES journal.

In Chapter 6, we **specialize** the JIDS rank reduction technique for **space-time** applications, more specifically, airborne phased-array radars. In Section 6.3 we present computer simulations and compare the performance results of the JIDS with other established rank reducing techniques. The JIDS has an impressive ability to significantly reduce the length of the space-time snapshots and achieves very good performance in Doppler SINR loss and probability of detection, especially in sample starving scenarios. These results are very promising and **new** within the radar literature. The conclusions of the rank reduced space-time processing topic is given in Section 6.4. The study on this topic carried out during this thesis preparation resulted in the conference paper [6].

Chapter 7 introduces the DFRC topic. We give the motivation for coupling radar and communications and make an overview of the current methods that address this problem, separating them in subareas according to their specificities. Our work is inserted in the DFRC based on sidelobe modulation subarea, which encompasses both amplitude and phase modulation of the sidelobe of the radar transmit beampattern. We also describe how the DFRC topic is structured within this thesis and we detail our contributions to the topic.

Chapter 8 explains in detail the main sidelobe modulation methods present in the literature with added simulation and analysis. We focus on the main idea of the existent methods and we highlight their pros and cons, so that the reader can place our contributions among the existent work. Chapter 9 thoroughly explains our contributions to the topic, which can be summarized as:

- we propose **two original sidelobe modulation methods** with the exclusive features of

    - being applicable to both **amplitude** and **phase** modulation, (there is no need of redesigning of the optimization formulation);
    - being **robust** against small angular errors of the relative position between the radar and the communication receiver (to the best of our knowledge, there is no method in the literature with this advantage) and

- having **low** computational complexity (we derive closed form solutions and we simplify them as possible);

– we derive **update** equations for keeping the communication link when there is relative movement between the radar and the communication receiver, (this subject is mentioned in the literature, but no other method is simple enough for effectively dealing with this issue);

– we derive a **recursive** version of one of the proposed methods, allowing the investigation of interesting **stop criteria**;

– we propose a non-coherent **signalling strategy** for sidelobe phase modulation which is much **simpler** than the others found in the DFRC literature;

– we derive an **analytical** bit error rate (BER) **expression** necessary for the DFRC sidelobe phase modulation performance evaluation;

– we present the **first** (and so far the only) **analysis** of the effect of sidelobe modulation in clutter mitigation techniques.

Chapter 10 shows several computer simulations of the proposed techniques and compares the results of the proposed methods with the existent ones. In Section 10.9 of this chapter we summarize our conclusions related to the DFRC topic. Part of the studies relative to this topic carried out during this thesis preparation led to papers [7] and [8].

Chapter 11 reviews some of the conclusions given throughout this thesis, presents possibilities to build on, insights about the studied fields and possibilities to explore.

Notation: the superscripts T and H denote transpose and conjugate transpose respectively, $\odot$ denotes the Hadamard matrix product, $\otimes$ represents the Kronecker product, $\mathrm{E}\{\cdot\}$ stands for the expected value and $\Re\{\cdot\}$ returns the real part of the argument.

PUC-Rio - Certificação Digital Nº 1321805/CA

2
Introduction to Beamforming

Beamforming or spatial filtering is a signal processing technique used in sensor arrays to provide a versatile directional signal transmission or reception. This is achieved by combining the spatial samples of the propagating wave fields in such a way that signals at particular angles (or more correctly wavenumbers) experience constructive interference while others experience destructive interference. This combination is accomplished by the beamformer. Beamforming can be applied for both transmitting and receiving purposes.

Beamforming can be used for electromagnetic or sound waves. It has found numerous applications in radar, sonar, seismology, wireless communications, radio astronomy, acoustics, and biomedicine. Adaptive beamforming is used, for example, to detect and estimate the signal-of-interest at the output of a sensor array by means of optimal (e.g., least-squares) spatial filtering and interference rejection.

In this chapter we will describe the beamforming signal model and define some fundamentals concepts in beamforming.

2.1 General RF Signal Model

Consider a real-valued RF signal, $\bar{x}(t)$, of the form

$$\bar{x}(t) = \sqrt{2E}g(t)\cos(2\pi f_c t + \rho(t) + \psi), \qquad (2.1)$$

where E is a constant that accounts for the signal energy, f_c is the RF radar carrier frequency, $g(t)$ is the low-pass transmitted pulse envelope of duration T_P, $\rho(t)$ represents the phase or frequency modulation and ψ is the initial phase.

The real-valued signal described in (2.1) can be written in its complex, low-pass, equivalent representation

$$\bar{x}(t) = \Re\left\{x(t)e^{j2\pi f_c t}\right\}, \qquad (2.2)$$

where the complex envelope of $\bar{x}(t)$ with respect to f_c is given by

$$x(t) = \sqrt{2E}g(t)e^{j\psi}e^{j\rho(t)}. \qquad (2.3)$$

The product
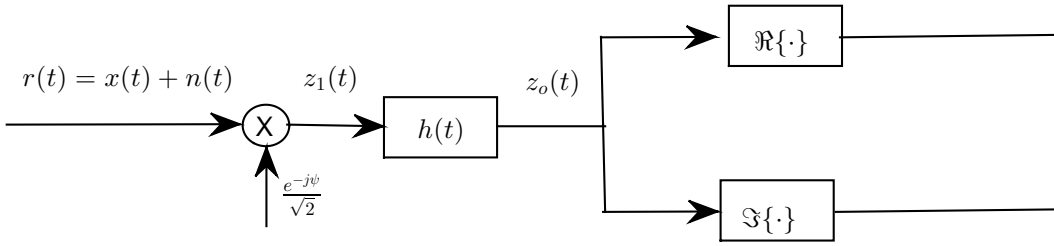
Figure 2.1: Reception process in the low-pass equivalent representation.

$$s(t) = g(t)e^{j\rho(t)}, \tag{2.4}$$

in (2.3) has bandwidth W, $W << f_c$, is normalized to unitary energy,

$$\int_0^{T_P} |s(t)|^2 dt = 1, \tag{2.5}$$

and is considered to be the waveform within this thesis.

The general demodulation scheme of the received signal can be further improved in terms of maximizing the signal to noise ratio (SNR) by the use of a matched filter, $h(t)$, as the reception filter. The matched filter, $h(t)$, is given by

$$H(f) = S^*(f)e^{-j2\pi fT_P} \text{ or} \tag{2.6}$$

$$h(t) = s^*(T_P - t). \tag{2.7}$$

The complete reception process in its low-complex equivalent representation is depicted in Fig. 2.1.

In Fig. 2.1, the input of the receiver is $r(t)$, given by

$$r(t) = x(t) + n(t), \tag{2.8}$$

$$= \sqrt{2E}s(t)e^{j\psi} + n(t), \tag{2.9}$$

where $s(t)$ is defined in (2.4) and $n(t)$ is the low-pass equivalent AWGN (Additive White Gaussian Noise) process, which has a flat power spectrum $S_n(f) = 2N_0$, for $f > -f_c$ [9]. The input after the first stage of the receiver, $z_1(t)$, is given by

$$z_1(t) = \sqrt{E}s(t) + n_1(t), \tag{2.10}$$

where $n_1(t)$ has a flat power spectrum $S_{n_1}(f) = N_0$, for $f > -f_c$. In Fig. 2.1, the output of the matched filter, $z_o(t)$, is composed by

$$z_o(t) = y(t) + n_o(t), \tag{2.11}$$

where the portion of the desired signal, $y(t)$, is given by

$$y(t) = \sqrt{E} \int_{-\infty}^{\infty} s(\alpha)s^*(\alpha + T_p - t)\mathrm{d}\alpha, \tag{2.12}$$

$$= \sqrt{E}\mathcal{R}_{ss}(T_p - t), \tag{2.13}$$

where

$$\mathcal{R}_{ss}(t) = \int_{-\infty}^{\infty} s(\alpha)s^*(\alpha + t)\mathrm{d}\alpha \tag{2.14}$$

is the autocorrelation function of $s(t)$. The noise $n_o(t)$ has a power spectral density $S_{n_o}(f) = N_0|H(f)|^2$ and variance $E[|n_o(t)|^2] = N_0 \int_{-\infty}^{\infty} |H(f)|^2\mathrm{d}f = N_0 \int_{-\infty}^{\infty} |h(t)|^2\mathrm{d}t = N_0$.

2.2 Signal Model in Beamforming

In this section we describe the particularities of the signal transmitted (or received) at a generic sensor array. Now, suppose that the signal of equation (2.1) is transmitted (or received) at the origin of the Cartesian coordinate system (depicted in Fig. 2.2). The signal transmitted (or received) at an arbitrary m-th element of a sensor array with M elements displaced arbitrarily in the $\mathbb{R}^3$ space, is given by

$$\bar{x}(t, \mathbf{d}_m) = \Re\left\{ x(t, \mathbf{d}_m)e^{j2\pi f_c t} \right\}, \tag{2.15}$$

where $\mathbf{d}_m$ is the position vector, given by

$$\mathbf{d}_m = \begin{bmatrix} d_{x,m} \\ d_{y,m} \\ d_{z,m} \end{bmatrix}, \tag{2.16}$$

where $\{d_{x/m}, d_{y/m}, d_{z/m}\}$ are the Cartesian coordinates of the m-th element phase center. The complex envelope $x(t, \mathbf{d}_m)$ is given by

$$x(t, \mathbf{d}_m) = \sqrt{2E}s(t - \tau_m)e^{j\psi}e^{-j2\pi f_c \tau_m}, \tag{2.17}$$

where $s(t)$ is defined in equation (2.4). The time-delay between transmission (or reception) of the plane wave at the reference point (origin of the coordinate system) and the m-th channel, τ_m, is computed from the geometry given in Fig. 2.2 as follows [10]

$$\tau_m = \frac{\mathbf{k}(\phi, \theta)^T \mathbf{d}_m}{c}, \tag{2.18}$$

where c is the velocity of the propagating wave and $\mathbf{k}(\phi, \theta)$ is a unit vector normal to the plane wave, given by
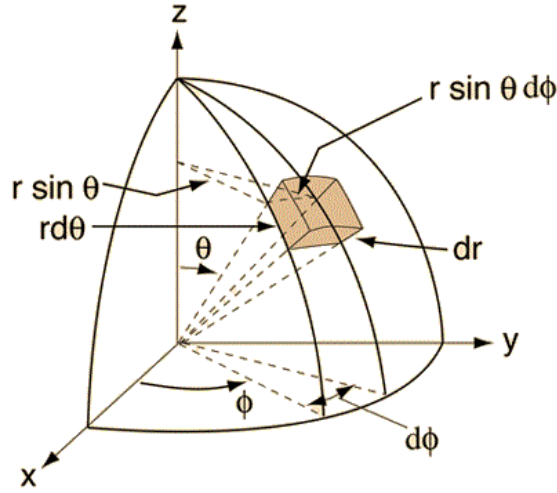
Figure 2.2: Coordinate system.

$$\mathbf{k}(\phi, \theta) = \begin{bmatrix} \sin(\theta)\cos(\phi) \\ \sin(\theta)\sin(\phi) \\ \cos(\theta) \end{bmatrix}, \tag{2.19}$$

where ϕ and θ represent azimuth and elevation angles respectively.

If the narrowband assumption holds, which is the bandwidth of $s(t)$, W, being much smaller than the carrier frequency, f_c, and if we place the center of the coordinate system somewhere close to the sensor array, then we can use the following approximation

$$s(t - \tau_m) \cong s(t). \tag{2.20}$$

Substituting (2.20) into (2.17), we have that the complex envelope at the m-th element is

$$x(t, \mathbf{d}_m) = \sqrt{2E}s(t)e^{j\psi}e^{-j2\pi f_c \tau_m}. \tag{2.21}$$

The spatial dependence on the element can be separated as

$$x(t, \mathbf{d}_m) = x(t)s_m, \tag{2.22}$$

where

$$x(t) = \sqrt{2E}s(t)e^{j\psi} \tag{2.23}$$

and

$$s_m = e^{-j2\pi f_c \tau_m}. \tag{2.24}$$

The M complex envelopes, $\mathbf{x}(t)$, due to the transmission of the M elements can be compactly described in a vector form as

$$\mathbf{x}(t) = x(t)\mathbf{s}, \tag{2.25}$$
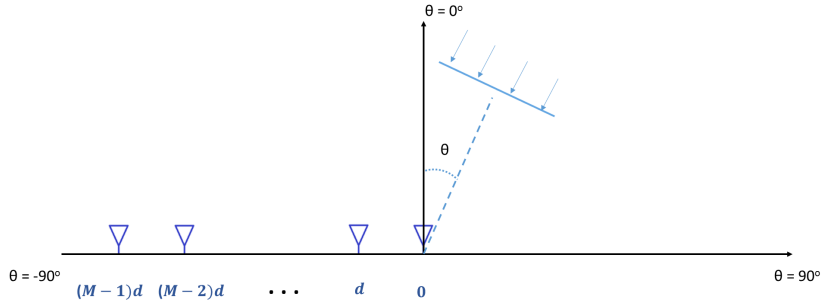
Figure 2.3: Possible coordinate system for a ULA.

where $\mathbf{s}$ is the steering vector (also known as the array manifold) given by stacking s_m, $m = 0, \ldots, M - 1$, in a vector form,

$$\mathbf{s} = \begin{bmatrix} e^{-j2\pi f_c \tau_0} \\ e^{-j2\pi f_c \tau_1} \\ \vdots \\ e^{-j2\pi f_c \tau_{M-1}} \end{bmatrix}. \tag{2.26}$$

Depending on where we place the coordinate system relative to the array we can achieve different forms of writing the steering vector. A given form may be more convenient than others depending on the application. For example, let d be the uniform sub-array spacing of an M channel uniform linear array (ULA). Also, place the first sensor at the origin and designate it as the phase reference, define θ as the angle formed by the normal to the planewave and the normal to the ULA as illustrated in Figure 2.3. Thus, the visible region is $\theta \in [-90^o, 90^o]$ and the steering vector is given by

$$\mathbf{s} = \begin{bmatrix} 1 \\ e^{-j2\pi \frac{d}{\lambda_c} \sin(\theta)} \\ e^{-j2\pi 2 \frac{d}{\lambda_c} \sin\theta)} \\ \vdots \\ e^{-j2\pi(M-1)\frac{d}{\lambda_c}\sin(\theta)} \end{bmatrix}. \tag{2.27}$$

Now, place the center of the coordinate system at the center of a M element ULA and define θ as the angle formed by the normal to the plane wave and the line of the ULA, as depicted in Fig. 2.4. Thus, the visible region corresponds to the interval $\theta \in [0^o, 180^o]$ and the steering vector, $\mathbf{s}$, can be written as

$$\mathbf{s} = \begin{bmatrix} e^{j\left(-\frac{M-1}{2}\right)\frac{2\pi d}{\lambda_c}\cos(\theta)} \\ e^{j\left(1-\frac{M-1}{2}\right)\frac{2\pi d}{\lambda_c}\cos(\theta)} \\ \vdots \\ e^{j\left(M-1-\frac{M-1}{2}\right)\frac{2\pi d}{\lambda_c}\cos(\theta)} \end{bmatrix}. \tag{2.28}$$
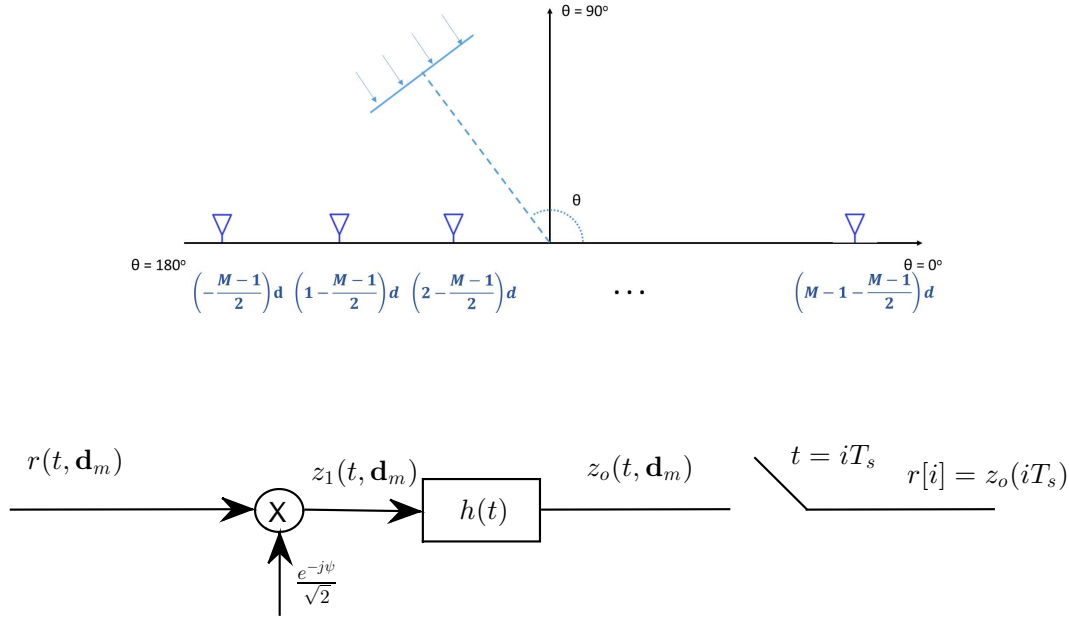
Figure 2.5: Complete reception in the equivalent low-pass representation for the m-th array element.

2.3 Snapshot in Beamforming

The reception happens at each element, therefore, for the m-th element at position $\mathbf{d}_m$, the received signal, in the complex equivalent form, after matched filtering, $z_o(t, \mathbf{d}_m)$, is given by

$$z_o(t, \mathbf{d}_m) = y(t, \mathbf{d}_m) + n_m(t), \tag{2.29}$$

where $n_m(t)$ is the AWGN low-pass equivalent noise process with flat power spectrum S_{n_m}, given by $S_{n_m} = N_0$ within the frequencies limited by the matched filter and $y(t, \mathbf{d}_m)$ is given by

$$y(t, \mathbf{d}_m) = y(t)s_m, \tag{2.30}$$

where $y(t)$ is described in (2.12) and s_m, defined in (2.24), is the term which contains the spatial dependence

$$s_m = e^{-j2\pi f_c \tau_m}.$$

The signal is then sampled in a rate of $R_s = 1/T_s$, where T_s is the sampling interval. This process is depicted in Fig. 2.5. The output of the sampling process results in samples given by $r[i]$, as

$$r_m[i] = z_o(t, \mathbf{d_m})|_{t=iT_s}, \tag{2.31}$$

$$= y(iT_s)s_m + n_m(iT_s). \tag{2.32}$$

The snapshot stacks the information of all sensor elements at the same sampling instant, like a photograph of the output of all sensors at a given instant. The snapshot is, thus, given by

$$\mathbf{r}[i] \;=\; y(iT_s)\mathbf{s} + \mathbf{n}_o(i), \tag{2.33}$$

where $\mathbf{s}$ is the spatial steering vector defined in (2.26) and $\mathbf{n}_o(i) = [n_0(iT_s), n_1(iT_s), \ldots, n_{M-1}(iT_s)]^T$ is the noise vector.

2.4 Spatial Filtering (Beamforming)

When all sensor elements are able to add independently a gain and a phase shift to their transmitted (or received) signals, we say that the sensor array is able to beamform. The joint operation of individual sensors modifying amplitude and phase of the transmitted (or received) signals is called beamforming. Due to the composition of the gain and phase-shifts with the array delay of all elements, the amplitude towards each direction within the visible region doesn't necessarily follow the omnidirectional radiation pattern, though the individual sensors are usually omnidirectional. The result of this joint operation allows the sensor array to perform spatial filtering.

The transmitted (or received) signal, composed of the individual contribution of all sensor elements, depends on the gain and phase shift of each sensor and depends on the intrinsic array delay, τ_m. The delay, τ_m, depends on both the array geometry and the direction of the transmitted plane wave. Given the array geometry and the plane wave direction, one can define the steering vector, $\mathbf{s}$. Having defined the steering vector for a specific direction, θ, $\mathbf{s}(\theta)$, we can visualize the beamforming effect over the visible region.

The beamforming process for transmission in a M element array is depicted in Fig. 2.6. The transmitted signal, $x(t, \theta)$, irradiated towards θ due to the contribution of all elements of the sensor array is given by

$$x(t, \theta) = \mathbf{w}^H \mathbf{s}(\theta) x(t), \tag{2.34}$$

where $x(t)$ is the complex envelope of $\bar{x}(t)$ with respect to f_c defined in (2.3) and $\mathbf{w} = [w_0, \ldots, w_{M-1}]^T \in \mathbb{C}^{M \times 1}$ is the complex weighting vector with the weights of each branch of the array.

The beamforming process for reception is depicted in Fig. 2.7. As we multiply by the beamformer weight, which is equivalently to adding a gain and a phase-shift to the individual sensor branches, the received signal will also be modified by the overall composition of gain, phase-shifts and array delay. The received sample due to the contribution of all sensors, $r_B[i]$, as
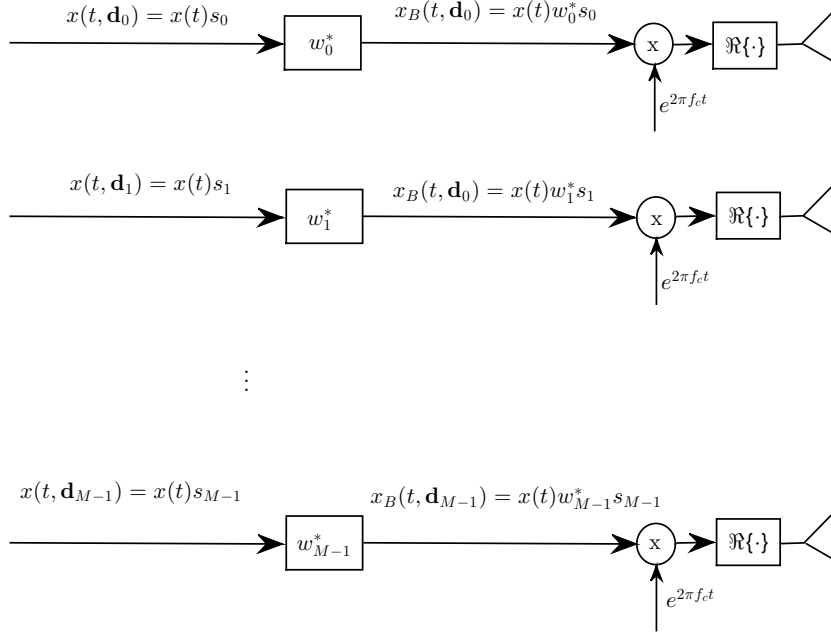
Figure 2.6: Diagram of beamforming in transmission.
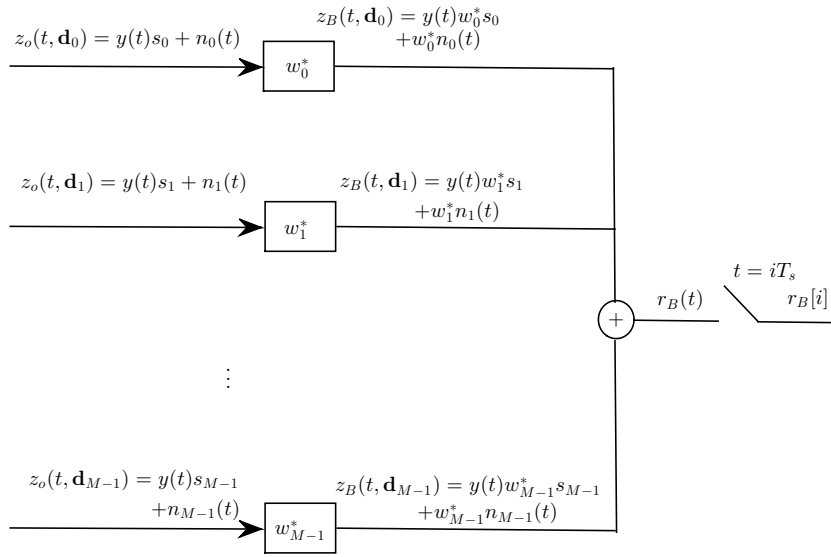
Figure 2.7: Diagram of beamforming in reception.

depicted in Fig. 2.7, can be written as

$$r_B[i] = \mathbf{w}^H \mathbf{r}[i], \tag{2.35}$$

with $\mathbf{r}[i]$ defined in (2.33). Thus,

$$r_B[i] = y(iT_s)\mathbf{w}^H \mathbf{s}(\theta) + \mathbf{w}^H \mathbf{n}_o. \tag{2.36}$$

We define the beampattern, $B(\theta)$, as

$$B(\theta) \triangleq \mathbf{w}^H \mathbf{s}(\theta) \tag{2.37}$$

and the normalized beampattern, $\bar{B}(\theta)$, as

$$\bar{B}(\theta) \triangleq \frac{B(\theta)}{B(\theta_o)},\tag{2.38}$$

where θ_o is the direction towards which the beampattern, $B(\theta)$, is maximum. If we vary θ within the visible region we can visualize the radiation power pattern of the array.

The beampattern allows us to visualize the effect of constructive and destructive interference within the visible region in space.

Many methods exist for defining the weights, w_m, in order to emphasize the signals impinging from a desired direction and to cancel signals impinging from other directions.

3
Introduction to Space-Time Processing

So far, in Chapter 2, we have derived the signal model for spatial filtering (or beamforming). The understanding of this model is necessary for understanding the model of radars which have the transmitting or receiving parts composed of an array of sensors. But in radar applications, targets are commonly moving. It implies that the echoes from a target moving relative to the radar with a radial velocity of v m/s will have a Doppler shift proportional to its velocity. Exploiting the angle (spatial) dependency and Doppler (temporal) dependency, one can achieve better results in terms of radar signal processing. In this chapter we will derive the signal model and explain the common metrics of space-time processing, or space-time adaptive processing (STAP), as it is usually known in the literature.

The most fundamental problem in radar signal detection is to uncover an object or physical phenomenon against a background of interference consisting of clutter (echoes from the environment), one or more jammers (intentional interference) and background noise. This requires determining whether the receiver output at a given time (or cell under test - CUT - which is associated to an specific range gate) represents the echo from a reflecting target or only noise. Detection decisions are usually made by comparison of some statistic test to a threshold.

By dealing simultaneously with both domains, spatial and temporal, we can achieve more degrees of freedom (DoF). Spatial and temporal signal DoF greatly enhance radar detection rate when the target competes with ground clutter (echoes from the environment at the ground level) and barrage noise jamming [11]. Ground clutter returns exhibit correlation in both spatial and temporal dimensions, while jamming is predominantly correlated in angle for modest bandwidth. The Doppler-wavenumber or angle-Doppler spectrum provides a unique representation of a signal in a three dimensional plane.

3.1 General Radar Signal Model

The low-pass complex envelope of a typical RF pulsed radar burst composed of J pulses is given by
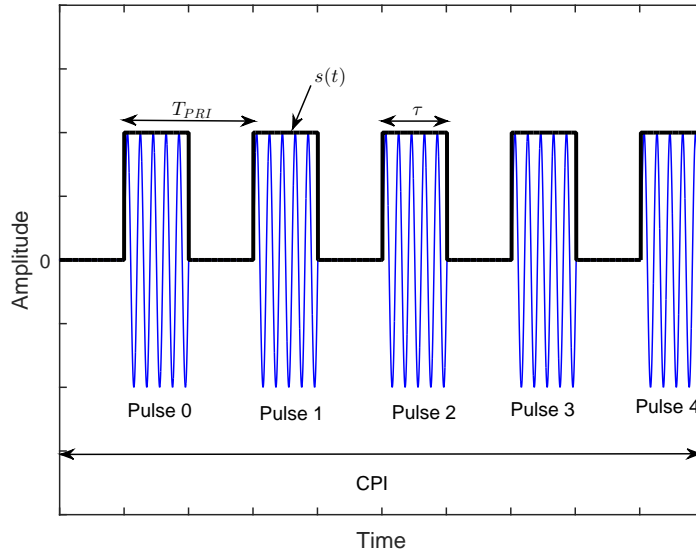
Figure 3.1: Illustration of radar burst.

$$\bar{x}_B(t) = \sqrt{2E_t}e^{j\psi}\sum_{k=0}^{J-1}s(t - kT_{PRI}), \quad 0 \leq t < JT_{PRI}, \tag{3.1}$$

where E_t is the RF pulse energy, ψ is the initial carrier phase, T_{PRI} is the pulse repetition interval (PRI) and $s(t)$ is the radar waveform, which is a low-pass pulse of duration τ, with bandwidth $W << f_c$, where f_c is the carrier frequency, normalized to unitary energy,

$$\int_0^\tau |s(t)|^2 \mathrm{d}t = 1. \tag{3.2}$$

The radar waveform, $s(t)$, is usually of the form

$$s(t) = g(t)e^{j\rho(t)}, \tag{3.3}$$

where $g(t)$ is the low-pass transmitted pulse envelope of duration τ and $\rho(t)$ represents the phase or frequency modulation.

In Fig. 3.1 we illustrate a burst of five (J=5) simple pulses of duration τ. The total duration (JT_{PRI}) is the coherent processing interval (CPI).

The time required for a pulse to propagate a distance R and return, travelling a total distance $2R$, is $2R/c$, where c is the speed of light. Thus, if at delay time t_0, the received amplitude of the radar echo is greater than a given threshold, it is assumed that a target is present at range

$$R = \frac{ct_0}{2}. \tag{3.4}$$

The maximum unambiguous range, R_{max}, is related to the radar PRI, T_{PRI}, by

$$R_{\max} = \frac{cT_{PRI}}{2}. \tag{3.5}$$

In order to maximize the detection range, most radar systems try to maximize the transmitted energy. One way to do this is to always operate the transmitter at full power during a pulse. That is why radars generally do not use amplitude modulation. The longer the pulse, the higher is the average energy as well. On the other hand, the nominal range resolution ΔR is determined by the waveform bandwidth W, as

$$\Delta R = \frac{c}{2W}. \tag{3.6}$$

For an unmodulated pulse, the bandwidth is inversely proportional to its duration, what would lead to a resolution of $\Delta R = \frac{c\tau}{2}$. To increase the waveform bandwidth without reducing its pulse length and therefore without sacrificing energy, many radars routinely use phase or frequency modulation. Two scatterers are resolved if they produce two separately identifiable signals at the system output, as opposed to combining into a single undifferentiated output.

Desirable values of range resolution vary from a few kilometers in long-range surveillance systems, which tend to operate at lower RFs, to a meter or less in very fine resolution imaging systems, which tend to operate at high RFs. Corresponding waveform bandwidths are on the order of 100 KHz to 1 GHz, and are typically 1 percent or less of the RF. Few radars achieve 10 percent bandwidth. Thus, most radar waveforms can be considered narrowband bandpass functions [12].

3.2 System Model in Space-Time Processing

We consider a pulsed-Doppler radar with K radiating elements placed in a uniform linear array (ULA), for simplicity of calculations, but the array can have an arbitrary shape to which the system model can be adapted. All elements are assumed to have the same radiation pattern. In order to perform pulse integration [12], J pulses are transmitted within a CPI. Pulses are transmitted in a pulse repetition frequency of $1/T_{PRI}$.

The analytical signal of the echo waveform, $r_k(t)$, from a target modelled as a single scatterer, received by the k-th element, ignoring relativistic effects, is given by

$$r_k(t) = a_r s(t - \tau_e) e^{j2\pi(f_c + f_D)(t - \tau_e)} e^{j\psi}, \tag{3.7}$$

where a_r is the echo amplitude and

$$f_D = \frac{2v_t}{\lambda_c} \tag{3.8}$$

is the target Doppler frequency, v_t is the relative radial target velocity with respect to the radar and λ_c is the carrier wavelength. The target delay is given

by

$$\tau_e = \tau_{RT} + \tau_k, \tag{3.9}$$

where $\tau_{RT} = 2R_t/c$ is the target round-trip time measured at the phase reference, R_t is the distance to the target and c is the speed of light. If the target is moving then R_t is actually a function of the time, $R_t(t)$, but for instantaneous velocities that are a small fraction of the speed of light, the commonly quasi-stationary assumption is made [12], so that $R_t(t) \cong R_t$. Variable τ_k is the relative delay measured from the phase reference to the k-th element.

The received analytical signal, $r_k(t)$, is thus

$$
\begin{aligned}
r_k(t) &= a_r s(t - \tau_{RT} - \tau_k) e^{j2\pi(f_c + f_D)(t - \tau_{RT} - \tau_k)} e^{j\psi}, \\
&= a_r e^{j\psi} s(t - \tau_{RT} - \tau_k) \cdot \\
&\quad \cdot e^{j2\pi f_c t} e^{-j2\pi(f_c + f_D)\tau_{RT}} e^{-j2\pi(f_c + f_D)\tau_k} e^{j2\pi f_D t}.
\end{aligned}
\tag{3.10}
$$

If the narrowband assumption is valid, which is that the bandwidth of $s(t)$, W, is much smaller than the carrier frequency, f_c, if we place the center of the coordinate system somewhere close to the sensor array and assuming that $f_D << f_c$, we can make the following approximations,

$$s(t - \tau_{RT} - \tau_k) \cong s(t - \tau_{RT}), \tag{3.11}$$

$$e^{-j2\pi(f_c + f_D)\tau_k} \cong e^{-j2\pi f_c \tau_k}. \tag{3.12}$$

The analytical signal $r_k(t)$ is approximated to

$$r_k(t) \cong a_r e^{j\psi'} s(t - \tau_{RT}) e^{j2\pi f_c t} e^{-j2\pi f_c \tau_k} e^{j2\pi f_D t}, \tag{3.13}$$

where $e^{j\psi'} = e^{j\psi} e^{-j2\pi(f_c + f_D)\tau_{RT}}$.

The coordinate system assumed here is depicted in Figs. 3.2, which is the same as the one described in [1]. The variables ϕ and θ refer to true azimuth and elevation respectively, and not the standard spherical coordinate system angles.

A unit vector $\mathbf{k}(\phi, \theta)$, pointing in the (ϕ, θ) direction according to this coordinate system is given by

$$\mathbf{k}(\phi, \theta) = \begin{bmatrix} \cos(\theta)\sin(\phi) \\ \cos(\theta)\cos(\phi) \\ \sin(\theta) \end{bmatrix}. \tag{3.14}$$

In our work we consider that the array is located at $z = 0$, as depicted in Fig. 3.3. The k-th, $k = 0, \ldots, K - 1$, element of the ULA is located at position
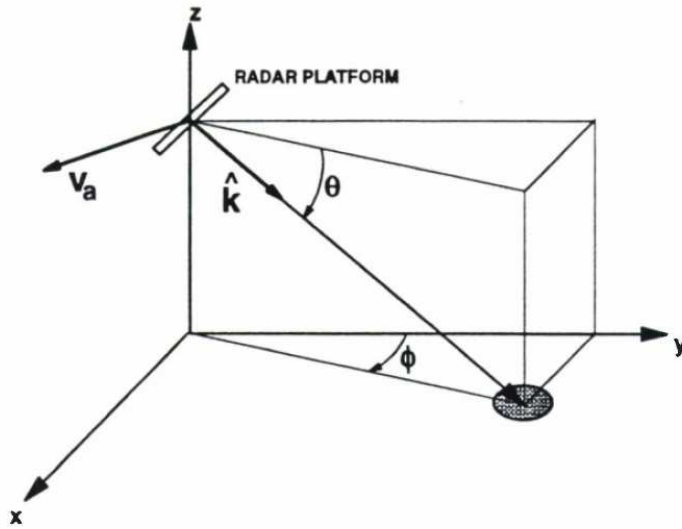
Figure 3.2: Platform geometry [1].
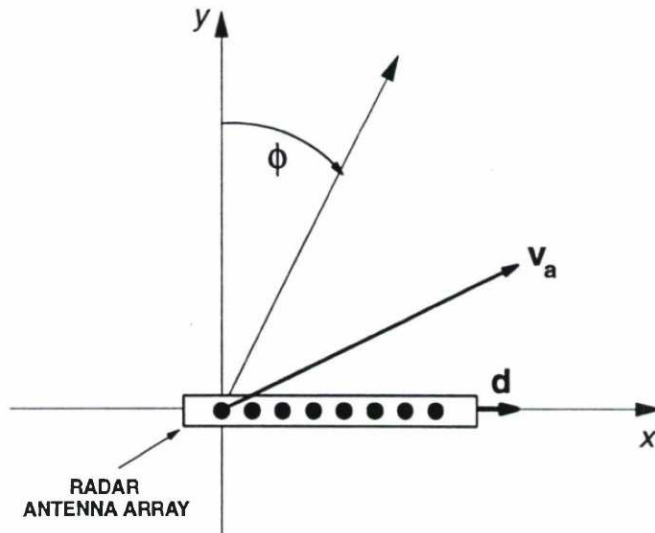
Figure 3.3: Top view of the platform geometry [1].

$$\mathbf{d}_k = \begin{bmatrix} kd \\ 0 \\ 0 \end{bmatrix}, \tag{3.15}$$

where d is the ULA inter-element. Thus, the time-delay τ_k is expressed as

$$\tau_k = \frac{\mathbf{k}^T \mathbf{d}_k}{c} = k\frac{d}{c}\cos(\theta_t)\sin(\phi_t), \tag{3.16}$$

where (θ_t, ϕ_t) are the elevation and azimuth angles of the target, and c is the speed of light. The quantity, ϑ, the target spatial frequency, is conveniently defined as

$$\vartheta_t = \frac{d}{\lambda_c}\cos(\theta_t)\sin(\phi_t), \tag{3.17}$$

where, λ_c is the carrier wavelength, so that

$$2\pi f_c \tau_k = 2\pi k \vartheta_t. \tag{3.18}$$

Assuming an ideal coherent receiver, the analytical complex downconverted received signal is given by

$$\bar{r}_k(t) = r_k(t)\frac{e^{-j2\pi f_c t}}{\sqrt{2}}, \tag{3.19}$$

$$\bar{r}_k(t) = \sigma_t s(t - \tau_{RT})e^{j2\pi k\vartheta_t}e^{j2\pi f_D t}, \tag{3.20}$$

where $\sigma_t = \frac{a_r e^{j\psi}e^{-j2\pi(f_c+f_D)\tau_{RT}}}{\sqrt{2}}$. In each element, $\bar{r}_k(t)$, is match filtered with the receiver filter, $h(t) = s^*(\tau - t)$. The output of the k-th channel, $y_k(t)$, is given by

$$
\begin{aligned}
y_k(t) &= \int_{-\infty}^{\infty} \bar{r}_k(\alpha)h(t-\alpha)\mathrm{d}\alpha, \\
&= \int_{-\infty}^{\infty} \bar{r}_k(\alpha)s^*(\alpha + \tau - t)\mathrm{d}\alpha. \tag{3.21}
\end{aligned}
$$

Substituting (3.20) into (3.21) we have

$$y_k(t) = \int_{-\infty}^{\infty} \sigma_t s(\alpha - \tau_{RT})e^{j2\pi k\vartheta_t}e^{j2\pi f_D \alpha}s^*(\alpha + \tau - t)\mathrm{d}\alpha. \tag{3.22}$$

Substituting $\alpha - \tau_{RT}$ by β in (3.22) we have

$$y_k(t) = \sigma_t e^{j2\pi k\vartheta_t}e^{j2\pi f_D \tau_{RT}}\int_{-\infty}^{\infty} s(\beta)e^{j2\pi f_D \beta}s^*(\beta + \tau_{RT} + \tau - t)\mathrm{d}\beta, \tag{3.23}$$

which can be written in terms of the waveform ambiguity function [12],

$$\chi(t, f) = \int_{-\infty}^{\infty} s(\beta)s^*(\beta - t)e^{j2\pi f\beta}\mathrm{d}\beta, \tag{3.24}$$

as

$$y_k(t) = \sigma_t e^{j2\pi k\vartheta_t}e^{j2\pi f_D \tau_{RT}}\chi(t - \tau_{RT} - \tau, f_D). \tag{3.25}$$

The output corresponding to the m-th pulse of the burst, $y_{k,m}(t)$, is done

by considering the round-trip time as $\tau_{RT} + mT_{PRI}$ in (3.25), as

$$
\begin{aligned}
y_{k,m}(t) &= \sigma_t e^{j2\pi k\vartheta_t} e^{j2\pi f_D(\tau_{RT}+mT_{PRI})} \chi(t - \tau_{RT} - \tau - mT_{PRI}, f_D), \\
&= \sigma'_t e^{j2\pi k\vartheta_t} e^{j2\pi f_D mT_{PRI}} \chi(t - \tau_{RT} - \tau - mT_{PRI}, f_D), \quad (3.26)
\end{aligned}
$$

where $\sigma'_t = \sigma_t e^{j2\pi f_D \tau_{RT}}$. Assuming that the pulse time-bandwidth product and the expected target Doppler frequencies are such that the waveform is insensitive to target Doppler shift, the following approximation is valid

$$
\chi(t, f_D) \cong \chi(t, 0) = \int_{-\infty}^{\infty} s(\beta) s^*(\beta - t) \mathrm{d}\beta. \quad (3.27)
$$

Thus, $y_{k,m}(t)$ becomes

$$
y_{k,m}(t) = \sigma'_t e^{j2\pi k\vartheta_t} e^{j2\pi f_D mT_{PRI}} \chi(t - \tau_{RT} - \tau - mT_{PRI}, 0). \quad (3.28)
$$

Since $\chi(t, 0)$ has a maximum for $t = 0$, then the maximum of $|y_{k,m}(t)|$ occurs for $t = \tau_{RT} + \tau + mT_{PRI}$ and is given by

$$
\max |y_{k,m}(t)| = |\sigma_t||\chi(0, 0)| = |\sigma_t| \int_{-\infty}^{\infty} |s(\beta)|^2 \mathrm{d}\beta, \quad (3.29)
$$

that due to the pulse waveform normalization,

$$
\int_{-\infty}^{\infty} |s(\beta)|^2 \mathrm{d}\beta = 1, \quad (3.30)
$$

is simplified to $|\sigma_t|$.

Sampling $y_{k,m}(t)$ at instants $t = t_0 + lT_f + mT_{PRI}$, where t_0 is the beginning of the range gate of interest, T_f is the sample interval that determines the range resolution cell and l, $l = 0, \ldots, L-1$, is known as the fast time index, yields the samples

$$
y_{k,m}[l] = \sigma'_t e^{j2\pi k\vartheta_t} e^{j2\pi f_D mT_{PRI}} \chi(t_0 + lT_f - \tau_{RT} - \tau, 0), \quad (3.31)
$$

or equivalently,

$$
\begin{aligned}
y_{k,m}[l] &= \alpha_l e^{j2\pi k\vartheta_t} e^{j2\pi f_D mT_{PRI}}, \quad (3.32) \\
k &= 0, \ldots, K-1, \\
m &= 0, \ldots, J-1, \\
l &= 0, \ldots, L-1,
\end{aligned}
$$

where α_l, which depends on l, is given by

$$
\alpha_l = \sigma'_t \chi(t_0 + lT_f - \tau_{RT} - \tau, 0). \quad (3.33)
$$

The magnitude of the samples in (3.32) is given by

$$|y_{k,m}[l]| = |\sigma_t||\chi(t_0 + lT_f - \tau_{RT} - \tau, 0)|, \tag{3.34}$$

which is maximal for the l^* which satisfies

$$t_0 + l^*T_f \cong \tau_{RT} + \tau, \tag{3.35}$$

where τ_{RT} corresponds to the target range, so, as expected, the maximum happens exactly at the target range. In the case where the equality in (3.35) can be achieved and considering the pulse waveform normalization, the maximum is given by

$$\max |y_{k,m}[l]| = |y_{k,m}[l^*]| = |\alpha_{l^*}| = |\sigma_t|. \tag{3.36}$$

For a given l, which corresponds to the l-th range gate, the values of $y_{k,m}[l]$ can be organized in a $K \times J$ matrix. The $L \times J \times K$ structure formed by L range samples of each of the J pulses of all K elements is called the radar datacube and may be visualized in Fig. 3.4. Each datacube corresponds to a single CPI. Though the radar doesn't store data like this, the datacube is a good representation in order to help the understanding of the STAP process. The processor is able to beamform along the column dimension and Doppler process along the rows.

Examination of (3.32) shows that one exponential term depends on the spatial index k and the other depends on the temporal index m. We can write a target space-time steering vector, $\mathbf{s}_{st}$, as in [1], where, for a given range gate, $\alpha_l \mathbf{s}_{st} = [y_{0,0}, \ldots, y_{K-1,0}, y_{0,1}, \ldots, y_{K-1,1}, \ldots, y_{0,J-1}, \ldots, y_{K-1,J-1}]^T$, and

$$\mathbf{s}_{st} = \mathbf{s}_t(f_D) \otimes \mathbf{s}_s(\vartheta_t), \tag{3.37}$$

where $\otimes$ is the Kronecker product operator, $\mathbf{s}_s(\vartheta_t) \in \mathbb{C}^{K \times 1}$ is the spatial array manifold vector given by

$$\mathbf{s}_s(\vartheta_t) = [1, e^{j2\pi\vartheta_t}, ..., e^{j2\pi(K-1)\vartheta_t}]^T, \tag{3.38}$$

and $\mathbf{s}_t(f_D) \in \mathbb{C}^{J \times 1}$ is the temporal steering vector, defined by

$$\mathbf{s}_t(f_D) = [1, e^{j2\pi f_D T_{PRI}}, ..., e^{j2\pi(J-1)f_D T_{PRI}}]^T. \tag{3.39}$$

The radar detection is a binary hypothesis problem, where the null hypothesis, H_0, corresponds to target absence and H_1 corresponds to target presence. The STAP algorithms are applied to every range of interest, which corresponds to a slice $J \times K$ of the CPI data cube. Each range slice can be stacked to form the $M \times 1$, $M = KJ$, space-time snapshot, $\mathbf{r}[l]$, [1, 13], and after detection filtering each range slice is tested under both hypothesis.

Under hypothesis H_1 of target presence, each space-time snapshot $\mathbf{r}$ at
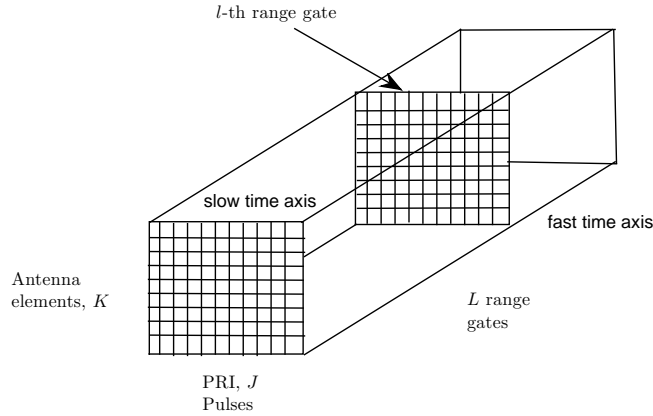
Figure 3.4: Radar CPI datacube.

the l-th range, $\mathbf{r}[l] \in \mathrm{C}^{M \times 1}$, is then given by the sum of the desired signal $\alpha_l \mathbf{s}_{st}$, interference, $\mathbf{i}[l]$, clutter, $\mathbf{c}[l]$ and noise, $\mathbf{n}[l]$,

$$\mathbf{r}[l] = \alpha_l \mathbf{s}_{st} + \underbrace{\mathbf{i}[l] + \mathbf{c}[l] + \mathbf{n}[l]}_{\mathbf{x}[l]}. \tag{3.40}$$

The target space-time steering vector $\mathbf{s}_{st}$ is described in (3.37). The target's return power is $E[|\alpha_l|^2] = \sigma_n^2 \xi_l$, where σ_n^2 is the thermal noise power per element and ξ_l is the signal to noise ratio (SNR).

The vector $\mathbf{n}[l] \in \mathrm{C}^{M \times 1}$ in (3.40) is the complex vector of sensor noise, which is assumed to be a zero-mean spatially and temporally circular complex Gaussian process. The space-time covariance matrix of the noise is given by

$$\mathbf{R}_n = \mathrm{E}\left[\mathbf{n}[l]\mathbf{n}^H[l]\right] = \sigma_n^2 \mathbf{I}_M, \tag{3.41}$$

where $\mathbf{I}_M$ is the $M \times M$ identity matrix.

The jamming interference, $\mathbf{i}[l] \in \mathrm{C}^{M \times 1}$, considered here consists of barrage noise jamming originated from land-based or airborne platforms far from the radar impinging on the ULA. We assume that the radar pulse repetition frequency (PRF), $f_r = 1/T_{PRI}$, is significantly less than the instantaneous jammer's bandwidth so that the jamming is temporally uncorrelated from pulse to pulse and we assume that the jammer's bandwidth is small compared to the carrier frequency so the jammer's signal is spatially correlated from element to element.

The simple jammer model described here is based in [11] and neglects jammer correlation in fast-time. Assuming there are Q jammers in the environment, the interference component at the l-th range, $i[l]$, in (3.40), is given by the sum of the contribution of the Q jammers as

$$\mathbf{i}[l] = \sum_{q=1}^{Q} \mathbf{i}_q[l]. \tag{3.42}$$

The contribution of the q-th jammer at the l-th range, $\mathbf{i}_q[l]$, is given by

$$\mathbf{i}_q[l] = \mathbf{a}_q \otimes \mathbf{s}_s(\vartheta_q), \tag{3.43}$$

where $\mathbf{a}_q = [a_{q,1}, \ldots, a_{q,J}]$ is a random vector containing the q-th jamming signal's amplitudes for all J pulses and $\mathbf{s}_s(\vartheta_q)$ is the q-th jammer spatial steering vector. Assuming that the jammer samples from different pulses are uncorrelated and that the jamming signal is stationary over a CPI, thus

$$\mathrm{E}\left[\mathbf{a}_q \mathbf{a}_q^H\right] = \sigma_n^2 \xi_q \mathbf{I}_J, \tag{3.44}$$

where ξ_q is the q-th received jammer to noise ratio (JNR) at an element and σ_n^2 is the single channel noise power.

The total jammer space-time covariance matrix, $\mathbf{R}_j$, is then given by

$$\mathbf{R}_j = \mathbf{I}_J \otimes \mathbf{\Phi}_j, \tag{3.45}$$

where $\mathbf{\Phi}_j$ is the total jammer spatial covariance matrix given by

$$\mathbf{\Phi}_j = \mathbf{A}(\bar{\vartheta})\Xi_j\mathbf{A}^H(\bar{\vartheta}), \tag{3.46}$$

where $\mathbf{A}(\bar{\vartheta}) = [\mathbf{s}_s(\vartheta_1), ..., \mathbf{s}_s(\vartheta_Q)] \in \mathrm{C}^{K \times Q}$ is the complex matrix composed of the interferers spatial steering vectors at spatial frequencies $\vartheta_1, ..., \vartheta_Q$ and Ξ_j is the diagonal matrix with the jammer's power given by

$$\Xi_j = \mathrm{diag}[\sigma_n^2\xi_1, \sigma_n^2\xi_2, \ldots, \sigma_n^2\xi_Q]. \tag{3.47}$$

The clutter component, $\mathbf{c}[l]$, is originated by the echoes from the environment, the earth's surface, known as ground clutter. The clutter is distributed in both angle and range and is spread in Doppler frequency due to the platform motion. The clutter component consists of the superposition of returns from all ambiguous ranges within the radar horizon. In the model assumed here we suppose unambiguous range [1].

As an approximation to a continuous field of clutter, the clutter return from a single range will be modeled according to [1] as the superposition of a large number, N_c, of independent clutter sources that are uniformly distributed in azimuth about the radar. The location of the (l, p)-th clutter patch is described by its azimuth, ϕ_p, and range, R_l, (or elevation, θ_l). The corresponding spatial frequency is

$$\vartheta_{l,p} = \frac{d}{\lambda_c} \cos\theta_l \sin\phi_p. \tag{3.48}$$

The Doppler frequency of the l,p-th patch will be denoted $f_{l,p}$. The clutter component of the space-time snapshot at the l-th range is then given by

$$\mathbf{c}[l] = \sum_{p=1}^{N_c} \alpha_{l,p} \mathbf{v}(\vartheta_{l,p}, f_{l,p}), \qquad (3.49)$$

where $\alpha_{l,p}$ is the random amplitude from the l,p-th clutter patch and $\mathbf{v}(\vartheta_{l,p}, f_{l,p})$ is the space-time steering vector of the l,p-th clutter patch given by

$$\mathbf{v}(\vartheta_{l,p}, f_{l,p}) = \mathbf{b}_{l,p}(f_{l,p}) \otimes \mathbf{a}_{l,p}(\vartheta_{l,p}), \qquad (3.50)$$

where $\mathbf{a}_{l,p}(\vartheta_{l,p})$ is the corresponding steering vector of the l,p-th clutter patch with spatial frequency $\vartheta_{l,p}$ and $\mathbf{b}_{l,p}(f_{l,p})$ is the corresponding temporal steering vector of the l,p-th clutter patch with Doppler frequency $f_{l,p}$.

The contribution from the l,p-th clutter patch has a clutter to noise ratio (CNR) given by $\xi_{l,p}$. The clutter amplitudes satisfy $\mathrm{E}\left[|\alpha_{l,p}|^2\right] = \sigma_n^2 \xi_{l,p}$. Assuming that the returns from different clutter patches are uncorrelated and assuming unambiguous range, only range R_l is contributing to the clutter, the clutter space-time covariance matrix is given by

$$\mathbf{R}_c = \mathrm{E}\left[\mathbf{c}[l]\mathbf{c}^H[l]\right] = \sigma_n^2 \sum_{p=1}^{N_c} \xi_{l,p} \mathbf{v}(\vartheta_{l,p}, f_{l,p}) \mathbf{v}^H(\vartheta_{l,p}, f_{l,p}). \qquad (3.51)$$

An aircraft platform motion induces a very special structure to the clutter due to the dependence of the Doppler frequency on angle. Assuming that the velocity vector is aligned with the array axis, the clutter Doppler frequency is given by

$$f_{l,p} = \frac{2v_a}{\lambda_c} \cos\theta_l \sin\phi_p, \qquad (3.52)$$

where v_a is the platform velocity, which in terms of normalized Doppler, $\omega_{l,p} = f_{l,p}T_{PRI}$, and spatial frequency is given by

$$\omega_{l,p} = f_{l,p}T_{PRI} = \left(\frac{2v_a T_{PRI}}{d}\right)\vartheta_{l,p}. \qquad (3.53)$$

From (3.53), we can note that normalized Doppler is linear in spatial frequency, more specifically the azimuth sine, $\sin\phi_p$. With normalized coordinates the slope of the clutter line is

$$\beta_c = \frac{2v_a T_{PRI}}{d}, \qquad (3.54)$$

which represents the number of half-interelement spacings traversed by the platform during one PRI. For half-wavelength interelement spacing, $\beta_c = 4v_a/\lambda_c f_r$ is equivalently the number of times the clutter Doppler spectrum aliases into the unambiguous Doppler space. Equation (3.53) defines the relation of the presence of clutter in the angle-Doppler space. This is referred to as the clutter ridge.
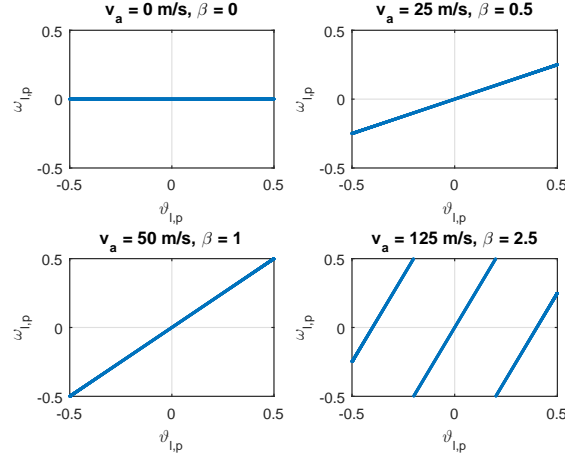
Figure 3.5: Example of clutter ridges for $\beta_c = 0$, $\beta_c = 0.5$, $\beta_c = 1.0$ and $\beta_c = 2.5$ for a PRF $= 300$ Hz.

A clutter ridge of $\beta_c = 1$ corresponds to the clutter exactly filling the Doppler space once. In general, the clutter ridge may span a portion of the Doppler space, or the whole Doppler space, depending on the platform velocity, the operating wavelength, and the radar PRF. Fig. 3.5 depicts the default case of a stationary platform ($\beta_c = 0$), an unambiguous clutter ($\beta_c \leq 1$), the clutter filling the Doppler space once ($\beta_c = 1$) and a Doppler ambiguous clutter ($\beta_c > 1$). In the Doppler ambiguous case the clutter spectrum extends over a region larger than the PRF and folds over (aliases) into the observable Doppler space. In this case there may be multiple angles at which sidelobe clutter has the same Doppler as a target. Furthermore, as β_c increases, the mainlobe clutter occupies a larger portion of the Doppler space. The more Doppler-ambiguous the clutter, the more difficult it will be to suppress it.

The total noise-clutter-interference covariance matrix $\mathbf{R} = \mathrm{E}\left[\mathbf{x}[l]\mathbf{x}^H[l]\right]$ is given by

$$\mathbf{R} = \mathbf{R}_c + \mathbf{R}_j + \mathbf{R}_n, \tag{3.55}$$

where $\mathbf{R}_c$ is given in (3.51), $\mathbf{R}_j$ is given in (3.45) and $\mathbf{R}_n$ is given in (3.41).

The output of l-th range slice of the datacube, stacked into the space-time vector $\mathbf{r}[l]$ after filtering by a space-time filter $\mathbf{w}$ is given by

$$z[l] = \mathbf{w}^H \mathbf{r}[l], \tag{3.56}$$

where $\mathbf{w} = [w_1, ..., w_M]^T \in \mathrm{C}^{M \times 1}$ is the complex weight vector of the space-time filter.

The optimal space-time filter weight vector, $\mathbf{w}$, that maximizes the probability of detection for a given P_{FA} [14] in a gaussian interference environment takes the form

$$\mathbf{w} = \beta \mathbf{R}^{-1} \mathbf{s}_{st}, \tag{3.57}$$

where $\mathbf{R}$ is the autocorrelation matrix of the clutter, jammers and noise as in (3.55), and β is a complex constant. In [14], it is proven that maximizing the SIR also maximizes the probability of detection. Therefore, different choices of β do not affect the probability of detection, since they don't alter the SIR. Nevertheless, wisely choosing β leads to some advantages that will become clear in the next section. If we set

$$\beta = \frac{1}{\mathbf{s}_{st}^H \mathbf{R}^{-1} \mathbf{s}_{st}}, \tag{3.58}$$

then the space-time filter is given by

$$\mathbf{w} = \frac{\mathbf{R}^{-1} \mathbf{s}_{st}}{\mathbf{s}_{st}^H \mathbf{R}^{-1} \mathbf{s}_{st}}, \tag{3.59}$$

which is the solution to the space-time minimum variance distortionless response (MVDR) design criterion. The optimal space-time filter normalized as in equation (3.59) is called the MVDR space-time filter.

3.3 Space-Time Metrics

In this section we will explain the most important figures of merit and metrics used to evaluate the performance of space-time filters.

(a) Adapted Pattern

Given the space-time filter $\mathbf{w}$, its response as a function of angle and Doppler is one indicator of the processor performance. That is called the adapted pattern and is given by

$$P(\vartheta, f) = |\mathbf{w}^H \mathbf{s}(\vartheta, f)|^2, \tag{3.60}$$

where $\mathbf{s}(\vartheta, f)$ is given by

$$\mathbf{s}(\vartheta, f) = \mathbf{s}_t(f) \otimes \mathbf{s}_s(\vartheta), \tag{3.61}$$

where $\mathbf{s}_s(\vartheta)$ is the spatial steering vector of the form of (3.38) and $\mathbf{s}_t(f)$ is the temporal steering vector of the form of (3.39).

The adapted pattern is a two-dimensional angle-Doppler response. The analogous of the adapted pattern in beamforming is the beampattern. Ideally, the adapted pattern has nulls in the directions of interference sources and high gain at the angle and Doppler of the presumed target direction. The shape and sidelobe levels of the adapted pattern are also of interest. The adapted pattern generated by using the matched space-time steering vector, $\mathbf{w} = \mathbf{s}_{st}$, where

$$\mathbf{s}_{st} = \mathbf{s}_t(f_t) \otimes \mathbf{s}_s(\vartheta_t), \tag{3.62}$$

where f_t and ϑ_t are the Doppler and spatial frequency of the target respectively, is commonly called the **quiescent** pattern. The quiescent pattern is the analogous to a simple Capon beamforming [15] at the target spatial angle followed by pulse integration. This process is optimal in the absence of clutter and jammers. Note that the quiescent space-time filter given by $\mathbf{w} = \mathbf{s}_{st}$ is not data dependent in the sense that it does not need data from the returned echoes for its generation. Given an arbitrary Doppler and spatial frequency it is possible to construct the quiescent filter. Its construction doesn't take into account neither the clutter nor the jammers of the scenario.

Now we will show a few simulation results to give the reader a feeling about what we discussed so far. We simulated an airborne radar with $K = 18$ elements displaced in a ULA separated by half of the carrier wavelength, which transmits $J = 18$ pulses per CPI with a PRF of 300 Hz. We included two broadband jammers (broadband in Doppler spectrum) located at $\vartheta_1 = -0.64$ and $\vartheta_2 = 0.42$ with jammer to noise ratio (JNR) per element of 38 dB and clutter uniformly distributed in azimuth, composed of $N_c = 360$ patches with clutter to noise ratio (CNR) per element per pulse of 47 dB. A target was introduced at angle $\vartheta_t = 0$ and Doppler frequency $f_t = 100$ Hz. Fig. 3.6 shows the Capon spectrum of the described interference scenario (the target is absent). The Capon spectrum, $S_C(\vartheta, f)$, is the inverse of the maximum SIR achievable, as a function of target spatial and Doppler frequencies,

$$S_C(\vartheta, f) = \frac{1}{\mathbf{s}^H(\vartheta, f)\mathbf{R}^{-1}\mathbf{s}(\vartheta, f))}. \tag{3.63}$$

The clutter is in the diagonal and the jammers are the two vertical lines.

Fig. 3.7 shows the normalized quiescent pattern using the known target's space-time steering vector $\mathbf{w} = \mathbf{s}_{st}$ in (3.60) and Fig. 3.8 shows the principal cuts at the target's coordinates in angle and Doppler. Fig. 3.9 shows the normalized adapted pattern of the space-time MVDR filter of (3.59) obtained with perfect knowledge of the interference (clutter, noise and jammer) covariance matrix in (3.60) and Fig. 3.10 shows the principal cuts at the target's coordinates in angle and Doppler. Analyzing Figs. 3.7, 3.8, 3.9 and 3.10 we can't really foresee the output SIR. It is possible to guess, though, by the position of the blue lines in Fig. 3.9, that the MVDR space-time filter severely attenuates the jammers and clutter.

(b) SIR and SIR Loss

A common metric used for analysing a space-time filter performance is the output signal-to-interference-ratio (SIR), where by interference it is understood the contribution of clutter, jammers and noise. Given the received
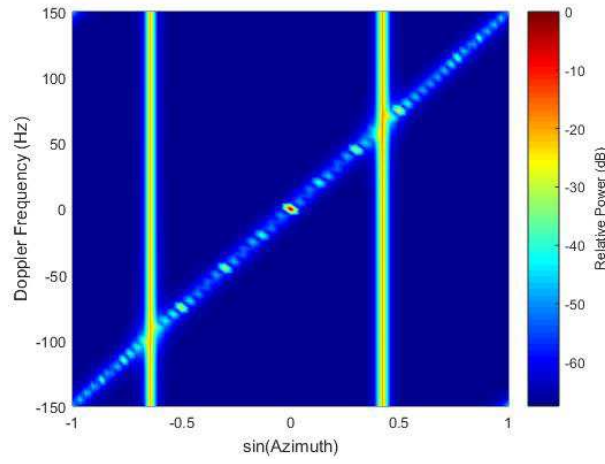
Figure 3.6: Capon spectrum of **R**.
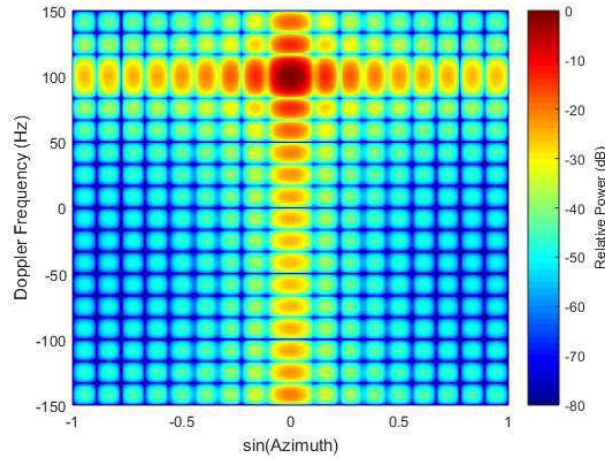
Figure 3.7: Normalized quiescent pattern.
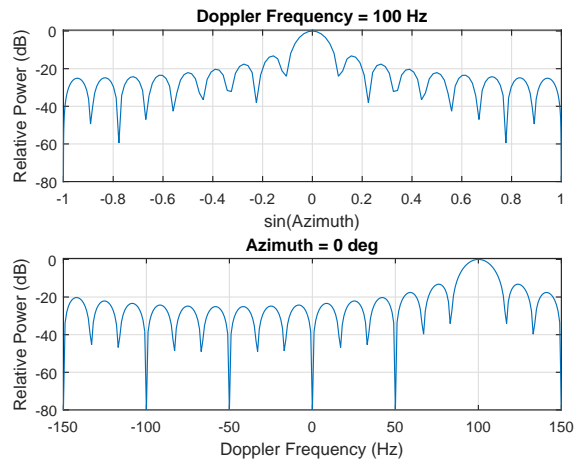
Figure 3.8: Principal cuts of the normalized quiescent pattern.
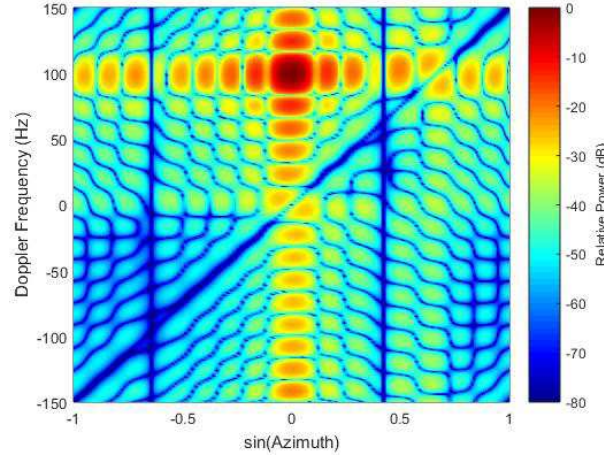
Figure 3.9: normalized adapted pattern of the space-time MVDR with perfect knowledge of the space-time covariance matrix.
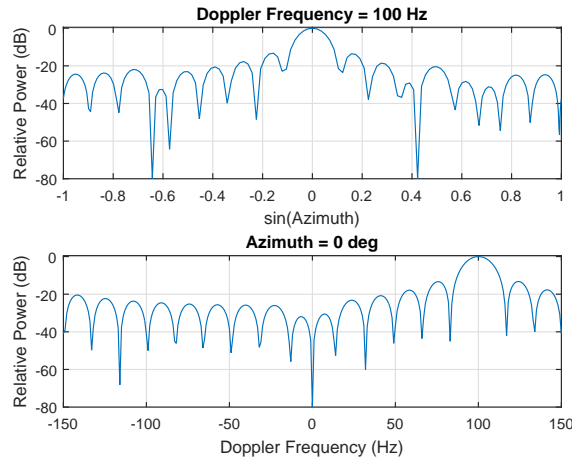
Figure 3.10: Principal cuts of the normalized adapted pattern given by the space-time MVDR with perfect knowledge of the space-time covariance matrix at the target coordinates.

signal as (3.40) under the target presence hypothesis, the output of filter $\mathbf{w}$ is given by

$$\mathbf{z}[l] = \mathbf{w}^H \mathbf{s}_{st}\alpha_l + \underbrace{\mathbf{w}^H \mathbf{i}[l] + \mathbf{w}^H \mathbf{c}[l] + \mathbf{w}^H \mathbf{n}[l]}_{\mathbf{w}^H \mathbf{x}[l]}. \tag{3.64}$$

The SIR for a target towards direction ϑ_t and Doppler frequency f_t is defined as

$$SIR = \frac{\mathrm{E}[|\mathbf{w}^H \mathbf{s}_{st}\alpha_l|^2]}{\mathrm{E}[|\mathbf{w}^H \mathbf{x}[l]|^2]} = \frac{\sigma_n^2 \xi_l |\mathbf{w}^H \mathbf{s}_{st}|^2}{\mathbf{w}^H \mathbf{R} \mathbf{w}}. \tag{3.65}$$

Substituting the optimum weight vector (3.57) into (3.65) leads to the optimum SIR given by

$$SIR_{\mathrm{op}} = \sigma_n^2 \xi_l \mathbf{s}_{st}^H \mathbf{R}^{-1} \mathbf{s}_{st}. \tag{3.66}$$

For the described example, considering $\xi_l = 1$, the quiescent space-time filter led to a SIR of -17.3 dB, while the MVDR space-time filter led to a SIR of

25 dB, which is almost the maximum gain achievable for a matched space-time filter in a noise-only scenario, that is $10\log(\xi_l KJ) = 10\log(18 \cdot 18) = 25.1$ dB. The dramatic difference between the results of both filters reveals the importance of data dependent space-time filters, and also corroborate the fact that just by visualizing the adapted pattern it is quite difficult to have an idea of what the SIR output will be.

Another common metric used in space-time literature is the SIR loss, namely L_{SIR}, defined as

$$L_{\text{SIR}} = \frac{\text{SIR}}{\text{SIR}_0},\qquad(3.67)$$

where SIR_0 is the maximum SNR achievable in a noise-only environment with an array of K elements and integration of J pulses, which is [1]

$$\text{SIR}_0 = \xi_l KJ.\qquad(3.68)$$

(c) Doppler Space Performance

The SIR is obtained for a specific angle and Doppler. If the target velocity is unknown, the interest in SIR performance is a function of the target Doppler. The metric used to evaluate the Doppler space performance is the SIR considered by holding the target spatial frequency fixed and varying the target Doppler, computing a separate space-time filter for each Doppler frequency, f. In practice, a separate space-time filter is computed for every potential target Doppler, forming a bank of space-time filters that cover the Doppler space. The number of filters is typically equal to J, the number of pulses in one CPI. Let f_j be the Doppler which the j-th space-time weighting vector, $\mathbf{w}_j$, is tuned to. Then, the Doppler performance can be computed as

$$SIR(f_j) = \frac{\sigma_n^2 \xi_l |\mathbf{w}_j^H \mathbf{s}(\vartheta_t, f_j)|^2}{\mathbf{w}_j^H \mathbf{R} \mathbf{w}_j},\qquad(3.69)$$

where $\mathbf{s}(\vartheta_t, f_j)$ is the space-time steering vector formed as in (3.61), $\mathbf{w}_j$ is equal to $\mathbf{s}(\vartheta_t, f_j)$ for the quiescent space-time filter and equal to the one defined in (3.59) substituting $\mathbf{s}_{st}$ for $\mathbf{s}(\vartheta_t, f_j)$ for the MVDR space-time filter.

The Doppler performance is usually presented using the SIR loss, computed as

$$L_{\text{SIR}}(f_j) = \frac{SIR(f_j)}{\text{SIR}_0},\qquad(3.70)$$

where SIR_0 is defined in (3.68).

Fig. 3.11 shows the Doppler performance of the quiescent and the MVDR space-time filters. We can see that the MVDR achieves about 0 dB SIR loss over the majority of the Doppler space, which is near the maximum gain on target, due to its ability to suppress both clutter and jamming, while the quiescent filter shows a poor performance. When the target is near 0 Hz or any multiple
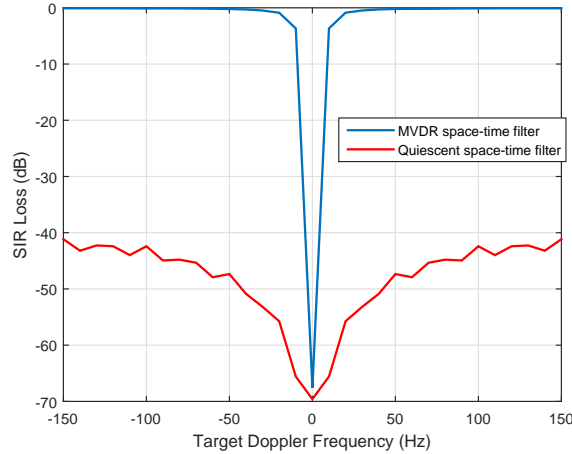
Figure 3.11: SIR Loss vs. Doppler frequency for quiescent space-time filter and MVDR space-time filter, fixed $\vartheta = 0$.

of 300 Hz, which is the radar PRF, the performance of the MVDR space-time filter degrades greatly. That is because the target falls into the null the filter places to attenuate the mainlobe clutter in both angle and Doppler.

(d) Probability of Detection

In this section we will compute the probability of detection, P_D, for a given space-time filter, $\mathbf{w}$, using the following test,

$$|\mathbf{w}^H \mathbf{r}[l]| \gtrless_{H_0}^{H_1} T, \qquad (3.71)$$

where the quantity $|\mathbf{w}^H \mathbf{r}[l]|$ is called test statistic, $\mathbf{r}[l]$ is defined in (3.40) and T is a comparison threshold. If the test statistic is greater than T, the target is said to be present (hypothesis H_1) and if it is smaller than T the target is said to be absent (null hypothesis, H_0).

The threshold T can be found in terms of the probability of false alarm, P_{FA}. The test is the magnitude of the complex random variable, $z = \mathbf{w}^H \mathbf{r}$. We assume as usual that $\mathbf{a}_q$ in (3.43) is a Gaussian vector and variables $\alpha_{l,p}$ in (3.49) are Gaussian [1]. Under hypothesis H_0, when the target is absent, the variable $x = |z|$ has the Rayleigh pdf given by [16]

$$p_x(X|H_0) = \begin{cases} \frac{2X}{\bar{X}} e^{-(X^2)/\bar{X}}, & X \geq 0 \\ 0, & X < 0 \end{cases}, \qquad (3.72)$$

where $\bar{X} = \mathrm{E}\{|z|^2\} = \mathbf{w}^H \mathbf{R} \mathbf{w}$ and $\mathbf{R}$ is defined in (3.55). Thus P_{FA} is given by

$$P_{\mathrm{FA}} = \int_T^\infty \frac{2X}{\bar{X}} e^{X^2/\bar{X}} \mathrm{d}X = e^{-T^2/\mathbf{w}^H \mathbf{R} \mathbf{w}}. \qquad (3.73)$$

From equation (3.73) we have the threshold, T,

$$T = \sqrt{-\mathbf{w}^H \mathbf{R} \mathbf{w} \ln(P_{\text{FA}})}. \tag{3.74}$$

Under hypothesis H_1, when the target is present, the variable $x = |z|$ has the Rician pdf given by [16]

$$p_x(X|H_1) = \begin{cases} \frac{2X}{\bar{X}} e^{(X^2+\mu^2)/\bar{X}} I_0\left(\sqrt{\frac{2\mu^2}{\bar{X}}}X\right), & X \geq 0 \\ 0, & X < 0 \end{cases}, \tag{3.75}$$

where $\mu = |\sigma_n \sqrt{\xi_l} \mathbf{w}^H \mathbf{s}_{st}|$ and $I_0(\cdot)$ is the modified Bessel function of first order. Thus P_{D} is given by

$$P_{\text{D}} = \int_T^\infty \frac{2X}{\bar{X}} e^{(X^2+\mu^2)/\bar{X}} I_0\left(\sqrt{\frac{2\mu^2}{\bar{X}}}X\right) \mathrm{d}X. \tag{3.76}$$

After manipulation it is possible to write (3.76) in terms of the Marcum's Q function, $Q_M(\alpha, \gamma)$, [12]

$$P_{\text{D}} = Q_M\left(\sqrt{\frac{2\mu^2}{\bar{X}}}, \sqrt{\frac{2T^2}{\bar{X}}}\right), \tag{3.77}$$

where

$$Q_M(\alpha, \gamma) = \int_\gamma^{+\infty} X e^{-(X^2+\alpha^2)/2} I_0(\alpha X) \mathrm{d}X. \tag{3.78}$$

Substituting $\bar{X} = \mathbf{w}^H \mathbf{R} \mathbf{w}$ and $\mu = |\sigma_n \sqrt{\xi_l} \mathbf{w}^H \mathbf{s}_{st}|$ into (3.77), we have

$$P_{\text{D}} = Q_M\left(\sqrt{\frac{2\sigma_n^2 \xi_l |\mathbf{w}^H \mathbf{s}_{st}|^2}{\mathbf{w}^H \mathbf{R} \mathbf{w}}}, \sqrt{\frac{2T^2}{\mathbf{w}^H \mathbf{R} \mathbf{w}}}\right). \tag{3.79}$$

Substituting T given in equation (3.74) into (3.79) and noticing that SIR $= \frac{\sigma_n^2 \xi_l |\mathbf{w}^H \mathbf{s}_{st}|^2}{\mathbf{w}^H \mathbf{R} \mathbf{w}}$, we can rewrite (3.79) as

$$P_{\text{D}} = Q_M\left(\sqrt{2\text{SIR}}, \sqrt{-2\ln(P_{\text{FA}})}\right), \tag{3.80}$$

which is the probability of detection, P_D, for a given probability of false alarm, P_{FA}, and a given space-time filter, $\mathbf{w}$, that leads to a certain SIR.

(e) Adaptive Matched Filter (AMF)

The radar system tests each range gate for a series of discrete points over the spatial and Doppler frequencies of interest, generating hypothesized space-time steering vectors as in equation (3.61), $\mathbf{s}(\vartheta_n, f_m)$. The processor usually chooses several guesses of ϑ_n and f_m equally spaced over a range of spatial and Doppler frequencies respectively. Since the target real pair (ϑ_t, f_t) is likely to be different from the tested ones, this mismatch causes the phenomenon of straddle loss.

A popular test statistic criterion is given by [17]

$$|\mathbf{w}^H\mathbf{r}[l]|^2 \underset{H_0}{\overset{H_1}{\gtrless}} T, \tag{3.81}$$

where $\mathbf{w}$ is the space-time filter, $\mathbf{r}[l]$ is defined in (3.40) and T can be found in terms of the probability of false alarm, P_{FA}. The test statistic is the magnitude square of the complex random variable, $z = \mathbf{w}^H\mathbf{r}$. Under hypothesis H_0, when the target is absent, the variable $x = |z|^2$ has the exponential pdf given by [16]

$$p_x(X|H_0) = \begin{cases} \frac{1}{X}e^{X/\bar{X}}, & X \geq 0 \\ 0, & X < 0 \end{cases}, \tag{3.82}$$

where $\bar{X} = \mathrm{E}\{|z|^2\} = \mathbf{w}^H\mathbf{R}\mathbf{w}$. Thus, the P_{FA} is given by

$$P_{\text{FA}} = \int_T^\infty \frac{1}{\bar{X}}e^{X/\bar{X}}\mathrm{d}X = e^{-T/\mathbf{w}^H\mathbf{R}\mathbf{w}}. \tag{3.83}$$

From equation (3.83) we have the threshold, T,

$$T = -\mathbf{w}^H\mathbf{R}\mathbf{w}\ln(P_{\text{FA}}). \tag{3.84}$$

Substituting the space-time filter given in equation (3.57) into the formula of T in equation (3.84), we have

$$T = -\beta^2\mathbf{s}_{st}^H\mathbf{R}^{-1}\mathbf{s}_{st}\ln(P_{\text{FA}}), \tag{3.85}$$

If we choose a normalization factor β as

$$\beta = \frac{1}{\sqrt{\mathbf{s}_{st}^H\mathbf{R}^{-1}\mathbf{s}_{st}}}, \tag{3.86}$$

and make

$$\bar{\mathbf{w}} = \frac{\mathbf{R}^{-1}\mathbf{s}_{st}}{\sqrt{\mathbf{s}_{st}^H\mathbf{R}^{-1}\mathbf{s}_{st}}}, \tag{3.87}$$

it follows that the test statistic becomes

$$|\bar{\mathbf{w}}^H\mathbf{r}[l]|^2 \underset{H_0}{\overset{H_1}{\gtrless}} T', \tag{3.88}$$

where

$$T' = \frac{-\mathbf{s}_{st}^H\mathbf{R}^{-1}\mathbf{s}_{st}\ln(P_{\text{FA}})}{\mathbf{s}_{st}^H\mathbf{R}^{-1}\mathbf{s}_{st}} = -\ln(P_{\text{FA}}). \tag{3.89}$$

From equation (3.89) we can notice that the threshold does not depend on the data, it is a constant that depends only on the desired P_{FA}. The space-time filter with the normalization of (3.86) and test statistic of the magnitude square as in (3.81) shows a constant false alarm rate (CFAR) behavior even for a fixed threshold. The use of a fixed threshold for a desired probability of false alarm is a desirable feature in practical systems. The normalized filter $\bar{\mathbf{w}}$ is also known as the space-time adaptive matched filter (AMF).

We can visualize this test statistic as an output power range profile, that
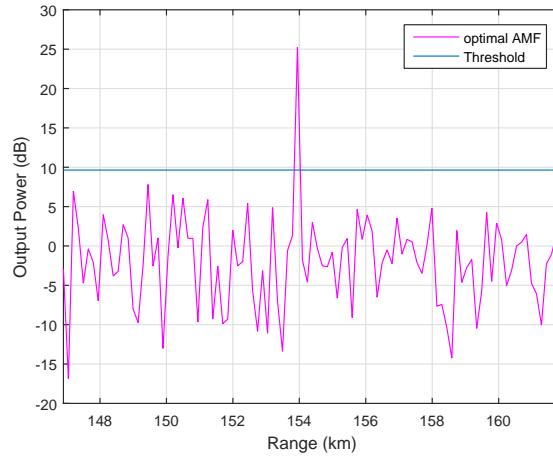
Figure 3.12: Normalized output power range profile.

shows the test statistic for each l-th range. We expect the output power range profile to show a peak at the range where the target is present, this peak should be high enough to be discernable when using a threshold for target detection.

Fig. 3.12 shows the output power range profile for the AMF space-time filter, whose normalized adapted pattern is shown in Fig. 3.9. For this scenario, a target was introduced at range 154 km and $P_{\mathrm{FA}} = 10^{-4}$. We can see that the result of the output power range profile shows a clear peak at range 154 Km, as expected.

4
Reduced Rank Array Processing

Reducing the dimensionality of the received data in array signal processing (e.g. beamforming and space-time processing) is becoming increasingly more essential, mainly due to the increasing number of sensor elements in antenna arrays, which generate prohibitively large data sets. Another issue is the small sample support available in practice for estimation of statistical quantities [1].

Most uses of STAP are related to the problems of detection, tracking or imaging [12] in radars. In this thesis, we concern ourselves with the detection problem in airborne radar systems that employ electronically scanned antennas (ESA).

In order to detect targets, i.e. uncover objects against noise, ground clutter and jamming, it is interesting to work with both spatial and temporal domains. Space-time adaptive processing (STAP) involves adaptively (or dynamically) adjusting the two-dimensional space-time filter response in an attempt to maximize output signal to interference ratio (SIR), where interference encompasses everything different from the desired signal, and consequently, improving radar detection performance. Succinctly stated, most classical STAP algorithms consist of the following steps [18]:

1. Estimating interference covariance matrix and target complex amplitude;

2. Forming a weight vector based on the inverse covariance matrix, the space-time filter;

3. Calculating the inner product of the space-time filter and the data vector from a cell under test;

4. Comparing the test statistic based on the value obtained in the former step with a threshold determined according to a specified false alarm probability.

From a practical standpoint the key issues associated to these steps include [18]:

– Sufficient target-free training data support to form an estimated interference covariance matrix;

– Non-singular estimated covariance matrix to form an weight vector;

– Computational complexity in forming the weight vector;

– The ability to maintain a constant false alarm rate (CFAR) and robust detection performance.

Reduced rank techniques are able to mitigate the nocuous effects of insufficient target-free training data support to form the estimate of the interference covariance matrix, which leads to a singular matrix that cannot be inverted, which in its turn prevents the formation of the space-time filter. Reduced rank techniques may also reduce dramatically the computational complexity, while achieving better SIR than full rank techniques in some situations [1].

The Minimum Variance Distortionless Response (MVDR) beamforming filter [10] is a well-known beamforming technique, also applied in STAP, based on the inverse of the covariance matrix. The MVDR filter exploits the second-order statistics of the interference vector to minimize the array variance while constraining the array response towards the direction of the signal of interest (SOI). The Minimum Power Distortionless Response (MPDR) beamforming filter, using the notation of [10], exploits the second-order statistics of the received vector to minimize the array output power while constraining the array response towards the direction of the SOI. When the direction of arrival (DOA) of the SOI and the interference statistics are known exactly the output of the MPDR reduces to the output of the MVDR.

There are many techniques to implement the MVDR filter with less computational load, basically to avoid the MVDR matrix inversion step, e.g. the the stochastic-gradient (SG) [19, 20] technique. But full rank algorithms usually require a large number of snapshots to reach steady-state. In large arrays arrangements, this may cause degradation in convergence speed, especially in environments where a small support of independent and identically distributed (IID) samples are available for estimation of the statistical quantities [1].

Reduced-rank techniques can mitigate the effects of these drawbacks. Principal Components (PC) [21, 22] and Cross-Spectral Metric (CSM) [13] are examples of reduced-rank filtering schemes based on eigen-decomposition. The Multistage Wiener Filter (MWF) achieves rank reduction through the Krylov subspace, which has the added benefit of a further reduction in computational complexity based for example on the Lanczos [23, 24, 25] or the Arnoldi [26, 25] algorithms, or a conjugate gradient-based (CG) implementation [27, 28], CG-MWF. Yet another rank-reducing algorithm is the Auxiliary Vector Filter (AVF) [29, 30] that generates a sequence of linear auxiliary filters that converge to the MVDR filter.

But rank reduction methods that are optimal in a statistical sense, like PC, CSM, MWF and AVF may suffer degradation from subspace leakage in small sample support scenarios [31]. Therefore suboptimal strategies to reduce the dimensionality of the received data, like the family of adaptive joint iterative optimization (JIO) algorithms [32, 33], are receiving increasingly more attention.

4.1 Interpolation-and-Decimation-based Dimensionality Reduction Scheme

In the following Chapters, 5 and 6, we apply a dimensionality reduction technique based on a joint interpolation and decimation scheme applied to beamforming and space-time processing respectively.

This dimensionality reduction strategy is composed by two stages. The first stage interpolates the array snapshots in order to generate correlation between its samples using a finite impulse response (FIR) filter. The second stage is the decimation stage, which eliminates some samples, reducing the snapshots' length. A notable point of this strategy is the elegant and effective way to design the interpolation filter. The design is such that, for a given decimation pattern, the interpolation filter maximizes the signal-to-interference-and-noise ratio (SINR) after the decimation stage.

Interpolation and decimation algorithms were extensively studied for sampling rate alteration or related applications [34]. In these algorithms, the filter is applied prior to the decimation stage in order to avoid aliasing. As the sampling rate is an important cost factor in digital signal processor implementation, so is the length of the input data an important cost factor in ever increasing sophisticated algorithms.

Professor Raimundo Sampaio Neto, in CETUC, started to investigate the interpolation and decimation concept focusing on the dimensionality reduction of the observed data prior to the digital processing algorithms. The idea was to design the interpolation filter aiming at the minimization of a certain cost function. At first, this idea originated an algorithm where the rank reducing stage is coupled with the final application filter (the detection filter for example), adaptively adjusting both the interpolation and detection filter weights. This idea proved to give excellent results at low computational cost in DS-CDMA communication scenarios using MMSE filters [35, 36, 37, 38].

Building on this concept, another strategy was later proposed: designing a filter that maximizes the signal-to-noise ratio (SNR) after the decimation stage, completely decoupled from the final application. The advantage of this stand-alone dimensionality reduction block is that it can be applied prior to

any desired application filter, for example, any kind of detection or estimation filter, without the need of redesigning it from the cost function, as it has to be done for different applications in [35, 36, 37, 38]. This work was tested in UWB communication scenarios, and had excellent results [39, 40, 41].

An evolution of this work was carried on leading to the design of a filter that maximizes the signal-to-interference-and-noise ratio (SINR), instead of only the SNR as in [39, 40, 41]. The design of this new interpolation filter is creative and effective. This method was applied for DS-CDMA and UWB communication scenarios and reported, in Portuguese, in [42] and [43]. This method will be now on called: joint interpolation and decimation scheme (JIDS).

5
JIDS Dimensionality Reduction Applied to Beamforming

In this chapter, we present the JIDS, which is a dimensionality reduction technique based on a joint interpolation and decimation scheme, and we specialize it here for beamforming applications. Investigation of the method considering the particularities of the beamforming signal model led to simplifications of the method, which allowed for a significant reduction of its overall complexity. Comparisons with renowned robust and rank reducing techniques show that the proposed approach has an excellent SINR loss performance with superior robustness and low computational complexity.

In this chapter, we recast the JIDS algorithm for beamforming applications and specialize it considering the particularities of this new scenario. We propose simplified methods for selecting the algorithm parameters and for defining the best decimation strategy: we investigate the dependence of two of the JIDS parameters, the decimation factor, F, and the interpolation filter length, L_v, and obtain a straightforward method to set the length of the interpolation filter. We also derive a new low complexity criterion for selecting the best decimation pattern. The proposed specialized JIDS for beamforming will be referred to as JIDSB.

Another concern in beamforming is robustness, which indicates how the algorithms perform under certain unfavorable situations, e.g. calibration errors, look of direction errors, distortions caused by source spreading and poor estimation of statistical quantities due to small sample support. This problem may be especially dramatic when the MPDR beamformer filter is applied. Many approaches have been proposed to improve beamformers robustness, for example, diagonal loading, linear point or derivative constraints, [44, 19, 45, 46], robust estimation using random matrices theory [47] and eigenspace-based robust beamformers [48]. It is within this context that the JIDSB algorithm is inserted.

This chapter is organized as follows. Section 5.1 describes the signal model. Section 5.2 combines the rank reduction transforms with the beamformer detection filter. Section 5.3 recasts the JIDS, specialized here for the beamforming application. The proposed simplification procedures are explained in Subsection 5.3.2 and 5.3.3. Subsection 5.3.4 addresses the computa-

tional complexity issue. The performance assessment examples of the proposed specialized and simplified JIDS (JIDSB) are provided in Section 5.4. We apply the Minimum Variance Distortionless Response (MVDR) [10] detection filter in the subspace created by the dimensionality reduction stage and compare the JIDSB results in terms of SINR loss with the full rank MVDR filter and other rank reduction techniques such as Principal Components (PC) [21, 22], Cross-Spectral Metric (CSM) [13] and the conjugate gradient-based (CG) Multistage Wiener Filter (MWF) [27, 28]. In terms of robustness, we compare the JIDSB with the former methods with diagonal loading when the MPDR [10] filter is applied. Finally, conclusions are given in Section 5.5.

5.1 System Model

We consider a beamforming application with a uniform linear array (ULA) with M elements. The sensor array vector received at the i-th time snapshot $\mathbf{r}[i] \in \mathbb{C}^{M \times 1}$ is given by

$$\mathbf{r}[i] = \mathbf{s}(\theta_0)b_0[i] + \underbrace{\mathbf{i}[i] + \mathbf{n}[i]}_{\mathbf{x}[i]}, \tag{5.1}$$

where without loss of generality, the signal of interest is represented as b_0, a complex random variable with power $E[|b_0|^2] = \sigma_0^2$ and steering vector $\mathbf{s}(\theta_0) = [1, e^{-j\frac{2\pi d}{\lambda_c}\sin(\theta_0)}, ..., e^{-j\frac{2\pi(M-1)d}{\lambda_c}\sin(\theta_0)}]^T$, where λ_c is the carrier wavelength and d is the inter-element spacing of the ULA, as depicted in Fig. 2.3. The term $\mathbf{x}[i] \in \mathbb{C}^{M \times 1}$ is the interference plus noise vector, where

$$\mathbf{i}[i] = \mathbf{A}(\mathbf{\Theta})\mathbf{b}[i], \tag{5.2}$$

$\mathbf{\Theta} = [\theta_1, ..., \theta_Q]^T \in \mathbb{R}^{Q \times 1}$ is the vector of directions of arrival of Q $(Q < M)$ narrowband interference signals impinging the ULA, $\mathbf{A}(\mathbf{\Theta}) = [\mathbf{s}(\theta_1), ..., \mathbf{s}(\theta_Q)] \in \mathbb{C}^{M \times Q}$ is the complex matrix composed of the interference steering vectors, $\mathbf{s}(\theta_k) \in \mathbb{C}^{M \times 1}$, $k = 1, ..., Q$, given by:

$$\mathbf{s}(\theta_k) = [1, e^{-j\frac{2\pi d}{\lambda_c}\sin(\theta_k)}, ..., e^{-j\frac{2\pi(M-1)d}{\lambda_c}\sin(\theta_k)}]^T. \tag{5.3}$$

The elements of vector $\mathbf{b}[i] = [b_1[i], ..., b_Q[i]]^T \in \mathbb{C}^{Q \times 1}$ are modeled as random variables from uncorrelated zero-mean, circular complex processes, with variances given by $\sigma_1^2, \sigma_2^2, ..., \sigma_Q^2$. The vector $\mathbf{n}[i] \in \mathbb{C}^{M \times 1}$ is the complex vector of sensor noise, which is assumed to be a zero-mean spatially and temporally circular complex Gaussian vector. The beamformer output is then given by

$$z[i] = \mathbf{w}^H \mathbf{r}[i], \tag{5.4}$$

where $\mathbf{w} = [w_1, ..., w_M]^T \in \mathbb{C}^{M \times 1}$ is the complex weighting vector.

The beamformer weighting vector $\mathbf{w}$ can be designed to maximize the signal-to-interference-plus-noise ratio (SINR) in $z[i]$, according to the minimum variance distortionless response criterion (MVDR) [10]

$$\min_{\mathbf{w}} \mathbf{w}^H \mathbf{R} \mathbf{w}, \text{ subject to } \mathbf{w}^H \mathbf{s}(\theta_0) = 1, \tag{5.5}$$

where $\mathbf{R} = \mathbb{E}[\mathbf{x}[i]\mathbf{x}^H[i]]$ is the autocorrelation matrix of the interference and noise. The well-known solution of (5.5) is the optimal weighting vector given by:

$$\mathbf{w}_{\text{op}} = \frac{\mathbf{R}^{-1}\mathbf{s}(\theta_0)}{\mathbf{s}^H(\theta_0)\mathbf{R}^{-1}\mathbf{s}(\theta_0)}. \tag{5.6}$$

It is easy to show that the SINR achieved with the optimal filter of (5.6) is given by

$$\text{SINR}(\mathbf{w}_{\text{op}}) = \sigma_0^2 \mathbf{s}^H(\theta_0)\mathbf{R}^{-1}\mathbf{s}(\theta_0). \tag{5.7}$$

When the autocorrelation matrix is not known *a priori* it has to be estimated from the observed data. In statistical stationary signal scenarios, the autocorrelation matrix can be estimated from the available sample support with N_s snapshots as

$$\hat{\mathbf{R}} = \frac{1}{N_s} \sum_{i=1}^{N_s} \mathbf{x}[i]\mathbf{x}^H[i]. \tag{5.8}$$

The solution in (5.6) that entails the computation of the inverse of the estimated autocorrelation matrix, $\hat{\mathbf{R}}$, is called the MVDR sample matrix inversion (SMI) beamformer [10].

The optimization problem that arises when we use the autocorrelation matrix of the whole incoming signal, $\mathbf{R} = \mathbb{E}[\mathbf{r}[i]\mathbf{r}^H[i]]$, is known as minimum power distortionless response (MPDR) [10]. The MPDR and the MVDR solutions are identical in conditions of perfect knowledge of the autocorrelation matrix and the desired steering vector. But SMI-based MPDR beamformers are known to suffer from performance degradation [10, 44, 49]. The performance degradation is due to signal cancelation, termed as signal self-nulling. This problem becomes especially dramatic in practical scenarios, when there are mismatches between the assumed array response and the true array response. This situation arises, for example, when there is a finite sample support for estimating the covariance matrix.

Diagonal loading is a popular approach to improve the MPDR-SMI beamformer robustness, it is derived by imposing an additional quadratic constraint either on the Euclidian norm of the weight vector itself or on its difference from a desired weight vector, [44]. The estimated autocorrelation matrix added with a diagonal loading $\gamma \in \mathbb{R}^+$, $\hat{\mathbf{R}}_{DL}$ is given by

$$\hat{\mathbf{R}}_{DL} = \hat{\mathbf{R}} + \gamma\mathbf{I}. \tag{5.9}$$
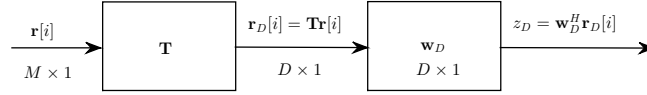
Figure 5.1: Block diagram of rank reduction stage followed by MVDR beamformer filter.

5.2 Rank Reduction Technique for Beamforming Application

Consider a rank reducing transformation matrix $\mathbf{T} \in \mathbb{C}^{D \times M}$. The observed i-th snapshot $\mathbf{r}_D[i] \in \mathbb{C}^{D \times 1}$ after the rank reduction, given by

$$\mathbf{r}_D[i] = \mathbf{Tr}[i], \tag{5.10}$$

is then processed by the beamforming filter, $\mathbf{w}_D \in \mathbb{C}^{D \times 1}$, to produce the output $z_D[i]$, given by

$$z_D[i] = \mathbf{w}_D^H \mathbf{r}_D[i]. \tag{5.11}$$

The complex weighting vector $\mathbf{w}_D = [w_1, ..., w_D]^T \in \mathbb{C}^{D \times 1}$ is designed according to the MVDR criteria for the reduced observation $\mathbf{r}_D$ and is given by

$$\mathbf{w}_D = \frac{\mathbf{R}_D^{-1} \mathbf{s_D}(\theta_0)}{\mathbf{s}_D^H(\theta_0) \mathbf{R}_D^{-1} \mathbf{s}_D(\theta_0)}, \tag{5.12}$$

where $\mathbf{R}_D = \mathbf{T}\mathbf{R}\mathbf{T}^H = \mathbb{E}[\mathbf{x}_D[i]\mathbf{x}_D^H[i]]$ is the autocorrelation matrix of the interference plus noise after the rank reducing stage, with $\mathbf{R} \in \mathbb{C}^{M \times M}$ the autocorrelation matrix of the interference plus noise of the original data and $\mathbf{s}_D(\theta_0) = \mathbf{Ts}(\theta_0)$ is the desired signal steering vector after the rank reducing stage. The block diagram of this process is illustrated in Fig. 5.1.

5.3 JIDS Rank Reduction Technique

The JIDS rank reduction technique was presented in a regional conference in Portuguese [42] for DS-CDMA and UWB communications. For the sake of completeness, this section gives an overview of the method adjusting it for the beamforming system model. In general terms, the JIDS is based on two operations: interpolation and decimation, as depicted in Fig 5.2. At the interpolation stage the i-th received snapshot $\mathbf{r}[i]$ is filtered by $\mathbf{v} \in \mathbb{C}^{L_v \times 1}$ ($L_v << M$) in order to correlate its components before the decimation stage. The decimation stage is implemented by means of a decimation matrix, $\mathbf{D}$, that selects certain components, reducing the original dimension M by a factor of F. The resulting vector length is $D = \lfloor M/F \rfloor$, where $\lfloor x \rfloor$ is the operation that selects the largest integer not greater than x. For a uniform decimation by a factor of F, there are in fact F possible patterns, $l \in \{0, ..., F-1\}$. The index l, that designates the decimation pattern, $\mathbf{D}_l \in \mathbb{C}^{D \times M}$, corresponds to the row of the first component of $\mathbf{r}[i]$ selected by the decimation block, that is
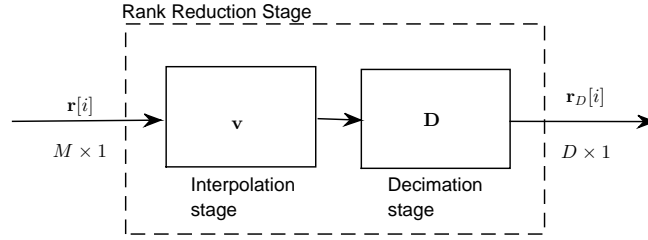
Figure 5.2: Illustration of the JIDS rank reduction stage.

$$\mathbf{D}_l = \begin{pmatrix} \phi_{l,0} \\ \phi_{l,1} \\ \vdots \\ \phi_{l,D-1} \end{pmatrix}, \tag{5.13}$$

where

$$\phi_{l,i} = [\underbrace{0, \cdots, 0}_{iF+l}, 1, 0, \cdots, 0]. \tag{5.14}$$

The JIDS rank reducing technique makes a joint choice of the interpolation filter, $\mathbf{v}_l$, and the decimation pattern, $\mathbf{D}_l$ as will be explained in the following subsection.

(a) An Effective Design of the Interpolation Filter Specialized for Beamforming

Given a decimation pattern, l, we seek the interpolation filter, $\mathbf{v}_l^*$, that maximizes the SINR at the output of the rank reduction stage. Furthermore, we also seek the decimation pattern, l^*, that results in the highest SINR among all F possible decimation patterns, $l \in \{0, \ldots, F-1\}$. The problem of choosing the decimation pattern, l^*, will be shown to simplify to a trivial comparison of scalars.

The output of the rank reducing stage using the l-th decimation pattern, at the i-th snapshot, is given by

$$
\begin{align}
\mathbf{r}_{D_l}[i] &= \mathbf{D}_l \mathcal{V}_l \mathbf{r}[i] \tag{5.15} \\
&= \mathbf{D}_l \mathcal{V}_l \left(\mathbf{s}(\theta_0) b_0[i] + \mathbf{i}[i] + \mathbf{n}[i] \right) \tag{5.16} \\
&= \mathbf{s}_{D_l} b_0[i] + \mathbf{i}_{D_l}[i] + \mathbf{n}_{D_l}[i], \tag{5.17}
\end{align}
$$

where $\mathcal{V}_l \in \mathbb{C}^{M \times M}$ is a Toeplitz matrix that implements the discrete convolution between $\mathbf{v}_l \in \mathbb{C}^{L_v \times 1}$ and $\mathbf{r}[i] \in \mathbb{C}^{M \times 1}$. The first column of $\mathcal{V}_l$ is given by $[\mathbf{v}_l^T, 0, ..., 0]^T \in \mathbb{C}^{M \times 1}$. Due to the convolution commutation property,

$$\mathcal{V}_l \mathbf{r}[i] = \mathcal{R}[i] \mathbf{v}_l, \tag{5.18}$$

where $\mathcal{R} \in \mathbb{C}^{M \times L_v}$ is a Toeplitz matrix whose first column is given by $\mathbf{r}[i] \in \mathbb{C}^{M \times 1}$. Using (5.18) we can rewrite (5.15) as

$$\mathbf{r}_{D_l}[i] = \mathbf{D}_l \mathcal{R}[i] \mathbf{v}_l. \tag{5.19}$$

Similarly, $\mathbf{s}_{D_l}$, $\mathbf{i}_{D_l}[i]$ and $\mathbf{n}_{D_l}[i]$ are defined as

$$\mathbf{s}_{D_l} = \mathbf{D}_l \mathcal{V}_l \mathbf{s}(\theta_0) = \mathbf{D}_l \mathcal{S} \mathbf{v}_l, \tag{5.20}$$

$$\mathbf{i}_{D_l}[i] = \mathbf{D}_l \mathcal{V}_l \mathbf{i}[i] = \mathbf{D}_l \mathcal{I}[i] \mathbf{v}_l, \tag{5.21}$$

$$\mathbf{n}_{D_l}[i] = \mathbf{D}_l \mathcal{V}_l \mathbf{n}[i] = \mathbf{D}_l \mathcal{N}[i] \mathbf{v}_l, \tag{5.22}$$

where $\mathcal{S} \in \mathbb{C}^{M \times L_v}$, $\mathcal{I} \in \mathbb{C}^{M \times L_v}$ and $\mathcal{N} \in \mathbb{C}^{M \times L_v}$ are Toeplitz matrices with their first columns given respectively by $\mathbf{s}(\theta_0) \in \mathbb{C}^{M \times 1}$, $\mathbf{i}[i] \in \mathbb{C}^{M \times 1}$ and $\mathbf{n}[i] \in \mathbb{C}^{M \times 1}$.

The SINR after the rank reducing stage using the l-th decimation pattern is given by (dropping the snapshot index i for convenience)

$$\text{SINR}_l = \frac{\sigma_0^2 \, \| \, \mathbf{s}_{D_l} \, \|^2}{E[\| \, \mathbf{i}_{D_l} + \mathbf{n}_{D_l} \, \|^2]}. \tag{5.23}$$

The filter $\mathbf{v}_l^*$ that maximizes (5.23) is the one that satisfies

$$\mathbf{v}_l^* = \arg \max_{\mathbf{v}} \frac{\| \, \mathbf{s}_{D_l} \, \|^2}{E[\| \, \mathbf{i}_{D_l} + \mathbf{n}_{D_l} \, \|^2]}, \tag{5.24}$$

which is equivalent to

$$\mathbf{v}_l^* = \arg \max_{\mathbf{v}} \frac{\| \, \mathbf{s}_{D_l} \, \|^2}{E[\| \, \mathbf{r}_{D_l} \, \|^2]}, \tag{5.25}$$

since

$$\begin{aligned}
\frac{E[\| \, \mathbf{r}_{D_l} \, \|^2]}{\sigma_0^2 E[\| \, \mathbf{s}_{D_l} \, \|^2]} &= \frac{E[\| \, \mathbf{s}_{D_l} b_0 + \mathbf{i}_{D_l} + \mathbf{n}_{D_l} \, \|^2]}{\sigma_0^2 \, \| \, \mathbf{s}_{D_l} \, \|^2} \\
&= \frac{\sigma_0^2 \, \| \, \mathbf{s}_{D_l} \, \|^2 + E[\| \, \mathbf{i}_{D_l} + \mathbf{n}_{D_l} \, \|^2]}{\sigma_0^2 \, \| \, \mathbf{s}_{D_l} \, \|^2} \\
&= 1 + \frac{1}{\text{SINR}_l}. \tag{5.26}
\end{aligned}$$

The numerator in (5.25) may be written as

$$\begin{aligned}
\|\mathbf{s}_{D_l}\|^2 &= \|\mathbf{D}_l \mathcal{S} \mathbf{v}_l\|^2 \tag{5.27} \\
&= \mathbf{v}_l^H \mathbf{A}_l \mathbf{v}_l, \tag{5.28}
\end{aligned}$$

where $\mathbf{A}_l \in \mathbb{C}^{L_v \times L_v}$ is the symmetric, Hermitian, non-negative matrix given by

$$\mathbf{A}_l = \mathcal{S}^H \mathbf{D}_l^H \mathbf{D}_l \mathcal{S} \tag{5.29}$$

$$= \mathcal{S}^H \mathrm{diag}(\mathbf{p}_l) \mathcal{S}. \tag{5.30}$$

The matrix $\mathrm{diag}(\mathbf{p}_l)$ is a diagonal matrix that is formed with the elements of the vector $\mathbf{p}_l$ along the main diagonal. The vector $\mathbf{p}_l$ identifies the l-th, $l \in \{0, ..., F-1\}$, decimation pattern: it has zeros at the positions where the elements will be discarded and ones where the elements will be selected, that is, the elements with indices $\{l, l + F, l + 2F, ..., l + \lfloor M/F \rfloor\}$ are retained.

The denominator in (5.25) may be written as

$$E[\| \mathbf{r}_{D_l} \|^2] = E[\| \mathbf{D}_l \mathcal{R} \mathbf{v}_l \|^2] \tag{5.31}$$

$$= \mathbf{v}_l^H \mathbf{B}_l \mathbf{v}_l, \tag{5.32}$$

where $\mathbf{B}_l \in \mathbb{C}^{L_v \times L_v}$ is a hermitian symmetric, non-negative matrix given by

$$\mathbf{B}_l = E[\mathcal{R}^H \mathbf{D}_l^H \mathbf{D}_l \mathcal{R}] \tag{5.33}$$

$$= E[\mathcal{R}^H \mathrm{diag}(\mathbf{p}_l) \mathcal{R}]. \tag{5.34}$$

The maximization problem in (5.25) can be restated as

$$\mathbf{v}_l^* = \arg\max_{\mathbf{v}} f_l(\mathbf{v}), \tag{5.35}$$

where $f_l(\mathbf{v})$ is defined as

$$f_l(\mathbf{v}) = \frac{\mathbf{v}^H \mathbf{A}_l \mathbf{v}}{\mathbf{v}^H \mathbf{B}_l \mathbf{v}} = \mathbf{v}^H \mathbf{A}_l \mathbf{v} (\mathbf{v}^H \mathbf{B}_l \mathbf{v})^{-1}. \tag{5.36}$$

The gradient of $f_l(\mathbf{v})$ is computed as

$$\nabla_{\mathbf{v}} f_l(\mathbf{v}) = -\mathbf{v}^H \mathbf{A}_l \mathbf{v} (\mathbf{v}^H \mathbf{B}_l \mathbf{v})^{-2} \mathbf{B}_l \mathbf{v} + (\mathbf{v}^H \mathbf{B}_l \mathbf{v})^{-1} \mathbf{A}_l \mathbf{v}. \tag{5.37}$$

The values that null (5.37), or equivalently,

$$-(\mathbf{v}^H \mathbf{A}_l \mathbf{v}) \mathbf{B}_l \mathbf{v} + (\mathbf{v}^H \mathbf{B}_l \mathbf{v}) \mathbf{A}_l \mathbf{v} = 0, \tag{5.38}$$

must satisfy

$$\mathbf{A}_l \mathbf{v} = \lambda \mathbf{B}_l \mathbf{v}, \tag{5.39}$$

or

$$\mathbf{F}_l \mathbf{v} = \lambda \mathbf{v}, \tag{5.40}$$

where $\mathbf{F}_l = \mathbf{B}_l^{-1}\mathbf{A}_l$ and λ is the scalar given by

$$\lambda = \frac{\mathbf{v}^H\mathbf{A}_l\mathbf{v}}{\mathbf{v}^H\mathbf{B}_l\mathbf{v}} = f_l(\mathbf{v}). \tag{5.41}$$

We can notice that (5.40) is the eigenvalue equation of matrix $\mathbf{F}_l$. Therefore, vector $\mathbf{v}$ that solves (5.40) must be the eigenvector of $\mathbf{F}_l$ associated to λ. But as can be seen comparing (5.41) with (5.36), λ is the SINR itself! Thus, in order to maximize the SINR we need to find the eigenvector associated to the largest eigenvalue of $\mathbf{F}_l$. By doing so, we are choosing the interpolation filter, $\mathbf{v}_l^*$, that will produce the maximal SINR for the l-th decimation pattern!

That is the solution to our problem of seeking the interpolation filter $\mathbf{v}_l^*$ that maximizes the SINR after the decimation stage. Now, what about our problem of seeking the decimation pattern, l^*, that results in the highest SINR among all F decimation patterns? The answer is simple, we just have to compare the largest eigenvalue of $\mathbf{F}_l$ for $l \in \{0, \ldots, F-1\}$ and select l^* as the decimation pattern that produces $\mathbf{F}_{l^*}$ with the largest eigenvalue. This process can be done in a parallel multiple branch structure with F branches, where each branch uses a different decimation pattern followed by a simple scalar comparison. By doing so, we are choosing the interpolation filter $\mathbf{v}_{l^*}^*$, that will produce the maximal SINR among all F decimation patterns!

We can now recast the JIDS for beamforming applications:

1. Construct the Toeplitz matrix of the desired steering vector $\mathbf{s}(\theta_0)$, $\mathcal{S}$;

2. Compute the $L_v \times L_v$ matrix $\mathbf{A}_l = \mathcal{S}^H\mathrm{diag}(\mathbf{p}_l)\mathcal{S}$, as in (5.30);

3. Estimate the $L_v \times L_v$ matrix $\mathbf{B}_l$ in (5.34) using N_B snapshots as

$$\hat{\mathbf{B}}_l = \frac{1}{N_B}\sum_{i=1}^{N_B}\mathcal{R}^H[i]\mathrm{diag}(\mathbf{p}_l)\mathcal{R}[i]; \tag{5.42}$$

4. Compute the $L_v \times L_v$ matrix $\hat{\mathbf{F}}_l = \hat{\mathbf{B}}_l^{-1}\mathbf{A}_l$;

5. Compute the largest eigenvalue, $\lambda_{\mathrm{max},l}$, of $\hat{\mathbf{F}}_l$;

6. Repeat steps 2 to 5 for the F possible decimation patterns and choose the decimation pattern l^* that provides the largest eigenvalue of $\hat{\mathbf{F}}_l$

$$l^* = \arg\max_l \lambda_{\mathrm{max},l}, \tag{5.43}$$
$$l \in [0, .., F-1]. \tag{5.44}$$

7. Choose the interpolation filter, $\mathbf{v}_{l^*}^*$, that corresponds to the decimation pattern, l^*, which is the eigenvector associated to the largest eigenvalue of $\hat{\mathbf{F}}_{l^*}$.

After determining $\mathbf{D}$ and $\mathcal{V}$ using the steps described above, the JIDS rank reducing transformation matrix $\mathbf{T}_J \in \mathbb{C}^{D \times M}$ is, thus, given by

$$\mathbf{T}_J = \mathbf{D}\mathcal{V}. \tag{5.45}$$

(b) Selection of the Interpolator Length

The step of selecting the interpolator length, L_v, and decimation factor, F, may require an extensive search. In this section we will examine the particularities of the beamforming scenario in order to suggest a good selection for those parameters adjustments.

Previous researches in scenarios where the observed data is corrupted only by white noise [39], showed that the best results occurred for interpolation filter lengths equal to the decimation factor, $L_v = F$. This may be explained by the fact that, $L_v = F$ is the filter length that combines the largest number of samples while preserving the statistical characteristics of the white noise vector. For this choice of L_v, the time interval between the preserved noise samples is greater than the memory of the interpolator filter and the white noise vector remains white after filtering and decimation operations.

That is a good starting point for investigating the parameters setting in beamforming scenarios as well. It is to be expected that in cases where the jammer-to-noise-ratio (JNR) is very low, using $L_v = F$ is the best choice, as it approaches the white noise scenario. In scenarios where the JNR is very high it may not be the best setting, but it may still be a good choice. We checked this through extensive computer simulations and verified that, for beamforming applications, setting $L_v = F$ is indeed a good setting. In this subsection we will show only two representative results for illustration purposes.

We simulated a beamforming scenario consisting of: $M = 64$ elements; signal of interest (SOI) at 0° and SNR $= 10$ dB. We varied the number of jammers and their JNR and evaluated the SINR loss for the decimation factors of 2, 4, 8 and 16 for a range of filter lengths. The SINR loss (L_{SINR}) was computed as

$$L_{\text{SINR}} = \frac{\|\mathbf{w}_D^H \mathbf{s}_D\|^2}{(\mathbf{w}_D^H \mathbf{R}_D \mathbf{w}_D)(\mathbf{s}^H(\theta_0)\mathbf{R}^{-1}\mathbf{s}(\theta_0))}, \tag{5.46}$$

where $\mathbf{R}$ is the true autocorrelation of the noise and interference known a
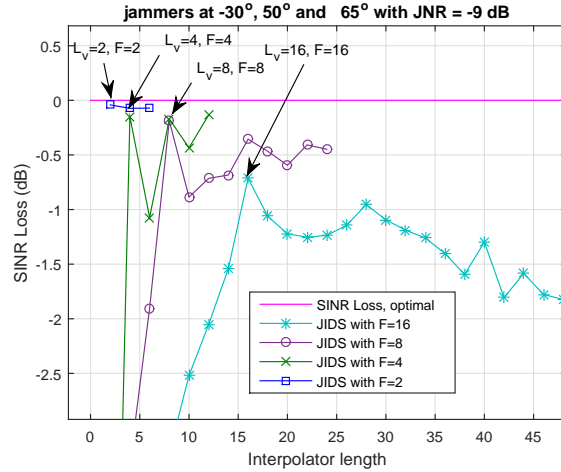
Figure 5.3: SINR loss as a function of the filter lengths, L_v, for different decimation factor, F, for an array with $M = 64$ elements, SNR = 10 dB and 3 jammers with JNR = -9 dB.

priori and

$$\mathbf{R}_D = \mathbf{T}_J \mathbf{R} \mathbf{T}_J^H, \tag{5.47}$$

$$\mathbf{w}_D = \frac{\mathbf{R}_D^{-1}\mathbf{s}_D(\theta)}{\mathbf{s}_D^H(\theta)\mathbf{R}_D^{-1}\mathbf{s}_D(\theta)}, \tag{5.48}$$

$$\mathbf{s}_D = \mathbf{T}_J\mathbf{s}(\theta_0), \tag{5.49}$$

where $\mathbf{T}_J$ is defined in (5.45). The number of training samples for estimating $\mathbf{B}_l$ is $N_B = 128$, averaged over 200 Montecarlo trials.

In Fig. 5.3 we simulated three jammers impinging on the ULA at angles -30°, 50° and 65°. All jammers have a JNR of -9 dB. One can see that for all decimation factors, F, the lowest SINR losses occur for filter lengths set as $L_v = F$, as we expected. The arrows in the figure indicate where the interpolator lengths are equal to the decimation factors. The presentation of the SINR loss in dB is equivalent to $10\log_{10}(L_{\mathrm{SINR}})$.

In Fig. 5.4 we simulated four jammers impinging on the ULA at angles -60°, -30°, 10° and 50°. All jammers have a high JNR of 15 dB. One can see that for all decimation factors, except for $F = 4$ (which is not the best reduction factor for this scenario anyway), the lowest SINR losses occur for filter lengths $L_v = F$. The arrows in the figure indicate where the interpolator lengths are equal to the decimation factors.

This procedure of setting $L_V = F$ avoids the additional step of jointly optimizing the filter length and the decimation factor. We, therefore, only need to optimize the decimation factor.
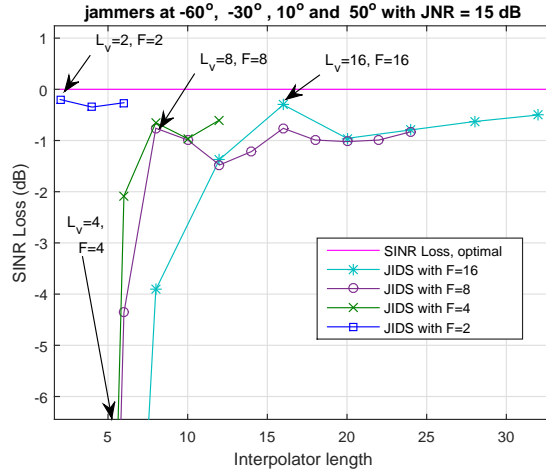
Figure 5.4: SINR loss as a function of the filter lengths, L_v, for different decimation factor, F, for an array with $M = 64$ elements, SNR $= 10$ dB and 4 jammers with JNR $= 15$ dB.

(c) JIDS Simplification for Beamforming Environment - JIDSB

Deeper investigation of the ULA structure into the JIDS revealed that the JIDS can be further simplified. In this context, we propose a low complexity criterium for selecting the best decimation pattern for ULAs. Considering the structure of the steering vector in a ULA, we can, instead of selecting the decimation pattern related to the largest eigenvalue, $\lambda_{\max,l}$, of $\mathbf{F}_l$, among all decimation patterns, $l \in \{0, .., F-1\}$, select the decimation pattern, l^*, that corresponds to the largest trace of $\mathbf{F}_l$, denoted $tr(\mathbf{F}_l)$,

$$l^* = \arg\max_{l} \{tr(\mathbf{F}_l)\}, \tag{5.50}$$

$$l \in \{0, \ldots, F-1\}. \tag{5.51}$$

This procedure leads to similar performance and avoids the need of eigenvalue decompositions during the decimation pattern decision process. The trace of $\mathbf{F}_l$ (which is equal to the sum of all eigenvalues of $\mathbf{F}_l$) is approximately equal to the largest eigenvalue of $\mathbf{F}_l$, because, when using the length of the interpolation filter L_v equal to the reduction factor F, the rank of $\mathbf{F}_l$ is at most two, meaning that $\mathbf{F}_l$ has at most two non-zero eigenvalues.

Proof: The rank of $\mathbf{F}_l = \mathbf{B}_l^{-1}\mathbf{A}_l$ is upper bounded by the minimum between the rank of $\mathbf{B}_l^{-1}$ and $\mathbf{A}_l$. Since $\mathbf{B}_l$ is invertible, $\mathbf{B}_l$ is a full rank matrix, leaving us with the analysis of $\mathbf{A}_l$. Matrix $\mathbf{A}_l$ can be written as

$$\mathbf{A}_l = \mathbf{A}_{D_l}^H \mathbf{A}_{D_l}, \tag{5.52}$$

where

$$\mathbf{A}_{D_l} = \mathbf{D}_l \mathcal{S}. \tag{5.53}$$

The application of the JIDS in beamforming allows us to use the structure of the steering vector $\mathbf{s}(\theta_0) = [s_0, s_1, \ldots, s_{M-1}]^T$ to go deeper into the structure of $\mathbf{A}_{D_l}$. Matrix $\mathcal{S} \in \mathbb{C}^{M \times L_v}$ is Toeplitz i.e.,

$$\mathcal{S} = \begin{pmatrix} s_0 & 0 & \ldots & 0 \\ s_1 & s_0 & \ldots & 0 \\ \vdots & \vdots & \vdots & \vdots \\ s_{L_v-1} & s_{L_v-2} & \ldots & s_0 \\ \vdots & \vdots & \vdots & \vdots \\ s_{M-1} & s_{M-2} & \ldots & s_{M-L_v} \end{pmatrix}, \tag{5.54}$$

with its element, $\mathcal{S}_{p,q}$, at the p-th row, $p \in \{0, \ldots, M-1\}$, and q-th column, $q \in \{0, \ldots, L_v - 1\}$, formed by

$$\mathcal{S}_{p,q} = \begin{cases} s_{p-q}, & p \geq q \\ 0, & \text{otherwise.} \end{cases} \tag{5.55}$$

The m-th element, s_m, of the steering vector $\mathbf{s}(\theta_0) \in \mathbb{C}^{M \times 1}$ corresponds to the signal impinging on the m-th antenna element and is given by

$$s_m = e^{-j\frac{2\pi d}{\lambda_c} m \sin(\theta_0)}, \quad m \in \{0, \ldots, M-1\}. \tag{5.56}$$

Substituting (5.56) into (5.55),

$$\mathcal{S}_{p,q} = \begin{cases} e^{-j\frac{2\pi d}{\lambda_c}(p-q)\sin(\theta_0)}, & p \geq q \\ 0, & \text{otherwise,} \end{cases} \tag{5.57}$$

or equivalently

$$\mathcal{S}_{p,q} = \begin{cases} e^{\alpha p} e^{-\alpha q}, & p \geq q \\ 0, & \text{otherwise,} \end{cases} \tag{5.58}$$

where

$$\alpha = -j\frac{2\pi d}{\lambda_c}\sin(\theta_0). \tag{5.59}$$

We can then rewrite the "tall" matrix $\mathcal{S}$ as

$$
\mathcal{S} = \begin{pmatrix}
e^{\alpha 0}e^{-\alpha 0} & 0 & \cdots & 0 \\
e^{\alpha 1}e^{-\alpha 0} & e^{\alpha 1}e^{-\alpha 1} & \cdots & 0 \\
\vdots & \vdots & \vdots & \vdots \\
e^{\alpha(L_v-1)}e^{-\alpha 0} & e^{\alpha(L_v-1)}e^{-\alpha 1} & \cdots & e^{\alpha(L_v-1)}e^{-\alpha(L_v-1)} \\
\vdots & \vdots & \vdots & \vdots \\
e^{\alpha(M-1)}e^{-\alpha 0} & e^{\alpha(M-1)}e^{-\alpha 1} & \cdots & e^{\alpha(M-1)}e^{-\alpha(L_v-1)}
\end{pmatrix}. \tag{5.60}
$$

Matrix $\mathcal{S} \in \mathbb{C}^{M \times L_v}$ has at most L_v linearly independent rows. Indeed, from (5.60), we note that the $M - L_v$ last rows of $\mathcal{S}$ are linearly dependent: they can be expressed as the multiplication of the row vector, $[e^{-\alpha 0}, e^{-\alpha 1}, \dots, e^{-\alpha(L_v-1)}]$, by a complex scalar. This means that the L_v linearly independent rows of $\mathcal{S}$ are precisely the first L_v rows of $\mathcal{S}$.

After decimation using the l-th uniform pattern, the i-th row of the resulting matrix $\mathbf{A}_{D_l}$, denoted $\mathbf{A}_{D_l}(i, :)$, corresponds to the $(iF + l)$-th row of matrix $\mathcal{S}$, denoted $\mathcal{S}(iF + l, :)$,

$$
\begin{aligned}
\mathbf{A}_{D_l}(i, :) &= \mathcal{S}(iF + l, :), \tag{5.61} \\
i &\in \{0, \dots, D - 1\} \\
l &\in \{0, \dots, F - 1\}.
\end{aligned}
$$

Using $L_v = F$, the l-th uniform decimation pattern, $l \in [0, \dots, F - 2]$ has two linearly independent rows, while decimation pattern $l = F - 1$ has only one linearly independent row. Therefore, the rank of $\mathbf{F}_l$ is limited by the rank of $\mathbf{A}_l$ which in turn is limited by the rank of $\mathbf{A}_{D_l}$, consequently the rank is at most two. This finishes the proof that $\mathbf{F}_l$ has at most two nonzero eigenvalues.

As a result, we can choose the $\mathbf{F}_l$, $l \in \{0, \cdots, F-1\}$, which has the largest trace (which is equal to the sum of all eigenvalues), instead of the one that has the largest eigenvalue without any meaningful performance degradation. ∎

To compute the trace of $\mathbf{F}_l$, we can use the fact that the trace of a matrix $\mathbf{C} = \mathbf{AB}$, with $\mathbf{A}, \mathbf{B}, \mathbf{C} \in \mathbb{C}^{N \times N}$, is given by $tr(\mathbf{C}) = \sum_{i=0}^{N-1} \mathbf{A}(i, :)\mathbf{B}(:, i)$, where $\mathbf{A}(i, :)$ denotes the i-th row of $\mathbf{A}$ and $\mathbf{B}(:, i)$ denotes the i-th column of $\mathbf{B}$. Thus the trace of $\mathbf{F}_l$ is computed as

$$
tr(\mathbf{F}_l) = \sum_{i=0}^{L_v-1} \mathbf{B}_l^{-1}(i, :)\mathbf{A}_l(:, i). \tag{5.62}
$$

A representative result is depicted in Fig. 5.5, showing that the proposed decimation pattern selection procedure is in good agreement with the original one. In Fig. 5.5 we simulate a ULA wiht $M = 64$ elements; signal of interest
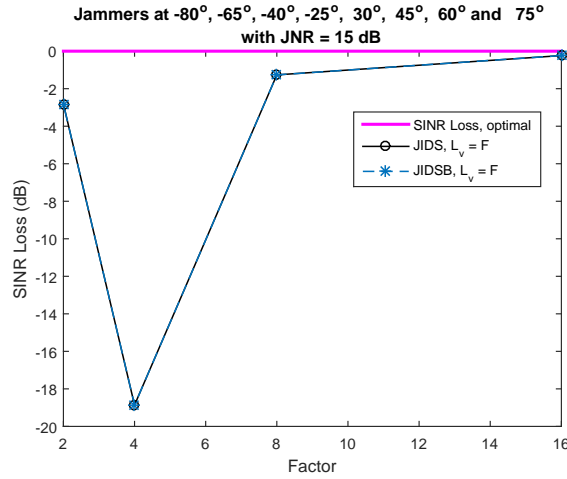
Figure 5.5: SINR loss as a function of the decimation factor, F, for the proposed and the optimal decimation pattern selection strategies for an array with $M = 64$ elements, SNR = 10 dB and 8 jammers with JNR = 15 dB.

(SOI) at 0°, SNR = 10 dB; 8 jammers impinging at angles -80°, -65°, -40°, -25°, 30°, 45°, 60° and 75° with a JNR of 15 dB each. We selected the interpolator length, $L_v = F$, as described in subsection 5.3.2.

The algorithm JIDS specialized for beamforming with the proposed simplification is named the JIDSB rank reduction algorithm.

(d) Computational Complexity

In this subsection, we discriminate the computational complexity of the algorithms: JIDS and the JIDSB, which is the JIDS with the specialization and simplification for beamforming environment described in Subsection 5.3.3. We also compare the total computational complexity of the JIDSB algorithm applied for reducing the rank of the MVDR-SMI beamformer (JIDSB-SMI) against the gradient-based multistage Wiener filter (CG-MWF), which is known to have a reduced computational complexity.

The main steps of the proposed algorithms take place in a lower dimensional subspace, because the practical effect of the decimation matrix $\mathbf{D}_l$ is to select just D lines of $\mathcal{S}$ and $\mathcal{R}[i]$. Thus, the computation of matrices $\mathbf{A}_l = \mathcal{S}^H \mathbf{D}_l^H \mathbf{D}_l \mathcal{S}$ and $\hat{\mathbf{B}}_l[i] = \mathcal{R}^H[i] \mathbf{D}_l^H \mathbf{D}_l \mathcal{R}[i]$ are reduced to the multiplication of two matrices of size $D \times L_v$. Table 5.1 shows the computational complexity of the main parts of the JIDS algorithm and Table 5.2 shows the computational complexity of the main parts of the JIDSB algorithm.

Fig. 5.6 shows how the computational complexity of the stage of decimation pattern selection is decreased by the simplification described in Subsection 5.3.3 as a function of the reduction factor F. In order to assess the number of operations required for finding the eigenvector associated with the largest

Table 5.1: Complex operations of the JIDS.

Algorithm main steps	Multiplications	Additions
Computation of $\mathbf{A}_l$	FDL_v^2	$F(D-1)L_v^2$
Estimation of $\mathbf{B}_l$	$N_B FDL_v^2 + FL_v^2$	$N_B F(D-1)L_v^2 + (N_B - 1)FL_v^2$
Inversion of $\mathbf{B}_l$	$O(FL_v^3)$	$O(FL_v^3)$
Computation of $\mathbf{F}_l$	FL_v^3	$F(L_v - 1)L_v^2$
Eigenvalue decomposition	$O(FL_v^3)$	$O(FL_v^3)$

Table 5.2: Complex operations of the JIDSB.

Algorithm main steps	Multiplications	Additions
Computation of $\mathbf{A}_l$	FDL_v^2	$F(D-1)L_v^2$
Estimation of $\mathbf{B}_l$	$N_B FDL_v^2 + FL_v^2$	$N_B F(D-1)L_v^2 + (N_B - 1)FL_v^2$
Inversion of $\mathbf{B}_l$	$O(FL_v^3)$	$O(FL_v^3)$
Computation of $tr(\mathbf{F}_l)$	FL_v^2	$F(L_v^2 - 1)$
Computation of $\mathbf{F}_l$	L_v^3	$(L_v - 1)L_v^2$
Eigenvalue decomposition	$O(L_v^3)$	$O(L_v^3)$

eigenvalue of a $N \times N$ matrix we used the power method [25], which takes N_{it} iterations and involves $N_{\text{it}}N^2$ complex multiplications and $N_{\text{it}}N(N-1)$ complex additions. For both algorithms (JIDS and JIDSB), we set the filter length equal to the reduction factor, $L_v = F$ and $N_{\text{it}} = 5$. We can see that the proposed simplification significantly reduces the number of complex operations for the stage of decimation pattern selection.

Tables 5.3 and 5.4 show step by step how the JIDSB-SMI and the CG-MWF algorithms implement the MVDR beamformer respectively. The rank of the CG-MWF algorithm, D_{MWF}, is the number of basis vectors used to describe the Krylov subspace of the estimated covariance matrix, $\hat{\mathbf{R}}$ [27]. Tables 5.5 and 5.6 shows the number of operations needed to complete all the steps described in Tables 5.3 and 5.4. In order to assess the number of operations required to compute the inverse of a $N \times N$ matrix we used the Gauss-Jordan method that takes $2N^3/6 + 3N^2/6 - 5N/6$ complex multiplications and additions.

In Fig. 5.7, according to Tables 5.5 and 5.6, we compare the computational complexity of the JIDSB algorithm with the CG-MWF for different decimation factors, F, for different sizes of sample support, N_s. We set $D_{\text{MWF}} = 30$, as it leads to good performance in small sample supports, as can be verified in Section 5.4. The number of elements in the array is set to $M = 64$, $N_{\text{it}} = 5$ and the number of snapshots, N_B, used to estimate $\mathbf{B}_l \in \mathbb{C}^{L_v \times L_v}$ is the total number of snapshots available, $N_B = N_s$. We can note from Fig. 5.7 that the JIDSB has a remarkably smaller computational complexity than the CG-MWF for factors $F = 2$ and $F = 4$. For $F = 8$, the complexity is notably lower for smaller sample supports and it is almost the same as the computa-
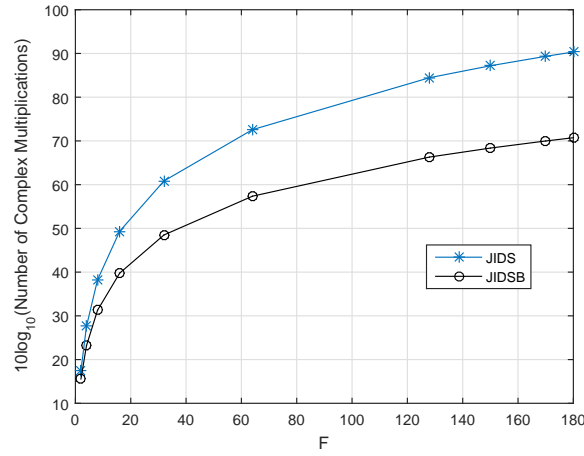
Figure 5.6: Comparison of the number of complex multiplications of the stage of decimation pattern selection of the JIDS and JIDSB for $L_v = F$ and $N_{\mathrm{it}} = 5$.

Table 5.3: JIDSB-SMI Strategy

initialization $\hat{\mathbf{R}}_D(0) = \mathbf{0}_{D \times D}$, F
$\mathcal{S} = \mathrm{Toeplitz}(\mathbf{s}(\theta_0))$
JIDSB for rank reduction
for $l = 1, \dots, F$
$\quad \mathbf{p}_l = l$-th fixed decimation pattern,
$\quad \mathbf{A}_l = \mathcal{S}^H \mathrm{diag}(\mathbf{p}_l)\mathcal{S}$,
$\quad \hat{\mathbf{B}}_l = \frac{1}{N_B} \sum_{i=1}^{N_B} \mathcal{R}^H[i]\mathrm{diag}(\mathbf{p}_l)\mathcal{R}[i]$,
$\quad$ where $\mathcal{R}[i] = \mathrm{Toeplitz}(\mathbf{x}[i])$
end
$l^* = \arg\max_l \sum_{i=1}^{L_v} \mathbf{B}_l^{-1}(i,:)\mathbf{A}_l(:,1)$,
$\hat{\mathbf{F}}_{l^*} = \hat{\mathbf{B}}_{l^*}^{-1}\mathbf{A}_{l^*}$
$\mathbf{v}$ = eigenvector associated with the largest eigenvalue of $\hat{\mathbf{F}}_{l^*}$
$\mathcal{V} = \mathrm{Toeplitz}(\mathbf{v})$
$\mathbf{D}$ is constructed according to (5.13)
MVDR-SMI after rank reduction stage
$\mathbf{T}_D = \mathbf{D}\mathcal{V}$
$\mathbf{s}_D = \mathbf{T}_D\mathbf{s}(\theta_0)$
$\hat{\mathbf{R}}_D = \frac{1}{N_s} \sum_{i=1}^{N_s} \mathbf{T}_D\mathbf{r}[i]\mathbf{r}^H[i]\mathbf{T}_D^H = \mathbf{T}_D\hat{\mathbf{R}}\mathbf{T}_D^H$
$\mathbf{w}_D = \hat{\mathbf{R}}_D^{-1}\mathbf{s}_D / \mathbf{s}_D^H\hat{\mathbf{R}}_D^{-1}\mathbf{s}_D$

Table 5.4: CG-MWF Strategy

initialization $\mathbf{u}_1 = -\mathbf{g}_0 = \mathbf{s}(\theta_0)$, $\gamma_0 = \|\mathbf{g}_0\|^2$, $\mathbf{w}_0 = \mathbf{0}_{M \times 1}$, $K = D$ $\hat{\mathbf{R}} = \frac{1}{N_s}\sum_{i=1}^{N_s} \mathbf{x}[i]\mathbf{x}^H[i]$
CG-MWF   **for each iteration $k = 1,\ldots,K$** $\mathbf{v}_k = \hat{\mathbf{R}}\mathbf{u}_k$ $\eta_k = \frac{\gamma_{k-1}}{\mathbf{u}_k^H \mathbf{v}_k}$ $\mathbf{w}_k = \mathbf{w}_{k-1} + \eta_k \mathbf{u}_k$ $\mathbf{g}_k = \mathbf{g}_{k-1} + \eta_k \mathbf{v}_k$ $\gamma_k = \|\mathbf{g}_k\|^2$ $\mathbf{u}_{k+1}[i] = -\mathbf{g}_k[i] + \frac{\gamma_{k-1}}{\gamma_k}\mathbf{u}_k$
Output: $\mathbf{w}_{\text{CG-MWF}} = \frac{\mathbf{w}_K}{\mathbf{s}^H(\theta_0)\mathbf{w}_K}$

Table 5.5: Complex products of the JIDSB-SMI and CG-MWF algorithms.

Algorithm	Multiplications
JIDSB-SMI	$(N_s + 1)DM + D^2(N_s + 2) + 2D$ $+2D^3/6 + 3D^2/6 - 5D/6$ $+FDL_v^2(1 + N_B) + L_v^2(2F + N_{\text{it}}) + L_v^3$ $+2FL_v^3/6 + 3FL_v^2/6 - 5FL_v/6$
CG-MWF	$(N_s + 1)M^2 + D_{\text{MWF}}(M^2 + 5M + 2) + 4M$

Table 5.6: Complex additions of the JIDSB-SMI and CG-MWF algorithms.

Algorithm	Additions
JIDSB-SMI	$N_sD(M - 1) + N_sD^2 + D(M - 1) - 1$ $+2D^3/6 + 3D^2/6 - 5D/6$ $+FDL_v^2(1 + N_B) - L_v^2(F + 1) - F + N_{\text{it}}L_v(L_v - 1)$ $+L_v^3 + 2FL_v^3/6 + 3FL_v^2/6 - 5FL_v/6$
CG-MWF	$M^2(N_s - 1) + D_{\text{MWF}}(M^2 + 4M - 2) + 2(M - 1)$

tional complexity of the CG-MWF for larger sample supports. For $F = 16$, the JIDSB has a significantly greater computational complexity, that is because for this pair of array size, M, and factor, F, the JIDSB pre-processing steps take place in a not so reduced subspace, increasing significantly the computational complexity.

5.4 Simulations

In this section, we compare the performance results in terms of SINR loss *vs.* sample support of the JIDSB with renowned rank reducing algorithms. We apply the MVDR detection filter with and without diagonal loading. In order to assess the JIDSB robustness, we compare results of the MPDR detection filter (which is the MVDR solution when the desired signal is present during estimation of the autocorrelation matrix) for the JIDSB and the other rank
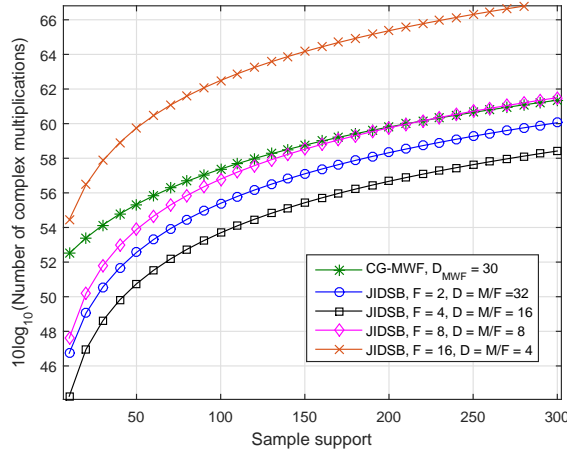
Figure 5.7: Comparison of the number of complex multiplications of the JIDSB with the CG-MWF as a function of the sample support, N_s, for $F = \{2, 4, 8, 16\}$, $M = 64$, $N_{\text{it}} = 5$, $D_{\text{MWF}} = 30$ and $N_B = N_s$.

reducing algorithms with diagonal loading. We illustrate all the algorithm's beampattern and we also simulate a communication application and present results in terms of bit error rate (BER) performance.

At first, we evaluate the SINR loss performance of the proposed JIDSB-SMI algorithm and compare it with the performance of the JIDS-SMI, PC-SMI, CSM-SMI and a gradient-based multistage wiener filter (CG-MWF) algorithm. The PC-SMI and CSM-SMI algorithms follow the same structure of the JIDS-SMI as explained in Section 5.2: the received array snapshots go through the rank reduction stage and then are used to estimate the lower dimension covariance matrix which is then inverted and used in the computation of the MVDR or MPDR filter. The rank of the PC-SMI algorithm is the number of vectors used to form the subspace, which is spanned by the D eigenvectors of the estimated covariance matrix, $\hat{\mathbf{R}}$, associated with the D largest eigenvalues [21]. The rank of the CSM-SMI algorithm is the number of vectors used to form the subspace, which is spanned by the D eigenvectors of the estimated covariance matrix, $\hat{\mathbf{R}}$, that maximizes the cross spectral metric [13]. The rank of the CG-MWF algorithm is the number of basis vectors used to describe the Krylov subspace of the estimated covariance matrix, $\hat{\mathbf{R}}$ [27]. The CG-MWF algorithm converges to the MVDR or MPDR result without the need of inverting the estimated covariance matrix, $\hat{\mathbf{R}}$. The rank of the JIDSB-SMI is $\lfloor M/F \rfloor = D$, which is the final length of the vectors after the rank reduction stage.

The mean SINR loss, $L_{\text{SINR}} = \text{SINR}/\text{SNR}_0$, where the SINR is computed as

$$\text{SINR} = \frac{\sigma_0^2 \text{E}\left\{|\mathbf{w}^H \mathbf{T} \mathbf{s}(\theta_0)|^2\right\}}{\text{E}\left\{\mathbf{w}^H \mathbf{T} \mathbf{R} \mathbf{T}^H \mathbf{w}\right\}}, \tag{5.63}$$

where $\mathbf{w}$ is the beamforming filter, $\mathbf{T}$ is the rank reducing transformation (applied when necessary), $\text{SNR}_0 = \mathbf{s}^H(\theta_0)\mathbf{R}^{-1}\mathbf{s}(\theta_0)$, $\mathbf{R}$ is the true autocorrelation matrix of noise and interference and the expectation , $E\{\cdot\}$, is estimated by averaging 200 Montecarlo runs. Note that although $\mathbf{R}$ is the true autocorrelation matrix, $\mathbf{w}$ and $\mathbf{T}$ are computed using the estimated $\mathbf{R}$, $\hat{\mathbf{R}}$, and are, therefore, stochastic quantities.

In these simulations we adopt a uniform linear array (ULA) consisting of $M = 64$ sensor elements whose inter-element spacing is half a signal wavelength. The signal of interest (SOI) is at 0°. We simulate two scenarios and compare the algorithms SINR loss for different sample supports. In the first scenario, there are two narrowband jammers impinging at angles 30° and 50° and for the second scenario, there are 6 narrowband jammers impinging at angles -65°, -40°, -25°, 30°, 45° and 60° . Each jammer has a JNR of 15 dB.

For both scenarios, we examine the case when the amount of diagonal loading is set to $\gamma = \sigma_n^2$ in (5.9), just in order to avoid computational instabilities in the algorithms and the case when the diagonal loading is set as $\gamma = 10\sigma_n^2$, which is empirically shown in [50] to be a suitable value. We compare the former case using two different detection filters: the MVDR, when the desired signal is not present during estimation of the covariance matrix and the MPDR, when the desired signal is present during the autocorrelation matrix estimation.

For all simulations the JIDS and JIDSB had equivalent performances, as expected, so in the following we will mention only the JIDSB. Figs 5.8 and 5.11 show the SINR loss *vs.* sample support with a diagonal loading of σ_n^2. We can see that the JIDSB had an impressive superior performance compared to full rank MVDR-SMI, CG-MWF, CSM-SMI and PC-SMI algorithms.

Figs. 5.9 and 5.12 show the SINR loss *vs.* sample support with a diagonal loading of $10\sigma_n^2$. As expected, all algorithms improved their convergence rate when compared to the case of a diagonal loading of σ_n^2 depicted in Figs 5.8 and 5.11. Even with the great improvement of the full rank MVDR-SMI and CG-MWF, the proposed JIDSB still had similar performance, with a significantly lower computational complexity for the case of Fig. 5.12 (L=F=2) and a lower computational complexity for small sample supports and similar computational complexity as the CG-MWF for large sample supports for the case of Fig. 5.9 (L=F=8), as can be verified in Fig. 5.7.

Now we examine what happens when the desired signal is present in the observed data during estimation of the autocorrelation matrix. Figs 5.10 and 5.13 show how the performance is affected by the self-nulling when the
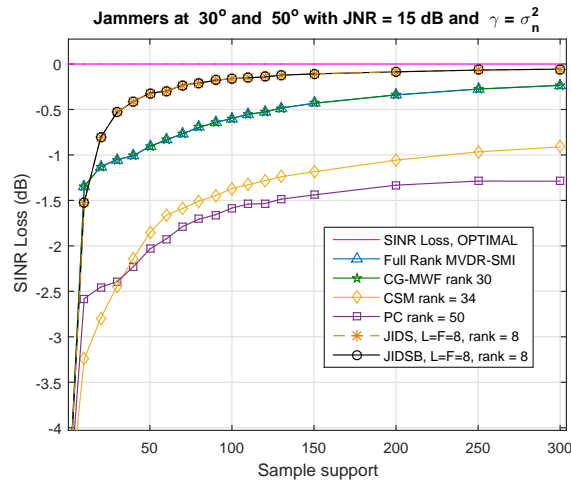
Figure 5.8: Output SINR loss versus the sample support with $M = 64$, 2 jammers with JNR = 15 dB and $\gamma = \sigma_n^2$.
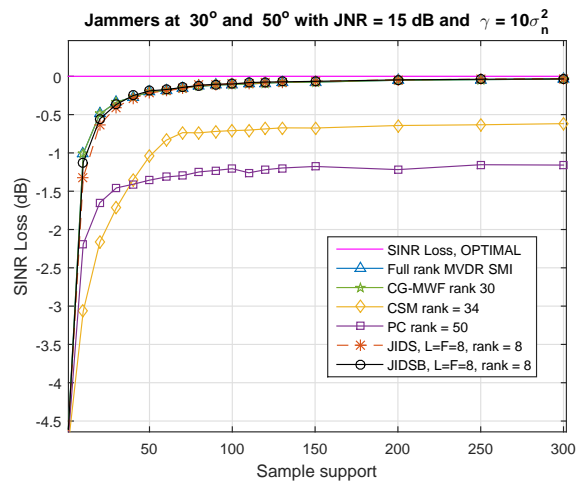
Figure 5.9: Output SINR loss versus the sample support with $M = 64$, 2 jammers with JNR = 15 dB and $\gamma = 10\sigma_n^2$.

MPDR detection filter is applied. As expected, for a high SNR such as 10 dB, there is a great degradation in performance of all algorithms. The JIDSB had better performance than all other algorithms. Emphasizing that in Fig. 5.10 the JIDSB showed an impressive superior behavior.

Fig. 5.14 shows the beampattern of all algorithms with the configuration that led to the results in Fig. 5.12 with a sample support of 200 snapshots. The arrows indicate the positions of the jammers. All curves were averaged over 200 Montecarlo runs. We can see that all algorithms were able to set deep nulls at the jammers positions. The JIDSB beampattern follows the same beampattern as the CG-MWF and the full rank MVDR-SMI.

Fig. 5.15 illustrates the application of the sensor array for a communication system and show the bit error rate (BER), for all algorithms for a small
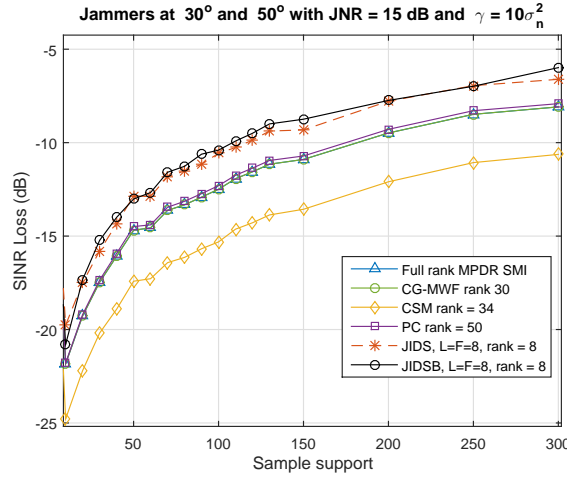
Figure 5.10: Output SINR loss versus the sample support with M = 64, 2 jammers with JNR = 15 dB and $\gamma = 10\sigma_n^2$ when the desired signal is present during estimation of the autocorrelation matrix.

sample support. The system model is as described in (5.1) and the scenario is again the same related to Fig. 5.12. The simulated desired signal, b_0, represents a symbol of a QPSK constellation with power $\sigma_0^2 = E[|b_0|^2]$ and impinges on the array from direction $\theta_0 = 0^o$. The outputs of the beamformer filters, $z[i]$ as in (5.4) and $z_D[i]$ as in (5.11), are fed to a minimum-distance QPSK detector, which is the optimal detector for gaussian channels.

Since noise and jammers are modelled as independent complex Gaussian random vectors, it is possible to compute semi-analytically the bit error probability, $P(e)$, as

$$P(e) = E\left[P\left(e|SINR(\mathbf{w})\right)\right], \tag{5.64}$$

which can be estimated by the average

$$BER = \frac{1}{N_p} \sum_{i=1}^{N_p} P\left(e|SINR(\mathbf{w}_i)\right), \tag{5.65}$$

where

$$P(e|SINR(\mathbf{w}_i)) = Q\left(\sqrt{SINR(\mathbf{w}_i)}\right), \tag{5.66}$$

with

$$Q(\alpha) = \int_{\alpha}^{\infty} \frac{1}{\sqrt{2\pi}} e^{\frac{-t^2}{2}} \mathrm{d}t, \tag{5.67}$$

and

$$SINR(\mathbf{w}_i) = \frac{\sigma_0^2 ||\mathbf{w}_i^H \mathbf{T}_i \mathbf{s}(\theta_0)||^2}{\mathbf{w}_i^H \mathbf{T}_i \mathbf{R} \mathbf{T}_i^H \mathbf{w}_i}, \tag{5.68}$$

where $\mathbf{w}_i$ and $\mathbf{T}_i$ are the detection filter and the rank reducing transformation obtained in the i-th simulation run and $\mathbf{R}$ is the autocorrelation matrix of the noise and interference. Fig. 5.15 depict the semi-analytical bit error rate, BER, of the described QPSK system using $N_p = 1000$ for a sample support of 20. In the horizontal axis we show the SNR based on the reference detection SNR of
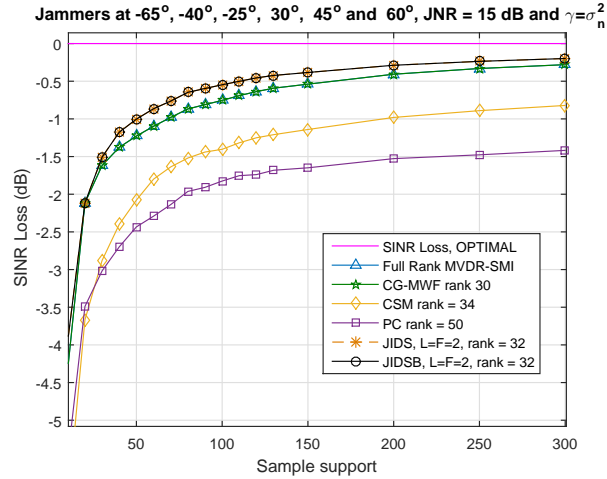
Figure 5.11: Output SINR loss versus the sample support with M = 64, 6 jammers with JNR = 15 dB and $\gamma = \sigma_n^2$.
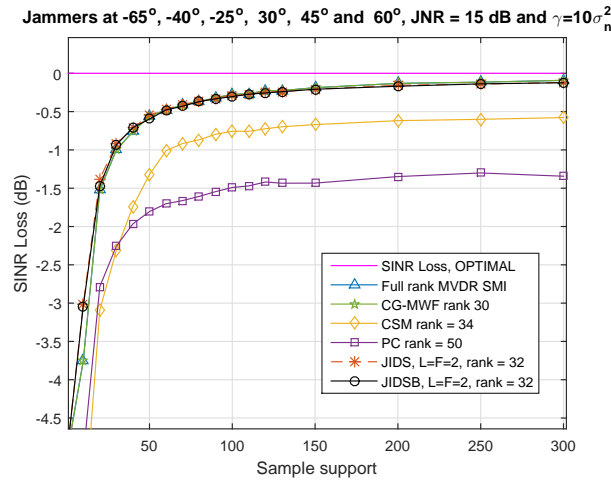
Figure 5.12: Output SINR loss versus the sample support with M = 64, 6 jammers with JNR = 15 dB and $\gamma = 10\sigma_n^2$.

the optimal full rank case without interference, given as

$$\text{SNR} = 10\log_{10}\left(\frac{\sigma_0^2}{\sigma_n^2}||\mathbf{s}(\theta_0)||^2\right) = 10\log_{10}\left(\frac{M\sigma_0^2}{\sigma_n^2}\right). \tag{5.69}$$

We can see that the JIDSB performance is slightly better than the full rank MVDR-SMI and CG-MWF, that is because the mean SINR for that scenario, with a sample support of only 20 snapshots is slightly better for the JIDSB than for the CG-MWF.
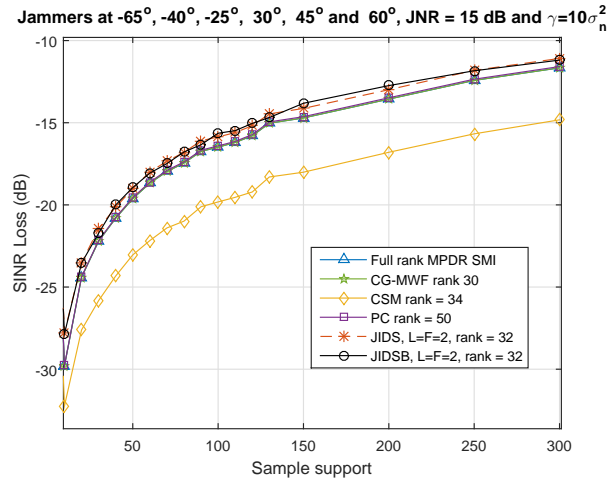
Figure 5.13: Output SINR loss versus the sample support with M = 64, 6 jammers with JNR = 15 dB and $\gamma = 10\sigma_n^2$ when the desired signal is present during estimation of the autocorrelation matrix.
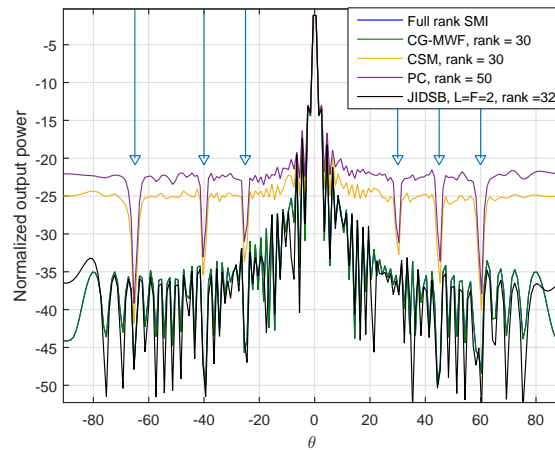
Figure 5.14: Adapted beampattern for different algorithms for sample support $N_s = 100$, $M = 64$ and 6 jammers with JNR = 15 dB.
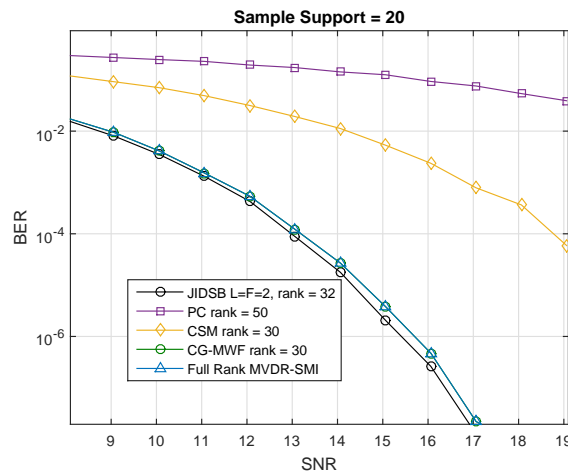
Figure 5.15: Semi-analytical BER for different algorithms for sample support $N_s = 20$, $M = 64$, 6 jammers with JNR = 15 dB.

5.5 Conclusion

In this chapter we reported the JIDS rank reducing technique and adapted it for beamforming. We also proposed the JIDSB algorithm, which is a specialized version of the JIDS technique for beamforming with new proposed simplification procedures that resulted from analysis of the combination of the beamforming system model with the JIDS structure. The proposed simplifications reduce its number of operations and complexity without degrading its performance. The JIDS algorithm consists in a stage of dimensionality reduction decoupled from the detection filter, based on a joint interpolation and decimation scheme. The JIDS strategy design is an elegant and effective way to obtain the joint interpolation filter and decimation pattern, taking advantage of the correlation generated by the interpolation filter in order to eliminate samples and still achieve a high SINR after the decimation stage.

We presented performance results in terms of SINR loss *vs.* sample support applying the MVDR filter with and without diagonal loading and the MPDR filter with diagonal loading. We could see the superiority of the JIDSB-SMI in terms of SINR loss performance for the MPDR filter and for the MVDR filter without diagonal loading. In the case of the MVDR filter with diagonal loading the JIDSB had similar performance as the full rank MVDR-SMI and CG-MWF, with an impressive low computational complexity especially for small sample supports.

In our understanding, the proposed JIDSB algorithm shows great advantages in beamforming scenarios. It is an inherently robust method, it has similar or superior SINR loss performance than the full rank MVDR-SMI and CG-MWF, low computational complexity and it reduces significantly the length of the processed data.

6
JIDS Applied to Space-Time Processing

In this chapter we specialize the JIDS rank reduction technique for space-time applications, more specifically, airborne phased-array radars. We start by recasting the JIDS algorithm for STAP applications and we use the method described in Chapter 5 for setting the decimation factor, F, and the interpolation filter length, L_v.

We compare results of the JIDS algorithm in terms of probability of detection and Doppler performance with the full rank Minimum Variance Distortionless Response sample matrix inversion (MVDR-SMI) space-time filter and other rank reduction techniques such as Principal Components (PC), Cross-Spectral Metric (CSM) and Multistage Wiener Filter (MWF).

Simulation results show that the proposed approach has an impressive ability to reduce significantly the length of the space-time snapshots and to achieve very good performance in Doppler SINR loss and probability of detection, especially in sample starving scenarios.

The study on this topic carried out during the preparation of this thesis produced the conference paper [6].

This chapter is organized as follows: the system model is described in Section 6.1; the proposed technique is explained in Section 6.2; computer simulations are presented in Section 6.3 and, finally, conclusions are given in Section 6.4.

6.1 System Model

The system model considered here is explained in detail in Section 3.2.

The output of the i-th range slice of the datacube, stacked into the space-time vector $\mathbf{r}[i]$ defined in (3.40), after filtering by a space-time filter, $\mathbf{w}$, is given by

$$z[i] = \mathbf{w}^H \mathbf{r}[i]. \tag{6.1}$$

where $\mathbf{w} = [w_1, ..., w_M]^T \in \mathrm{C}^{M \times 1}$ is the complex weight vector of the space-time filter. The optimal space-time filter weight vector, $\mathbf{w}$, that maximizes the probability of detection, P_{D}, for a given P_{FA} takes the form (3.57)

$$\mathbf{w} = \beta \mathbf{R}^{-1} \mathbf{s}_{st},$$
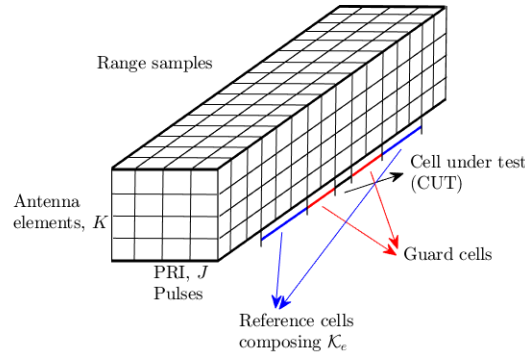
Figure 6.1: Datacube showing selection of reference and guard cells for estimating the covariance matrix for a given cell under test (CUT).

where β is a complex constant, $\mathbf{R}$ is the total noise-clutter-interference covariance matrix defined in (3.55) and $\mathbf{s}_{st}$ is the target space-time steering vector defined in (3.37). If we set $\beta = (\mathbf{s}_{st}^H \mathbf{R}^{-1} \mathbf{s}_{st})^{-1}$, then the space-time filter is given by

$$\mathbf{w} = \frac{\mathbf{R}^{-1}\mathbf{s}_{st}}{\mathbf{s}_{st}^H \mathbf{R}^{-1} \mathbf{s}_{st}}, \tag{6.2}$$

which is the solution to the space-time minimum variance distortionless response (MVDR) design criterion, the MVDR space-time filter. In practice, the assumption of perfect knowledge of the covariance matrix, $\mathbf{R}$, is not realistic. It must be estimated from an available finite sample support, $\mathcal{K}_e$, with K_e elements, as

$$\hat{\mathbf{R}} = \frac{1}{K_e} \sum_{i \in \mathcal{K}_e} \mathbf{r}[i]\mathbf{r}^H[i]. \tag{6.3}$$

Typically, the training data, $\mathbf{r}[i]$, cover a range interval surrounding but not including the range gate of interest as shown in Fig. 6.1 in order to the target-free assumption to hold in practice.

The optimum space-time filter in (6.2) replacing $\mathbf{R}^{-1}$ by the inverted estimated covariance matrix, $\hat{\mathbf{R}}^{-1}$, is known as the MVDR sample matrix inversion (SMI) space-time filter. An additional performance loss dependent on the number of samples is incurred due to the covariance matrix estimation. If all training data are independent and identically distributed (iid) with respect to the null hypothesis, choosing $K_e \approx 2JK$, where J is the number of pulses and K is the number of sensors, yields an average performance loss of roughly 3 dB [51].

The sample support availability becomes more critical because of the nonstationary nature of real radar clutter and jamming. Clutter heterogeneity in range, combined with power and elevation angle dependence, reduce the number of range gates over which the clutter scenario is effectively stationary.

Reduced rank techniques are able to mitigate the deleterious effects of

small sample support in the space-time covariance matrix estimation. The reduced rank solution, $\mathbf{w}_D$, of (6.2) is given by

$$\mathbf{w}_D = \frac{\mathbf{R}_D^{-1}\mathbf{s_D}}{\mathbf{s}_D^H \mathbf{R}_D^{-1}\mathbf{s}_D}, \tag{6.4}$$

where $\mathbf{R}_D = \mathbf{TRT}^H = \mathbb{E}[\mathbf{x}_D[i]\mathbf{x}_D^H[i]]$ is the autocorrelation matrix of the interference plus noise plus clutter after the rank reducing stage, $\mathbf{x}_D[i] = \mathbf{Tx}[i]$, $\mathbf{s}_D = \mathbf{Ts}_{st}$ is the desired signal space-time steering vector after the rank reducing stage and finally, $\mathbf{T}$, is the rank reducing transformation.

6.2 Recast of the JIDS applied to STAP

The JIDS rank reduction technique is here specialized for space-time applications. The JIDS rank reducing technique makes a joint choice of the interpolation filter, $\mathbf{v}_l$, and the decimation pattern, $\mathbf{D}_l$. Given a decimation pattern, the interpolation filter, $\mathbf{v}_l^*$, is the one that maximizes the SINR after the rank reduction stage.

Now we will briefly recast the process of generating the JIDS interpolator filter given the decimation pattern, $\mathbf{D}_l$, explained in Section 5.3.1 for space-time applications:

1. Construct the Toeplitz matrix of the desired space-time steering vector $\mathbf{s}_{st}$, $\mathcal{S}$;

2. Compute $\mathbf{A}_l = \mathcal{S}^H \text{diag}(\mathbf{p}_l)\mathcal{S}$, as in (5.30);

3. Estimate $\mathbf{B}_l$ in (5.34) using N_B space-time snapshots as

$$\hat{\mathbf{B}}_l = \frac{1}{N_B} \sum_{i=1}^{N_B} \mathcal{X}^H[i]\text{diag}(\mathbf{p}_l)\mathcal{X}[i]; \tag{6.5}$$

4. Compute $\hat{\mathbf{F}}_l = \hat{\mathbf{B}}_l^{-1}\mathbf{A}_l$;

5. Compute the largest eigenvalue, $\lambda_{\text{max},l}$, of $\hat{\mathbf{F}}_l$;

6. Repeat steps 2 to 5 for the F possible decimation patterns and choose the decimation pattern l^* that provides the largest eigenvalue of $\hat{\mathbf{F}}_l$

$$l^* = \arg\max_l \lambda_{\text{max},l}, \quad l = \{0,..,F-1\}. \tag{6.6}$$

7. Set the interpolation filter as $\mathbf{v}_{l^*}$, which is the eigenvector associated to the largest eigenvalue of $\hat{\mathbf{F}}_{l^*}$. The interpolation filter obtained using this procedure is the one that maximizes the SINR.
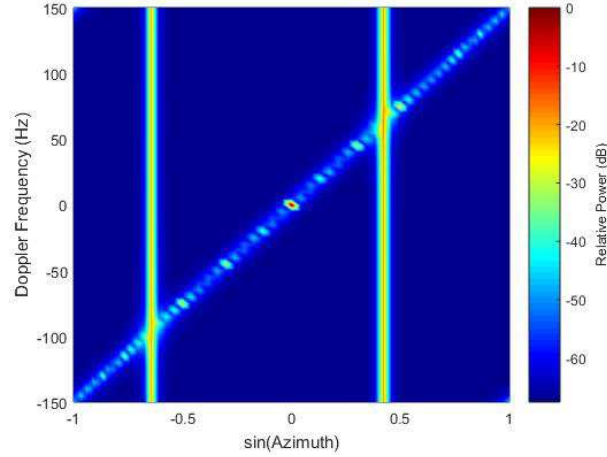
Figure 6.2: Capon spectrum of **R**.

The method used here for setting the interpolator length and the decimation factor is explained in Section 5.3.2.

After determining $\mathbf{D}$ and $\mathcal{V}$ using the steps described above, the JIDS rank reducing transformation matrix, $\mathbf{T}_J \in \mathbb{C}^{D \times M}$, is given by

$$\mathbf{T}_J = \mathbf{D}\mathcal{V}, \tag{6.7}$$

therefore, $\mathbf{w}_D$ in (6.4) is computed by substituting $\mathbf{T}$ by $\mathbf{T}_J$ in (6.4).

6.3 Simulations

In this section we show some performance results using the full rank MVDR-SMI and reduced rank algorithms for sufficient and for small sample supports. The reduced rank algorithms selected for these examples are the same as used in Chapter 5: Principal Components (PC) [21, 52], Cross Spectral Metric (CSM) [53, 54, 13] and the Multistage Wiener Filter (MWF) [27] algorithms.

We simulated an airborne radar with $K = 18$ elements displaced in a ULA separated by half of the carrier wavelength, which transmits $J = 18$ pulses per CPI with a pulse repetition frequency (PRF) of 300 Hz. We included two broadband jammers, $n_j = 2$, located at $\vartheta_1 = -0.64$ and $\vartheta_2 = 0.42$ with jammer to noise ratio (JNR) per element of 38 dB and clutter uniformly distributed in azimuth, unambiguous in Doppler ($\beta_c = 1$), with no velocity misalignment and no inner clutter motion [1], composed of $N_c = 360$ patches with clutter to noise ratio (CNR) per element per pulse of 47 dB.

Fig. 6.2 shows the Capon spectrum of the described scenario. A target was introduced at spatial frequency $\vartheta_t = 0$ and Doppler frequency $f_t = 100$ Hz.
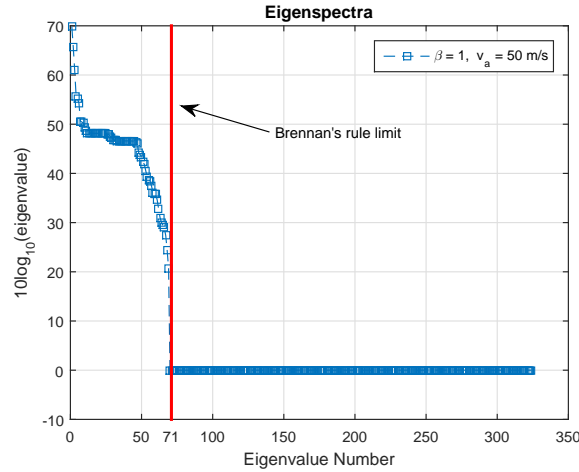
Figure 6.3: Eigenspectrum of the covariance matrix $\mathbf{R}$.

The rank of the interference covariance matrix, r_i, is given by

$$r_i = r_j + r_c, \tag{6.8}$$

where r_j is the rank of the jammers and r_c is the rank of the clutter. The rank of the jammers, r_j, is given by [1]

$$r_j = J n_J, \tag{6.9}$$

where J is the number of pulses per CPI and n_J is the number of active jammers. The rank of the clutter, r_c, is given approximately by the Brennan's rule [1]

$$r_c \simeq \lfloor K + (J-1)\beta_c \rfloor, \tag{6.10}$$

where K is the number sensors in the array, J is the number of pulses per CPI and β_c is the clutter ridge. When β_c is an integer, the equality in (6.10) holds.

Using (6.8), (6.9) and (6.10) with the data used for simulation we have that the total interference covariance matrix rank is 71. From Fig. 6.3 we can confirm that, from the 324 total eigenvalues of $\mathbf{R}$, the largest 71 encompasses the most significant part of the spectrum, thus we set the rank for the PC-SMI and CSM-SMI algorithms equal to 71. Even though the MWF decomposes the signal using the Krylov subspace instead of the eigenspace, we also set its total number of stages to 71 for the sake of comparison.

Fig. 6.4 depicts the SINR Loss (L_{SINR}) *vs.* the decimation factor, F, for the JIDS algorithm assuming the length of the interpolator filter $L_v = F$, $L_v = \lfloor F/2 \rfloor$ and $L_v = \lfloor 1.5F \rfloor$. This example empirically confirms that setting the interpolator length equals to the decimation factor is a good choice. This plot shows that we have better performance in terms of L_{SINR} for a decimation factor and filter length of 54, which reduces the length of the space-time snapshot from 324 to 6. That is a very impressive reduction!
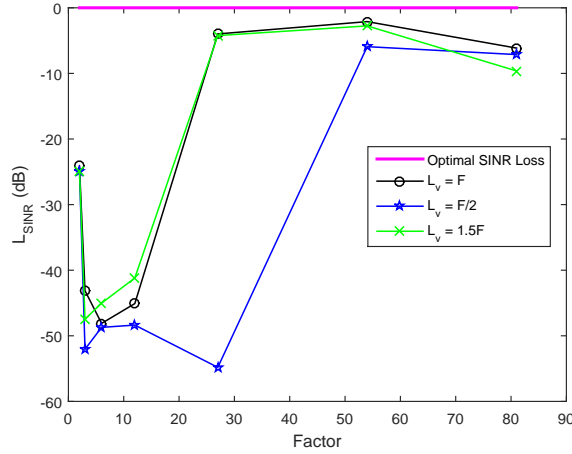
Figure 6.4: SINR Loss (L_{SINR}) *vs.* decimation factor for the JIDS algorithm according the described example and with $K_e = 648$, $\xi_t = 1$, $\vartheta_t = 0$ and $f_t = 100$ Hz.

We added an empirical value of diagonal loading ($\delta = 10\sigma_n^2$) used in practice for the estimate of matrix $\mathbf{R}$ for all algorithms in order to improve robustness and to avoid numerical instabilities when computing the inverse in (6.2) for small sample support. Figs. 6.5 and 6.6 show the SINR Loss *vs.* target Doppler of the optimal MVDR, the full rank MVDR-SMI, PC-SMI, CSM-SMI, MWF and the JIDS-SMI for a sample support of 648 and 50 respectively. Curves were averaged over 100 runs. The Doppler performance is computed by holding fixed the target spatial frequency, ϑ_t, and evaluating for different target Doppler frequencies, f_j, the SINR loss, $L_{\text{SINR}} = \text{SINR}/\text{SNR}_0$, given by

$$L_{\text{SINR}}(f_j) = \frac{\sigma_n^2 \xi_t |\mathbf{w}_j^H \mathbf{T}_j^H \mathbf{s}(\vartheta_t, f_j)|^2}{\mathbf{w}_j^H \mathbf{T}_j^H \mathbf{R} \mathbf{T}_j \mathbf{w}_j \text{SNR}_0}, \tag{6.11}$$

where $\mathbf{w}_j$ is the space-time filter computed for a target at spatial frequency, ϑ_t, and Doppler frequency, f_j, $\mathbf{T}_j$ is the rank reducing transformation (applied when necessary) and $\text{SNR}_0 = \xi_t K J$.

In Figs. 6.5 and 6.6 we can see that the SINR loss is very large when the target is near 0 Hz, because in this case the target falls into the filters' notch used to suppress the mainlobe clutter. We can also see that as the sample support decreases from one figure to the other, so does the Doppler performance of all but the JIDS algorithm. The JIDS is probably more robust to small sample supports because it is able to achieve the largest rank reduction. The JIDS used a reduced vector of size 6, instead of 71 or 324, therefore, a sample support of 50 is not so dramatically small.

Figs. 6.7 and 6.8 show the probability of detection, P_{D}, *vs.* the probability of false alarm, P_{FA}, for the MVDR-SMI and the reduced rank algorithms,
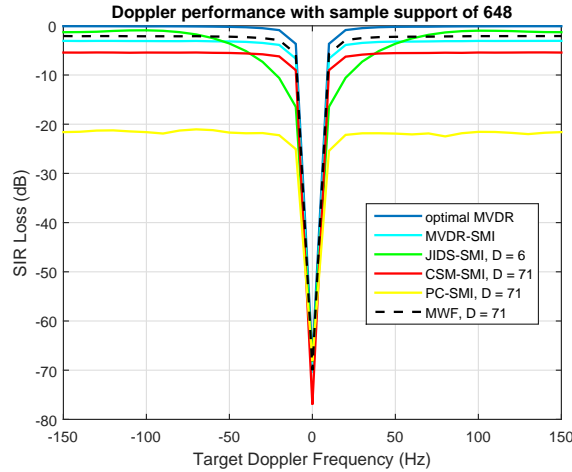
Figure 6.5: L_{SINR} *vs.* Doppler with sample support of $K_e = 648$, fixed $\vartheta_t = 0$.
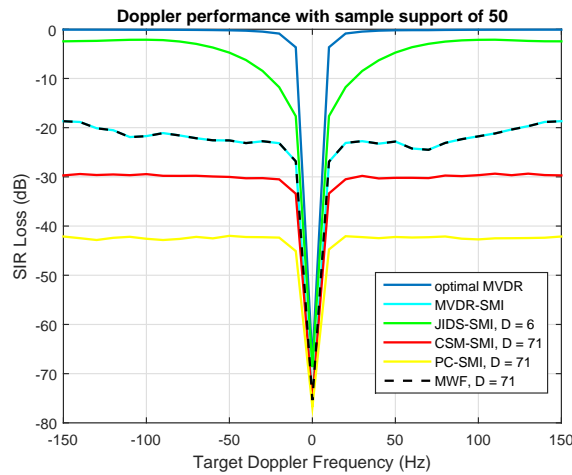
Figure 6.6: L_{SINR} *vs.* Doppler with sample support of $K_e = 50$, fixed $\vartheta_t = 0$.

computed as [12]

$$P_{\text{D}} = Q_M \left(\sqrt{2\text{SINR}}, \sqrt{-2\ln(P_{\text{FA}})} \right), \tag{6.12}$$

where $Q_M(\cdot)$ is the Marcum's Q function. It was assessed at $\vartheta_t = 0$ and $f_t = 100$ Hz for a sample support of 50. The mean SINR attained is also displayed. The curves were averaged over 100 runs. The SNR was set as $\xi_t = 1$. From Fig. 6.8 we can see that the only algorithm that does not collapse for such a low sample support is the JIDS.

Just for the sake of curiosity we show the adapted pattern of the SMI algorithms for a sample support of 648 and 50. Figs. 6.9, 6.10, 6.11, 6.12, 6.13 show the adapted pattern for a sample support of 648 of the MVDR-SMI, JIDS-SMI, MWF, CSM-SMI and PC-SMI algorithms respectively. Figs. 6.14, 6.15, 6.16, 6.17, 6.18 show the adapted pattern for a sample support of 50 of the MVDR-SMI, JIDS-SMI, MWF, CSM-SMI and PC-SMI algorithms
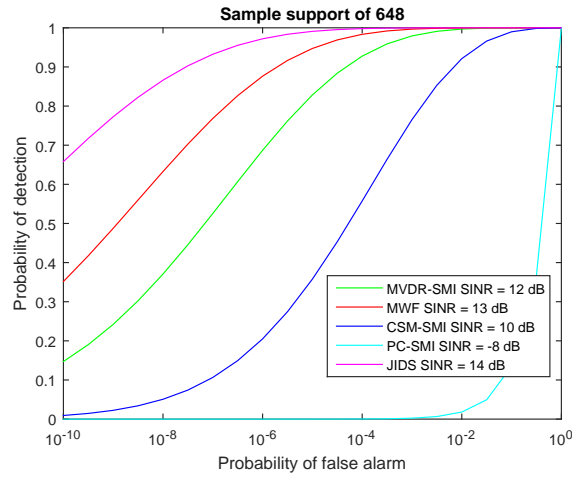
Figure 6.7: P_{D} vs. P_{FA} for $K_e = 648$, $\xi_t = 1$, $\vartheta_t = 0$ and $f_t = 100$ Hz, all other parameters are the same as the former examples.
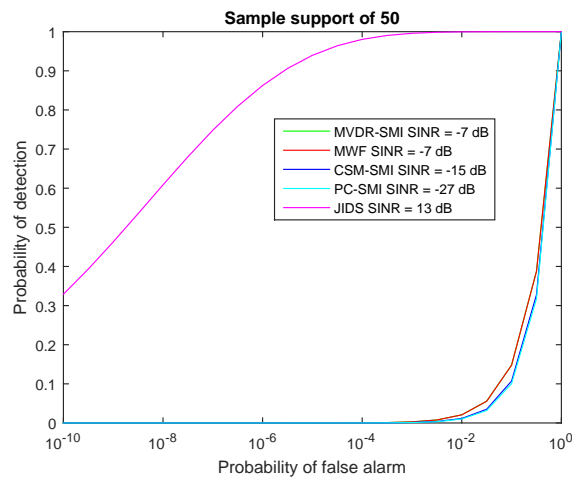
Figure 6.8: P_{D} *vs.* P_{FA} for $K_e = 50$, $\xi_t = 1$, $\vartheta_t = 0$ and $f_t = 100$ Hz, all other parameters are the same as the former examples.

respectively. It is interesting to note that comparing Fig. 6.16 of the MWF adapted pattern for a sample support of 50 and Fig. 6.15 of the JIDS adapted pattern for a sample support of 50, it seems that their adapted patterns are "similar", but Fig. 6.8 shows the clear superior performance in probability of detection of the JIDS.
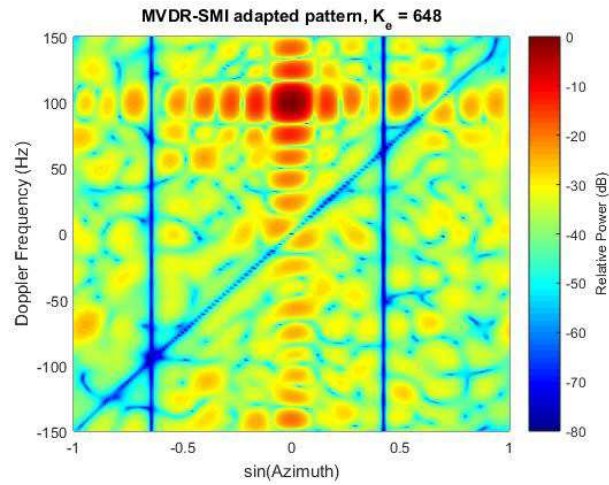
Figure 6.9: Pattern of the space-time MVDR-SMI with sample support of 648 - SINR = 12 dB.
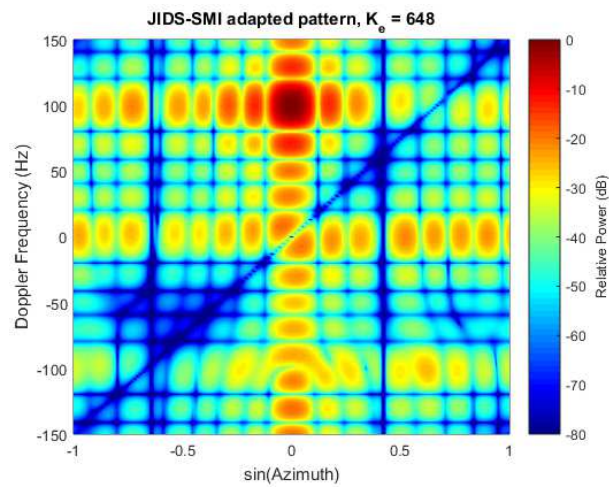
Figure 6.10: Pattern of the space-time JIDS-SMI with sample support of 648 - SINR = 14 dB.
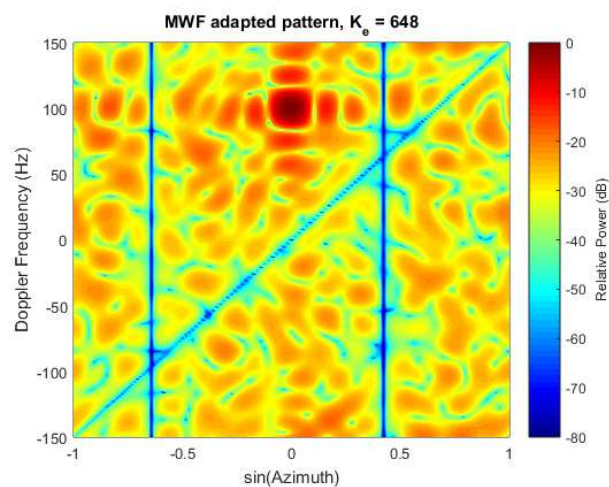
Figure 6.11: Pattern of the space-time MWF-SMI with sample support of 648 - SINR = 13 dB.
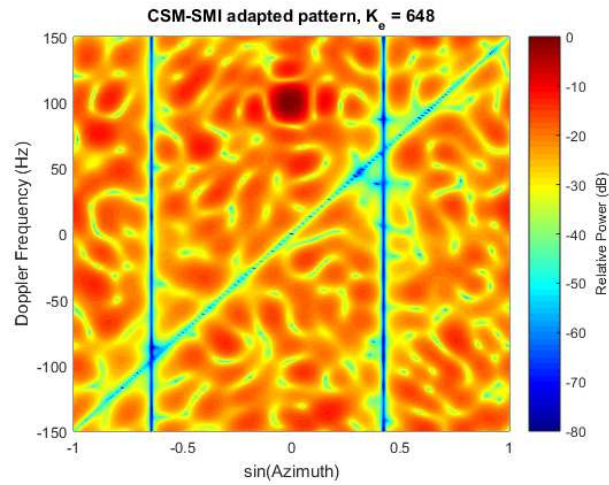
Figure 6.12: Pattern of the space-time CSM-SMI with sample support of 648 - SINR = 10 dB.
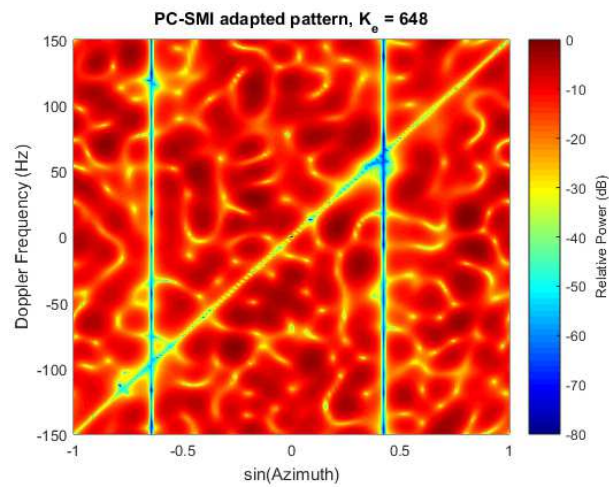
Figure 6.13: Pattern of the space-time PC-SMI with sample support of 648 - SINR = -8 dB.
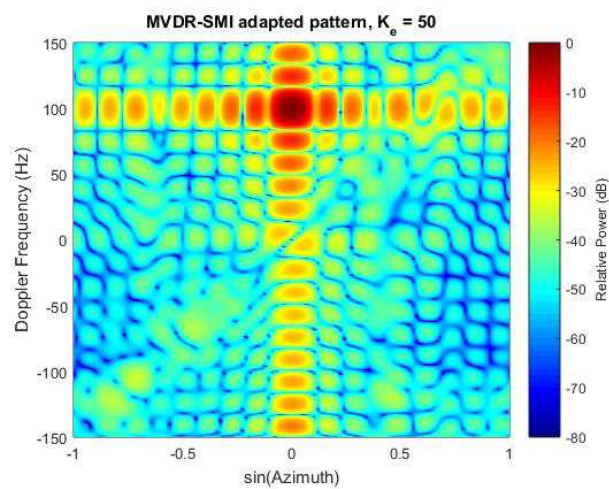
Figure 6.14: Pattern of the space-time MVDR-SMI with sample support of 50 - SINR = -7 dB.
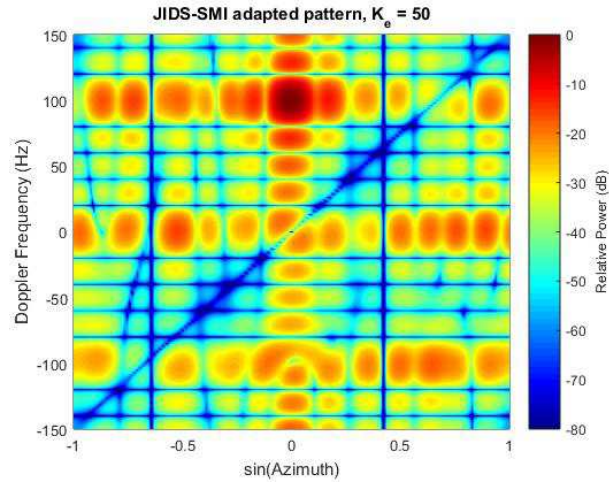
Figure 6.15: Pattern of the space-time JIDS-SMI with sample support of 50 - SINR = 13 dB.
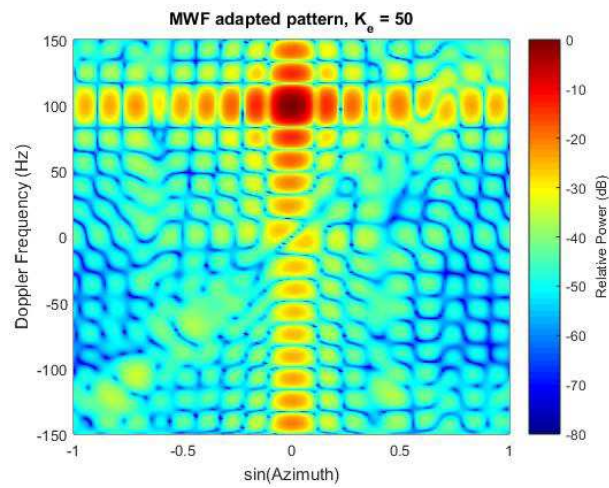
Figure 6.16: Pattern of the space-time MWF-SMI with sample support of 50 - SINR = -7 dB.
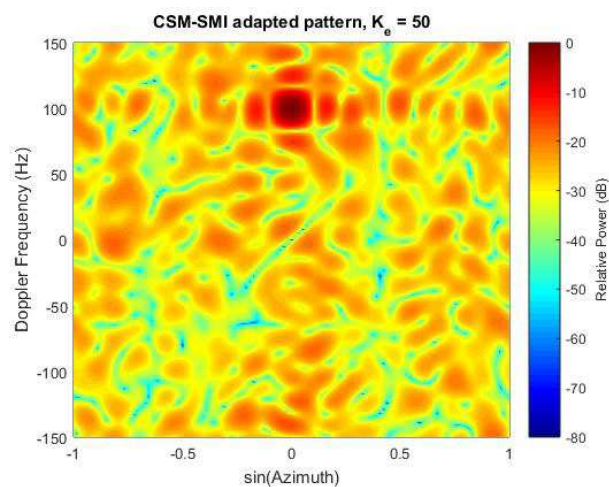
Figure 6.17: Pattern of the space-time CSM-SMI with sample support of 50 - SINR = -15 dB.
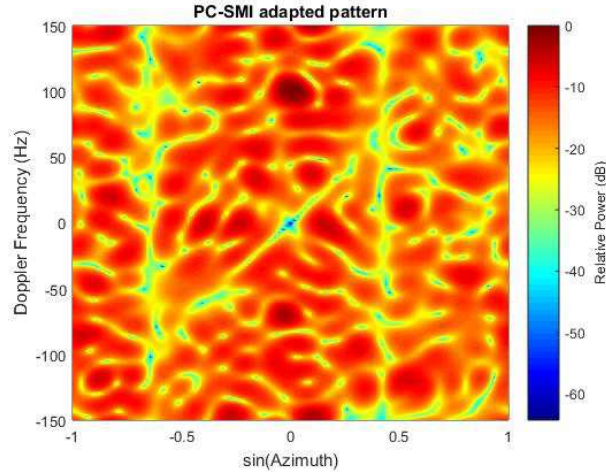
Figure 6.18: Pattern of the space-time PC-SMI with sample support of 50 - SINR = -27 dB.

The next example shows the application of the reduced-rank algorithms in a real data experiment. We use the Mountain-top data set. This data set can be downloaded from the internet [55]. The area where the samples were collected is a desert area, with a river, suburban areas, and mountains within the field of view. There are 14 sensor elements displaced in a ULA horizontally oriented with respect to the ground with a inter-element spacing of 0.333m. Although the radar system is installed at a fixed ground site, radar platform motion is emulated using the Inverse Displaced Phase Center array (IDPCA).

The data are organized in CPIs of 16 pulses. Here, we used the data file *t38pre01v1* CPI6. The transmitted pulse is a linear frequency modulated chirp. The stored data has been demodulated, equalized across the system bandwidth in each channel, and calibrated from channel to channel. The data is not pulse compressed; satisfactory pulse compression may be obtained by constructing a matched filter based on the 500 kHz LFM transmit pulse. The range samples are collected in intervals of 1 μs. The radar PRF is 625 Hz.

This data contains ground clutter primarily from a single large scatterer (a mountain) which is isolated in angle, 245°, with a Doppler of 156 Hz (due to platform motion). The target is located at the same range (154 Km) and Doppler of the clutter with a different azimuth, 275°.

Figs. 6.19, 6.20, 6.21, 6.22, 6.23 and 6.24 depict the normalized output power of the statistical test $|\mathbf{w}^H[l]\mathbf{s}_{st}|^2$ for all cells under test (CUTs), which implies in a range of 147 to 162 Km. The covariance matrix, $\mathbf{R}$, is estimated using a symmetrical sliding window with a total of 20 snapshots, respecting a guard interval of 3 snapshots before the CUT and 3 snapshots after the CUT.

Fig. 6.19 depicts the unadapted weight vector, which corresponds to the space-time matched filter $\mathbf{w}[l] = \mathbf{s}_{st}$. From Fig. 6.19, we can note that the
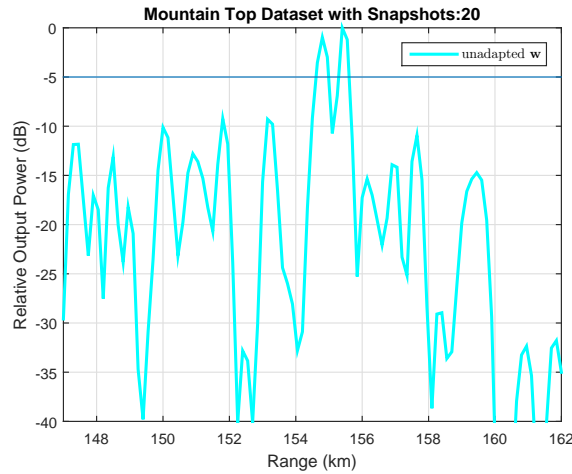
Figure 6.19: Range profile for the Mountain Top data set using the unadapted space-time filter $\mathbf{w}_Q = \mathbf{s}_{st}$ and a sample support of 20 snapshots.

target is not detectable without space-time processing.

Fig. 6.20 depicts the output of the full rank MVDR-SMI algorithm with a diagonal loading of $\delta = 10^7$. After extensive tests, this value was chosen because it leads to better results. For all other algorithms the same diagonal loading was applied.

We can see, comparing Fig. 6.22 with Figs. 6.20, 6.21, 6.23 and 6.24, that the results of the JIDS algorithm is impressively better than the others for such a small sample support (only 20 snapshots to estimate a covariance matrix of 224×224). While the others are able to detect the target using a threshold of around 5 dB less than the peak, the JIDS is able to detect the target with a threshold of more than 8 dB of difference.
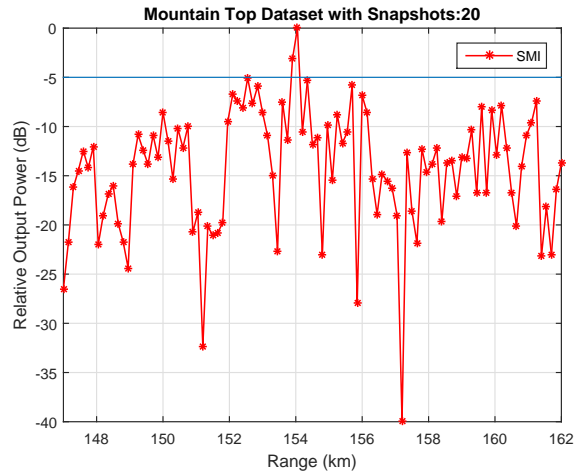
Figure 6.20: Range profile for the Mountain Top data set using the full rank MVDR-SMI algorithm with diagonal loading and a sample support of 20 snapshots.
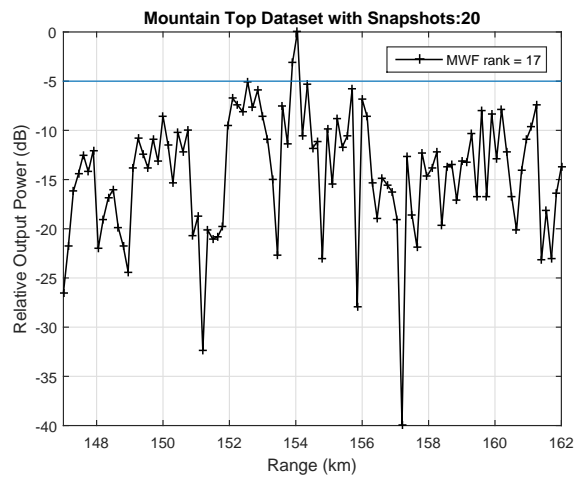
Figure 6.21: Range profile for the Mountain Top data set using the MWF algorithm and a sample support of 20 snapshots.
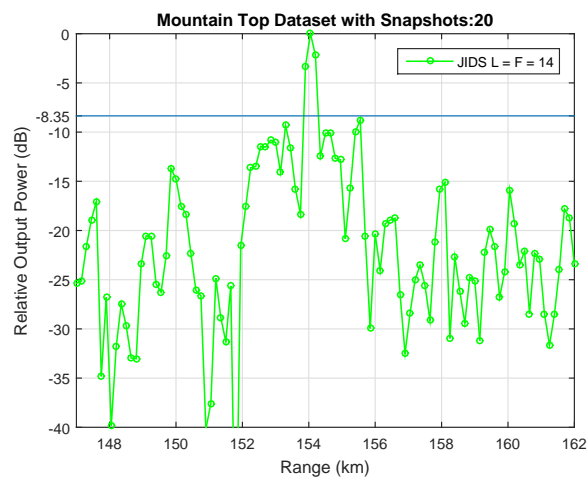
Figure 6.22: Range profile for the Mountain Top data set using the JIDS algorithm and a sample support of 20 snapshots.
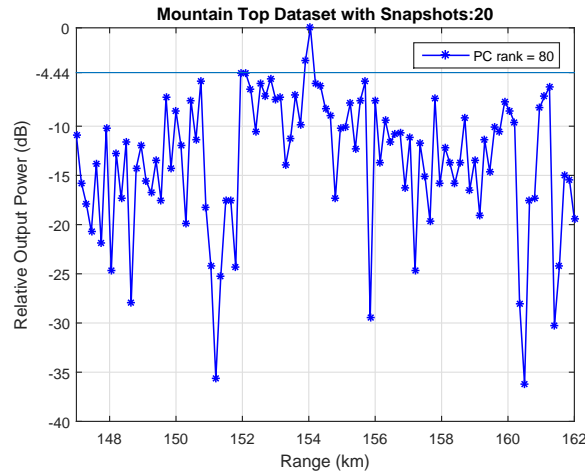
Figure 6.23: Range profile for the Mountain Top data set using the PC-SMI algorithm and a sample support of 20 snapshots.
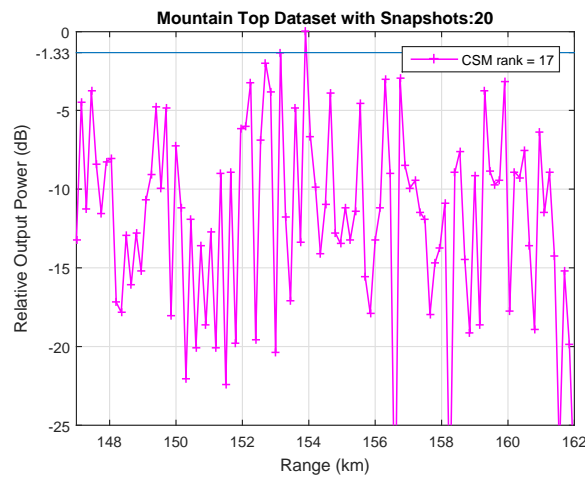
Figure 6.24: Range profile for the Mountain Top data set using the CSM-SMI algorithm and a sample support of 20 snapshots.

6.4 Conclusion

In this chapter we reported the JIDS rank reducing technique specialized for space-time applications. The JIDS algorithm consists in a stage of dimensionality reduction decoupled from the space-time target detection filter, based on a joint interpolation and decimation scheme. This strategy design takes advantage of the correlation generated by the interpolation filter in order to eliminate samples and still achieve low SINR loss. It is able to work in a very reduced Krylov subspace. Numerical results obtained for a simulated sample starving airborne radar scenario showed that the JIDS achieves superior Doppler SINR loss performance and increased probability of detection when compared to the full rank MVDR-SMI, PC-SMI, CSM-SMI and MWF. Tests with real airborne data show that the JIDS algorithm has an impressive

superior detection performance for a real heterogeneous clutter scenario.

7
Radar and Communications

The topic of coexistence of radar and communications has acquired high importance due to the problem of spectrum encroachment and interference in passive sensors, [56, 57, 58]. Extensive efforts have been directed towards this matter and many different alternatives have been proposed to deal with it, for example, sophisticated interference mitigation techniques [59, 60], spectrum-sharing for simultaneous operation of radar and communications [61, 62, 63, 64, 65, 66] and dual-functionality platforms, where waveform and irradiating sensors are jointly managed for both radar and communication functions. Pulsed radars enable synchronization for embedded communications and usually operate over considerable ranges with high power [67]. The combination of this characteristics with the high radar pulse repetition frequency (PRF) makes pulsed radars able to meet the communication service operational requirements [56].

The alternative of dual-functionality platform approach is divided into two categories that can be combined: embedding information into radar emissions via waveform diversity [68, 69, 70] and embedding information towards a specific receiver direction by changing the amplitude and/or phase of the sidelobe transmit beampattern towards that direction [71, 2, 3, 5, 4, 7, 8]. The first category of embedding information into a radar emission by changing the waveform during each radar pulse may affect the radar main function even within a coherent processing interval (CPI). We are especially interested in the second category: embedding communication symbols by changing amplitude and/or phase of the transmit beampattern.

In this context of varying parameters of the transmit beampattern, we can also differentiate signaling strategies by the number of simultaneous waveforms transmitted during each pulse period and by the type of modulation applied to the transmit beampattern: a) amplitude modulation or sidelobe level modulation (SLL), which is equivalent to embedding symbols from an Amplitude Shift Keying (ASK) constellation, b) phase modulation, which is equivalent to embedding symbols from a Phase Shift Keying (PSK) constellation, or c) a combination of amplitude and phase modulation, which is equivalent to embedding symbols from an Amplitude and Phase Shift Keying (APSK)

constellation. But due to the difficulty of having coherency between the communication receivers and the radar, the work so far in this area is restricted to non-coherent receivers.

The works of [71, 5, 7, 8] describe different methodologies for embedding SLL modulation into the transmit beampattern. They require only one waveform, but as shown in [5], if more than one orthogonal waveform can be transmitted through different antenna arrays, one can use a different transmit beampattern for each waveform, thus increasing the bit rate (multi-waveform ASK).

The research in phase modulation is up to now restricted to non-coherent modes. Non-coherent phase modulation embeds information into the phase difference, so it requires a reference phase. So far this reference phase is achieved through the transmission of multiple orthogonal waveforms (at least two) during the same pulse period through different antenna arrays (multi-waveform Differential PSK-based methods). Many radars have the ability to transmit orthogonal waveforms simultaneously through different antenna arrays, MIMO radars are a good example [72], but it requires more sophisticated technology than the necessary to change only the transmit beampattern of only one array of sensors. To cope with this issue, we propose a signaling strategy that is suitable for more simple radars, that have only one transmit array.

In the work of [3], during each radar pulse, multiple pairs of orthogonal waveforms are transmitted, where each pair represents one phase symbol. At the communication receiver, each embedded symbol is detected by estimating the phase difference between the signals associated with the two waveforms in each pair. The phase embedded at the beampatterns are designed using phase rotational invariance [73]. In the work of [4] several waveforms are transmitted simultaneously and only one waveform is taken as a common reference to all other waveforms. Each communication symbol is embedded in the phase difference between the two signal components associated with each waveform pair. In [4], the phase embedded at the beampatterns are designed by using phase rotational invariance [73] or by convex optimization.

The option of using radar for communication purposes is also an alternative to deal with the security issue in defense-related applications, where it is essential to maintain secure communications with low probability of intercept. The secure behavior of the radar-embedded communication system based in varying the transmit beampattern parameters in specific directions is intrinsic to its design. The preassigment of the receiver direction may provide operational bit error rates (BER) only towards this direction. This advantage,

though, becomes a major disadvantage if the real receiver position doesn't match exactly the predefined one. This situation can easily arise if the communication receiver is moving relative to the radar.

In this thesis we address this problem. We have derived the optimal closed form solution to an optimization formulation that embeds sidelobe modulation and is robust to small receivers' direction errors. Our design uses a constrained optimization problem to generate transmit beampatterns, that satisfactorily match a given transmit profile (with high fidelity adjustment at the mainlobe), where each beampattern embeds a different symbol towards the communication receiver direction and sustains its value over a small angular region, making it robust against small angular deviations. In this thesis, we also propose an alternative way of dealing with the mainlobe adjustment requirement, while still keeping the robustness. The alternative proposed method is based on eigenvalue, point and derivative constraints, which also has a closed form solution.

Another important consideration, other than robustness, which was only addressed by us so far, is adaptation in real-time applications when the communication receiver is moving relative to the radar. We simplify our two proposed methods making them suitable for online real-time processing with very low computational load for updating the beampatterns for following a moving communication receiver platform.

In Section 7.1 we describe the system model that is used throughout the present and the following chapters. In Chapter 8, we give an overview of the main sidelobe modulation methods present in the literature, showing their pros and cons. In this overview, we focus only on the central ideas concerning sidelobe modulation and after addressing important topics we make brief comments, where the reader can find our independent conclusions about the described methods. The techniques of the methods in the literature were adapted to conform to the adopted system model and the notation was made uniform in agreement with this thesis notation.

In Section 9.1, we elaborate our thoughts about robustness and effects of relative movement between the communication receiver and the radar. This section links our proposed methods with the methods present in the literature, as we face this issue directly. In the next sections of Chapter 9 we describe our proposed techniques for embedding robust amplitude and phase modulation to the beampattern sidelobe. We also further develop them to real-time iterative low-complexity versions.

(a) What is a Dual Function Radar and Communications (DFRC) Radar?

A DFRC radar is a radar which is also used for communications purposes. The communication function is seen as a secondary task and shouldn't cause degradation to the primary radar function. It is within this context that radar-embedded sidelobe modulation was conceived. Theoretically, any usual communication's modulation can be adapted to this new concept, but in practice there are many restrictions which limit the overall possibilities. In the following we will explain the sidelobe modulation concept.

(b) What's the Idea of Sidelobe Modulation?

Sidelobe modulation within the DFRC context consists in varying parameters of the transmit beampattern towards a specific direction (the receiver's direction) from pulse to pulse according to the communication message to be transmitted. The variation of the parameters, i.e. amplitude and/or phase follows the communication symbol's constellation and is achieved through the use of different beamforming weighting vectors.

The low-pass complex envelope of the RF transmitted radar pulse, $x(t, u)$, irradiated towards direction $u = \cos(\theta)$, as defined in Section 2.4, due to the contribution of all elements of the sensor array is given by,

$$x(t, u) = \mathbf{w}^H \mathbf{s}(u) x(t),$$

and that

$$B(u) = \mathbf{w}^H \mathbf{s}(u),$$

is the beampattern, the goal of sidelobe modulation is that towards the communication receiver direction, $u_c = \cos(\theta_c)$, the complex value, that will multiply the pulse $x(t)$, belongs to a symbol constellation $\mathcal{C}$, which k-th symbol is C_k, $k = 1, \ldots, K$. In other words, we must impose that

$$B_k(u_c) = \mathbf{w}_k^H \mathbf{s}(u_c) = C_k, \tag{7.1}$$

where $\mathbf{w}_k \in \mathbb{C}^{M \times 1}$, $k = 1, \ldots, K$ is the transmit beamforming weighting vector that generates the k-th transmit power radiation pattern that embeds C_k towards u_c.

The general idea for a non-coherent ASK modulation is ideally depicted in Figs. 7.1 and 7.2, where two transmit power patterns, $P(u) = |B(u)|^2$, are depicted. Each power pattern has a different sidelobe level towards the communication receiver and each level corresponds to one of two symbols of a non-coherent ASK constellation. The dotted line corresponds to the maximum

sidelobe level allowed in terms of radar operation. Ideally we want to modify only the sidelobe related to the communication receiver and keep the rest unchanged.
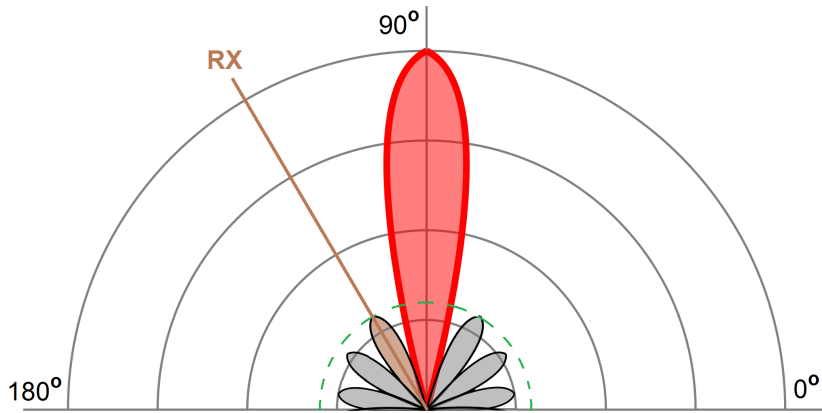
Figure 7.1: Transmit power pattern generated by the transmit beamformer $\mathbf{w}_0$, which embeds symbol "0" towards the receiver direction.
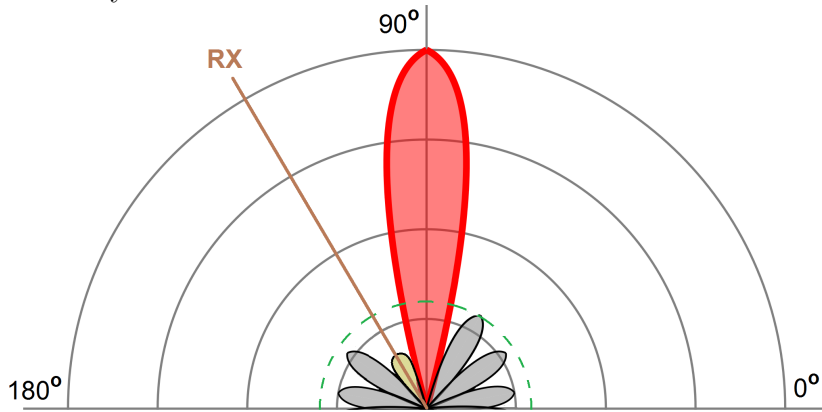
Figure 7.2: Transmit power pattern generated by the transmit beamformer $\mathbf{w}_1$, which embeds symbol "1" towards the receiver direction.

7.1 System Model

We consider a pulsed-Doppler phased array radar with M radiating elements, assumed to have the same radiation pattern, displaced in a uniform linear array (ULA) which is used for transmitting purpose. In order to perform pulse integration, during a CPI, M_I pulses are transmitted with a PRF of $1/T_r$, where T_r is the pulse repetition interval (PRI) [12].

As detailed in Section 2.4, the low-pass complex envelope of the RF transmitted radar pulse, $x(t, u)$, irradiated towards direction $u = \cos(\theta)$, due to the contribution of all elements of the sensor array is given by
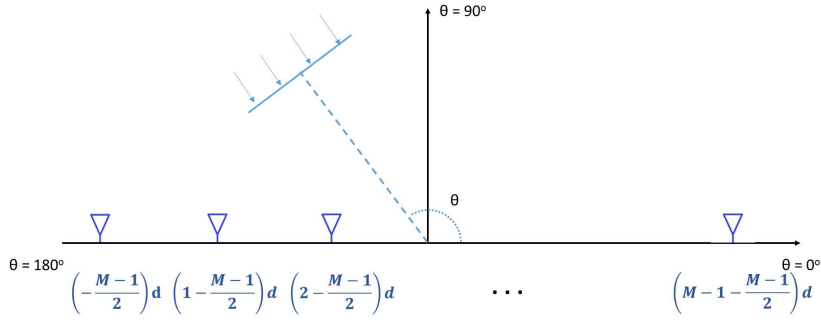
Figure 7.3: Coordinate system.

$$x(t, u) = \mathbf{w}^H \mathbf{s}(u) x(t), \tag{7.2}$$

where $\mathbf{w} = [w_0, \ldots, w_{M-1}]^T \in \mathbb{C}^{M \times 1}$ is the beamforming weighting vector, $\mathbf{s}(u)$ is the array steering vector pointed at u and $x(t)$ is given by

$$x(t) = \sqrt{2P_t} e^{j\psi} s(t), \tag{7.3}$$

where P_t is the signal power, ψ is the initial carrier phase and $s(t)$ is the radar waveform, which is a low-pass pulse of duration τ, with bandwidth W, normalized to unitary energy.

For the radar and communications topic we use the second example model of array geometry of Section 2.2, depicted here in Fig. 7.3, and we assume the steering vector defined in (2.28), in which we consider the inter-element spacing, d, as $d = \lambda_c/2$ without loss of generality.

8
Overview of the Sidelobe Modulation Methods

In this chapter, we explain in detail the main sidelobe modulation methods present in the literature, focussing only on their central ideas. We make several simulations of the methods and a deeper analysis than the original authors themselves. We also present our independent opinion about the pros and cons of the existing methods.

8.1 Sidelobe Level (SLL) Modulation

In this section we give an overview of the methods present in the literature to embed non-coherent amplitude modulation to the radar transmit beampattern. There are mainly two methods: the method of [71] and the method of [5]. The method proposed in [71] achieves the design of multiple transmit power patterns with the same mainlobe and different sidelobe levels (SLLs) by using time modulated arrays (TMA) and the method proposed by the Villanova Center of Advanced Communications Lab in [5], extended to a posterior work in [2], which solves a convex optimization problem by means of interior point techniques.

The optimization criterion involved in the method of [71] is highly nonlinear and computationally demanding, making it difficult to generate multiple transmit power distribution patterns with the same mainlobe. The situation is even worse if you think of multiple receivers and movement between the receivers and the radar platform. The other method uses a convex optimization formulation for this problem, which is much simpler to be solved. The authors of [2] remain very active in the area and claim that their strategy can cope with multiple receivers and adaptation in a real-time environment. This overview will explain in detail their strategy.

The main objective of any SLL modulation strategy is to deliver a communication message to a receiver (or multiple receivers) located within the sidelobe region of the radar transmit beampattern as a secondary task without affecting the radar operation. Therefore, one key requirement is to keep the magnitude of the mainbeam of the radar the same during the entire processing interval. On the other hand, in order to embed information in the beamformer, the SLL at the communication direction(s) should be permitted

to assume different values over the regions of interest.

These two key requirements can be achieved via appropriate transmit beamforming designs. The design described in [5] assumes that the mainbeam, where the radar task takes place, is defined by the spatial sector $\mathcal{U} = [u_{\min}, u_{\max}]$. The special case where the radar main beam is focused towards a single spatial direction corresponds to $u_{\min} = u_{\max}$. The sidelobe area is denoted as $\bar{\mathcal{U}}$. Assume that the number of communication receivers is L and the corresponding communication directions are u_l, $l = 1, \ldots, L$.

Let $\mathbf{w}_k$, $k = 0, \ldots, K-1$, where K is the total number of communication symbols, be the $M \times 1$ transmit beamforming weight vectors. One way to design the transmit weight vectors is to formulate the following optimization problem,

$$\min_{\mathbf{w}_k} \max_u \quad \left| |\mathbf{B}_d(u)| - |\mathbf{w}_k^H \mathbf{s}(u)| \right| \quad, \qquad u \in \mathcal{U} \tag{8.1}$$

$$\text{subject to} \qquad |\mathbf{w}_k^H \mathbf{s}(u)| \leq \epsilon \quad, \qquad u \in \bar{\mathcal{U}}, \tag{8.2}$$

$$\mathbf{w}_k^H \mathbf{s}(u_l) = \delta_{l,k} \quad, \qquad l = \{1, \ldots, L\}, \tag{8.3}$$

where $\mathbf{B}_d(u)$ is the desired beampattern within the main radar beam defined by the radar designers, ϵ is a positive number of user's choice used for controlling the overall SLLs, $\delta_{l,k}$ is a positive number used to determine the SLL associated with the k-th transmit beam towards the l-th communication direction and $\mathbf{s}(u)$ is the $M \times 1$ steering vector of the transmit array towards u defined in (2.28).

In (8.1) - (8.3), the objective function fits all K transmit beampatterns to the beampattern mandated by the radar operation. The set of constraints in (8.2) is used to upper-bound the transmit power leakage within the sidelobe areas, which is also mandated by the radar operation. Note that the upper bound determined by the parameter ϵ is the same for all transmit beams. The set of linear constraints (8.3) is associated with the secondary function of the system which is to embed information via different SLLs towards the communication directions. It is worth-noting that the parameter $\delta_{l,k}$ which determines the SLL is different for each one of the K transmit beams. Since ϵ is the highest sidelobe level as mandated by the main radar operation of the system, the conditions $|\delta_{l,k}| \leq \epsilon$, $k = 0, \ldots, K-1$ should be satisfied.

The optimization problem (8.1) - (8.3) is difficult to solve due to the non-convex objective function. Therefore, the authors of [2, 5] reformulate the problem by slightly modifying the objective function. They substitute $|B_d(u)|$ in (8.1) by $B_d(u)$ and set $B_d(u) = e^{j\phi(u)}$, yielding the following optimization

problem

$$\min_{\mathbf{w}_k} \max_{u_i} \left| e^{j\phi(u_i)} - \mathbf{w}_k^H \mathbf{s}(u_i) \right| \quad , \qquad u_i \in \mathcal{U}, \ i = 1, \dots, I \qquad (8.4)$$

$$\text{subject to} \qquad \left| \mathbf{w}_k^H \mathbf{s}(u_p) \right| \leq \epsilon \quad , \qquad u_p \in \bar{\mathcal{U}}, \ p = 1, \dots, P \qquad (8.5)$$

$$\mathbf{w}_k^H \mathbf{s}(u_l) = \delta_{l,k} \quad , \qquad l = \{1, \dots, L\}, \qquad (8.6)$$

where u_i, $i = 1, \dots, I$, and u_p, $p = 1, \dots, P$, are discrete grids of angles used to approximate $\mathcal{U}$ and $\bar{\mathcal{U}}$, respectively, and $\phi(u)$ is a phase profile of user's choice. The optimization problem (8.4) - (8.6) is convex and can be solved in a computationally efficient manner [74]. It is worth noting that the transmit beamforming weight vector obtained by solving (8.4) - (8.6) yields a unity magnitude within the main radar beam. However, in practice the transmit weight vector can be scaled up to the desired transmit gain as long as the total transmit power budget does not exceed the maximum allowed power of the actual system. Note that scaling up the transmit weight vector results in magnifying the transmit power distribution at all angles equally, i.e., the relative SLLs with respect to the mainlobe remains unchanged.

However, the parameter ϵ should be carefully chosen to guarantee a feasible solution. One way to do this is to solve the following auxiliary problem

$$\min_{\mathbf{w}_k, \epsilon} \epsilon \qquad (8.7)$$

$$\text{subject to} \qquad \left| \mathbf{w}_k^H \mathbf{s}(u_p) \right| \leq \epsilon \quad , \qquad u_p \in \bar{\mathcal{U}}, \ p = 1, \dots, P \qquad (8.8)$$

$$\mathbf{w}_k^H \mathbf{s}(u_l) = \delta_{l,k} \quad , \qquad l = \{1, \dots, L\}, \qquad (8.9)$$

which is guaranteed to have a feasible solution. Denote the solution to (8.7) - (8.9) as $\epsilon_{\min}$. Then, the range of values of ϵ which guarantees a feasible solution to the optimization problem (8.4) - (8.6) is given as $\epsilon \geq \epsilon_{\min}$.

(a) Brief Discussion about the Existing SLL Modulation Methods

As we have seen so far, we can note that an optimization problem must be solved by means of interior point technique each time any of the variables change. It means, if any of the L communication receivers is moving relative to the radar and u_l, $l = 1, \dots, L$, changes its value, a new optimization problem must be solved for the new value of u_l. The solution to the new problem can be achieved efficiently offline, but it takes time and resources that may not be available for real time applications.

It is also interesting to note that, though the authors of the described method say that the maximum allowable sidelobe level, ϵ, is defined by the radar operator, there is no guarantee that the solution to their problem

will lead to sidelobe levels below, ϵ. They can tell what is the minimum ϵ achievable given the communication receiver parameters, if this value is acceptable in terms of radar performance, then the communication function can be embedded to the radar. But it is important to emphasize that the minimum ϵ changes as the communication parameters change. It means that, even if the transmit beampatterns passed the sidelobe test for a given number of communication receivers at specific directions, it does not guarantee that they will pass the test again for a different set of directions or different number of communication receivers.

(b) Symbol Error Analysis

The discussion in this subsection follows a different approach than [5]. In [5], the authors, as radar experts, derive the symbol error expressions using their own methodology and nomenclature. Though the expressions are correct, it is possible to present the DFRC SLL modulation using the common digital communication theory. Here in this subsection we insert the digital communications platform into the DFRC SLL modulation context, which allows a reader familiar with digital communications to understand it more clearly. We generate illustrative examples and come up with some conclusions.

The low-pass complex envelope of the sequence of RF transmitted radar pulses, $x(t, u)$, irradiated towards direction $u = \cos(\theta)$, due to the contribution of all elements of the sensor array, is given by

$$x(t, u) = \sqrt{2E_t} e^{j\psi} \sum_{i=0}^{\infty} c_i(u) s(t - iT_{PRI}), \qquad (8.10)$$

where $c_i(u) \in \{C_k(u) = \mathbf{w}_k^H \mathbf{s}(u)\}_{k=0}^{K-1}$, T_{PRI} is the pulse repetition interval, E_t is the isotropically irradiated RF pulse energy, ψ is the initial carrier phase and $s(t)$ is the radar waveform, which is a low-pass pulse of duration τ, with bandwidth W, normalized to unitary energy. The average energy of the i-th transmitted radar pulse is then $2E_t E[|c_i(u)|^2]$. Towards the receiver communication direction, u_c, the information symbol is

$$c_i \in \{C_k = \mathbf{w}_k^H \mathbf{s}(u_c)\}_{k=0}^{K-1}, \qquad (8.11)$$

where C_k is a positive amplitude which corresponds to a symbol from an ASK modulation.

At the communication receiver located at direction u_c of the transmit beampattern, the output, $r[i]$, after demodulation, matched filtering with the waveform $s(t)$ and sampling at the point of maximum (see Fig. 8.1), is given
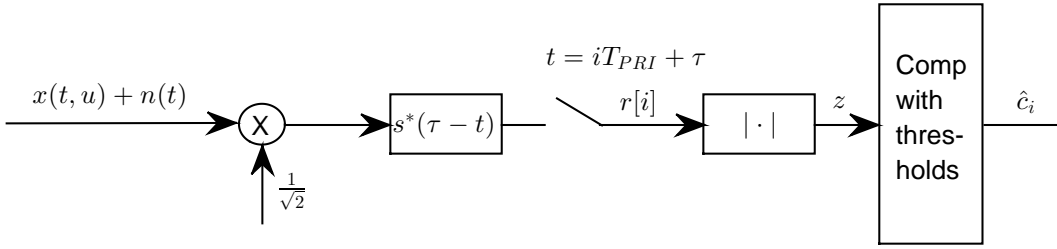
Figure 8.1: Illustration of the non-coherent ASK receiver.

by

$$r[i] = \sqrt{E_r}c_i e^{j\psi} + n_i, \tag{8.12}$$

where E_r is the energy, which was isotropically irradiated by the transmitter, at the receiver side, considering the propagation attenuation effect. Assuming equally likely symbols, the average energy of the signal term in (8.12) is then

$$E_s = E_r \mathrm{E}[|c_k|^2] = E_r \frac{1}{K} \sum_{k=0}^{K-1} |\mathbf{w}_k^H \mathbf{s}(u_c)|^2. \tag{8.13}$$

The noise, n_i, is a complex Gaussian random variable with zero mean and variance $\sigma_n^2 = N_0$. The signal to noise ratio, SNR, is given by

$$\mathrm{SNR} = \frac{E_r E[|c_k|^2]}{\sigma_n^2} = \frac{E_r}{N_0} \frac{1}{K} \sum_{k=0}^{K-1} |\mathbf{w}_k^H \mathbf{s}(u_c)|^2. \tag{8.14}$$

Dividing and multiplying (8.14) by $|B(u_{\max})|^2$, where $B(u_{\max})$ is the beampattern towards the direction of maximum, we have that the SNR can be written as

$$\mathrm{SNR} = \frac{E_r |B(u_{\max})|^2}{N_0} \frac{1}{K} \sum_{k=0}^{K-1} \frac{|\mathbf{w}_k^H \mathbf{s}(u_c)|^2}{|B(u_{\max})|^2}. \tag{8.15}$$

But $E_r |B(u_{\max})|^2$ is the energy at a receiver located towards the direction of maximum of the transmit beampattern, $E_{\max}$, and

$$\frac{|\mathbf{w}_k^H \mathbf{s}(u_c)|^2}{|B(u_{\max})|^2} = \frac{|B_k(u_c)|^2}{|B(u_{\max})|^2} = |\bar{B}_k(u_c)|^2. \tag{8.16}$$

Thus, the SNR may be written as

$$\mathrm{SNR} = \frac{E_{\max}}{N_0} \frac{1}{K} \sum_{k=0}^{K-1} |\bar{B}_k(u_c)|^2. \tag{8.17}$$

As we are dealing with a non-coherent ASK modulation, we take the absolute value of $r[i]$, $z = |r[i]|$, and compare to the thresholds. A decision is made for symbol k if z is inside the region Z_k, delimited by the thresholds, $T_{k-1,k} \leq z < T_{k,k+1}$. Fig. 8.2 depicts an example of the four decision regions for an illustrative 4-ASK constellation. In this example, we can define the
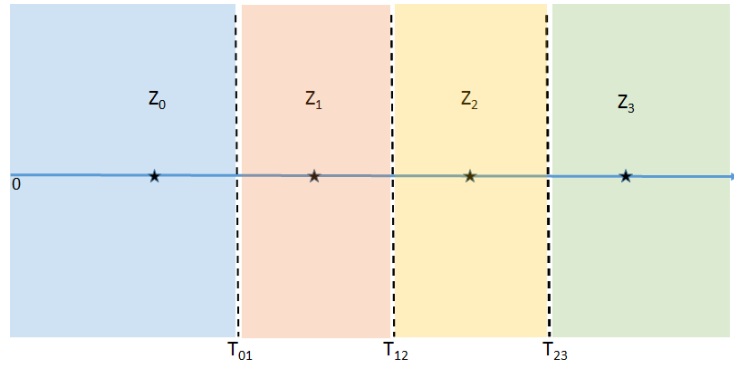
Figure 8.2: Illustration of decision regions for a 4-ASK constellation.

thresholds corresponding to the extremities as $T_{-1,0} = 0$ and $T_{3,4} = +\infty$ and the other thresholds are set in the median between two adjacent symbols for illustration purpose only.

The probability of wrong detection, $P(E)$, is given by

$$P(E) = 1 - P(R), \tag{8.18}$$

where $P(R)$ is the probability of right decision, which is given by

$$P(R) = \sum_{k=0}^{K-1} P_k P\left(z \in Z_k \mid k\right), \tag{8.19}$$

where P_k is the probability of transmitting the k-symbol and $P(z \in Z_k|k)$ is the probability of z being inside the decision region for symbol k, given that symbol k was transmitted. We can write this conditional probability as

$$P\left(z \in Z_k \mid k\right) = \int_{Z_k} p_{z|k}(Z)\mathrm{d}Z, \tag{8.20}$$

where $p_{z|k}(Z)$ is the conditional probability density of z given that symbol k was transmitted.

When symbol k is transmitted, r is a complex Gaussian variable with a non-zero mean, m_k, given by $m_k = \sqrt{E_r}C_k e^{j\psi}$ and variance given by σ_n^2, where the real and imaginary parts of r are statistically independent of each other with variance given by $\tilde{\sigma}_n^2 = \sigma_n^2/2 = N_0/2$. Therefore, the conditional density function of $z = |r[i]|$ given that symbol k is transmitted follows the Rician probability distribution,

$$p_{z|k}(Z) = \frac{Z\mathrm{e}^{-(Z^2+\mu_k^2)/(2\tilde{\sigma}_n^2)}}{\tilde{\sigma}_n^2}I_0\left(\frac{Z\mu_k}{\tilde{\sigma}_n^2}\right), \tag{8.21}$$

where $\mu_k = |m_k|$ and

$$I_0(\eta) \triangleq \frac{1}{\pi}\int_0^\pi \mathrm{e}^{\eta\cos\theta}\mathrm{d}\theta, \tag{8.22}$$

is the modified Bessel function of the first kind and zero-th order. Substituting

(8.21) into (8.20) and composing with (8.19) and (8.18), considering that the K symbols are equally probable of being transmitted, i.e. $P_k = 1/K$, we have the analytical error probability for the SLL modulation

$$P(E) = 1 - \frac{1}{K} \sum_{k=0}^{K-1} \int_{Z_k} \frac{Z \mathrm{e}^{-(Z^2+\mu_k^2)/(2\tilde{\sigma}_n^2)}}{\tilde{\sigma}_n^2} I_0\left(\frac{Z\mu_k}{\tilde{\sigma}_n^2}\right) \mathrm{d}Z, \qquad (8.23)$$

where $\mu_k = \left|\sqrt{E_r} C_k e^{j\psi}\right|$. Using the Marcum Q function, $\hat{Q}(a,b)$, defined as

$$\hat{Q}(a,b) = \int_b^\infty I_0(ax) \mathrm{e}^{-\frac{1}{2}(a^2+x^2)} x \mathrm{d}x, \qquad (8.24)$$

and substituting $a = \mu_k/\tilde{\sigma}_n$ and $x = Z/\tilde{\sigma}_n$ we can rewrite (8.23) as

$$P(E) = 1 - \frac{1}{K} \sum_{k=0}^{K-1} \left[\hat{Q}\left(\frac{\mu_k}{\tilde{\sigma}_n}, \frac{T_{k-1,k}}{\tilde{\sigma}_n}\right) - \hat{Q}\left(\frac{\mu_k}{\tilde{\sigma}_n}, \frac{T_{k,k+1}}{\tilde{\sigma}_n}\right)\right], \qquad (8.25)$$

where $T_{k-1,k}$ and $T_{k,k+1}$ are the thresholds that bound the region Z_k, $Z_k = [T_{k-1,k}, T_{k,k+1})$.

It is not so easy to define the thresholds that minimize the error probability. One approach is to set the thresholds in the point of intersection between the conditional probability density functions for each symbol, or the threshold can be found by minimizing the error probability, what can be somewhat cumbersome. It is important to note that the thresholds vary with the actual SNR, this will be clear through the next figures.

Examples of a 4-ASK and a BASK SLL Modulation

In Fig. 8.3, four beamformers generated through the solution of the convex optimization problem (8.4) - (8.6) are depicted, $\mathbf{w}_0$, $\mathbf{w}_1$, $\mathbf{w}_2$ and $\mathbf{w}_3$. They embed towards the communication receiver $u_c = -0.6$ or $\theta = 126^o$ the symbols $\delta_0 = \bar{B}_0(u_c) = \sqrt{10^{-20/10}} = 0.1$, $\delta_1 = \bar{B}_1(u_c) = \sqrt{10^{-23.1/10}} = 0.07$, $\delta_2 = \bar{B}_2(u_c) = \sqrt{10^{-27.96/10}} = 0.04$ and $\delta_3 = \bar{B}_3(u_c) = \sqrt{10^{-40/10}} = 0.01$ from the constellation $\mathcal{C} = \{C_i\}_{i=0}^3$, where $C_i = \delta_i$, $i = \{0,\ldots,3\}$. We consider a ULA consisting of $M = 10$ elements spaced by half a wavelength. The phase profile in (8.4) is given by $\phi(u_i) = 2\pi u_i$. The region $\mathcal{U}$ in (8.4) is given by $\mathcal{U} = [-0.1736, 0.1736]$, which corresponds to $\theta = [80^o, 100^o]$. The region $\bar{\mathcal{U}}$ in (8.5) is given by $\bar{\mathcal{U}} = \{[-1, -0.4226], [0.4226, 1]\}$, which corresponds to $\theta = \{[0^o, 65^o], [115^o, 180^o]\}$. Leaving the regions $u = [-0.4226, -0.1736]$ and $u = [0.1736, 0.4226]$, which correspond to $\theta = [65^o, 80^o]$ and $\theta = [100^o, 115^o]$ as the transition interval. Parameter ϵ in (8.5) is set so as to lead to -20 dB in the power pattern. We chose this 4-ASK constellation so as to be equal to the values assigned in [71].

Fig. 8.4 shows the conditional density function of the received symbols
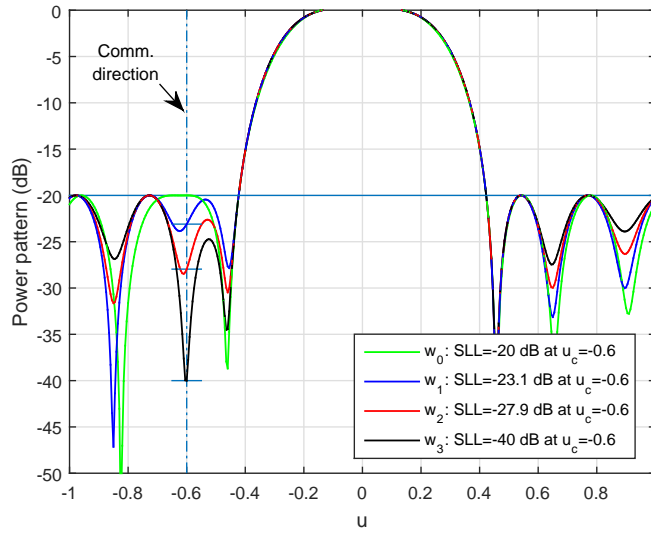
Figure 8.3: Power patterns with embedded amplitude modulation at $u_c = -0.6$ using (8.4) - (8.6).
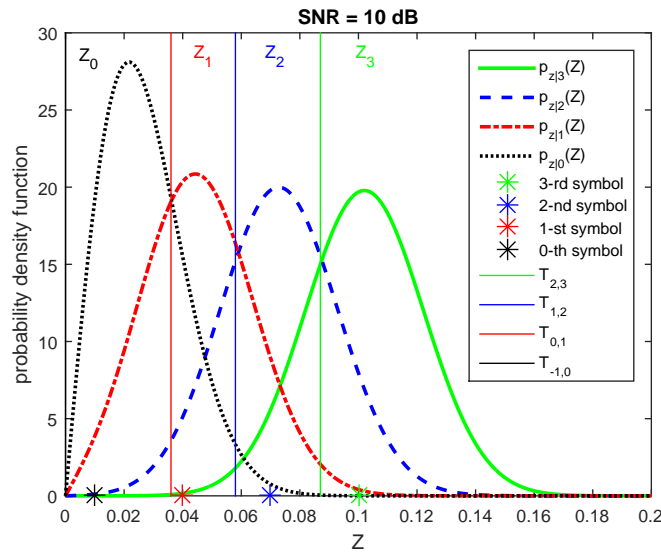
Figure 8.4: Conditional probability density function of the symbols transmitted using a 4-ASK constellation embedded using the beamformers of Fig. 8.3 and SNR = 10 dB.

using the beamformers depicted in Fig. 8.3, as well as the decision threshold in a scenario with SNR = 10 dB. Fig. 8.5 repeats Fig. 8.4 in a scenario with SNR = 20 dB. Fig. 8.6 repeats Fig. 8.4 in a scenario with SNR = 5 dB. The SNR in dB is defined as

$$\text{SNR} = 10 \log_{10} \left[E_r \frac{|C_0|^2 + |C_1|^2 + |C_2|^2 + |C_3|^2}{4\sigma_n^2} \right]. \qquad (8.26)$$

We will now analyse the binary ASK constellation (BASK). From Fig. 8.3 we choose two beamformers: $\mathbf{w}_0$ and $\mathbf{w}_3$. We show these beamformers
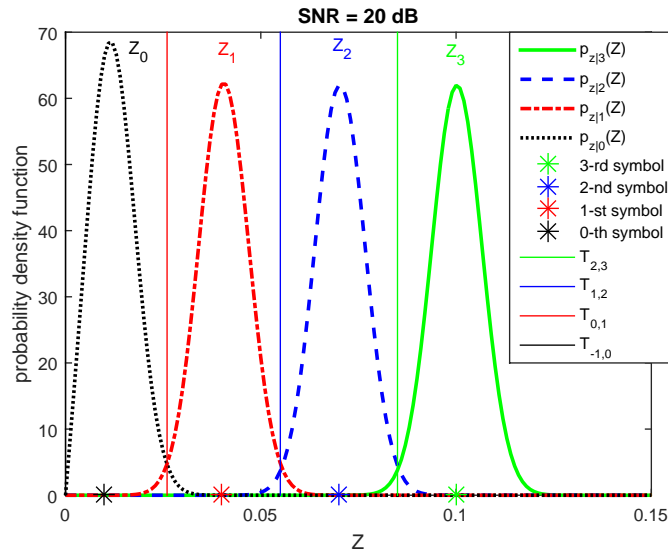
Figure 8.5: Conditional probability density function of the symbols transmitted using a 4-ASK constellation embedded using the beamformers of Fig. 8.3 and SNR = 20 dB.
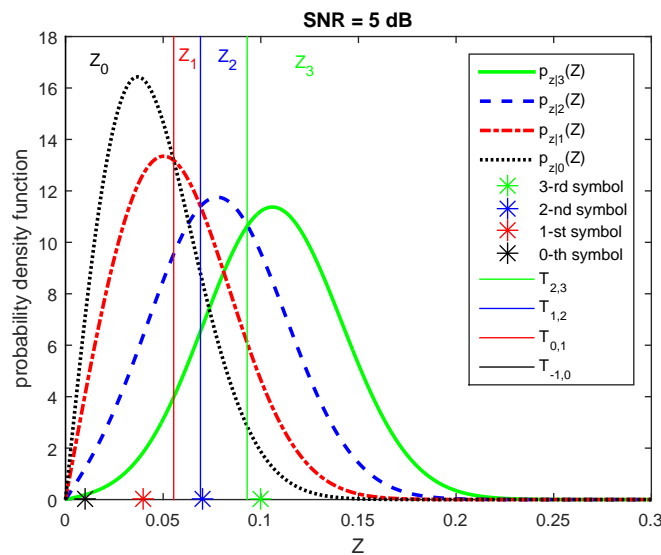
Figure 8.6: Conditional probability density function of the symbols transmitted using a 4-ASK constellation embedded using the beamformers of Fig. 8.3 and SNR = 5 dB.

separately in Fig. 8.7. They embed a binary constellation $\mathcal{C} = \{C_0, C_1\} = \{\sqrt{10^{-20/10}}, \sqrt{10^{-40/10}}\}$, where $\sqrt{10^{-20/10}}$ is associated to bit "1" and $\sqrt{10^{-40/10}}$ corresponds to bit "0". Fig. 8.8 shows the conditional density function of the received symbols using the beamformers depicted in Fig. 8.7, as well as the decision threshold in a scenario with SNR = 5 dB. Fig. 8.8 also shows the transmitted symbol in the horizontal axis and their conditional density function. Fig. 8.9 repeats Fig. 8.8 in a scenario with SNR = 10 dB. Fig. 8.10 repeats Fig. 8.8 in a scenario with SNR = 20 dB. From Figs. 8.8, 8.9 and
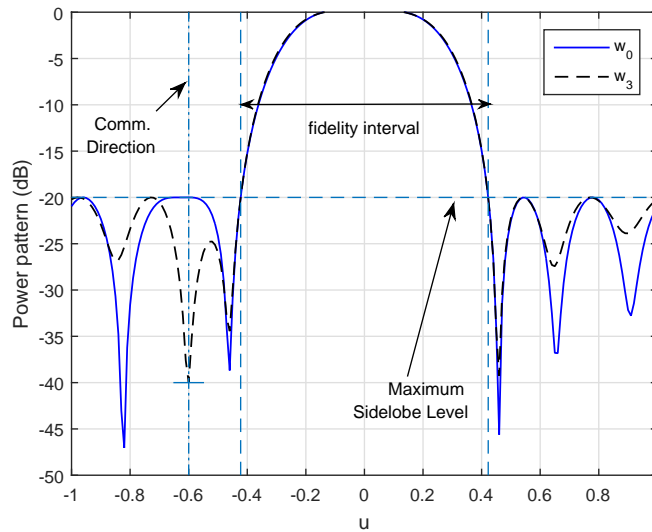
Figure 8.7: Beamformers chosen to embed a binary amplitude constellation towards $u_c = -0.6$.
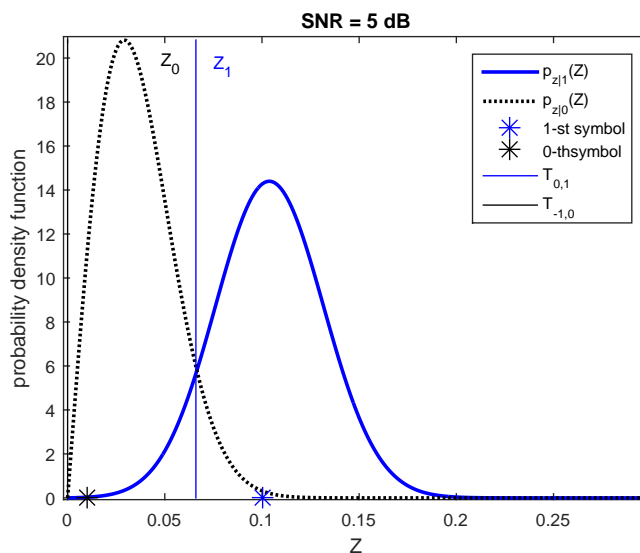
Figure 8.8: Conditional probability density function of the symbols transmitted using a BASK constellation embedded using the beamformers of Fig. 8.7 and SNR = 5 dB.

8.10 we can see that the conditional probability densities of symbols "0" and "1" are more distinguishable than the conditional probability densities of the 4-ASK case studied before.

Fig. 8.11 shows the symbol error probability, $P(E)$, which is equal to the BER, associated to the BASK signalling strategy and the symbol error probability, $P(E)$, associated to the 4-ASK signalling strategy discussed before. The error probability, $P(E)$, depicted in Fig. 8.11 was generated using (8.25), where the decision thresholds were set at the intersection of the conditional
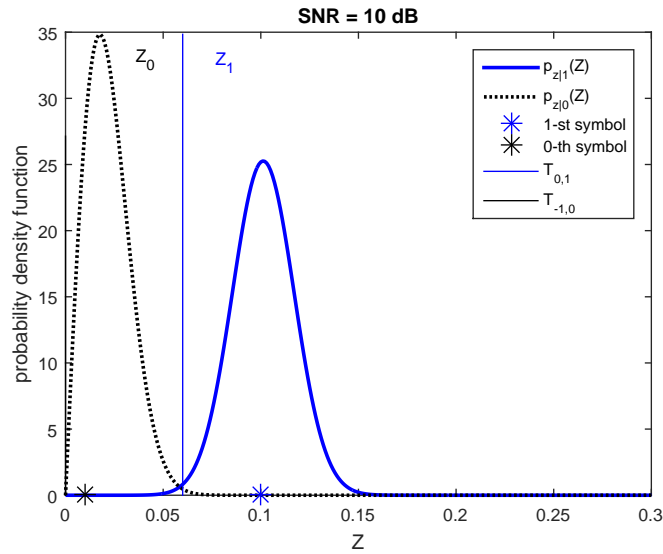
Figure 8.9: Conditional probability density function of the symbols transmitted using a BASK constellation embedded using the beamformers of Fig. 8.7 and SNR = 10 dB.
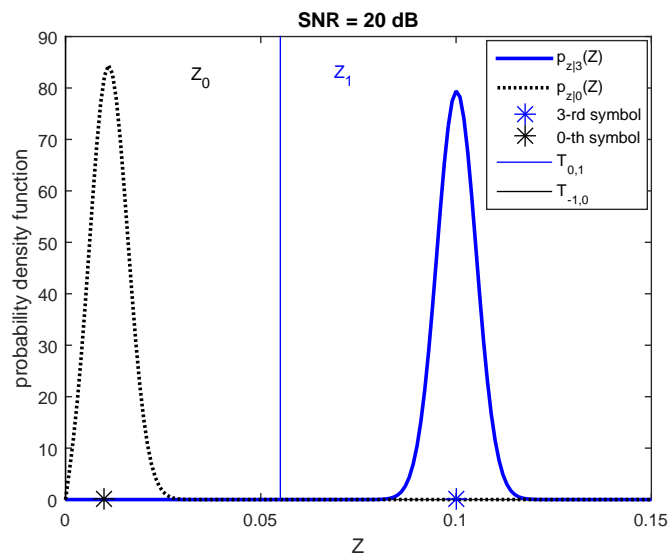
Figure 8.10: Conditional probability density function of the symbols transmitted using a BASK constellation embedded using the beamformers of Fig. 8.7 and SNR = 20 dB.

probabilities for each SNR. We can see that due to the radar constraints the BASK signalling strategy leads to more operational bit error rates than the 4-ASK signalling strategy and seems to be a more proper choice for dual-function radar-communications platform.
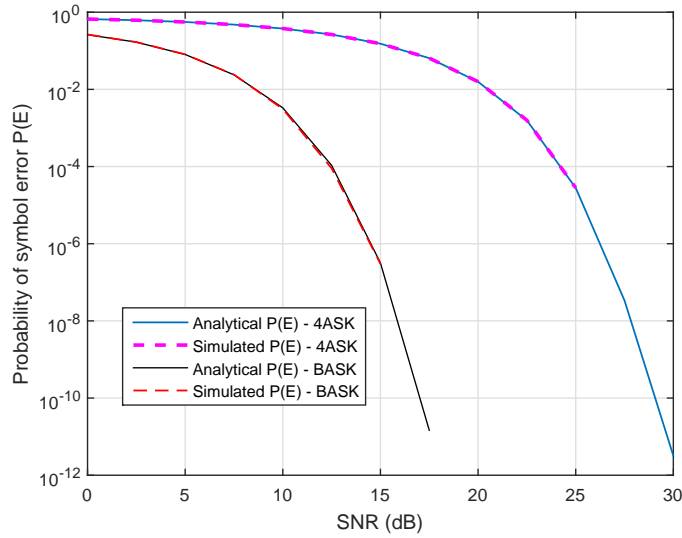
Figure 8.11: Symbol error probability for the BASK and 4-ASK constellation vs. SNR (dB).

Comments on the Security against Interception of the SLL Modulation

Now that we have chosen the BASK as a preferable SLL modulation for dual-function radar-communications platform, let's see how behaves the angular BER. We need this angular BER behavior to attest the secure communications property, that is, the property of leading to operational BER only towards the communication direction. We will also need this angular BER information in our discussion about robustness in Section 9.1.

In Fig. 8.12 we show the analytical angular BER associated to the chosen signalling strategy. The decision threshold is the same for all directions. We considered an AWGN channel for all angles and we scaled the noise power $\sigma_n^2 = \mathrm{E}\left[|n|^2\right]$ so as to lead to

$$10 \log_{10}\left(E_r \frac{|C_0|^2 + |C_1|^2}{2\sigma_n^2}\right) = 15 \text{ dB}, \, u \in [-1, 1]. \tag{8.27}$$

8.2 Sidelobe Phase Modulation

In this section, we will make an overview of the methods present in the literature to embed phase modulation to the sidelobe of the radar transmit beampattern. The methods so far described in the literature for this purpose were proposed by the Villanova University Center for Advanced Communications research team. The method proposed in [3] achieves the design of multiple transmit beampatterns which have exactly the same power radiation pattern
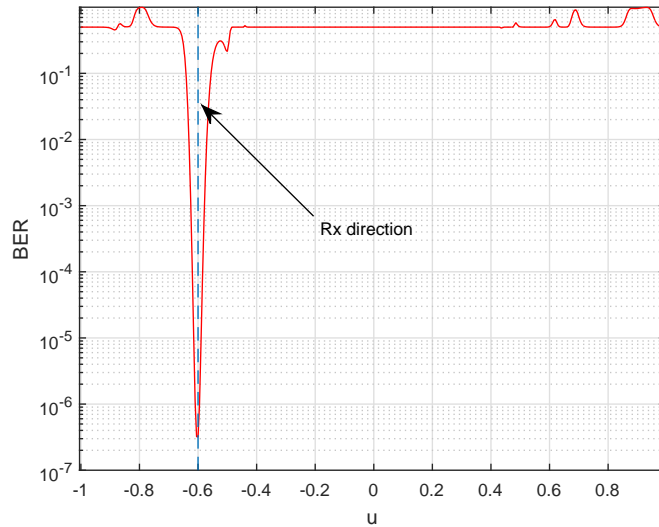
Figure 8.12: Angular BER for a binary amplitude modulation using the method of convex optimization described in [2].

and different phases towards a specific direction by exploring the beampattern phase rotational invariance. The method of [4] proposes the design of beampatterns with different phases towards a specific direction by means of convex optimization or, once again, by exploring the beampattern phase rotational invariance.

The signalling strategies proposed in [3, 4] are non-coherent, therefore it is necessary to work with phase differences. These methods suppose that there are at least two orthogonal waveforms being transmitted at the same time through different arrays with different beampatterns. The arrays are close enough so that no extra phase difference is added. Each orthogonal waveform is transmitted with a different beampattern that embeds a different phase towards the communication receiver. The communication receiver will perform matched filtering to each waveform and will compare the phase at the output of each matched filter with a reference.

(a) Method of Phase Rotational Invariance

In the method of [3], N pairs of transmit orthogonal waveforms, $(s_n(t), \tilde{s}_n(t))$, $n = 1, \ldots, N$, are used to transmit N PSK symbols from a constellation of size K, $\{\phi_k\}_{k=1}^{K}$, where the k-th symbol, ϕ_k, of the phase-rotation dictionary embedded towards direction u_c is given by

$$\phi_k = \angle \frac{\mathbf{w}_k^H \mathbf{s}(u_c)}{\tilde{\mathbf{w}}_k^H \mathbf{s}(u_c)}, \tag{8.28}$$

where $\mathbf{s}(u_c)$ is the steering vector pointed to the communication receiver.
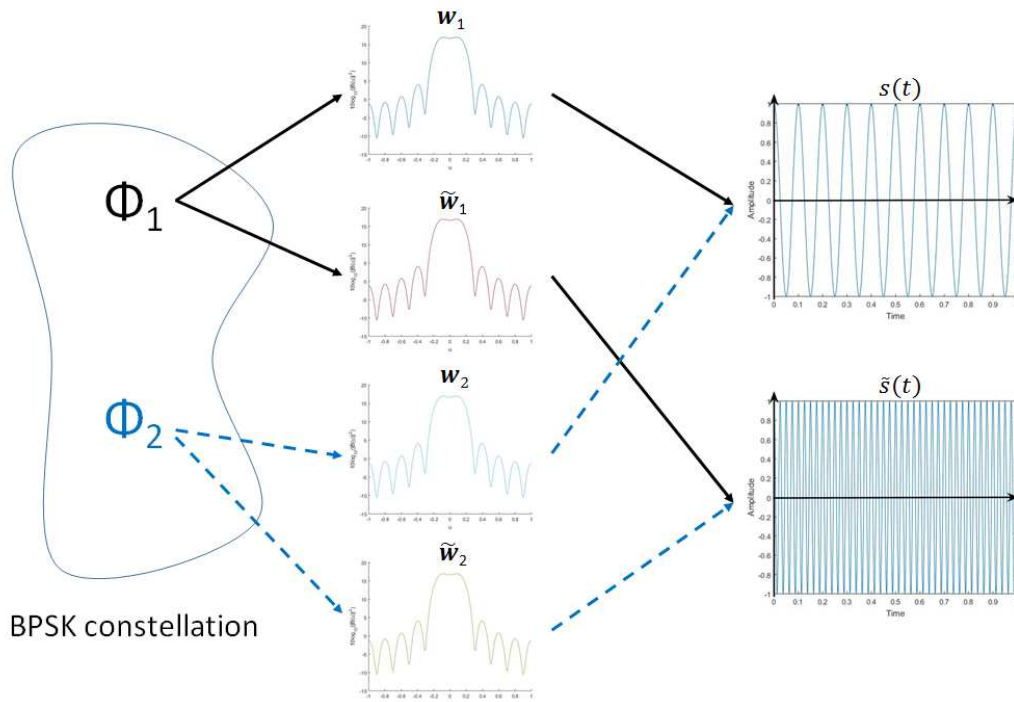
Figure 8.13: Illustration of the signalling method of [3].

The same pairs of waveforms are used during all pulses while the pairs of transmit beamforming weight vectors change from pulse to pulse based on which entries of the constellation are to be embedded.

In this subsection we explain how the pair $(N = 1)$ of transmit beamforming weight vectors $(\mathbf{w}_k, \tilde{\mathbf{w}}_k)$ is generated for embedding a certain entry of the PSK constellation.

In Fig. 8.13 the signalling strategy is illustrated for an example of a phase-rotation dictionary of size two $(K = 2)$, that composes a BPSK constellation with symbols ϕ_1 and ϕ_2. When symbol ϕ_1 is triggered to be transmitted, the pair of beamformers $\mathbf{w}_1$ and $\tilde{\mathbf{w}}_1$ are used for generating the beampattern of two sensor arrays. Through the sensor array of beamformer $\mathbf{w}_1$ the waveform $s(t)$ is irradiated and through the sensor array of beamformer $\tilde{\mathbf{w}}_1$ the waveform $\tilde{s}(t)$ is irradiated. Equivalently, when symbol ϕ_2 is triggered to be transmitted, the pair of beamformers $\mathbf{w}_2$ and $\tilde{\mathbf{w}}_2$ are used for generating the beampattern of two sensor arrays. Through the sensor array of beamformer $\mathbf{w}_2$ the waveform $s(t)$ is irradiated and through the sensor array of beamformer $\tilde{\mathbf{w}}_2$ the waveform $\tilde{s}(t)$ is irradiated.

The method proposed in [3] starts with a principal transmit beamforming weight vector, $\mathbf{w}$. which satisfies a certain desired transmit power radiation pattern. The $M \times 1$ principal weight vector can be used to generate a population of $2^{(M-1)}$ weight vectors of the same dimensionality which have the same transmit power radiation pattern as that of $\mathbf{w}$, [73]. The aforementioned
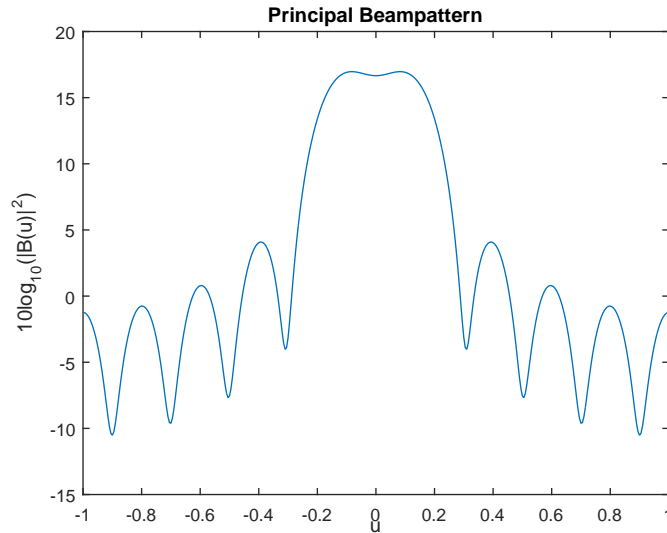
Figure 8.14: Principal beampattern.

population, denoted as $W = \{\mathbf{w}_1, \ldots, \mathbf{w}_{2(M-1)}\}$, can be obtained by viewing the principal weight vector as a polynomial of order $M - 1$ with $M - 1$ roots denoted as r_i, $i = 1, \ldots, 2M - 1$. Note that reflecting each root with respect to the unit circle does not change the magnitude of the beampattern.

Comments on the Method of Rotational Invariance for Embedding Sidelobe Phase Modulation

Let's observe an example of the phase rotational invariance method where the principal power beampattern is depicted in Fig. 8.14. In the simulation of Fig. 8.14 we used a transmit ULA of $M = 10$ antennas spaced half a wavelength apart and assume that a communication receiver is located at $u_c = 0.6428$, or equivalently, $\theta_c = 40^o$. The beamformer is designed to focus the transmit energy within the sector $\mathcal{U} = [-0.1736, 0.1736]$, which corresponds to $\Theta = [80^o, 100^o]$ using spheroidal sequences [75]. Specifically, it is computed as

$$\mathbf{w} = \sqrt{\frac{E_t}{2}}(\mathbf{u}_1 + \mathbf{u}_2), \tag{8.29}$$

where E_t is the isotropically irradiated signal energy, normalized to be equal to M, and $\mathbf{u}_1$ and $\mathbf{u}_2$ are the two principal eigenvectors of the matrix $\mathbf{A}$ given by

$$\mathbf{A} = \int_{\mathcal{U}} \mathbf{s}(u)\mathbf{s}^H(u)\mathrm{d}u. \tag{8.30}$$

The principal weight vector of Fig. 8.14 is used to generate a population of $2^{M-1} = 512$ weight vectors which have exactly the same transmit power patterns [73]. Fig. 8.15 shows the phase of each of the 512 beamformers towards $u = 0.6428$.
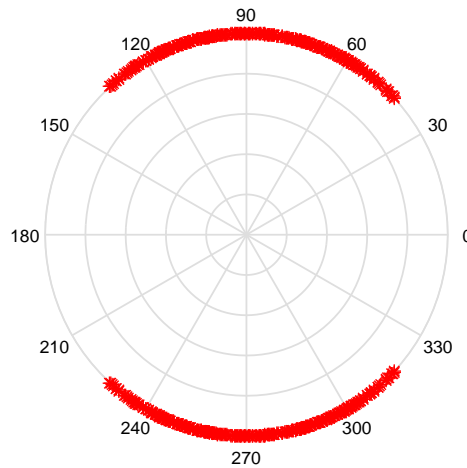
Figure 8.15: Phase towards $u = 0.6428$ generated by all the 512 beamformers.
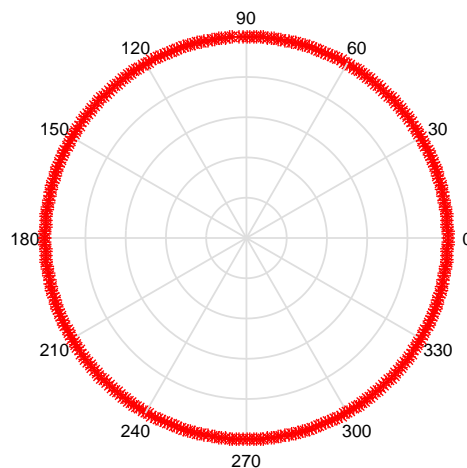
Figure 8.16: Phase difference towards $u = 0.6428$ generated by 262144 beamformer pairs.

From Fig. 8.15 we can note that if we could use coherent processing, this formulation wouldn't be appropriate for a QPSK modulation, for example, as we can't pick four beamformers that generate a QPSK modulation.

If we work with the phase difference between the pairs of beamformers this situation improves. In Fig. 8.16 the population W is used to build 512^2 pairs of vectors and the phase rotations associated with the communication direction $u = 0.6428$ for the 262144 available pairs are depicted. Fig. 8.16 shows that the available phase-rotations cover the entire phase domain between 0° and 360°. This enables choosing a suitable phase rotation for any phase constellation.
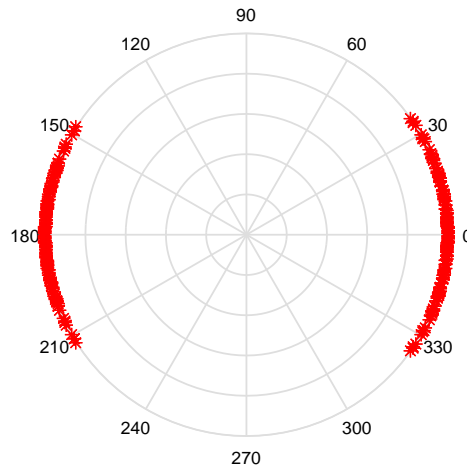
Figure 8.17: Phase towards $u = 0.5$ generated by all the 512 beamformers.
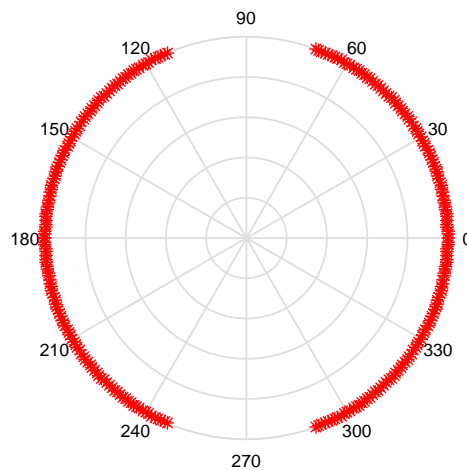
Figure 8.18: Phase difference towards $u = 0.5$ generated by 262144 beamformer pairs.

But as we can see in Figs. 8.17 and 8.18, this situation is different if the communication receiver is located at $u_c = 0.5$, or equivalently, $\theta_c = 60^o$. In Fig. 8.17 the phase of all 512 beamformers towards $u = 0.5$ is depicted. Fig. 8.18 shows the phase difference towards $u = 0.5$ for the same beamformer pairs used to generate Fig. 8.16. We can see from Fig. 8.18 that not all phase constellations can be used towards $u = 0.5$, as there are holes in the phase diagram shown in Fig. 8.18.

With this simple example we can readily realize that not all phase constellations are available towards all directions at the sidelobe. This fact is not mentioned in [3], but the phase constellation has to be designed

thoughtfully, thinking that the receiver may be anywhere within the sidelobe. Defining the beamformer pairs that will lead to the same phase constellation within the sidelobe is a study that would have to be carried offline. This fact also impacts directly on the storage capacity of the radar, as the pairs that generate the desired phase constellation for one direction are not necessarily the same that will generate the same phase constellation for other directions.

Another point that is not considered in [3] is the difficulty, probably the impossibility of embedding phase modulation towards more than one communication receiver. In [3] they consider that it would be possible to embed phase modulation to L receivers located at the sidelobe. But as the population W is limited, they don't lead to enough flexibility for generating beamformers that can embed phase modulation to more than one direction and deal with the dynamics at the same time. This subject needs a careful study.

Bit Error Rate for the Binary Case

The low-pass complex envelope of the sequence of RF transmitted radar pulses, $x(t, u)$, irradiated towards direction $u = \cos(\theta)$, using the phase-rotational invariance method to embed simultaneously N PSK symbols at the sidelobe, is given by

$$
\begin{aligned}
x(t, u) \;=\;& \sqrt{2E_t}\, e^{j\psi} \sum_{i=0}^{\infty} \left[\sum_{n=1}^{N} \left(\mathbf{w}_{n,i}^H \mathbf{s}(u) s_n(t - iT_{PRI}) \right. \right. \\
&+ \left. \left. \tilde{\mathbf{w}}_{n,i}^H \mathbf{s}(u) \tilde{s}_n(t - iT_{PRI}) \right) \right],
\end{aligned}
\tag{8.31}
$$

where the pair $(\mathbf{w}_{n,i}, \tilde{\mathbf{w}}_{n,i}) \in \{(\mathbf{w}_k, \tilde{\mathbf{w}}_k)\}_{k=1}^{K}$ is one of the K possible beamforming weighting vectors pairs, which embeds the n-th symbol during the i-th pulse, $\mathbf{s}(u)$ is the array steering vector pointed at u, E_t is the arrays' isotropically irradiated energy, ψ is the initial carrier phase, $(s_n(t), \tilde{s}_n(t))$, $n = 1, \ldots, N$, are N pairs of orthogonal radar waveforms, which are low-pass pulses of duration τ, normalized to unitary energy and T_{PRI} is the radar pulse repetition interval.

At the communication receiver located at direction u of the transmit beampattern, the outputs, $r_n[i]$ and $\tilde{r}_n[i]$, after demodulation, matched filtering with the waveforms $s_n(t)$ and $\tilde{s}_n(t)$, $n = 1, \ldots, N$, and sampling the outputs at the point of maximum (see Fig. 8.19) are given by

$$
r_n[i] \;=\; \sqrt{E_r}\, e^{j\psi} \mathbf{w}_{n,i}^H \mathbf{s}(u) + n_n,
\tag{8.32}
$$

$$
\tilde{r}_n[i] \;=\; \sqrt{E_r}\, e^{j\psi} \tilde{\mathbf{w}}_{n,i}^H \mathbf{s}(u) + \tilde{n}_n,
\tag{8.33}
$$
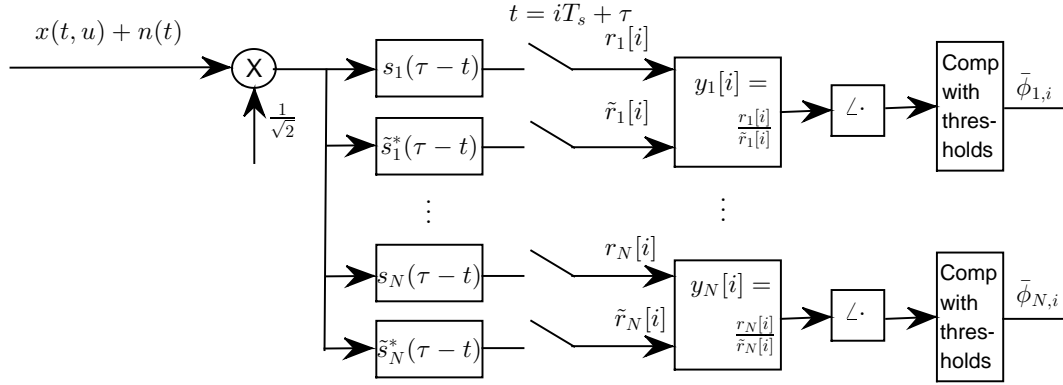
Figure 8.19: Illustration of the rotational invariance-based non-coherent PSK receiver.

where E_r is the energy at the receiver side which was isotropically irradiated by the transmitter, n_n and $\tilde{n}_n$, $n = 1, \ldots, N$, are independent complex Gaussian random variables with zero mean and variance $\sigma_{n_n}^2 = \sigma_{\tilde{n}_n}^2 = \sigma_n^2 = N_0$.

The authors take the angle of the ratio $y_n[i]$,

$$z_n[i] = \angle y_n[i], \tag{8.34}$$

where $y_n[i]$ is given by

$$y_n[i] = \frac{r_n[i]}{\tilde{r}_n[i]}, \tag{8.35}$$

for comparison with the angular thresholds in order to define the output of the n-th symbol of the i-th pulse, $\bar{\phi}_{n,i}$ (see Fig. 8.19).

Thus, the decision variable, $z_n[i]$, due to the n-th symbol of the i-th transmitted radar pulse at direction u, is given by

$$z_n[i] = \angle \frac{\sqrt{E_r}e^{j\psi}\mathbf{w}_{n,i}^H\mathbf{s}(u) + n_n}{\sqrt{E_r}e^{j\psi}\tilde{\mathbf{w}}_{n,i}^H\mathbf{s}(u) + \tilde{n}_n}. \tag{8.36}$$

Towards the receiver direction, u_c, in the noise free environment we have exactly $\bar{\phi}_{n,i} = \phi_{n,i}$, $\phi_{n,i} \in \{\phi_k\}_{k=1}^K$.

The non-coherent PSK receiver used in the rotational invariance-based sidelobe modulation method is depicted in Fig. 8.19.

In Figs. 8.20 and 8.21 we show an example of a set of beamformers, $\mathbf{w}_1$, $\tilde{\mathbf{w}}_1$, $\mathbf{w}_2$ and $\tilde{\mathbf{w}}_2$, used to embed a BPSK constellation $\phi_1 = 0$ corresponding to bit "0" and $\phi_2 = \pi$ corresponding to bit "1", in tandem with two orthogonal waveforms $s(t)$ and $\tilde{s}(t)$, using the method of rotational invariance described in [3]. We can note from Figs. 8.20 and 8.21 that the four beamformers have exactly the same power patterns as expected!

In Fig. 8.22 the phase difference towards u_c of the beamformer pairs $(\mathbf{w}_1, \tilde{\mathbf{w}}_1)$ and $(\mathbf{w}_2, \tilde{\mathbf{w}}_2)$ is depicted in polar coordinates. We can see that the BPSK constellation is met sharply.
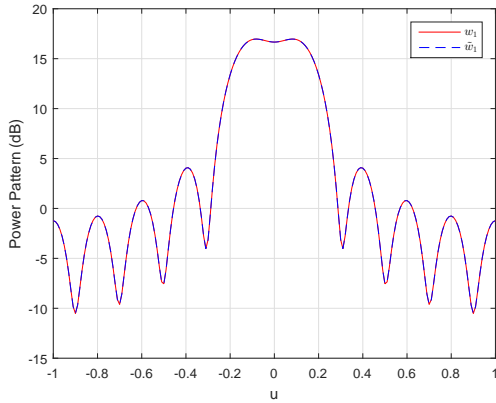
Figure 8.20: Transmit power pattern generated by the beamformers $\mathbf{w}_0$ and $\tilde{\mathbf{w}}_0$.
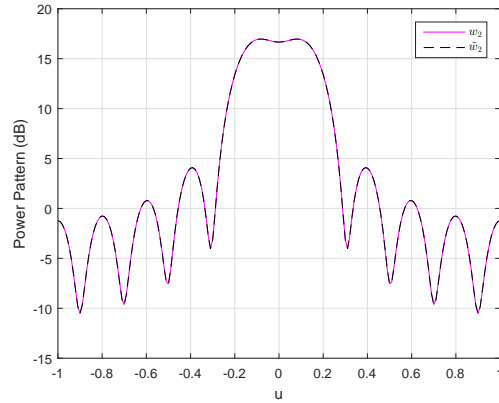
Figure 8.21: Transmit power pattern generated by the beamformers $\mathbf{w}_1$ and $\tilde{\mathbf{w}}_1$.
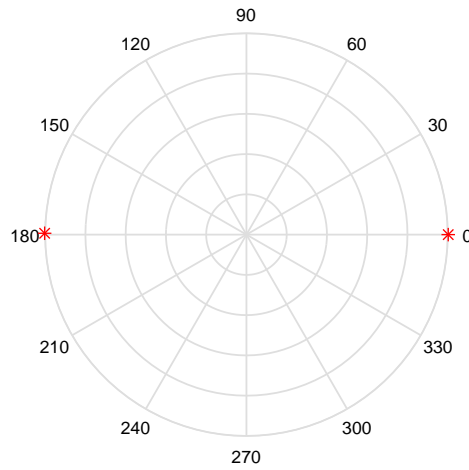
Figure 8.22: Phase difference towards $u_c = 0.6428$ of the beamformer pairs $(\mathbf{w}_1, \tilde{\mathbf{w}}_1)$ and $(\mathbf{w}_2, \tilde{\mathbf{w}}_2)$ in polar coordinates.

In this BPSK case, given that bit "0" is transmitted at the i-th radar pulse, the ratio $y_1[i] = r_1[i]/\tilde{r}_1[i]$ is

$$y_1[i] = \frac{\sqrt{E_r} e^{j\psi} \mathbf{w}_0^H \mathbf{s}(u_c)}{\sqrt{E_r} e^{j\psi} \tilde{\mathbf{w}}_0^H \mathbf{s}(u_c)} + n_0, \tag{8.37}$$

$$y_1[i] = 1 + n_0, \tag{8.38}$$

where n_0 is **non-Gaussian noise**. Given that bit "1" is transmitted the ratio
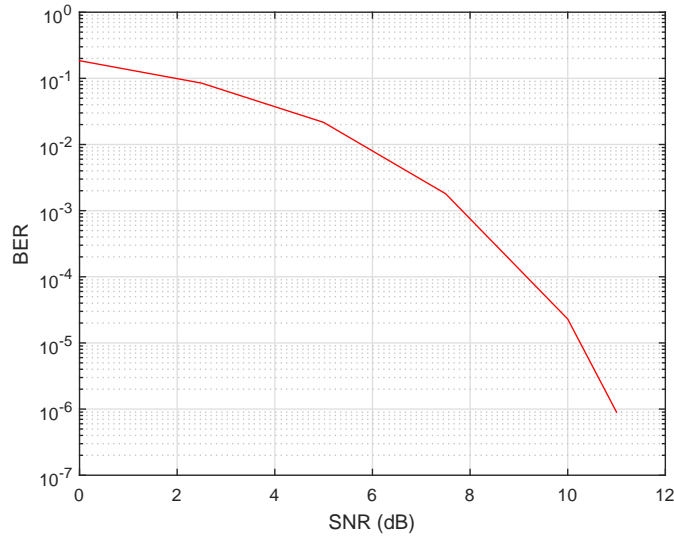
Figure 8.23: Bit error probability for the non-coherent BPSK vs. SNR (dB) using the phase rotational invariance method.

$y_1[i] = r_1[i]/\tilde{r}_1[i]$ is

$$y_1[i] \;=\; \frac{\sqrt{E_r}e^{j\psi}\mathbf{w}_1^H\mathbf{s}(u_c)}{\sqrt{E_r}e^{j\psi}\tilde{\mathbf{w}}_1^H\mathbf{s}(u_c)} + n_1, \tag{8.39}$$

$$y_1[i] \;=\; -1 + n_1, \tag{8.40}$$

where n_1 is **non-Gaussian noise**. Calling $z_1[i] = \Re\{y_1[i]\}$, the authors decide for bit "0" if $z_1[i] > 0$ and decide for bit "1" if $z_1[i] \leq 0$. Fig. 8.23 shows the simulated BER using the Monte Carlo method for the described non-coherent BPSK system where the SNR in dB is defined as

$$\mathrm{SNR} = 10\log_{10}\left[\frac{E_r(|\mathbf{w}_0^H\mathbf{s}(u_c)|^2 + |\tilde{\mathbf{w}}_0^H\mathbf{s}(u_c)|^2 + |\mathbf{w}_1^H\mathbf{s}(u)|^2 + |\tilde{\mathbf{w}}_1^H\mathbf{s}(u)|^2)}{4\sigma_n^2}\right]. \tag{8.41}$$

Comments on the Security against Interception of the Phase Rotational Invariance Method

Fig 8.24 shows the phase difference of the beamformer pairs $(\mathbf{w}_1,\tilde{\mathbf{w}}_1)$ and $(\mathbf{w}_2,\tilde{\mathbf{w}}_2)$ in the u-space for the considered non-coherent BPSK system. We can note from Fig. 8.24 that towards the communication receiver the phase difference is 180° and that this difference is repeated for many other directions as well. This fact is reflected in the angular BER as can be noted from Fig. 8.25.

In Fig. 8.25, we simulated the transmission of 10^6 symbols for each angle and guaranteed that at each angle the SNR was of 10 dB.

We can note that Fig. 8.25 is in agreement with Fig. 8.24 and that

the same BER obtained towards u_c can also be obtained for many other directions. We can note that the majority of the u-space is awarded with operational BERs. This characteristic of the rotational invariance method is not appropriate for secure communications, as it doesn't lead to operational BER only towards the communication receiver region.
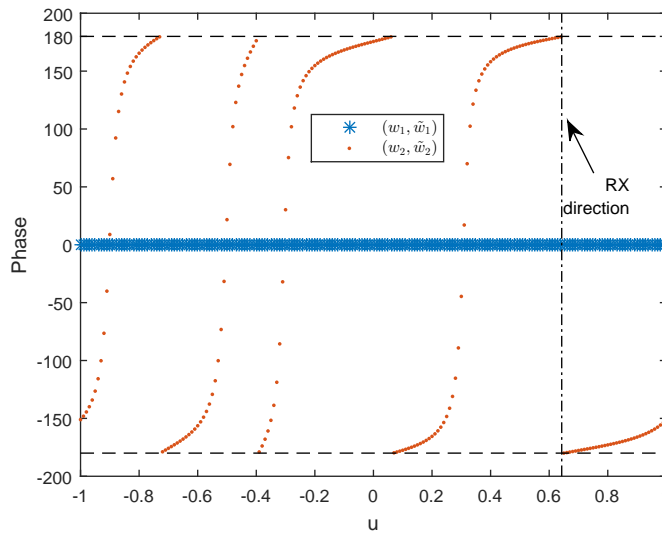
Figure 8.24: Phase difference in the u-space generated by the beamformer pairs $(\mathbf{w}_1, \tilde{\mathbf{w}}_1)$ and $(\mathbf{w}_2, \tilde{\mathbf{w}}_2)$.
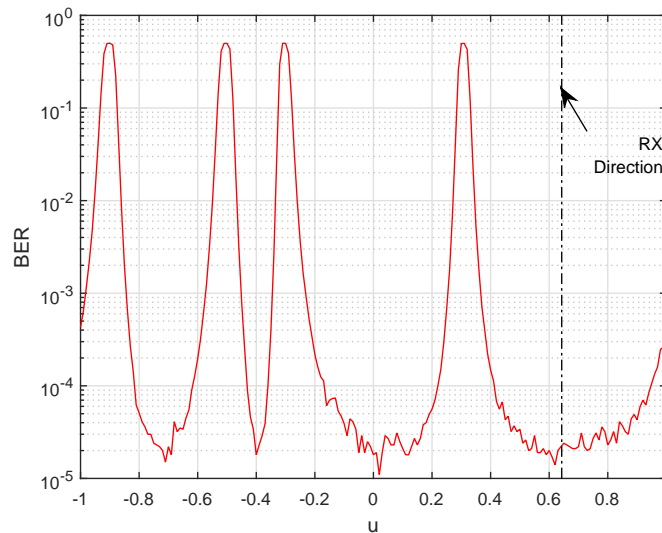
Figure 8.25: Angular BER for a BPSK modulation using the method of rotational invariance described in [3].

(b) Method of Common Reference

The method of [3] uses a pair of orthogonal waveforms in tandem with a pair of beamformers to non-coherently embed a PSK symbol. If there was

available, for example, four orthogonal waveforms, the method of [3] would use two pairs of orthogonal waveforms in tandem with two pairs of beamformers to transmit two PSK symbols during each pulse. What was noted in [4] is that one can make it better. In that example of having four orthogonal waveforms, one could use a common phase reference being transmitted by beamformer $\mathbf{w}_0$ thorough one of these orthogonal waveforms, then one could non-coherently embed three PSK symbols during each pulse in the difference of the other three beamformers used to transmit the other three orthogonal waveforms, increasing the symbol rate.

In Fig. 8.26 the signalling strategy of [4] is illustrated for an example where four orthogonal waveforms, $s_0(t)$, $s_1(t)$, $s_2(t)$ and $s_3(t)$, are available for transmitting simultaneously through four independent array of sensors. Each array is able to change its own beampattern from pulse to pulse. In this example, we use a PSK constellation of size three with symbols ϕ_1, ϕ_2 and ϕ_3. The three symbols are mapped to three pairs of beamformer, where a common beamformer is used in all of the pairs, $(\mathbf{w}_1, \mathbf{w}_0)$, $(\mathbf{w}_2, \mathbf{w}_0)$ and $(\mathbf{w}_3, \mathbf{w}_0)$. Beamformer $\mathbf{w}_0$ is always used to generate the beampattern that will irradiate waveform $s_0(t)$. The other three waveforms will have their radiation patterns generated according to the sequence of symbols to be embedded. In the example of Fig. 8.26, the sequence ϕ_1, ϕ_1 and ϕ_3 is triggered to be transmitted. Thus beamformer $\mathbf{w}_1$ is used to generate the radiation pattern of waveforms $s_1(t)$ and $s_2(t)$ and beamformer $\mathbf{w}_3$ is used to generate the radiation pattern of waveforms $s_3(t)$. If the signalling strategy used was of [3], only two symbols could be embedded using the four orthogonal waveforms simultaneously, instead of three.

In the method of [4], N orthogonal waveforms are used to simultaneously embed $N-1$ PSK symbols. The PSK symbols belong to a constellation of size K, where symbol $\phi_k \in \{\phi_i\}_{i=1}^K$, embedded towards direction u_c is given by

$$\phi_k = \angle \frac{\mathbf{w}_k^H \mathbf{s}(u_c)}{\mathbf{w}_0^H \mathbf{s}(u_c)}. \tag{8.42}$$

Also in [4], the authors suggest generating the beamformers using convex optimization, similarly to the SLL formulation. In the optimization problem formulation of [4], they suppose there is a reference beamformer $\mathbf{w}_0$ and the other beamformers, $\mathbf{w}_k$, $k = 1, \ldots, K$, will try to approach the beampattern of $\mathbf{w}_0$ the best as they can while embedding a certain phase towards the communication receiver direction, u_c. One way to design $\mathbf{w}_k$ is by minimizing the norm of the difference between the two weight vectors, i.e., by minimizing the deviation of $\mathbf{w}_k$ from $\mathbf{w}_0$, while enforcing one linear constraint to satisfy the phase requirements. This can be formulated as the following optimization
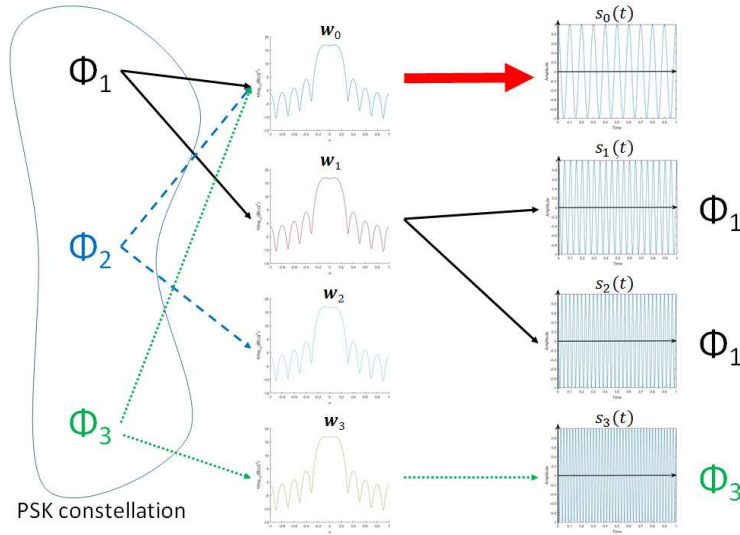
Figure 8.26: Illustration of the signalling method of [4] for the sequence of symbols ϕ_1, ϕ_2 and ϕ_3.

problem

$$\min_{\mathbf{w}_k} \quad ||\mathbf{w}_0 - \mathbf{w}_k||, \tag{8.43}$$
$$\text{s.t.} \quad \mathbf{w}_k^H \mathbf{s}(u_c) = G_0 e^{-j\phi_k},$$

where $G_0 = \mathbf{w}_0^H \mathbf{s}(u_c)$ and $\phi_k = \{\phi_1, \ldots, \phi_K\}$. The optimization problem (8.43) is convex and, therefore, can be efficiently solved using the interior point methods [74]. Another advantage to this convex optimization-based design compared to the phase rotational invariance design is that the desired phase rotations are satisfied with equality. However, the obtained solutions yield transmit weight vectors with very similar patterns to that of $\mathbf{w}_0$, but not identical as it happens using the phase rotational invariance design.

Bit Error Rate for the Binary Case

The low-pass complex envelope of the sequence of RF transmitted radar pulses, $x(t, u)$, irradiated towards direction $u = \cos(\theta)$, using the method of [4] to embed simultaneously $N - 1$ PSK symbols at the sidelobe, is given by

$$x(t, u) = \sqrt{2E_t} e^{j\psi} \sum_{i=0}^{\infty} \left(\mathbf{w}_0^H \mathbf{s}(u) s_0(t - iT_{PRI}) + \sum_{n=1}^{N-1} \mathbf{w}_{n,i}^H \mathbf{s}(u) s_n(t - iT_{PRI}) \right), \tag{8.44}$$

where $\mathbf{w}_0 \in \mathbb{C}^{M \times 1}$ is the reference beamformer which is always transmitted in tandem with waveform $s_0(t)$. The beamformers $\mathbf{w}_{n,i} \in \{\mathbf{w}_k\}_{k=1}^K$ embed the N-1 symbols $\phi_{n,i} = \mathbf{w}_{n,i}^H \mathbf{s}(u) / \mathbf{w}_0^H \mathbf{s}(u) \in \{\phi_k\}_{k=1}^K$ during the transmission of

the i-th radar pulse. The array steering vector pointed at u is $\mathbf{s}(u)$, E_t is the isotropically irradiated signal energy by each array, ψ is the initial carrier phase, $s_n(t)$, $n = \{0, \ldots, N-1\}$ are orthogonal waveforms, which are low-pass pulses of duration τ, normalized to unitary energy and T_{PRI} is the radar pulse repetition interval.

At the communication receiver located at direction u of the transmit beampattern, the outputs, $r_n[i]$, $n = \{0, \ldots, N-1\}$ after demodulation, matched filtering with the waveforms $s_n(t)$, $n = \{0, \ldots, N-1\}$ and sampling the N outputs at the point of maximum (see Fig. 8.27) are given by

$$r_0[i] = \sqrt{E_r}e^{j\psi}\mathbf{w}_0^H\mathbf{s}(u) + n_0, \tag{8.45}$$

$$r_n[i] = \sqrt{E_r}e^{j\psi}\mathbf{w}_{n,i}^H\mathbf{s}(u) + n_n, \quad n = \{1, \ldots, N-1\}, \tag{8.46}$$

where E_r is the energy, which was isotropically irradiated by the transmitter, at the receiver side, considering the propagation attenuation effect, n_n, $n = \{0, \ldots, N-1\}$ are independent complex Gaussian random variables with zero mean and variance $\sigma_{n_n}^2 = \sigma_n^2 = N_0$.

The authors take the angle of the ratio $y_n[i]$,

$$z_n[i] = \angle y_n[i], \tag{8.47}$$

where $y_n[i]$ is given by

$$y_n[i] = \frac{r_n[i]}{r_0[i]}, \quad n = 1, \ldots, N-1, \tag{8.48}$$

for comparison with the angular thresholds in order to define the output of the n-th symbol of the i-th pulse transmitted, $\bar{\phi}_{n,i}$ (see Fig. 8.27).

Thus, the n-th decision variable due to the i-th transmitted radar pulse, $z_n[i]$, $n = \{1, \ldots, N-1\}$, at direction u, is given by

$$z_n[i] = \angle \frac{\sqrt{E_r}e^{j\psi}\mathbf{w}_{n,i}^H\mathbf{s}(u) + n_n}{\sqrt{E_r}e^{j\psi}\mathbf{w}_0^H\mathbf{s}(u) + n_0}. \tag{8.49}$$

Towards the receiver direction, u_c, in the noise free environment we have exactly $\bar{\phi}_{n,i} = \phi_{n,i}$, $\phi_{n,i} \in \{\phi_k\}_{k=1}^K$.

The non-coherent PSK receiver used in the common reference-based sidelobe modulation method is depicted in Fig. 8.27.

In Fig. 8.28 we show an example of a set of beamformers, $\mathbf{w}_0$, $\mathbf{w}_1$ and $\mathbf{w}_2$, used in tandem with two orthogonal waveforms, $s_0(t)$ and $s_1(t)$, to embed a BPSK constellation towards $u_c = -0.6$, $\phi_1 = 0$ which corresponds to bit "0" and $\phi_2 = \pi$ which corresponds to bit "1", using the signalling strategy of [4]. The beamformers $\mathbf{w}_1$ and $\mathbf{w}_2$ were generated by solving the convex
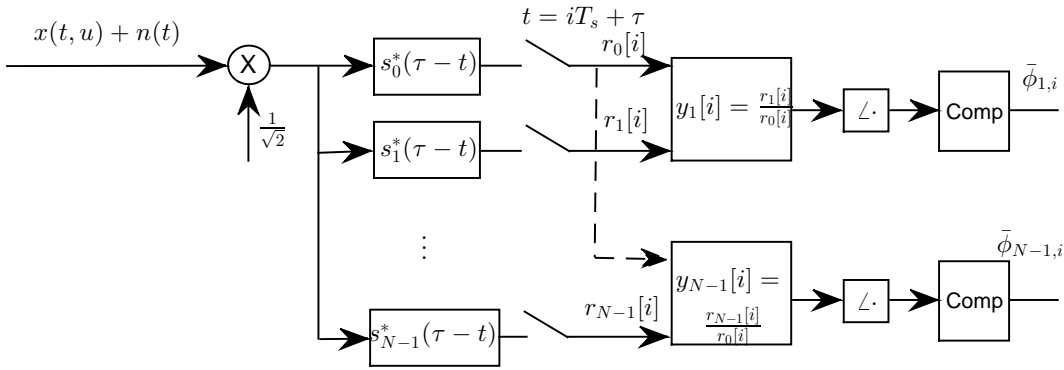
Figure 8.27: Illustration of the common reference-based non-coherent PSK receiver.
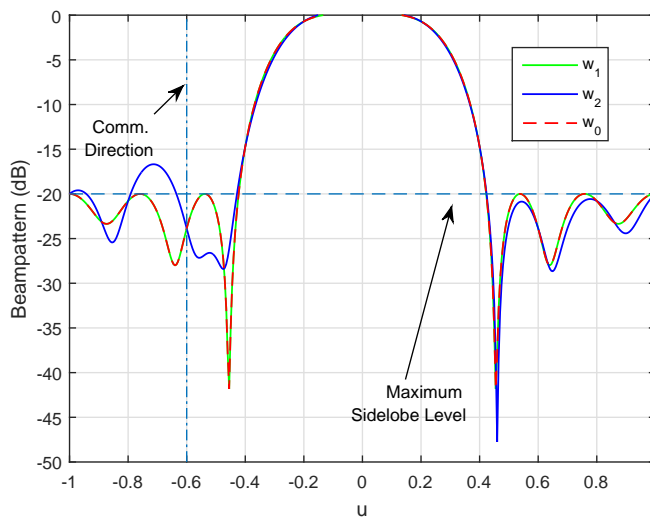
Figure 8.28: Set of beamformers, $\mathbf{w}_0$, $\mathbf{w}_1$ and $\mathbf{w}_2$, used to embed a BPSK constellation, $\phi_1 = 0$ and $\phi_2 = \pi$, using the signalling strategy of [4].

optimization problem of (8.43), where $G_0 = \mathbf{w}_0^H \mathbf{s}(u_c)$, $\phi_1 = 0$ and $\phi_2 = \pi$. We can note from Fig. 8.28 that beamformer $\mathbf{w}_1$ led to the same beampattern as $\mathbf{w}_0$ as expected, because the phase difference between them both is zero. On the other hand, beamformer $\mathbf{w}_2$, led to a similar, but not exactly the same beampattern as $\mathbf{w}_0$. In Fig. 8.29 the phase difference towards u_c of the beamformer pairs $(\mathbf{w}_1,\mathbf{w}_0)$ and $(\mathbf{w}_2,\mathbf{w}_0)$ is depicted in polar coordinates. We can see that the BPSK constellation is met sharply.

Note that the method of [4] does not explicitly states the formulation of maximum allowable sidelobe level, therefore, not necessarily, the beamformers will cope with this operational restriction, as can be seen in Fig. 8.28.

In this BPSK case, given that bit "0" is transmitted, the ratio $y_1[i] =$
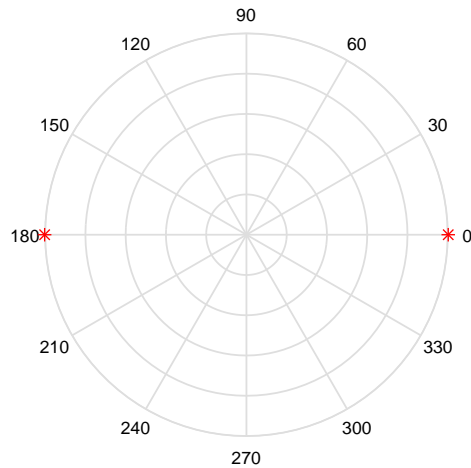
Figure 8.29: Phase difference towards u_c of the beamformer pairs $(\mathbf{w}_1,\mathbf{w}_0)$ and $(\mathbf{w}_2,\mathbf{w}_0)$.

$r_1[i]/r_0[i]$ is

$$y_1[i] \quad = \quad \frac{\sqrt{E_r}e^{j\psi}\mathbf{w}_1^H\mathbf{s}(u_c)}{\sqrt{E_r}e^{j\psi}\mathbf{w}_0^H\mathbf{s}(u_c)} + n_{b_0}, \tag{8.50}$$

$$y_1[i] \quad = \quad 1 + n_{b_0}, \tag{8.51}$$

where n_{b_0} is **non-Gaussian noise**. Given that bit "1" is transmitted the ratio $y_1[i] = r_1[i]/r_0[i]$ is

$$y_1[i] \quad = \quad \frac{\sqrt{E_r}e^{j\psi}\mathbf{w}_2^H\mathbf{s}(u_c)}{\sqrt{E_r}e^{j\psi}\mathbf{w}_0^H\mathbf{s}(u_c)} + n_{b_1}, \tag{8.52}$$

$$y_1[i] \quad = \quad -1 + n_{b_1}, \tag{8.53}$$

where n_{b_1} is **non-Gaussian noise**. Calling $z_1[i] = \Re\{y_1[i]\}$, the authors decide for bit "0" if $z_1[i] > 0$ and decide for bit "1" if $z_1[i] \leq 0$. Fig. 8.23 shows the simulated BER for the described non-coherent BPSK system, where the SNR in dB is defined as

$$\mathrm{SNR} = 10\log_{10}\left[\frac{E_r\left(|\mathbf{w}_0^H\mathbf{s}(u)|^2 + |\mathbf{w}_1^H\mathbf{s}(u)|^2 + |\mathbf{w}_2^H\mathbf{s}(u)|^2\right)}{3\sigma_n^2}\right]. \tag{8.54}$$

Comments on the Security against Interception of the Common Reference Method

Fig. 8.31 shows the phase difference of the beamformer pairs $(\mathbf{w}_1,\mathbf{w}_0)$ and $(\mathbf{w}_2,\mathbf{w}_0)$ in the u-space. We can note from Fig. 8.31 that the most expressive
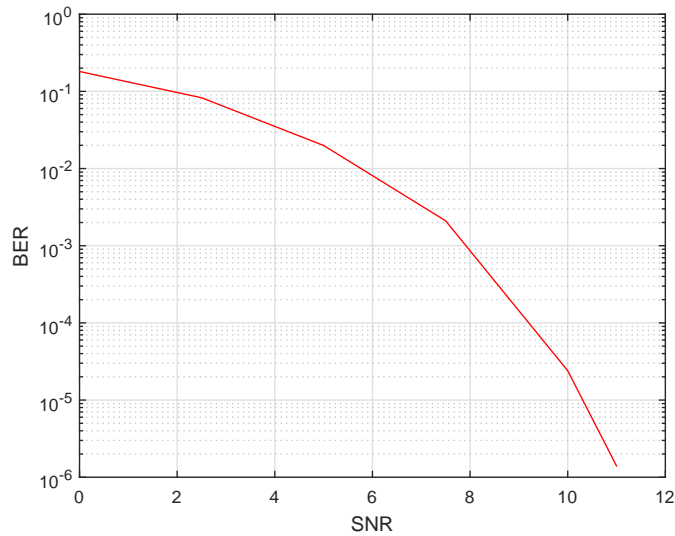
Figure 8.30: Bit error probability for the non-coherent BPSK vs. SNR (dB) using the common reference method.

phase changes happen only around the communication direction.

In Fig. 8.32 it is depicted the angular BER for a BPSK modulation embedded towards a communication receiver located at $u_c = -0.6$ using the method of [4]. The beamformers are the same as depicted in Fig. 8.31. In Fig. 8.32, we simulated the transmission of 10^6 symbols for each angle and guaranteed that at each angle the SNR was of 10 dB.

From Figs. 8.31 and 8.32 we can note that a highly secure communication system can be achieved using this method, differently than the rotational-invariance method of [3].
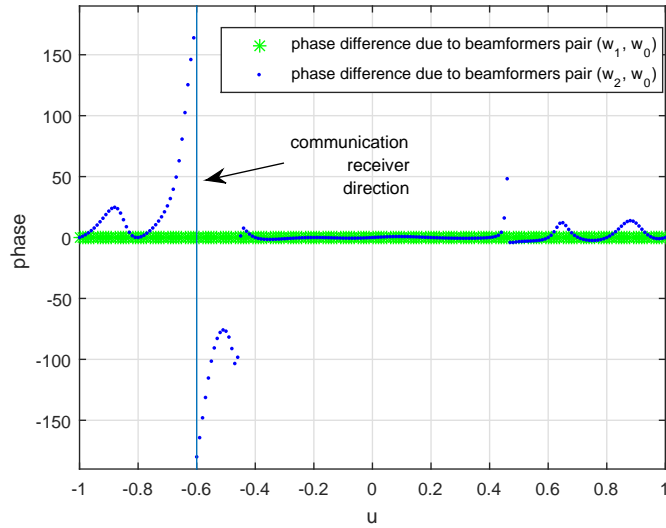
Figure 8.31: Phase difference of the beamformer pairs $(\mathbf{w}_1, \mathbf{w}_0)$ and $(\mathbf{w}_2, \mathbf{w}_0)$ in the u-space.
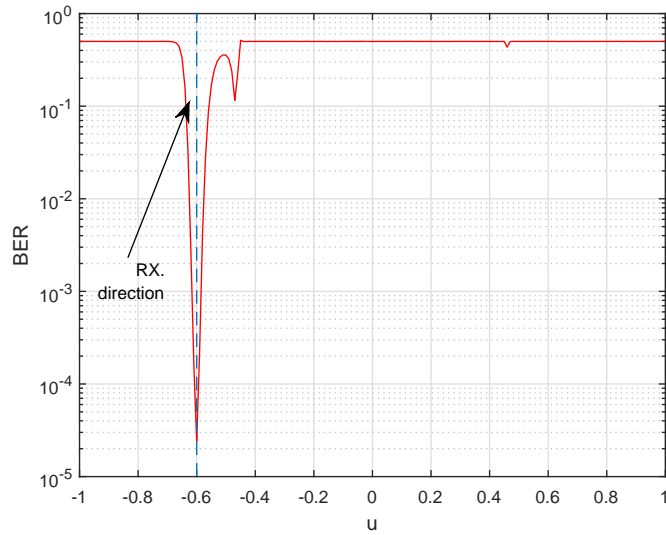
Figure 8.32: BER in the u-space for the described BPSK system using the beamformer pairs $(\mathbf{w}_1, \mathbf{w}_0)$ and $(\mathbf{w}_2, \mathbf{w}_0)$.

9
Proposed Radar-Embedded Sidelobe Modulation

In this chapter, we present our proposed methods for embedding sidelobe modulation to the radar transmit beampattern. In the former chapter we have called the reader's attention to the difficulty of having enough flexibility to pursue the communication receiver movement in a real-time application. We have also alerted about the need of secure communications and introduced the concept of robustness within this context. In Section 9.1 we deepen the discussion about robustness to emphasize the need of methods that deal with this issue. In this chapter, we focus on two, not yet explored, aspects of the dual-function radar-communications: **robustness** and **real-time tracking ability**.

In this thesis, we propose radar-embedded robust sidelobe modulation methods for dual-function radar-communication systems. One of our proposed techniques is based on quadratic and linear constrained optimization design, which has globally optimal closed-form solution. This proposed method generates transmit beampatterns that satisfactorily match a given transmit profile (with high fidelity adjustment at the mainlobe), where each beampattern embeds a different symbol towards the communication receiver direction and sustains it over a small angular region. This sustaining ability makes the proposed method robust against small errors over the expected position of the communication receiver. This characteristic provides more flexibility to the system and allows real-time processing to cope more easily with moving communication platforms, since operational BERs are achieved in a small region, rather than in a single point in the u-space. Part of this study resulted in the paper [7].

In this thesis, we also propose an iterative version of this proposed method. We apply the constrained gradient descent method for solving the constrained optimization problem iteratively. This new approach converges to the optimal solution. The recursive formula is very interesting within the DFRC context, because it it possible to come up with a stop criteria that are directly related to the radar operation, rather than minimization of the squared error. We derive simple equations for updating the beampatterns for following a moving communication receiver platform for both the closed form

and the iterative version of this proposed method.

We also propose an alternative method for radar-embedded robust sidelobe modulation for a dual-function radar-communication system. We derive this alternative method by modifying the robust optimization problem, in order to handle differently the mainlobe adjustment requirement. The proposed formulation is based on eigenvector, point and first derivative constraints. Though this solution is different, our alternative proposed method is also able to generate transmit beampatterns that match satisfactorily a given transmit profile (with high fidelity adjustment at the mainlobe), where each beampattern embeds a different symbol towards the communication receiver direction and sustains it over a small angular region. We derive its closed form solution and we simplify it through mathematical manipulation and eigenspectrum analysis. We also derive simple equations for updating the beampatterns for following a moving communication receiver platform. These procedures make the proposed alternative solution also very interesting and suitable for real-time processing. Part of this study resulted in the paper [8].

All proposed methods are applicable to both sidelobe amplitude and phase modulation. Referring to phase modulation, we propose a new non-coherent signalling strategy within the DFRC context. We also derive the bit error rate expression for the proposed phase modulation signalling strategy when two arbitrary symbols are transmitted. To the best of our knowledge, this expression is not found in the literature, but it is necessary for computing the angular BER figures, therefore, we derive it here.

In Chapter 10 we present some computer simulations and comparisons of the methods. In Section 10.8 we discuss the effects of sidelobe modulation in clutter mitigation techniques and in Section 10.9 we report some conclusions.

9.1 Considerations About Robustness

In this section, we will make some comments about the robustness of the methods seen so far. As mentioned before, the secure behavior of the radar-embedded communication system based on sidelobe modulation is intrinsic to its formulation. The preassignment of the receiver direction provides operational BER only towards this direction (except for the phase modulation using phase rotational invariance method), but this inherent advantage may become a major disadvantage if the real receiver position doesn't match exactly the preassigned one.

At this point, we use the one-round trip range equation to relate deterministically the received power at the communication receiver to the transmitted power in terms of a variety of system design parameters. After

that, we consider the random behavior inherent in communication signals.

First, assume an isotropic radiating element transmitting a waveform of power P_t Watts into a lossless medium. Thus, the power density at a range R, $S(R)$, is the transmitted power P_t divided by the surface area of a sphere of radius R,

$$S(R) = \frac{P_t}{4\pi R^2} \ \ \mathrm{W/m^2}. \tag{9.1}$$

But in practice, real radars use antenna arrays to focus the outgoing energy, thus the power density incident upon a communication receiver located towards u at range R from the radar, $S(R,u)$, is given by

$$S(R,u) = \frac{G_t|\bar{B}(u)|^2 P_t}{4\pi R^2} \ \ \mathrm{W/m^2}, \tag{9.2}$$

where G_t is the transmitting array gain, which is the ratio between the maximum power density to the isotropic density, and $\bar{B}(u)$ is the normalized beampattern. The quantity $G_t\bar{B}(u)$ defines the array gain towards u, $G(u)$, which is the ratio between the power density towards u to the isotropic density.

If the effective aperture size of the communication receiver antenna is A_e m^2, the total power collected by the receiving antenna, located towards u at range R from the transmitter, $P_r(R,u)$, will be

$$P_r(R,u) = \frac{A_e G_t|\bar{B}(u)|^2 P_t}{4\pi R^2} \ \ \mathrm{W}, \tag{9.3}$$

but the effective aperture of the receiver antenna is related to its gain, G_r, and operating wavelength, λ, according to

$$A_e = \frac{\lambda^2 G_r}{4\pi}, \tag{9.4}$$

thus, substituting (9.4) into (9.3) we have

$$P_r(R,u) = \frac{G_r G_t|\bar{B}(u)|^2 \lambda^2 P_t}{(4\pi)^2 R^2} \ \ \mathrm{W}. \tag{9.5}$$

We assume that the communication receiver antenna's direction of maximum gain is aligned with the radar, therefore, G_r, is the ratio between the maximum power density of the receiver antenna's radiation pattern to the isotropic density.

Various additional loss and gain factors are customarily added to (9.5) to account for a variety of additional considerations. For example, losses incurred in various components such as the duplexers, power dividers, waveguide and radome (a protective covering over the antenna), and the propagation effects not found in free space propagation can be lumped into a system loss factor, L_s, that reduces the received power. Considering the system loss factor, L_s, (9.5) becomes

$$P_r(R, u) = \frac{G_r G_t |\bar{B}(u)|^2 \lambda^2 P_t}{(4\pi)^2 R^2 L_s} \quad \text{W.} \tag{9.6}$$

The SNR at the input of the communication receiver at range R from the transmitter is given by dividing (9.6) by the receiver's noise power, kT_0BF,

$$\text{SNR} = \frac{P_r(R, u)}{kT_0BF}, \tag{9.7}$$

where $k = 1.38 \times 10^{-23}$ J/K is the Boltzmann's constant, $T_0 = 290$ K is the standard noise temperature, F is the receiver noise figure and B is the communication receiver's input bandwidth in Hz, which is assumed to be matched to the particular radar waveform bandwidth that is being transmitted. Multiplying and dividing (9.7) by the pulse duration, τ, we have the SNR written in function of the ratio of the signal and noise energy,

$$\text{SNR} = \frac{P_r(R, u)\tau}{kT_0FB\tau} = \frac{E_r(R, u)}{kT_0F(B\tau)}, \tag{9.8}$$

where $E_r(R, u)$ is the energy collected by the receiver's antenna located at range R and direction u relative to the radar. The minimum value for the product $B\tau$, in order to avoid intersymbol interference is one. A typical value of $B\tau$ for a pulse with roll-off is of 1.4.

But as we are considering a communication context, the SNR is then the ratio between the expected value of the energy relative to all the K symbols being transmitted and the receiver noise power kT_0BF,

$$\text{SNR} = \frac{\text{E}\left[E_r(R, u)\right]}{kT_0F(B\tau)}. \tag{9.9}$$

Considering that all communication symbols are equally likely of being transmitted the SNR at the communication receiver is thus given by

$$\text{SNR} = \frac{G_r G_t P_t \tau \lambda^2}{K kT_0 B\tau F (4\pi)^2 R^2 L_s} \sum_{k=1}^{K} |\bar{B}_k(u)|^2, \tag{9.10}$$

where $\bar{B}_k(u)$ is the normalized beamppattern towards u.

Let's define $R_{\max}$ as the maximum range at which the communication receiver can achieve its minimum operational SNR, $\text{SNR}_{\min}$. Any R greater than $R_{\max}$ leads to a lower SNR than $\text{SNR}_{\min}$, which in its turn makes communication impractical. From (9.10) we can find the maximum range, $R_{\max}$, at which the radar can communicate with the communication receiver as a function of the $\text{SNR}_{\min}$,

$$R_{\max} = \sqrt{\frac{G_r G_t P_t \tau \lambda^2}{K kT_0 B\tau F (4\pi)^2 \text{SNR}_{\min} L_s} \sum_{k=1}^{K} |\bar{B}_k(u)|^2}. \tag{9.11}$$
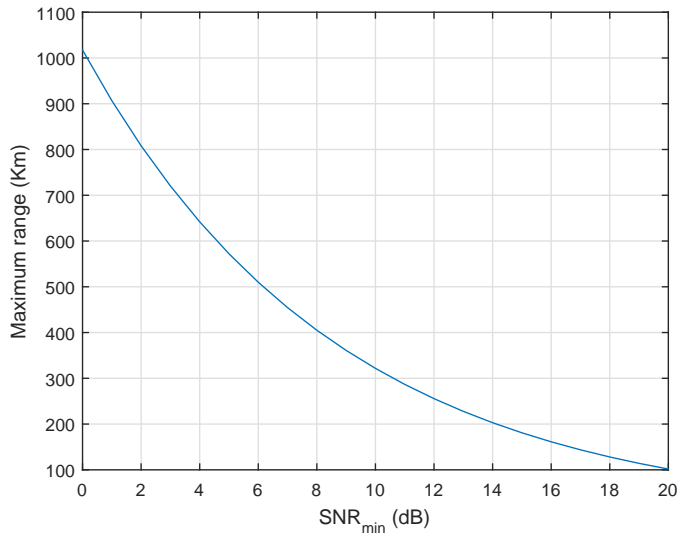
Figure 9.1: Maximum range as a function of SNR_{min} for the first example.

Let's use equation (9.11) for a simple, yet representative example. Consider a radar with transmission power of $P_t = 80$ W, transmit gain of $G_t = 20$ dB, waveform with a 2 MHz bandwidth and central frequency of $f = 9.375$ GHz. We choose the BASK SLL modulation of [3] that uses the two beampatterns depicted in Fig. 8.7 for embedding the binary constellation $\mathcal{C} = \{\sqrt{10^{-20/10}}, \sqrt{10^{-40/10}}\}$, where $\sqrt{10^{-20/10}}$ is associated to bit "1" and $\sqrt{10^{-40/10}}$ corresponds to bit "0" towards $u_c = -0.6$. The communication receiver has a noise figure of $F = 5$ dB, antenna gain of $G_r = 10$ dB and the systems losses are $L_s = 5$ dB. Fig. 9.1 shows the maximum range as a function of SNR_{min} at the input of the communication receiver.

According to Fig. 8.11 a SNR of 15 dB is operational for this signaling strategy as it leads to a BER of 3.17×10^{-7}. For this example the maximum range at which the radar can communicate with the communication receiver for a SNR at the input of the communication receiver of 15 dB is of 180 Km.

Now let's assume that the communication receiver is in a corvette moving further from the radar mainbeam with a cruising speed of 17 knots or equivalently 8.75 m/s in a direction tangential to the circumference of radius 180 Km centered at the radar as depicted in Fig. 9.2. In 10 minutes the relative angle between the radar and the communication receiver would have increased of $\Delta u = -0.025$. Checking the angular BER in Fig. 8.12 we can see that the BER would go from 3.17×10^{-7} to 1.1×10^{-3} in only 10 minutes. In 22 minutes $\Delta u = -0.05$ ($\Delta\theta = 3.67^o$) and the BER goes to 0.27. This BER dynamic is illustrated in a zoom of Fig. 8.12, Fig. 9.3.

Now let's see another example, this time the BPSK embedded phase modulation using the signalling and convex optimization method of [4]. In the
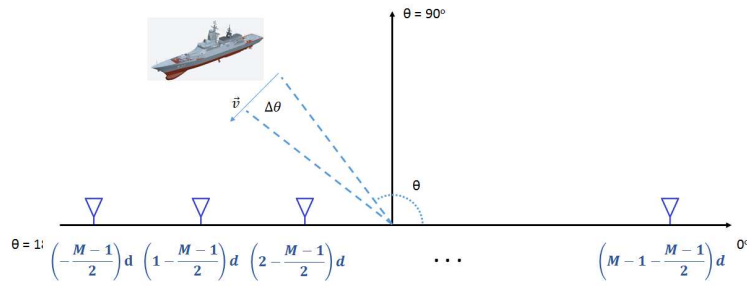
Figure 9.2: Moving communication receiver.
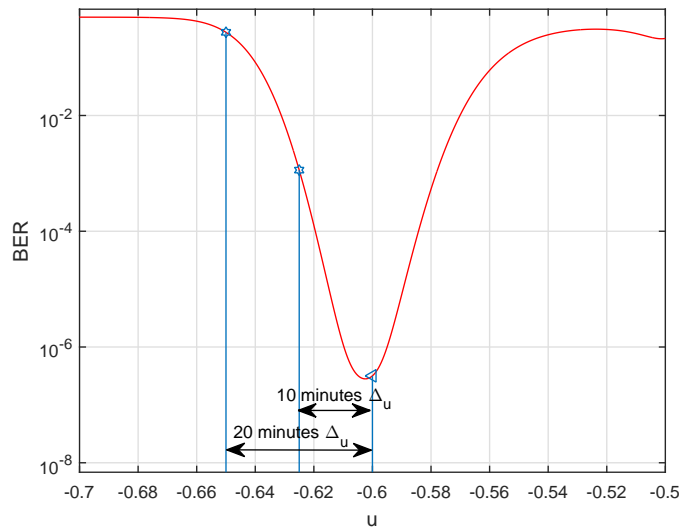
Figure 9.3: Zoom of BASK angular BER showing the BER degradation according to communication receiver motion for the first example for a SNR of 15 dB.

following simulation we used the beampatterns as in Fig. 8.28 that embed towards $u_c = -0.6$ the phase constellation $\phi_1 = 0$ which corresponds to bit "0" and $\phi_2 = \pi$ which corresponds to bit "1". The angular BER is depicted in Fig. 8.32. This signalling method uses two different arrays to simultaneously transmit two waveforms, so we will assume that each array has a transmit power P_t of $80/2 = 40$ W. We consider $G_t = 20$ dB, the waveforms have a 2 MHz bandwidth and central frequency of $f = 9.375$ GHz. The communication receiver has a noise figure of $F = 5$ dB, antenna gain of $G_r = 10$ dB and the systems losses is $L_s = 5$ dB. Fig. 9.4 shows the maximum range as a function of $\text{SNR}_{\min}$ at the input of the communication receiver.

According to Fig. 8.23 a SNR of 10 dB is operational for this signalling strategy as it leads to a BER of 2.25×10^{-5}. For this example the maximum range at which the radar can communicate with the communication receiver for a SNR at the input of the communication receiver of 10 dB is of 205 Km.

We will use the same receiver movement information as in the first
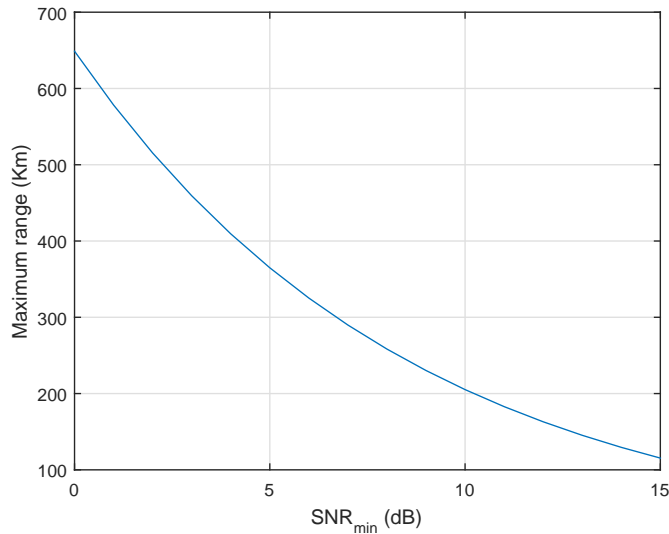
Figure 9.4: Maximum range as a function of $\mathrm{SNR}_{\mathrm{min}}$ for the second example.

example. After 12 minutes the relative angle between the radar and the communication receiver would have increased of $\Delta u = -0.025$. Checking the angular BER in Fig. 8.32 we can see that the BER would go from 2.25×10^{-5} to 0.009 in only 12 minutes. In 25 minutes $\Delta u = -0.05$ and the BER goes to 0.3341. This BER dynamic is illustrated in a zoom of Fig. 8.32, Fig. 9.5.

The relative movement assumed within this robustness analysis is just a simple and particular example. We assumed a fixed landbased radar and a ship movement, which is considerable slower than a flying target for example. Depending on the scenario, the time for the platform of the communication receiver to course this relative angular displacement may be considerably smaller.

These examples illustrate our idea of the necessity of robust and flexible methods for embedding SLL modulation to dual-function radar-communications platforms. We won't even consider here the case of a rotating radar. A rotating radar of 10 rpm would go from $u_c = $ -0.6 to -0.65 in mili-seconds! But we won't address this problem here.

9.2 Proposed Robust Real-Time Radar-Embedded Sidelobe Modulation - Method 1

In this section, we detail our first proposed robust radar-embedded sidelobe modulation method. We propose a new formulation of the sidelobe modulation problem for ULAs, which allows a simple, robust and closed form solution. The closed form solution can be achieved iteratively, which is developed in Subsection 9.2.2. We also derive simple update equations for pursuing a moving communication receiver for the proposed method 1 in its
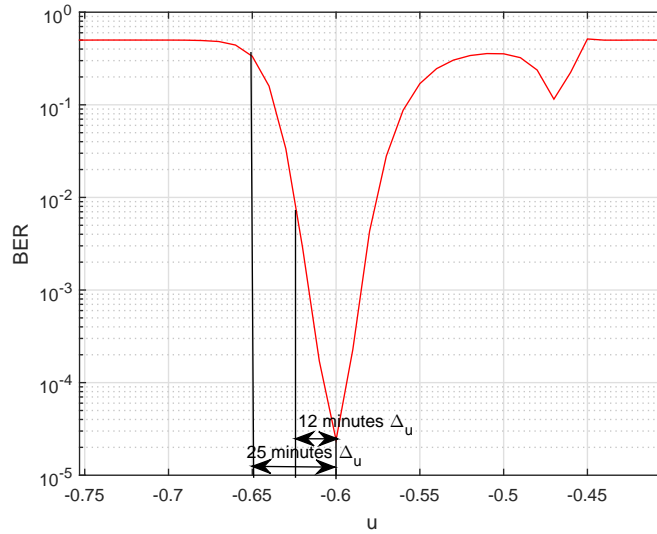
Figure 9.5: Zoom of non-coherent BPSK angular BER showing the BER degradation according to communication receiver motion for the second example for a SNR of 10 dB.

closed form and recursive version.

First, let us state our assumptions:

– The radar designers have already developed a transmit beampattern profile which meets the operational radar needs. The original transmit beampattern, $B_o(u)$, is described by the beamformer, $\mathbf{w}_o$, producing the beampattern $B_o(u) = \mathbf{w}_o^H \mathbf{s}(u)$, $u \in [-1, 1]$;

– The radar primary function takes place at the mainlobe of the transmit beampattern, $u \in U$, $U = [-u_d, u_d]$. In order to prevent performance degradation of the primary radar task, while embedding sidelobe modulation, we have to assure that the mainbeam of all beampatterns under design will be in good agreement with the original beampattern, $B_o(u)$.

– The receiver communication direction, u_c, is known *a priori*.

Now, let us define the difference beamforming vector $\mathbf{w}$, as

$$\mathbf{w} = \mathbf{w}_o - \mathbf{w}_k, \tag{9.12}$$

where $\mathbf{w}_o$ is the given beamforming vector that produces the specific radar transmit output power profile and $\mathbf{w}_k$ is the beamforming weighting vector under design, which will embed the k-th communication symbol towards u_c. Clearly, $\mathbf{w}$ depends on k. But this dependence will not be explicit in the notation for simplicity. We will limit the optimization formulation to finding the optimal $\mathbf{w}$, named $\mathbf{w}^{op}$, then $\mathbf{w}_k^{op}$ is obtained by

$$\mathbf{w}_k^{op} = \mathbf{w}_o - \mathbf{w}^{op}. \tag{9.13}$$

The original beampattern, $B_o(u)$, at the mainlobe spatial sector, $U = [-u_d, u_d]$, is given by

$$B_o(u) = \mathbf{w}_o^H \mathbf{s}(u), \quad u \in U. \tag{9.14}$$

One main design requirement of our beamforming vector, $\mathbf{w}_k$, is that in the mainlobe area, $u \in U$, the total mean squared error, e, should be held under a certain baseline, δ,

$$
\begin{aligned}
e &= \int_{u \in U} |\mathbf{w}_o^H \mathbf{s}(u) - \mathbf{w}_k^H \mathbf{s}(u)|^2 \mathrm{d}u \\
&= \int_{u \in U} |\mathbf{w}^H \mathbf{s}(u)|^2 \mathrm{d}u \leq \delta.
\end{aligned}
\tag{9.15}
$$

We can rewrite (9.15) as [10]

$$e = \mathbf{w}^H \mathbf{Q} \mathbf{w}, \tag{9.16}$$

where $\mathbf{Q} \in \mathbb{C}^{M \times M}$ is the hermitian symmetric positive semi-definite matrix, given by

$$\mathbf{Q} \triangleq \int_{u \in U} \mathbf{s}(u) \mathbf{s}^H(u) \mathrm{d}u. \tag{9.17}$$

We can note that $\mathbf{Q}$ in (9.17) does not depend on the beampattern shape, but only on the constraint region and the steering vector, $\mathbf{s}(u)$. The mn-th element of $\mathbf{Q}$, using $d = \lambda_c/2$, is given by [10]

$$[\mathbf{Q}]_{mn} = \int_{-u_d}^{u_d} e^{j\pi u(m-n)} \mathrm{d}u, \tag{9.18}$$

$$[\mathbf{Q}]_{mn} = \frac{2 \sin[\pi u_d(m-n)]}{(m-n)}. \tag{9.19}$$

According to (9.19), if we consider the squared error of the entire visible region, then $u_d = 1$ and $\mathbf{Q} = 2\pi \mathbf{I}_M$, thus, minimizing $||\mathbf{w}||^2$ is equivalent to minimizing the total squared error. Now we can formulate the optimization problem on $\mathbf{w}$ by stating that, $\mathbf{w}^{op}$ is the difference beamforming vector that satisfies the following

$$
\mathbf{w}^{op} = \min_{\mathbf{w}} ||\mathbf{w}||^2, \tag{9.20}
$$

$$
\text{s.t.} \quad
\begin{cases}
\mathbf{w}^H \mathbf{Q} \mathbf{w} \leq \delta \\
\mathbf{w}^H \mathbf{s}(u_c) = d_k
\end{cases},
$$

where $d_k = \mathbf{w}_o^H \mathbf{s}(u_c) - C_k$ and C_k is the k-th symbol of the constelation $\mathcal{C}$.

In order to be more robust against small deviations in u_c, we impose the

first derivative null constraint writing the optimization problem in (9.20) as

$$\mathbf{w}^{op} \quad = \quad \min_{\mathbf{w}} ||\mathbf{w}||^2, \tag{9.21}$$

$$\text{s.t.} \quad \begin{cases} \mathbf{w}^H \mathbf{Q} \mathbf{w} \leq \delta \\ \mathbf{w}^H \mathbf{s}(u_c) = d_k \\ \mathbf{w}^H \mathbf{s}'(u_c) = b \end{cases},$$

where $\mathbf{s}'(u_c)$ is the derivative of $\mathbf{s}(u)$ with respect to u evaluated in u_c and $b = \mathbf{w}_o^H \mathbf{s}'(u_c)$.

By changing the ellipsoid constraint inequality into an equality, as $\mathbf{w}^H \mathbf{Q} \mathbf{w} = \delta$, we can solve problem (9.21) by using the Lagrange multipliers methodology based on the real valued function

$$\begin{aligned} \mathcal{L} \quad &= \quad \mathbf{w}^H \mathbf{w} + \lambda_1 (\mathbf{w}^H \mathbf{Q} \mathbf{w} - \delta) \\ &+ \quad 2\Re\{\lambda_2 \mathbf{w}^H \mathbf{s}(u_c) - d_k\} + 2\Re\{\lambda_3 \mathbf{w}^H \mathbf{s}'(u_c) - b\}, \end{aligned} \tag{9.22}$$

where λ_1, λ_2 and λ_3 are the Lagrange multipliers. Employing the complex gradient approach of [76] we have that the gradient of (9.22) with respect to the conjugate of $\mathbf{w}$, $\mathbf{w}^*$, is

$$\frac{1}{2}\nabla_{\mathbf{w}^*}\mathcal{L} = \mathbf{w} + \lambda_1 \mathbf{Q}\mathbf{w} + \lambda_2 \mathbf{s}(u_c) + \lambda_3 \mathbf{s}'(u_c), \tag{9.23}$$

or equivalently,
$$\frac{1}{2}\nabla_{\mathbf{w}^*}\mathcal{L} = \mathbf{w} + \lambda_1 \mathbf{Q}\mathbf{w} + \mathbf{S}\boldsymbol{\lambda}, \tag{9.24}$$

where

$$\mathbf{S} \quad = \quad [\mathbf{s}(u_c), \mathbf{s}'(u_c)] \quad \in \mathbb{C}^{M \times 2}, \tag{9.25}$$

$$\boldsymbol{\lambda} \quad = \quad [\lambda_2, \lambda_3]^T \quad \in \mathbb{C}^{2 \times 1}. \tag{9.26}$$

The stationary point is given by nulling (9.24), thus

$$\mathbf{w} = -(\mathbf{I}_M + \lambda_1 \mathbf{Q})^{-1} \mathbf{S}\boldsymbol{\lambda}. \tag{9.27}$$

Employing the equality constraints in (9.21) it can be shown that

$$\boldsymbol{\lambda} = -[\mathbf{S}^H(\mathbf{I}_M + \lambda_1 \mathbf{Q})^{-1}\mathbf{S}]^{-1}\mathbf{f}_k, \tag{9.28}$$

where $\mathbf{f}_k$ is given by

$$\mathbf{f}_k = \begin{bmatrix} d_k^* \\ b^* \end{bmatrix} \quad \in \mathbb{C}^{2 \times 1}. \tag{9.29}$$

Substituting (9.28) into (9.27) we have that

$$\mathbf{w}^{op} = (\mathbf{I}_M + \lambda_1 \mathbf{Q})^{-1}\mathbf{S}[\mathbf{S}^H(\mathbf{I}_M + \lambda_1 \mathbf{Q})^{-1}\mathbf{S}]^{-1}\mathbf{f}_k. \tag{9.30}$$

The value of λ_1 is set so as to comply with the constraint $\mathbf{w}^H\mathbf{Q}\mathbf{w} \leq \delta$. In order to keep the consistency constraint of the optimization problem, we must have $\lambda_1 \in [0, +\infty)$ according to the Karush-Kuhn-Tucker condition [74]. Furthermore, since $\mathbf{Q}$ is positive semi-definite, its eigenvalues are all non negative, and thus, the eigenvalues of $(\mathbf{I}_M + \lambda_1\mathbf{Q})$ are all positive (in fact, they are not less than one). This guarantees that matrix $\mathbf{I}_M + \lambda_1\mathbf{Q}$ in (9.30) has an inverse for all $\lambda_1 \geq 0$. Let λ_1 be given by

$$\lambda_1 = \frac{\alpha}{1 - \alpha}, \quad \alpha \in [0, 1), \tag{9.31}$$

where α is the adjustment parameter. Its physical interpretation will be developed in the next subsection. Substituting (9.31) into (9.30), after some manipulation we have that, for a given α, the optimal solution is given by

$$\mathbf{w}^{op} = \hat{\mathbf{Q}}^{-1}(\alpha)\mathbf{S}(\mathbf{S}^H\hat{\mathbf{Q}}^{-1}(\alpha)\mathbf{S})^{-1}\mathbf{f}_k, \tag{9.32}$$

where

$$\hat{\mathbf{Q}}(\alpha) = (1 - \alpha)\mathbf{I}_M + \alpha\mathbf{Q}, \quad \alpha \in [0, 1]. \tag{9.33}$$

(a) Another Interpretation of the Proposed Technique

The optimal solution given in (9.32) can be found also by minimizing the intuitive convex combination of two functions

$$\mathbf{w}^{op} = \min_{\mathbf{w}} (1 - \alpha)||\mathbf{w}||^2 + \alpha\mathbf{w}\mathbf{Q}\mathbf{w}, \tag{9.34}$$

$$\text{s.t.} \quad \begin{cases} \mathbf{w}^H\mathbf{s}(u_c) = d_k \\ \mathbf{w}^H\mathbf{s}'(u_c) = b \end{cases},$$

where $\alpha \in [0, 1)$, $||\mathbf{w}||^2$ is the total squared difference between the beampattern under design and the original one and $\mathbf{w}\mathbf{Q}\mathbf{w}$ is the squared difference between the beampattern under design and the original one within the mainbeam sector. Employing the Lagrange multipliers methodology we have

$$\begin{aligned} \mathcal{L} &= (1 - \alpha)\mathbf{w}^H\mathbf{w} + \alpha\mathbf{w}^H\mathbf{Q}\mathbf{w} \\ &+ 2\Re\{\lambda_2\mathbf{w}^H\mathbf{s}(u_c) - d_k\} + 2\Re\{\lambda_3\mathbf{w}^H\mathbf{s}'(u_c) - b\}, \end{aligned} \tag{9.35}$$

differentiating (9.35) with respect to the conjugate of $\mathbf{w}$, $\mathbf{w}^*$, we have

$$\frac{1}{2}\nabla_{\mathbf{w}^*}\mathcal{L} = (1 - \alpha)\mathbf{w} + \alpha\mathbf{Q}\mathbf{w} + \mathbf{S}\boldsymbol{\lambda}, \tag{9.36}$$

where $\mathbf{S}$ is defined in (9.25) and $\boldsymbol{\lambda}$ is defined in (9.26). Nulling (9.36) to find the stationary point we achieve

$$\mathbf{w}^{op} = -[(1 - \alpha)\mathbf{I}_M + \alpha\mathbf{Q}]^{-1}\mathbf{S}\boldsymbol{\lambda}. \tag{9.37}$$

	Number of complex products	Number of complex additions
$\underbrace{(1-\alpha)\mathbf{I}_M + \alpha\mathbf{Q}}_{\hat{\mathbf{Q}}}$	M^2	$M+1$
$\underbrace{\hat{\mathbf{Q}}^{-1}}_{\mathbf{Q}_{in}}$	$O(M^3)$	$O(M^3)$
$\underbrace{\mathbf{S}^H\mathbf{Q}_{in}\mathbf{S}}_{\mathbf{A}}$	$2M^2 + 4M$	$2M^2 + 2M - 4$
$\underbrace{(\mathbf{A})^{-1}\mathbf{f}_k}_{-\boldsymbol{\lambda}}$	10	3
$-\mathbf{Q}_{in}\mathbf{S}\boldsymbol{\lambda}$	$M^2 + 2M$	M^2
Total	$O(M^3) + 4M^2 + 6M + 10$	$O(M^3) + 3M^2 + 3M$

Table 9.1: Complex operations of the proposed method 1 with the derivative null constraint.

Applying the constraints to (9.37) we derive that

$$\boldsymbol{\lambda} = -\{\mathbf{S}^H[(1-\alpha)\mathbf{I}_M + \alpha\mathbf{Q}]\mathbf{S}\}^{-1}\mathbf{f}_k, \qquad (9.38)$$

which leads, for a given α, to the same optimal solution (9.32).

This interpretation is interesting to clarify the physical aspect of parameter α. We can see α as an adjustment factor that composes the final minimization solution. As we increase α, we give emphasis on the constraint that controls the error at the mainbeam, as we decrease α, we relax the mainbeam fit constraint and emphasize the total error minimization. Sometimes, if we are too strict in the mainbeam fit, we can have the undesirable effect of high sidelobes, but, by understanding the role of α we can adjust it to have the best tradeoff between the mainbeam fit and sidelobe behavior. From the derivation above, for a given threshold, δ, or equivalently, for a given α, the solution to (9.32) is unique and optimal, implying that the solution to (9.32) achieves the desired mainbeam fit with minimum total squared error.

The number of complex multiplications and additions necessary to compute $\mathbf{w}^{op}$ given α is detailed in Table 9.1.

If the communication receiver is moving in the u-space and we have its displacement information, Δu, we can compute the new beamforming weighting vector $\mathbf{w}_k^{op}(u+\Delta u)$. Let's call $\mathbf{w}^{op}$ by $\mathbf{w}^{op}(u)$, $\mathbf{S}$ by $\mathbf{S}_u$ and $\mathbf{f}_k$ by $\mathbf{f}_{k,u}$ in (9.32). Thus we can compute $\mathbf{w}^{op}(u+\Delta u)$ by updating $\mathbf{S}_u$ and $\mathbf{f}_{k,u}$ as

$$\mathbf{S}_{u+\Delta u} = \mathbf{S}_u \odot \mathbf{S}_{\Delta u}, \qquad (9.39)$$

$$\mathbf{f}_{k,u+\Delta u} = \begin{pmatrix} \mathbf{w}_o^H[\mathbf{s}(u) \odot \mathbf{s}(\Delta u)] - d_k \\ \mathbf{w}_o^H[\mathbf{s}'(u) \odot \mathbf{s}(\Delta u)] \end{pmatrix}, \qquad (9.40)$$

and substituting them into equation (9.32). Symbol $\odot$ stands for the Hadamard

element-wise product. Therefore the updated $\mathbf{w}_k^{op}(u + \Delta u)$ is given by

$$\mathbf{w}_k^{op}(u + \Delta u) = \mathbf{w}_o - \hat{\mathbf{Q}}^{-1}(\alpha)\mathbf{S}_{u+\Delta u}(\mathbf{S}_{u+\Delta u}^H \hat{\mathbf{Q}}^{-1}(\alpha)\mathbf{S}_{u+\Delta u})^{-1}\mathbf{f}_{k,u+\Delta u}. \quad (9.41)$$

(b) Recursive Version of the Proposed Method 1

In this section, we propose a constrained gradient-descent technique for solving the robust radar embedded sidelobe modulation optimization problem (9.21). The proposed recursive method converges to the optimal solution. It is also very flexible in a sense that it is possible to add stop criteria that are related to radar metrics other than minimization of squared errors. This flexibility is very convenient in a DFRC context.

We will work with the simpler optimization formulation of (9.34), as it was shown in Section 9.2 that, for the same α, (9.34) and (9.21) lead to the same solution. The solution, $\mathbf{w}^{op}$ of (9.34), can be found iteratively through the update equation of the steepest descent methodology

$$\mathbf{w}(n + 1) = \mathbf{w}(n) - \mu\nabla_{\mathbf{w}^*}\mathcal{L}, \quad (9.42)$$

where

$$\frac{1}{2}\nabla_{\mathbf{w}^*}\mathcal{L} = (1 - \alpha)\mathbf{w} + \alpha\mathbf{Q}\mathbf{w} + \mathbf{S}\boldsymbol{\lambda}, \quad (9.43)$$

$\boldsymbol{\lambda} \in \mathbb{C}^{2\times 1}$ is the vector $\boldsymbol{\lambda} = [\lambda_2, \lambda_3]^T$ composed of the Lagrange multipliers λ_2 and λ_3 explicit in equation (9.35).

Substituting (9.43) into (9.42) and incorporating the factor $1/2$ to the step, μ, we have that

$$\begin{aligned} \mathbf{w}(n + 1) &= \mathbf{w}(n) - \mu\left[(1 - \alpha)\mathbf{w}(n) + \alpha\mathbf{Q}\mathbf{w}(n) + \mathbf{S}\boldsymbol{\lambda}\right], \\ &= \mathbf{w}(n) - \mu\left(\hat{\mathbf{Q}}\mathbf{w}(n) + \mathbf{S}\boldsymbol{\lambda}\right), \end{aligned} \quad (9.44)$$

where $\hat{\mathbf{Q}} = (1 - \alpha)\mathbf{I}_M + \alpha\mathbf{Q}$. The Lagrange multipliers are chosen so that $\mathbf{w}(n + 1)$ satisfies the constraint $\mathbf{S}^H\mathbf{w} = \mathbf{f}_k$,

$$\mathbf{S}^H\mathbf{w}(n + 1) = \mathbf{S}^H\mathbf{w}(n) - \mu\left(\mathbf{S}^H\hat{\mathbf{Q}}\mathbf{w}(n) + \mathbf{S}^H\mathbf{S}\boldsymbol{\lambda}\right). \quad (9.45)$$

Inspired by [19], we won't consider $\mathbf{S}^H\mathbf{w}(n) = \mathbf{f}$ in (9.45) (as it would be if $\mathbf{w}(n)$ satisfied the constraint precisely), in order to correct any small errors due to arithmetic inaccuracy, preventing their accumulation [19]. Thus, from (9.45), $\boldsymbol{\lambda}$ is given by

$$\boldsymbol{\lambda} = -(\mathbf{S}^H\mathbf{S})^{-1}\mathbf{S}^H\hat{\mathbf{Q}}\mathbf{w}(n) + \frac{(\mathbf{S}^H\mathbf{S})^{-1}}{\mu}\left(\mathbf{S}^H\mathbf{w}(n) - \mathbf{f}_k\right). \quad (9.46)$$

Substituting (9.46) into (9.44) we have the recursive expression for $\mathbf{w}$,

$$
\begin{aligned}
\mathbf{w}(n+1) &= \mathbf{w}(n) - \mu \left(\mathbf{I} - \mathbf{S}(\mathbf{S}^H\mathbf{S})^{-1}\mathbf{S}^H \right) \hat{\mathbf{Q}}\mathbf{w}(n) \\
&+ \mathbf{S}(\mathbf{S}^H\mathbf{S})^{-1} \left(\mathbf{f}_k - \mathbf{S}^H\mathbf{w}(n) \right).
\end{aligned}
\tag{9.47}
$$

Again inspired by [19], defining

$$
\mathbf{v}_k \triangleq \mathbf{S}(\mathbf{S}^H\mathbf{S})^{-1}\mathbf{f}_k \quad \in \mathbb{C}^{M\times 1}, \tag{9.48}
$$

$$
\mathbf{P} \triangleq \mathbf{I} - \mathbf{S}(\mathbf{S}^H\mathbf{S})^{-1}\mathbf{S}^H \quad \in \mathbb{C}^{M\times M}, \tag{9.49}
$$

and substituting into (9.47), we have that

$$
\mathbf{w}(n+1) = \mathbf{P}\left(\mathbf{I} - \mu\hat{\mathbf{Q}} \right)\mathbf{w}(n) + \mathbf{v}_k, \tag{9.50}
$$

where $\mathbf{w}(0) \triangleq \mathbf{v}_k$ and $0 < \mu < \frac{2}{3\mathrm{tr}(\hat{\mathbf{Q}})}$ in order to assure convergence.

If the communication receiver is moving in the u-space and we have its displacement information, Δu, we can modify the update equation (9.50) in order to follow the communication receiver, $\mathbf{w}(n+1, u+\Delta u)$. Let's make explicit the dependence on u by adding a subindex u to the quantities that are dependent on the direction of the communication receiver, $\mathbf{S}_u$, $\mathbf{f}_{k,u}$, $\mathbf{v}_{k,u}$ and $\mathbf{P}_u$. According to the communication receiver displacement Δu, $\mathbf{S}_{u+\Delta u}$ and $\mathbf{f}_{k,u+\Delta}$ are updated as in (9.39) and (9.40) respectively. The quantities $\mathbf{v}_{k,u+\Delta u}$ and $\mathbf{P}_{u+\Delta u}$ are updated as

$$
\mathbf{v}_{k,u+\Delta u} = \mathbf{S}_{u+\Delta u}(\mathbf{S}^H_{u+\Delta u}\mathbf{S}_{u+\Delta u})^{-1}\mathbf{f}_{k,u+\Delta u}, \tag{9.51}
$$

$$
\mathbf{P}_{u+\Delta u} = \mathbf{I} - \mathbf{S}_{u+\Delta u}(\mathbf{S}^H_{u+\Delta u}\mathbf{S}_{u+\Delta u})^{-1}\mathbf{S}^H_{u+\Delta u}. \tag{9.52}
$$

Substituting (9.51) and (9.52) into (9.50) we have that $\mathbf{w}(n+1, u+\Delta u)$ is given by

$$
\mathbf{w}(n+1, u+\Delta u) = \mathbf{P}_{u+\Delta u}\left(\mathbf{I} - \mu\hat{\mathbf{Q}} \right)\mathbf{w}(n, u+\Delta u) + \mathbf{v}_{k,u+\Delta u}. \tag{9.53}
$$

The number of complex multiplications and additions necessary to compute $\mathbf{w}^{op}$ given α using the recursive version of method 1 is detailed in Table 9.2.

	Number of complex products	Number of complex additions
Initial procedures		
$\underbrace{(\mathbf{S}^H\mathbf{S})^{-1}}_{\hat{\mathbf{S}}}$	$4M+6$	$4M-3$
$\underbrace{\mathbf{S}\hat{\mathbf{S}}\mathbf{f}_k}_{\mathbf{v}_k}$	8	4
$\underbrace{\mathbf{I}_M - \mathbf{S}\hat{\mathbf{S}}\mathbf{S}^H}_{\mathbf{P}}$	$2M^2+4M$	M^2+3M
$\underbrace{(1-\alpha)\mathbf{I}_M + \alpha\mathbf{Q}}_{\hat{\mathbf{Q}}}$	M^2	$M+1$
Start of a N_{it} iterations loop		
$\underbrace{(\mathbf{I}_M - \mu\hat{\mathbf{Q}})\mathbf{w}(n)}_{\mathbf{w}_\mu(n)}$	$2M^2$	M^2
$\mathbf{P}\mathbf{w}_\mu(n) + \mathbf{v}_k$	M^2	M^2
Total	$3M^2 + 8M + 14 + 3M^2N_{it}$	$M^2 + 8M + 2 + 2M^2N_{it}$

Table 9.2: Complex operations of the recursive version of the proposed method 1 with the derivative null constraint.

9.3 Proposed Robust Real-Time Radar-Embedded Sidelobe Modulation - Method 2

In this section we propose another approach to the robust radar-embedded sidelobe modulation optimization problem of (9.21). By means of null eigenvalues constrained optimization design, we derive a solution, which is also able to generate transmit beampatterns that match a given mainbeam output power profile and embed sidelobe modulation towards the communication receiver direction, sustaining the same value embedded over a small angular interval. We simplify the proposed solution, reducing significantly the number of necessary complex operations, thus, turning this proposed method also well suited for online adaptive processing. We also derive simple update equations for pursuing a moving communication receiver.

We propose another approach to deal with the requirement of constraining the error in the mainlobe, $\mathbf{w}^H\mathbf{Q}\mathbf{w}$. Since

$$\mathbf{w}^H\mathbf{Q}\mathbf{w} = \sum_{i=1}^{M} \lambda_i |\mathbf{w}^H\mathbf{u}_i|^2, \qquad (9.54)$$

where $\lambda_i \geq 0$, $i = 1,\ldots,M$, are the eigenvalues of $\mathbf{Q}$ and $\mathbf{u}_i$ is the eigenvector of $\mathbf{Q}$ associated to its i-th eigenvalue, we can force the reduction of the squared error, $\mathbf{w}^H\mathbf{Q}\mathbf{w}$, by canceling the contribution of some eigenvectors of $\mathbf{Q}$. We do this by imposing null eigenvector constraints as

$$\mathbf{w}^H\mathbf{u}_i = 0, \quad i = 1,\ldots,N_e, \qquad (9.55)$$

where $\{\mathbf{u}_i\}$, $i = 1, \ldots, N_e$, are the eigenvectors of $\mathbf{Q}$ associated to its N_e largest eigenvalues. We choose N_e to correspond to the number of significant eigenvalues of $\mathbf{Q}$. As we increase N_e, we reduce the squared error in (9.54), but we also reduce the number of available degrees of freedom left for imposing the sidelobe communication modulation. The value of N_e must be properly chosen to adequately suit both primary and secondary radar functions. The proposed optimization problem is, thus, given by

$$\mathbf{w}^{op} = \min_{\mathbf{w}} ||\mathbf{w}||^2, \text{ subject to } \mathbf{C}^H\mathbf{w} = \mathbf{g}, \tag{9.56}$$

where $\mathbf{C}$ is given by

$$\mathbf{C} = \left[\begin{array}{ccc} \mathbf{U} & \vdots & \mathbf{S} \end{array} \right], \tag{9.57}$$

where $\mathbf{S}$ is defined in (9.25), $\mathbf{U} \in \mathbb{C}^{M \times N_e}$ is the matrix whose columns are the N_e eigenvectors of $\mathbf{Q}$ associated to its N_e largest eigenvalues and $\mathbf{g} \in \mathcal{C}^{N_e+2\times 1}$ is given by $\mathbf{g} = [\mathbf{0}_{1 \times N_e}, \mathbf{f}_k^T]^T$, where $\mathbf{f}_k$ is defined in (9.29). Finally, for a given N_e, the solution of (9.56) is given by

$$\mathbf{w}^{op} = \mathbf{C}(\mathbf{C}^H\mathbf{C})^{-1}\mathbf{g}. \tag{9.58}$$

Therefore, $\mathbf{w}_k^*$ is given straightforwardly by

$$\mathbf{w}_k^{op} = \mathbf{w}_o - \mathbf{w}^{op}. \tag{9.59}$$

The proposed approach can be shown to be a suboptimal solution of (9.21) in a certain sense since, for the same total squared error in the mainlobe $\mathbf{w}^H\mathbf{Q}\mathbf{w} = \delta$, the beampattern, $\mathbf{w}$, which is the solution of (9.21) is the one that results in the minimum total error.

(a) Simplifications and Receiver Pursuit

In this section, we show how to simplify (9.58), avoiding the computation of the inverse of a full matrix $\mathbf{C}^H\mathbf{C} \in \mathbb{C}^{(N_e+2)\times(N_e+2)}$.

First, we can write $\mathbf{C}^H\mathbf{C}$ as

$$\mathbf{C}^H\mathbf{C} = \left[\begin{array}{cc} \mathbf{U}^H\mathbf{U} & \mathbf{U}^H\mathbf{S} \\ \mathbf{S}^H\mathbf{U} & \mathbf{S}^H\mathbf{S} \end{array} \right] = \left[\begin{array}{cc} \mathbf{I}_{N_e} & \mathbf{A} \\ \mathbf{A}^H & \mathbf{D} \end{array} \right], \tag{9.60}$$

where $\mathbf{U}^H\mathbf{U} = \mathbf{I}_{N_e}$ because the columns of $\mathbf{U}$ are eigenvectors of $\mathbf{Q}$, $\mathbf{A} \in \mathbb{C}^{N_e \times 2}$ and $\mathbf{D} \in \mathbb{C}^{2\times 2}$. We can use the inversion property of partitioned matrices [10] and write the inverse of $\mathbf{C}^H\mathbf{C}$ as

$$(\mathbf{C}^H\mathbf{C})^{-1} = \left[\begin{array}{cc} \mathbf{B}^{-1} & -\mathbf{B}^{-1}\mathbf{A}\mathbf{D}^{-1} \\ -\mathbf{F}^{-1}\mathbf{A}^H & \mathbf{F}^{-1} \end{array} \right], \tag{9.61}$$

where $\mathbf{B}$ and $\mathbf{F}$ are given respectively by

$$\mathbf{B} = \mathbf{I}_{N_e} - \mathbf{A}\mathbf{D}^{-1}\mathbf{A}^H \quad \in \mathbb{C}^{N_e \times N_e}, \tag{9.62}$$

$$\mathbf{F} = \mathbf{D} - \mathbf{A}^H\mathbf{A} \quad \in \mathbb{C}^{2 \times 2}. \tag{9.63}$$

At this point, we have the inversion of matrices $\mathbf{F}$ and $\mathbf{D}$ that are of size 2×2, which can be inverted efficiently with only a few complex product operations. But we still have to invert matrix $\mathbf{B}$, that is of size $N_e \times N_e$. In order to simplify $\mathbf{B}^{-1}$, we can apply the matrix inversion lemma [10] to (9.62) and derive that

$$\mathbf{B}^{-1} = \mathbf{I}_{N_e} + \mathbf{A}\mathbf{F}^{-1}\mathbf{A}^H, \tag{9.64}$$

where $\mathbf{F} \in \mathbb{C}^{2 \times 2}$ is defined in (9.63). Therefore we have simplified the computation of $(\mathbf{C}^H\mathbf{C})^{-1} \in \mathbb{C}^{N_e+2 \times N_e+2}$ into simple matrices products and the inversion of 2 matrices of size 2×2, which can be efficiently computed. We can now rewrite (9.58) as

$$
\begin{aligned}
\mathbf{w}^{op} &= \mathbf{C}(\mathbf{C}^H\mathbf{C})^{-1}\mathbf{g} = \begin{bmatrix} \mathbf{U} & \vdots & \mathbf{S} \end{bmatrix} \begin{bmatrix} \mathbf{B}^{-1} & -\mathbf{B}^{-1}\mathbf{A}\mathbf{D}^{-1} \\ -\mathbf{F}^{-1}\mathbf{A}^H & \mathbf{F}^{-1} \end{bmatrix} \begin{bmatrix} \mathbf{0}_{N_e \times 1} \\ \mathbf{f}_k \end{bmatrix} \\
&= \begin{bmatrix} \mathbf{U} & \vdots & \mathbf{S} \end{bmatrix} \begin{bmatrix} -\mathbf{B}^{-1}\mathbf{A}\mathbf{D}^{-1}\mathbf{f}_k \\ \mathbf{F}^{-1}\mathbf{f}_k \end{bmatrix} \tag{9.65} \\
&= -\mathbf{U}\mathbf{B}^{-1}\mathbf{A}\mathbf{D}^{-1}\mathbf{f}_k + \mathbf{S}\mathbf{F}^{-1}\mathbf{f}_k. \tag{9.66}
\end{aligned}
$$

Substituting

$$\mathbf{D}^{-1} = (\mathbf{S}^H\mathbf{S})^{-1} \quad \text{and} \tag{9.67}$$

$$\mathbf{A} = \mathbf{U}^H\mathbf{S} \tag{9.68}$$

into (9.66), we have that the final simplified solution $\mathbf{w}^{op}$ using method 2 is given by

$$\mathbf{w}^{op} = -\mathbf{U}\mathbf{B}^{-1}\mathbf{U}^H\mathbf{S}(\mathbf{S}^H\mathbf{S})^{-1}\mathbf{f}_k + \mathbf{S}\mathbf{F}^{-1}\mathbf{f}_k, \tag{9.69}$$

where

$$\mathbf{F} = \mathbf{S}^H\mathbf{S} - \mathbf{S}^H\mathbf{U}\mathbf{U}^H\mathbf{S} \quad \in \mathbb{C}^{2 \times 2}, \tag{9.70}$$

$$\mathbf{B}^{-1} = \mathbf{I}_{N_e} + \mathbf{U}^H\mathbf{S}\mathbf{F}^{-1}\mathbf{S}^H\mathbf{U} \quad \in \mathbb{C}^{N_e \times N_e}, \tag{9.71}$$

$\mathbf{U} \in \mathbb{C}^{M \times N_e}$ is the matrix whose columns are the N_e eigenvectors of $\mathbf{Q}$ associated to its N_e largest eigenvalues and $\mathbf{S}$ and $\mathbf{f}_k$ are defined in (9.25) and (9.29) respectively.

If the communication receiver is moving in the u-space and we have its displacement information, Δu, we can compute the new beamforming

	Num. of complex products	Num. of complex additions
Computation of the eigenvectors of $\mathbf{Q}$	$O(M^3)$	$O(M^3)$
$\underbrace{\mathbf{S}^H\mathbf{S}}_{\mathbf{D}}$	$4M$	$4(M-1) = 4M - 4$
$\underbrace{\mathbf{D}^{-1}}_{\mathbf{D}_{in}}$	6	1
$\underbrace{\mathbf{U}^H\mathbf{S}}_{\mathbf{A}}$	$2N_eM$	$2N_e(M-1) = 2N_eM - 2N_e$
$\underbrace{\mathbf{D} - \mathbf{A}^H\mathbf{A}}_{\mathbf{F}}$	$4N_e$	$4N_e$
$\underbrace{\mathbf{I}_{N_e} + \mathbf{A}\mathbf{F}^{-1}\mathbf{A}^H}_{\mathbf{B}^{-1}}$	$2N_e^2 + 4N_e + 6$	$N_e^2 + 3N_e + 1$
$\underbrace{\mathbf{S}\mathbf{F}^{-1}\mathbf{f}_k}_{\mathbf{X}}$	$2M + 4$	$M + 2$
$\underbrace{\mathbf{U}\mathbf{B}^{-1}\mathbf{A}\mathbf{D}_{in}\mathbf{f}_k}_{\mathbf{Y}}$	$N_e^2 + 2N_e + MN_e + 4$	$N_e^2 + MN_e - M + 2$
$\mathbf{X} - \mathbf{Y}$	0	M
Total	$O(M^3) + (6 + 3N_e)M + 20 + 10N_e + 3N_e^2$	$O(M^3) + (5 + 3N_e)M + +2 + 9N_e + 2N_e^2$

Table 9.3: Complex operations of the proposed method 2.

weighting vector $\mathbf{w}_k^{op}(u + \Delta u)$ by substituting $\mathbf{S}_{u+\Delta u}$ (9.39) and $\mathbf{f}_{k,u+\Delta}$ (9.40) into equations (9.69), (9.70) and (9.71).

Therefore the updated $\mathbf{w}_k^{op}(u + \Delta u)$ is given by

$$\mathbf{w}_k^{op}(u + \Delta u) = \mathbf{w}_o - \mathbf{w}^{op}(u + \Delta u). \tag{9.72}$$

The number of complex multiplications and additions necessary to compute $\mathbf{w}^{opt}$ given N_e is detailed in Table 9.3

(b) Eigenvalue Analysis

Method 2 is especially interesting in terms of computational complexity if $\mathbf{Q}$ has only a few significant eigenvalues. In Fig. 9.6 we show the eigenspectrum of matrix $\mathbf{Q}$ for $u_d = 0.4226$, which implies a fidelity region of 50°, and for $u_d = 0.1$, which implies a fidelity region of 11°, for different array sizes. We can see that the number of significant eigenvalues are smaller than the total number of eigenvalues for all array sizes, which is very convenient for the proposed method.

We can also experimentally notice from Fig. 9.7 that the ratio between the significant number of eigenvalues holds a similar proportion to the total number of eigenvalues for all array sizes. In Fig. 9.7 we show that for different fidelity regions, the proportion of the number of eigenvalues required to comprise 95% of all eigenvalues for different array lengths is kept almost the
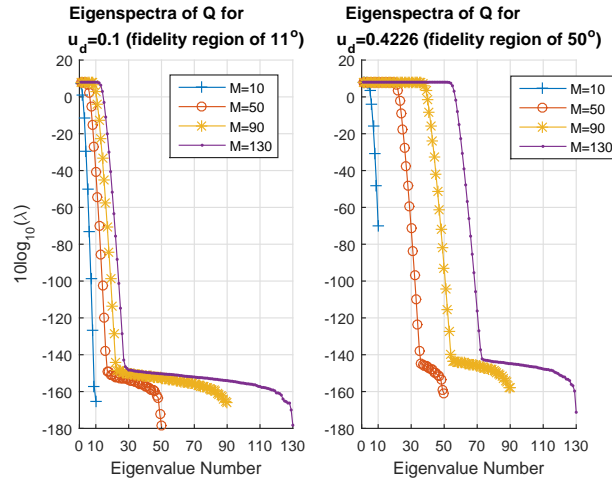
Figure 9.6: Eigenspectrum of $\mathbf{Q}$ for different values of M.
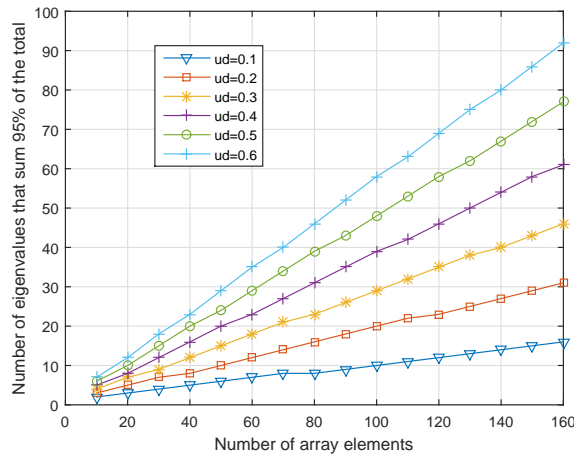
Figure 9.7: Number of eigenvalues necessary to comprise 95% of the sum of all eigenvalues vs. M, for several fidelity regions.

same. This fact motivates us to propose an empirical and efficient method for computing N_e. Based on the fact that the significant eigenvalues of $\mathbf{Q}$ can rapidly sum up 95% of the trace of $\mathbf{Q}$, which is the sum of all eigenvalues, we can use this as the value of N_e selection criterium. We can be almost sure that choosing N_e as the number of eigenvalues that sum up 95% of the trace of $\mathbf{Q}$ will lead to a total error bellow the δ threshold. By saying this, after computing the eigendecomposition, which has computational complexity of $O(M^3)$, one can choose the N_e that comprises 95% of the trace as

$$\sum_{n=1}^{N_e} \lambda_n > 0.95 \sum_{n=i}^{M} \lambda_n. \tag{9.73}$$
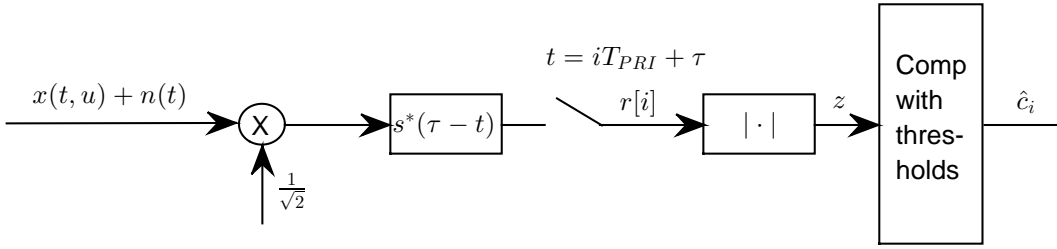
Figure 9.8: Illustration of the non-coherent ASK receiver.

9.4 Proposed Signalling Strategies

In Subsections 9.4.1 and 9.4.2, we briefly describe our proposed signalling strategies for embedding amplitude and phase modulation. The signalling strategy for embedding amplitude modulation to the sidelobe of the radar beampattern (not the method for generating the beampattern itself) is identical to the strategy described in 8.1. Therefore, we will explain it in 9.4.1 very briefly and we will repeat the bit error expressions derived in 8.1.2.

The signalling strategy for embedding phase modulation to the sidelobe of the radar beampattern is indeed different and is explained in 9.4.2. We don't assume that two or more orthogonal waveforms are transmitted simultaneously, but we do assume that the radar is coherent or, in other words, we assume that the initial carrier phase is the same within a coherent processing interval (CPI). We propose the, commonly used in digital communications, but new within the DFRC context, differentially encoded PSK (DPSK) modulation [9]. We derive in Subsection 9.4.2 the bit error rate for a generic binary DPSK (DBPSK) case. This derivation is not found in the literature and is extremely necessary within the DFRC radar context.

(a) Proposed Signalling Strategy for SLL Modulation

The output, $r[i]$, of the i-th received RF pulse after demodulation, matched filtering with the waveform $s(t)$ and sampling at the point of maximum (see Fig. 9.8) is given by

$$r[i] = \sqrt{E_r} c_i e^{j\psi} + n_i. \tag{9.74}$$

The non-coherent receiver diagram is depicted in Fig. 9.8. We take the absolute value of $r[i]$, $z = |r[i]|$, and compare to the thresholds, a decision is made for symbol k if z is inside the region Z_k, delimited by the thresholds, $T_{k-1,k} \leq |r| < T_{k,k+1}$.

The probability of wrong decision, $P(E)$, is given by (8.25) and repeated here for convenience,

$$P(E) = 1 - \frac{1}{K} \sum_{k=0}^{K-1} \left[\hat{Q}\left(\frac{\mu_k}{\tilde{\sigma}_n}, \frac{T_{k-1,k}}{\tilde{\sigma}_n} \right) - \hat{Q}\left(\frac{\mu_k}{\tilde{\sigma}_n}, \frac{T_{k,k+1}}{\tilde{\sigma}_n} \right) \right], \qquad (9.75)$$

where $\mu_k = \left| \sqrt{E_r} C_k e^{j\psi} \right|$, $\hat{Q}(a,b)$ is the Marcum Q function, $T_{k-1,k}$ and $T_{k,k+1}$ are the thresholds that bound the region Z_k, $Z_k = [T_{k-1,k}, T_{k,k+1})$ and $\tilde{\sigma}_n^2$ is the variance of the real and imaginary parts of n_i in (9.74).

(b) Proposed Signalling Strategy for Phase Modulation

For the phase modulation, we will take hand of a differentially encoded PSK (DPSK) modulation [9]. In the DPSK modulation, the information is encoded into the phase difference between two successive signals and not into the absolute phase.

In order to implement a DPSK modulation we need a reference phase, which is transmitted at the beginning of the transmitted message. Therefore, a sequence of N pulses, $m(t)$, is represented in its low-pass complex equivalent representation by

$$m(t) = \sqrt{2E_t} e^{j\psi} \sum_{i=0}^{N} c_i(u) s(t - iT_{PRI}), \qquad (9.76)$$

where $c_i(u) \in \{C_k(u) = \mathbf{w}_k^H \mathbf{s}(u)\}_{k=1}^{K}$, E_t is the RF pulse energy, ψ is the initial carrier phase, $\mathbf{w}_k$ is one of the K beamforming vectors triggered to be transmitted during the i-th pulse, $\mathbf{s}(u)$ is the array steering vector pointed towards direction u, $s(t)$ is the radar waveform, with bandwidth $W << f_c$, normalized to unitary energy and T_{PRI} is the radar pulse repetition interval.

Note that, in order to transmit N symbols, it is necessary to transmit $N+1$ absolute phases, i.e. $N+1$ pulses. The information phase transmitted during the i-th pulse is

$$\phi_i = \hat{\phi}_i - \hat{\phi}_{i-1}, \qquad (9.77)$$

where $\hat{\phi}_i$ and $\hat{\phi}_{i-1}$ are, respectively, the absolute phase of the i-th and $i-1$-th pulses at the receiver. In the absence of noise ϕ_i belongs to the set, $\mathcal{D}$, defined as

$$\mathcal{D} = \{\phi_k\}_{i=1}^{K} = \left\{ \frac{2\pi}{K}(k-1) + \Phi \right\}_{i=1}^{K}, \qquad (9.78)$$

where Φ is an arbitrary constant phase.

At the communication receiver located at direction u of the transmit beampattern, the output, $r[i]$, after demodulation, matched filtering with the waveform $s(t)$ and sampling at the point of maximum (see Fig. 9.9) is given by

$$r[i] = \sqrt{E_r} e^{j\psi} c_i(u) + n_i, \qquad (9.79)$$
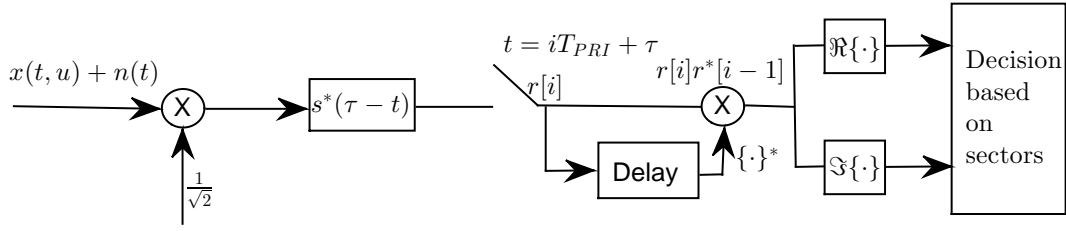
Figure 9.9: Diagram of the equivalent low-pass receiver for DPSK modulated signals.

where E_r is the received energy which was transmitted isotropically by the transmitter, considering the propagation attenuation effect, and n_i is an independent complex Gaussian random variable with zero mean and variance $\sigma_{n_i}^2 = \sigma_n^2 = N_0$.

We can write $c_i(u)$ as

$$c_i(u) = |c_i(u)|e^{j\alpha_i}, \tag{9.80}$$

thus, substituting (9.80) into (9.79) we have

$$
\begin{aligned}
r[i] &= \sqrt{E_r}e^{j\psi}|c_i(u)|e^{j\alpha_i} + n_i, & (9.81) \\
&= \sqrt{E_r}|c_i(u)|e^{j\hat{\phi}_i} + n_i. & (9.82)
\end{aligned}
$$

The delayed $r[i]$, $r[i-1]$ is given by

$$
r[i-1] = \sqrt{E_r}|c_{i-1}(u)|e^{j\hat{\phi}_{i-1}} + n_{i-1}, \tag{9.83}
$$

where $\sigma_{n_{i-1}}^2 = \sigma_{n_i}^2 = \sigma_n^2 = N_0$ and $\mathrm{E}[n_i n_{i-1}^*] = 0$.

Fig. 9.9 shows a diagram of the equivalent low-pass receiver for DPSK modulated signals.

The receiver bases its decision on the difference between the phases of the two variables (9.82) and (9.83), that is,

$$\Delta\beta_i = \arg[z[i]], \tag{9.84}$$

where

$$
\begin{aligned}
z[i] &= r[i]r^*[i-1], & (9.85) \\
&= E_r|c_i(u)||c_{i-1}(u)|e^{j(\hat{\phi}_i - \hat{\phi}_{i-1})} + N[i], & (9.86)
\end{aligned}
$$

where $N[i]$ is **non-Gaussian** complex noise.
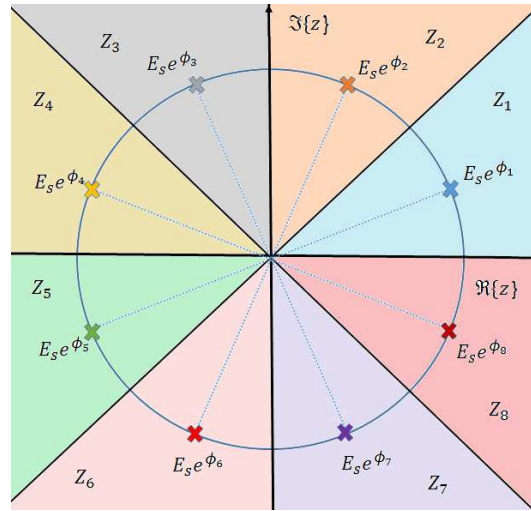
Figure 9.10: Illustration of a D8PSK modulation and its decision regions.

When $u = u_c$ we have that

$$|c_i| = |c_{i-1}| \text{ and} \tag{9.87}$$

$$\hat{\phi}_i - \hat{\phi}_{i-1} \in \{\phi_k\}_{k=1}^{K}. \tag{9.88}$$

In these conditions (9.85) resumes to

$$z[i] = E_r|c_i|^2 e^{j(\hat{\phi}_i - \hat{\phi}_{i-1})} + N[i], \tag{9.89}$$

$$= E_s e^{j\phi_k} + N[i], \tag{9.90}$$

where E_s is the symbol energy at the receiver and ϕ_k is a phase from the desired PSK constellation. Thus, the values assumed by $\Delta\beta_i$ in the absence of noise belong to the PSK constellation.

A correct decision is made if the point represented by $\Delta\beta_i$ lies inside a sector of width $2\pi/M$ centered around the correct value of $\Delta\beta_i$, which is $\phi_i \in \{\phi_k\}_{i=1}^{K}$. In Fig. 9.10 it is depicted a D8PSK constellation and the decision regions described by Z_k, $k = 1, \ldots, 8$. A right decision is made for ϕ_k if $\Delta\beta_i$ lies inside the sector described by Z_k.

Performance of the Non-Coherent DBPSK Receiver When Two Arbitrary Symbols Are Transmitted

We are especially interested in the binary case, DBPSK, where, towards u_c, $\phi_i = \hat{\phi}_i - \hat{\phi}_{i-1}$ may belong to the set $\mathcal{D} = \{\phi_k\}_{i=1}^{2} = \{0, \pi\}$. But what happens if the transmitted pulses have arbitrary amplitudes and arbitrary phase differences, $\phi_k \in \{0, \delta\}$, $\delta \in [0, 2\pi)$?

Within the DFRC radar context, the classic DBPSK modulation arises,

ideally, only towards u_c, towards the other directions we have arbitrary amplitudes and phase differences. This arbitrariness happens due to the non predictable behavior of the beamformers $\mathbf{w}_k$, $k = 1, \ldots, K$, in directions other than the receiver's direction. Though it is possible to find in the literature BER expressions for the classic DBPSK case, we haven't found a closed form for the DBPSK performance when two arbitrary amplitudes and phase differences are chosen for representing bits "0" and "1", possibly because it is not a practical situation in communications. Therefore, we derive, in this thesis this general DBPSK performance expression.

This derivation is detailed in the Appendix. A. At this point, we present only the final result. The error probability, $P(e)$, for the DBPSK modulation when two arbitrary symbols, C_0 and C_1, are transmitted is given by

$$P(e) = \frac{1}{8} e^{-\frac{E_r |C_0|^2}{4\sigma_w^2}} + \frac{1}{8} e^{-\frac{E_r |C_1|^2}{4\sigma_w^2}}$$

$$+ \frac{1}{2} \int_0^{+\infty} Q_M \left(\frac{\frac{\sqrt{E_r}|C_1 + C_0|}{2}}{\sigma_w}, \frac{\alpha}{\sigma_w} \right) \frac{\alpha}{\sigma_w^2} e^{-\frac{\alpha^2 + \frac{E_r |C_1 - C_0|^2}{4}}{2\sigma_w^2}} I_0 \left(\alpha \frac{\frac{\sqrt{E_r}|C_1 - C_0|}{2}}{\sigma_w^2} \right) d\alpha,$$

$$(9.91)$$

where $\sigma_w^2 = \sigma_n^2/2 = N_0/2$ and $Q_M(a, b)$ is the Marcum Q function.

Note that for the classic DBPSK case, i.e., when $C_0 = -C_1$, equation (9.91) reduces to the $P(e)$ of the classical DBPSK case [9],

$$P(e) = \frac{1}{2} e^{-\frac{E_r |C_0|^2}{4\sigma_w^2}} = \frac{1}{2} e^{-\frac{E_s}{N_0}}. \qquad (9.92)$$

10
DFRC Simulations

In this chapter, we show computer simulations of the proposed radar-embedded sidelobe modulation techniques. We compare the proposed techniques with and without the derivative constraint and we also compare them with the methods present in the literature described in Chapter 8.

We also present comparisons of the computational complexity in Section 10.7.

10.1 Example of the Proposed Method 1 for Sidelobe Amplitude Modulation

We consider a ULA consisting of $M = 10$ elements spaced by half a wavelength. We assume there is a given transmit beampattern and that the radar primary function takes place at the mainbeam, more precisely, the interval $u \in [-0.1736, 0.1736]$, which corresponds to $\theta \in [80^o, 100^o]$. We also assume that the sidelobes cannot exceed -20 dB and that the transition intervals are $u \in [-0.4226, -0.1736]$ and $u \in [0.1736, 0.4226]$, which correspond to $\theta \in [65^o, 80^o]$ and $\theta \in [100^o, 115^o]$. We define the transition intervals and the mainbeam as the "region of fidelity", where we want the new beamforming vectors under design to match the given profile. The communication receiver is located towards direction $u_c = -0.6$, or equivalently $\theta_c = 126^o$, and the transmitted symbols belong to the constellation $\mathcal{C} = \{C_1, C_2\} = \{\sqrt{10^{-20/10}}, \sqrt{10^{-40/10}}\}$, where $\sqrt{10^{-20/10}}$ and $\sqrt{10^{-40/10}}$ are associated to bits "1" and "0" respectively.

Fig. 10.1 shows the beamformers for the described example using the method of SLL of [5] from the Villanova Center of Advanced Communications lab explained in 8.1. In Fig. 10.1, $\mathbf{w}_{1,v}$ embeds C_1 towards u_c and $\mathbf{w}_{2,v}$ embeds C_2 towards u_c.

For the described example, Fig. 10.2 depicts the power pattern of the proposed beamformers, $\mathbf{w}_1$, which embeds C_1 towards u_c, and $\mathbf{w}_2$, which embeds C_2 towards u_c, according to proposed Method 1. We used the beamformer $\mathbf{w}_{1,v}$ of Fig. 10.1 as the given reference beamformer $\mathbf{w}_o$ for our proposed method. Fig. 10.2 shows the given transmit output power profile (generated by $\mathbf{w}_o = \mathbf{w}_{1,v}$) in green and the two power patterns that correspond to the two communica-
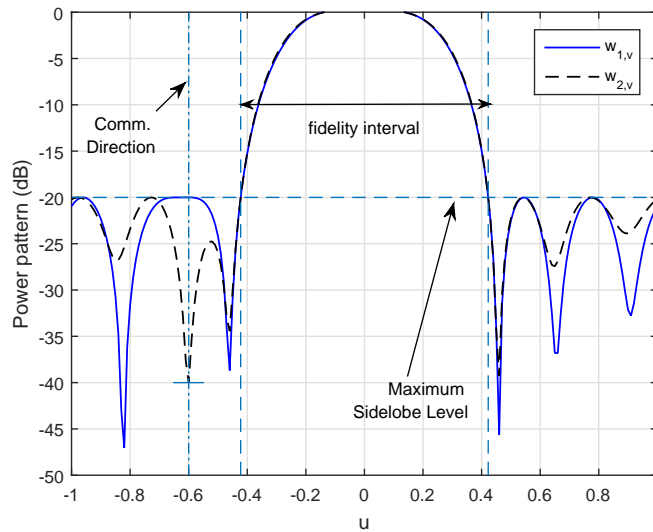
Figure 10.1: Beamformers that embed a binary amplitude constellation towards $u_c = -0.6$ using the method of [5].
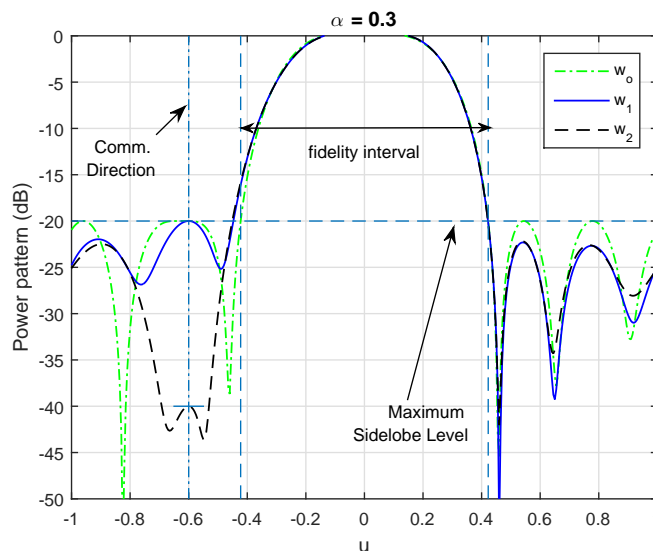
Figure 10.2: Power pattern of beamformers $\mathbf{w}_1$ and $\mathbf{w}_2$ that embed a binary amplitude constellation towards $u_c = -0.6$ generated using the proposed Method 1 for $\alpha = 0.3$.

tion symbols for the proposed Method 1 with first derivative null constraint and $\alpha = 0.3$. We chose this value of α because it led to better mainlobe fit without crossing the permitted sidelobe level.

We can see in Fig. 10.2 that around $u = -0.6$ the beampatterns generate a small plateau at their specific communication constraints. We can also notice that the mainbeam is closely matched by the two beamforming vectors and none of them lead to sidelobe levels higher than the permitted level. When α gets closer to 1, the sidelobes cross the permitted level in a few areas.
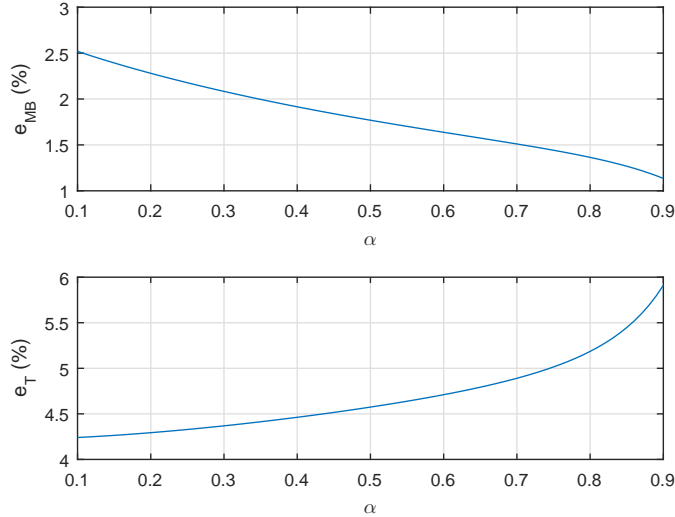
Figure 10.3: Mainbeam and total rms error vs. α due to beamformers $\mathbf{w}_1(\alpha)$ and $\mathbf{w}_2(\alpha)$ depicted in Fig. 10.2 for $\alpha = 0.3$.

Fig. 10.3 illustrates the behavior of the normalized RMS error of the mainbeam vs. α and the total normalized rms error vs. α due to beamformers $\mathbf{w}_1$ and $\mathbf{w}_2$ computed using Method 1 for different values of α, $\mathbf{w}_1(\alpha)$ and $\mathbf{w}_2(\alpha)$. The normalized rms error at the mainbeam, $e_{\mathrm{MB}}(\alpha)$, is

$$e_{\mathrm{MB}}(\alpha) \;=\; \sqrt{\frac{1}{2}\frac{(\mathbf{w}_o - \mathbf{w}_1(\alpha))^H \mathbf{Q}(\mathbf{w}_o - \mathbf{w}_1(\alpha)) + (\mathbf{w}_o - \mathbf{w}_2(\alpha))^H \mathbf{Q}(\mathbf{w}_o - \mathbf{w}_2(\alpha))}{\mathbf{w}_o^H \mathbf{Q} \mathbf{w}_o}}, \tag{10.1}$$

and the total rms normalized error, $e_{\mathrm{T}}(\alpha)$, is

$$e_{\mathrm{T}}(\alpha) \;=\; \sqrt{\frac{1}{2}\frac{||(\mathbf{w}_o - \mathbf{w}_1(\alpha))||^2 + ||(\mathbf{w}_o - \mathbf{w}_2(\alpha))||^2}{||\mathbf{w}_o||^2}}. \tag{10.2}$$

The behavior of the curves of $e_{\mathrm{MB}}(\alpha)$ and $e_{\mathrm{T}}(\alpha)$ depicted in Fig. 10.3 is as expected. As α increases, the total error in the mainbeam decreases, and as we force the beamformers to fit tightly the mainbeam, the sidelobes get more erroneous, increasing the total error. These curves give a good rule of thumb for setting α to achieve a desired tradeoff between sidelobe level and mainbeam fit.

(a) Recursive Version of Method 1

Fig. 10.4 depicts the power pattern of the proposed beamformers, $\mathbf{w}_{1,r}$ and $\mathbf{w}_{2,r}$, that embed the binary SLL modulation towards $u_c = -0.6$ according to the recursive version of the proposed Method 1 for 100 iterations. We can
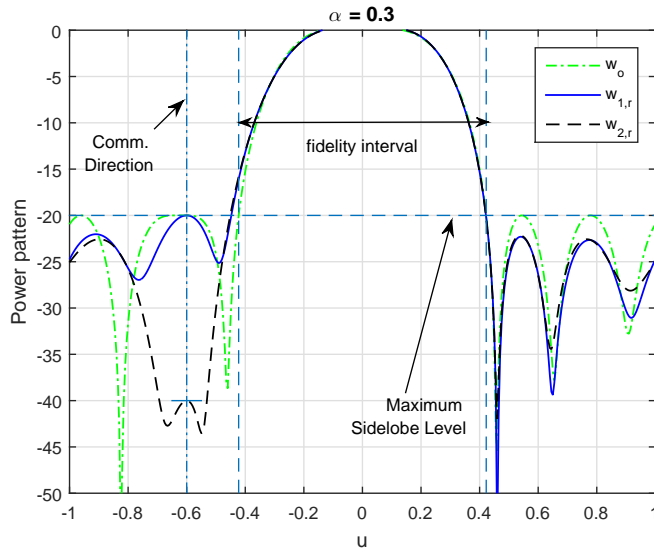
Figure 10.4: Power pattern of beamformers $\mathbf{w}_{1,r}$ and $\mathbf{w}_{2,r}$ that embed a binary amplitude constellation towards $u_c = -0.6$ generated using the recursive version of the proposed Method 1 for $\alpha = 0.3$.

note that Figs. 10.4 and 10.2 look exactly the same.

Fig. 10.5 depicts the squared error vs. number of iterations, n. The squared errors, $e_1(n)$ and $e_2(n)$, due to the convergence of $\mathbf{w}_{1,r}(n)$ and $\mathbf{w}_{2,r}(n)$ respectively are computed as

$$e_1(n) = ||\mathbf{w}_1 - \mathbf{w}_{1,r}(n)||^2, \qquad (10.3)$$

$$e_2(n) = ||\mathbf{w}_2 - \mathbf{w}_{2,r}(n)||^2. \qquad (10.4)$$
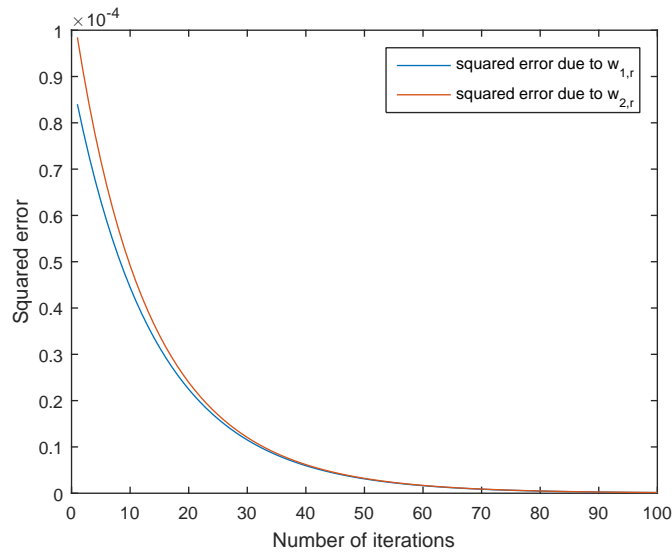
Figure 10.5: Squared error vs. number of iterations of the beamformers $\mathbf{w}_{1,r}$ and $\mathbf{w}_{2,r}$, depicted in Fig. 10.4, generated using the recursive version of the proposed Method 1 for $\alpha = 0.3$.

(b) Method 1 without the Derivative Constraint

Fig. 10.6 depicts the same example of Fig. 10.2 for the case **without** the first derivative null constraint and $\alpha = 0.5$. We chose this value of α because, for this case, it led to better mainlobe fit without crossing the permitted sidelobe level. The beamformers generated using the proposed Method 1 **without** the first derivative null constraint are denoted by $\bar{\mathbf{w}}_1$ and $\bar{\mathbf{w}}_2$. We can notice that the mainbeam is matched exactly by the two beamforming vectors and none of them lead to sidelobe levels higher than the permitted level. We can also note that our simple, closed form solution generates practically the same beampatterns as the method of [5], depicted in Fig. 10.1, which uses interior point technique for computing the solution to their problem formulation.

Fig. 10.7 illustrates the behavior of the normalized rms error of the mainbeam vs. α and the total normalized rms error vs. α for the case **without** the first derivative null constraint due to beamformers $\bar{\mathbf{w}}_1$ and $\bar{\mathbf{w}}_2$. We can note that the behavior is the same as for the case with the derivative null constraint depicted in Fig. 10.3.
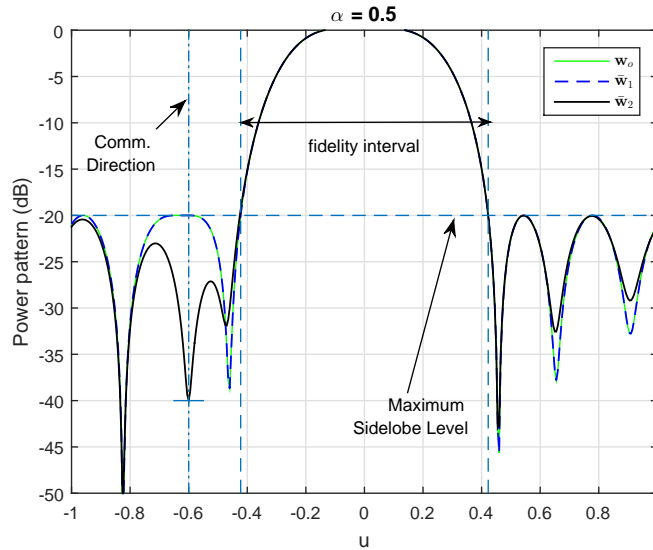
Figure 10.6: Beamformers that embed a binary amplitude constellation towards $u_c = -0.6$ using the proposed Method 1 for $\alpha = 0.5$ **without** the first derivative null constraint.
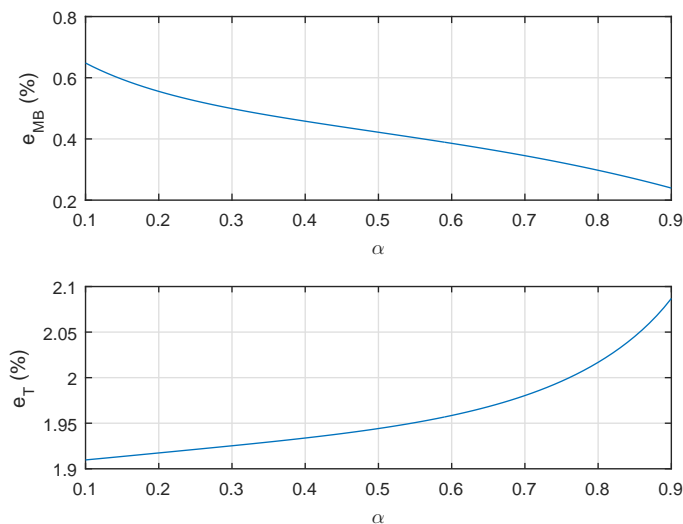
Figure 10.7: Mainbeam and total rms error vs. α for the case **without** the first derivative null constraint due to beamformers $\bar{\mathbf{w}}_1(\alpha)$ and $\bar{\mathbf{w}}_2(\alpha)$ depicted in Fig. 10.6.

(c) Recursive Version of Method 1 without the Derivative Constraint

Fig. 10.8 depicts the power pattern of the proposed beamformers, $\bar{\mathbf{w}}_{1,r}$ and $\bar{\mathbf{w}}_{2,r}$, that embed the binary SLL modulation towards $u_c = -0.6$ according to the recursive version of the proposed Method 1 for 100 iterations. We can note that Figs. 10.8 and 10.6 look exactly the same.

Fig. 10.9 depicts the squared error, $e_1(n)$ and $e_2(n)$, due to the convergence of $\bar{\mathbf{w}}_{1,r}(n)$ and $\bar{\mathbf{w}}_{2,r}(n)$ respectively, vs. number of iterations.
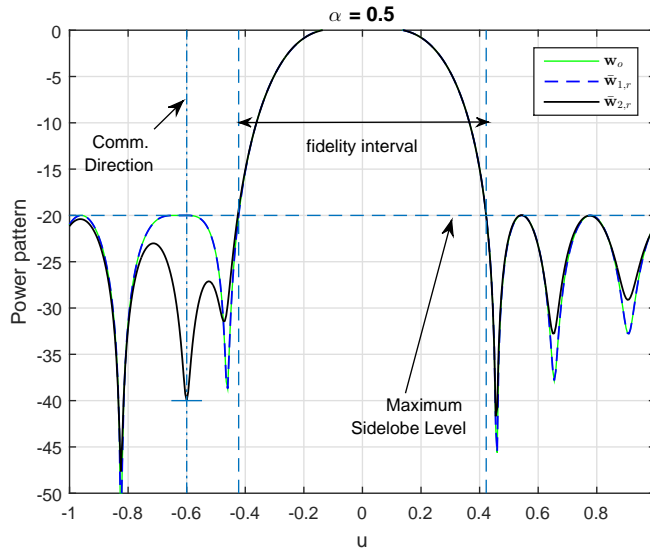
Figure 10.8: Power pattern of beamformers $\bar{\mathbf{w}}_{1,r}$ and $\bar{\mathbf{w}}_{2,r}$ that embed a binary amplitude constellation towards $u_c = -0.6$ generated using the recursive version of the proposed Method 1 for $\alpha = 0.5$ for the case **without** the first derivative null constraint.
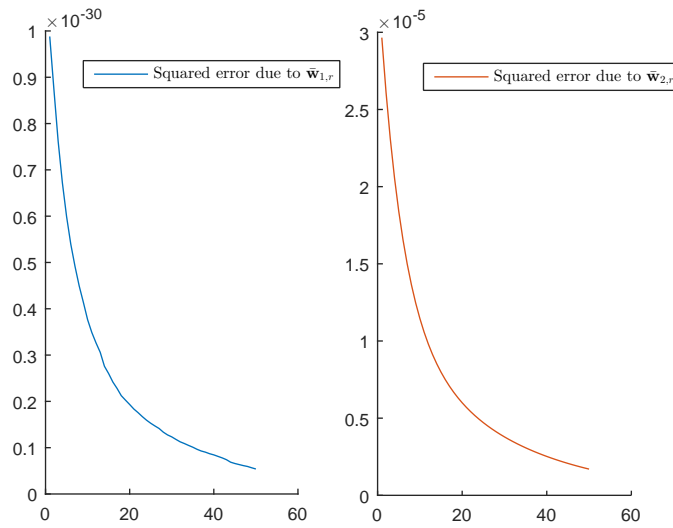

Figure 10.9: Squared error vs. number of iterations of the beamformers $\bar{\mathbf{w}}_{1,r}$ and $\bar{\mathbf{w}}_{2,r}$, depicted in Fig. 10.8, generated using the recursive version of the proposed Method 1 for $\alpha = 0.5$ for the case **without** the first derivative null constraint.

10.2 Example of the Proposed Method 2 for Sidelobe Amplitude Modulation

In this section we repeat the data of the example of Section 10.1 and we apply Method 2, described in Section 9.3, for generating the beamformers that embed the amplitude modulation. The power patterns of the beamformers generated using Method 2, $\mathbf{w}_{1,e}$ and $\mathbf{w}_{2,e}$, are depicted in Fig. 10.10 for $N_e = 5$
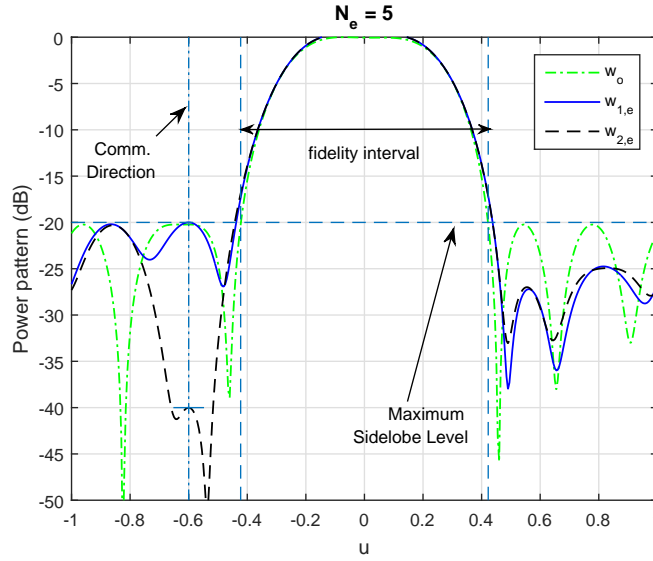
Figure 10.10: Power pattern of beamformers $\mathbf{w}_{1,e}$ and $\mathbf{w}_{2,e}$ that embed a binary amplitude constellation towards $u_c = -0.6$ generated using the proposed Method 2 for $N_e = 5$.

(which is the value that sum up 95% of the trace of $\mathbf{Q}$).

Fig. 10.11 illustrates the behavior of the normalized rms error of the mainbeam $e_{\mathrm{MB}}(N_e)$ vs. N_e and the total normalized rms error $e_{\mathrm{T}}(N_e)$ vs. N_e due to beamformers $\mathbf{w}_{1,e}$ and $\mathbf{w}_{2,e}$, computed using Method 2 for different values of N_e, $\mathbf{w}_{1,e}(N_e)$ and $\mathbf{w}_{2,e}(N_e)$. The mainbeam error, $e_{\mathrm{MB}}(N_e)$, is computed as

$$e_{\mathrm{MB}}(N_e) = \sqrt{\frac{1}{2} \frac{(\mathbf{w}_o - \mathbf{w}_{1,e}(N_e))^H \mathbf{Q}(\mathbf{w}_o - \mathbf{w}_{1,e}(N_e)) + (\mathbf{w}_o - \mathbf{w}_{2,e}(N_e))^H \mathbf{Q}(\mathbf{w}_o - \mathbf{w}_{2,e}(N_e))}{\mathbf{w}_o^H \mathbf{Q} \mathbf{w}_o}},$$
(10.5)

and the total rms normalized error, $e_{\mathrm{T}}(N_e)$, is computed as

$$e_{\mathrm{T}}(N_e) = \sqrt{\frac{1}{2} \frac{||(\mathbf{w}_o - \mathbf{w}_{1,e}(N_e))||^2 + ||(\mathbf{w}_o - \mathbf{w}_{2,e}(N_e))||^2}{||\mathbf{w}_o||^2}}.$$
(10.6)

The behavior of the curves of e_{MB} and e_{T} seen in Fig. 10.11 is as expected. We can compare N_e of Method 2 to α of Method 1. Similarly to α, as N_e increases, the total error in the mainbeam decreases, and as we force the beamformers to fit tightly the mainbeam, the sidelobes get more erroneous, increasing the total error.

Comparing the power patterns generated using Methods 1 and 2 in Figs. 10.2 and 10.10 respectively, we can note that they differ a little visually. The mainbeam and total errors for Method 1 and $\alpha = 0.3$ are of $e_{MB}(\alpha = 0.3) =$
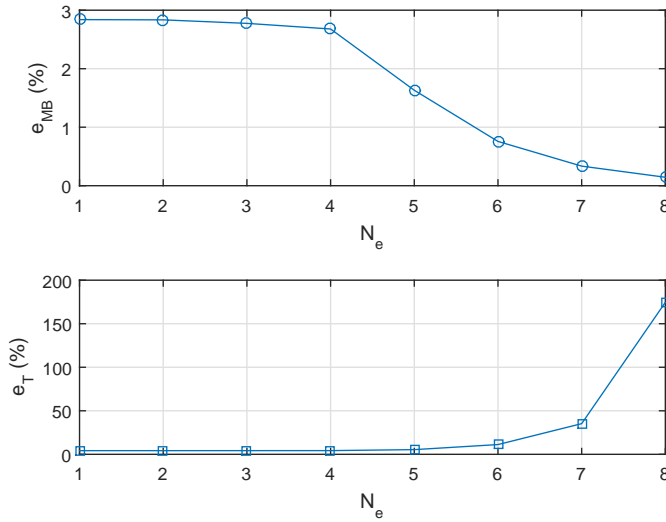
Figure 10.11: Mainbeam and total rms error vs. N_e due to beamformers $\mathbf{w}_{1,e}(N_e)$ and $\mathbf{w}_{2,e}(N_e)$ depicted in Fig. 10.10.

2.08% and $e_T(\alpha = 0.3) = 4.36\%$ respectively, while for Method 2 with $N_e = 5$ they are of $e_{MB}(N_e = 5) = 1.63\%$ and $e_T(N_e = 5) = 5.39\%$ respectively. The difference between the two methods is very small. Anyway, as long as the sidelobe levels are below the maximum permitted level and the mainbeam is fit properly by the designed beamformers, both methods are useful for DFRC radars.

(a) Method 2 without the Derivative Constraint

Fig. 10.12 depicts the same example of Fig. 10.10 for the case **without** the first derivative null constraint and $N_e = 5$. The value of N_e does not change because the number of eigenvalues necessary to reduce the error at the mainbeam depends only on matrix $\mathbf{Q}$, which in its turn depends only on the array geometry and the sector of the mainbeam. The beamformers generated using the proposed Method 2 without the first derivative null constraint are denoted here by $\bar{\mathbf{w}}_{1,e}$ and $\bar{\mathbf{w}}_{2,e}$. We can notice that the mainbeam is matched exactly by the two beamforming vectors and none of them lead to sidelobe levels higher than the permitted level.

Fig. 10.13 illustrates the behavior of the normalized rms error of the mainbeam vs. N_e and the total normalized rms error vs. N_e for the case **without** the first derivative null constraint due to beamformers $\bar{\mathbf{w}}_{1,e}$ and $\bar{\mathbf{w}}_{2,e}$.

Comparing the power patterns generated using Methods 1 and 2 in Figs. 10.6 and 10.12 respectively, for the case **without** the first derivative null constraint, we can note that they differ minimally visually. The mainbeam and total errors for Method 1 and $\alpha = 0.5$ are of $e_{MB}(\alpha = 0.5) = 0.38\%$ and
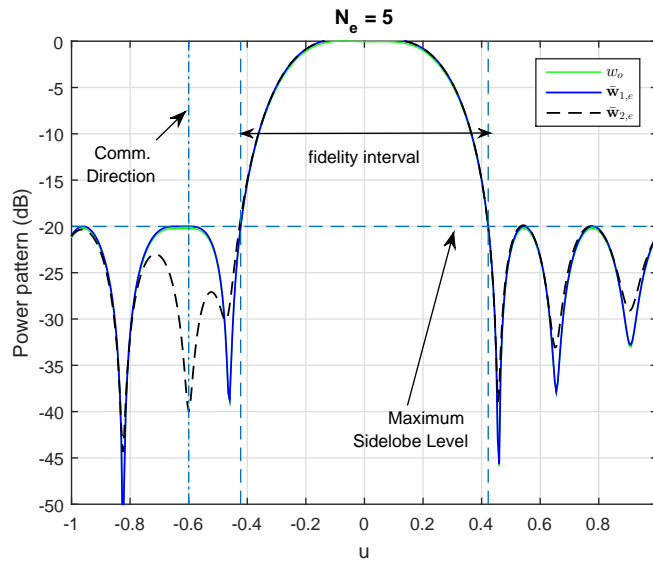
Figure 10.12: Beamformers, $\bar{\mathbf{w}}_{1,e}$ and $\bar{\mathbf{w}}_{2,e}$, that embed a binary amplitude constellation towards $u_c = -0.6$ using the proposed Method 2 for $N_e = 5$ **without** the first derivative null constraint.
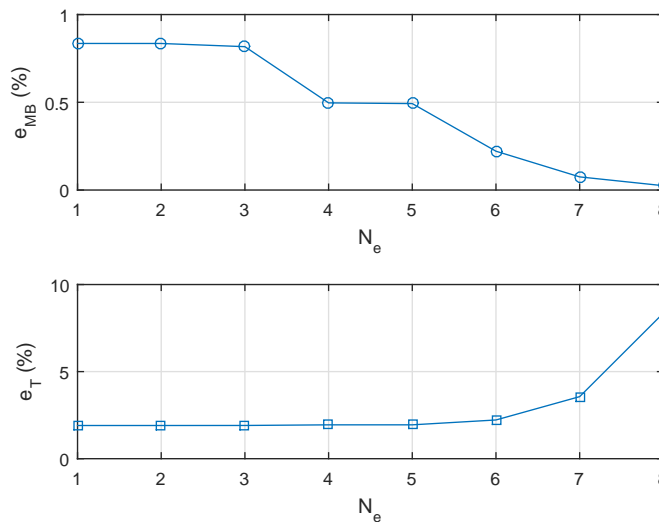
Figure 10.13: Mainbeam and total rms error vs. N_e for the case **without** the first derivative null constraint due to beamformers $\bar{\mathbf{w}}_{1,e}(N_e)$ and $\bar{\mathbf{w}}_{2,e}(N_e)$ depicted in Fig. 10.12.

$e_T(\alpha = 0.5) = 1.95\%$ respectively, while for the Method 2 with $N_e = 5$ they are of $e_{MB}(N_e = 5) = 0.49\%$ and $e_T(N_e = 5) = 1.94\%$ respectively. The difference between the two methods is indeed very small.

The proposed Method 2 **without** the first derivative null constraint is also able to generate practically the same beamformers as the ones achieved using the complex method of of [5], depicted in Fig. 10.1, in a much simpler manner.
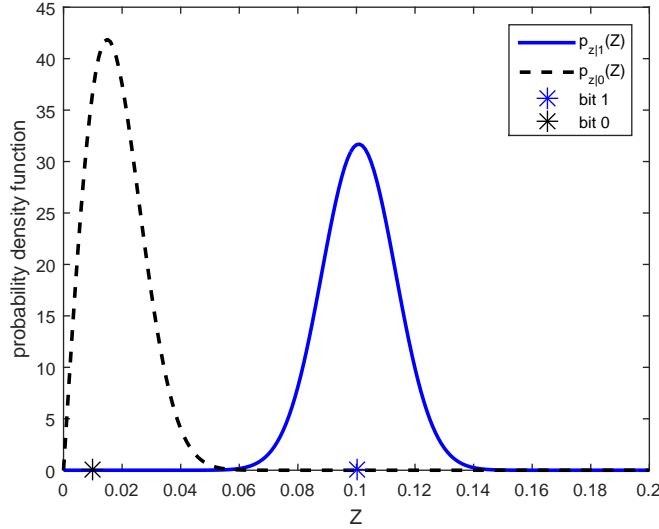
Figure 10.14: Conditional probability density function of the symbols transmitted using the binary constellation $\mathcal{C} = \{C_1, C_2\} = \{\sqrt{10^{-20/10}}, \sqrt{10^{-40/10}}\}$ and SNR = 15 dB.

10.3 Robustness Analysis for the Proposed Sidelobe Amplitude Modulation Methods

Fig. 10.14 depicts the conditional density function of the received symbols for the embedded constellation $\mathcal{C} = \{C_1, C_2\} = \{\sqrt{10^{-20/10}}, \sqrt{10^{-40/10}}\}$, where $C_1 = \sqrt{10^{-20/10}}$ is associated to bit "1" and symbol $C_2 = \sqrt{10^{-40/10}}$ corresponds to bit "0", for a SNR of 15 dB.

The SNR in dB is defined as

$$\text{SNR} = 10 \log_{10} \frac{0.5|C_1|^2 + 0.5|C_2|^2}{\sigma_n^2}, \tag{10.7}$$

where σ_n^2 is the noise variance of the received samples (after demodulation and matched filtering).

From Fig. 10.14 we can check that the threshold for computing the analytical angular BER for a SNR of 15 dB is $T = 0.056$, which is the point where the conditional density functions cross each other. Having defined the decision threshold, we can now compute the angular BER for all beamformers seen so far using the analytical BER expression of (9.75).

Fig. 10.15 depicts the angular BER (more precisely the BER in u-space plane) of the proposed Method 1, with and without the derivative null constraint ($\alpha = 0.3$ and $\alpha = 0.5$ respectively), and the method of the Villanova Center [5]. As the results of Method 1 and its recursive version are the same, assuming that convergence is achieved, we will depict only the results for Method 1 in its closed form. Fig. 10.16 depicts the angular BER of the proposed Method 2, with and without the derivative null constraint ($N_e = 5$ for both
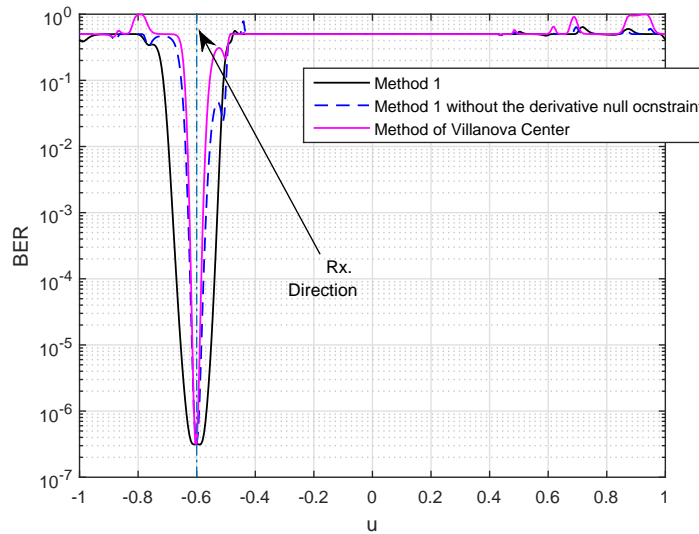
Figure 10.15: BER × u, for embedded amplitude modulation at $u_c = -0.6$, for the proposed Method 1 with and without the derivative constraint and the method of [5].
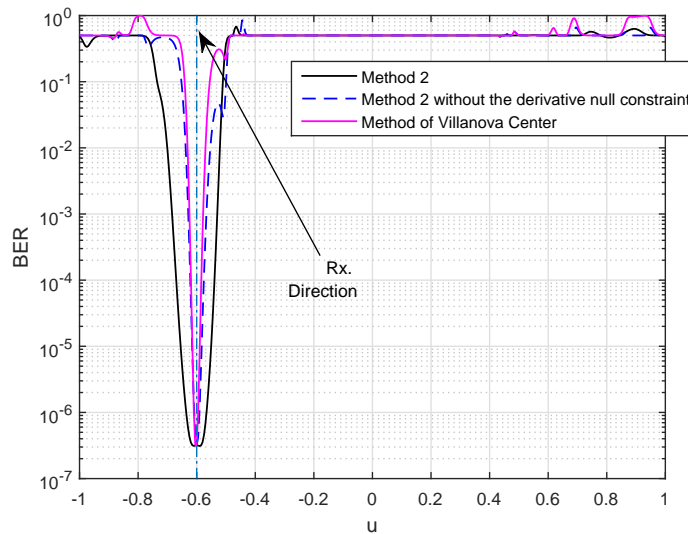
Figure 10.16: BER × u, for embedded amplitude modulation at $u_c = -0.6$, for the proposed Method 2 with and without the derivative constraint and the method of [5].

cases), and the method of [5].

We can confirm by looking at Figs. 10.15 and 10.16 that the results of the proposed methods without the derivative null constraint and the method of [5] are very similar, as expected, given that the beampatterns of both methods are practically the same. The angular BER curve falls rapidly with a very narrow pit to the operational BER at the direction of the communication receiver.

On the other hand, the outcome of the proposed methods with first
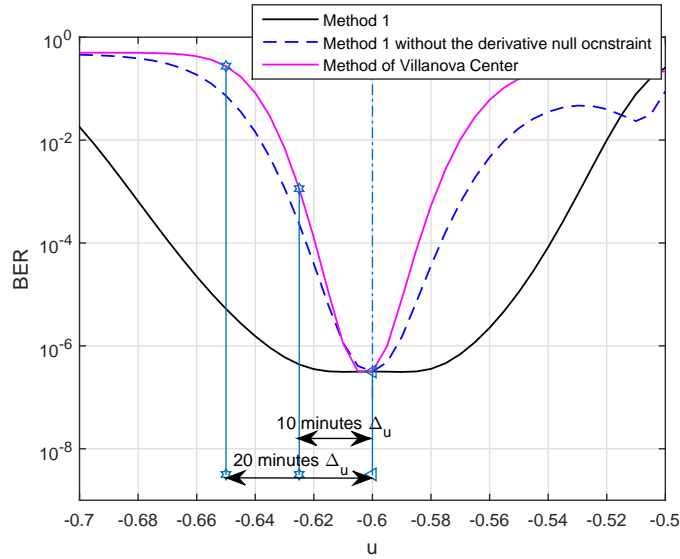
Figure 10.17: Zoom of the BER $\times$ u, for embedded amplitude modulation at $u_c = -0.6$, for the proposed Method 1 with and without the derivative constraint and the method of [5].

derivative null constraint is a flat operational BER over a small region. This property makes the proposed techniques robust to small deviation errors on the preassigned direction, which is fundamental for the communication system service, since involuntary small deviation errors in the relative positioning of the communication receiver and the radar is likely to happen.

Fig. 10.17 assumes the data of the sidelobe amplitude example of Section 9.1. The communication receiver is in a corvette moving away from the radar mainbeam with a cruising speed of 17 knots or equivalently 8.75 m/s in a direction tangential to the circumference of radius 180 Km centered at the radar. In 10 minutes the relative angle between the radar and the communication receiver would have increased of $\Delta u = -0.025$. Checking the angular BER in Fig. 10.15 we can see that the BER of the method of the Villanova Center would go from 3.17×10^{-7} to 1.1×10^{-3} in only 10 minutes. In 20 minutes $\Delta u = -0.05$ and the BER goes to 0.27. The BER of the proposed method, on the other side, goes from 3.17×10^{-7} to 4.35×10^{-7} in 10 minutes and to 5.24×10^{-6} in 20 minutes, which keeps the communication operational during the whole time.

This BER dynamic is illustrated in Fig. 10.17, a zoom of Fig. 10.15.

10.4 Example of the Proposed Method 1 for Sidelobe Phase Modulation

In this example, we will embed the BPSK constellation $\mathcal{C} = \{\phi_1, \phi_2\} = \{0^o, 180^o\}$ towards $u_c = -0.6$. We will use the same reference beamformer, $\mathbf{w}_o$, as the one used for the amplitude modulation example of the former Section
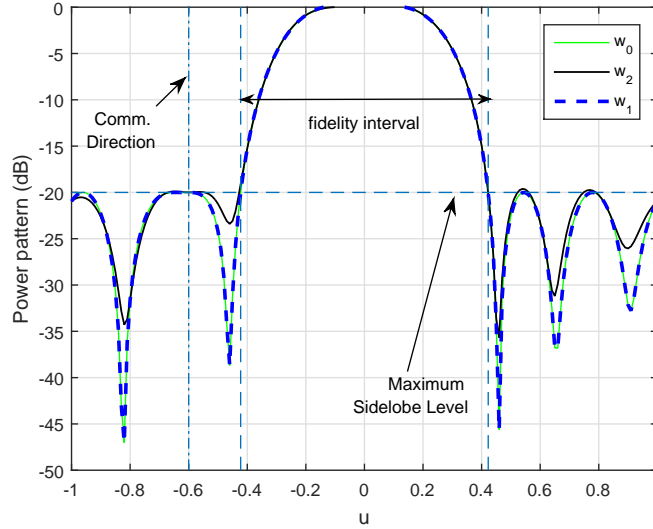
Figure 10.18: Beamformers that embed a DBPSK constellation towards $u_c = -0.6$ using the method of [4].

10.1 ($\mathbf{w}_o$ is beamformer $\mathbf{w}_{1,v}$ of Fig. 10.1).

In Fig. 10.18 we simulate the method of common reference from the Villanova Center, [4], explained in 8.2.2, using $\mathbf{w}_{1,v}$ of Fig. 10.1 as the common reference beamformer, $\mathbf{w}_0$. The common reference, $\mathbf{w}_0$, is always used with its own sensor array and is transmitted in tandem with a certain waveform. Beamformers $\mathbf{w}_1$ and $\mathbf{w}_2$ are designed according to the optimization problem (8.43) and are applied to another sensor array and transmitted in tandem with an orthogonal waveform according to the current message. Beamformer $\mathbf{w}_1$ embeds $\phi_1 = 0^o$ into the phase difference between the beampattern of $\mathbf{w}_1$ and $\mathbf{w}_0$ towards u_c and $\mathbf{w}_2$ embeds $\phi_1 = 180^o$ into the phase difference between the beampattern of $\mathbf{w}_2$ and $\mathbf{w}_0$ towards u_c. We won't simulate the method of rotational invariance because this method doesn't lead to secure communications as discussed in 8.2.1.

We can see from Fig. 10.18 that the sidelobes are just in the limit of crossing the permitted level line. That is because the method of [4], differently from their proposed method for sidelobe amplitude modulation, doesn't impose this sidelobe constraint to the optimization problem formulation. Since they use interior point technique for solving their optimization problem, the reason for not adding this important constraint is not clear to us.

Fig. 10.19 shows the phase difference of the beamformer pairs of Fig. 10.18 ($\mathbf{w}_1$,$\mathbf{w}_0$) and ($\mathbf{w}_2$,$\mathbf{w}_0$) in the u-space. We can note that, towards $u_c = -0.6$, the phase difference between $\mathbf{w}_1$ and $\mathbf{w}_0$ is zero, which corresponds to embedding $\phi_1 = 0$, and the phase difference between $\mathbf{w}_2$ and $\mathbf{w}_0$ is 180°, which corresponds to embedding $\phi_2 = 180^o$.
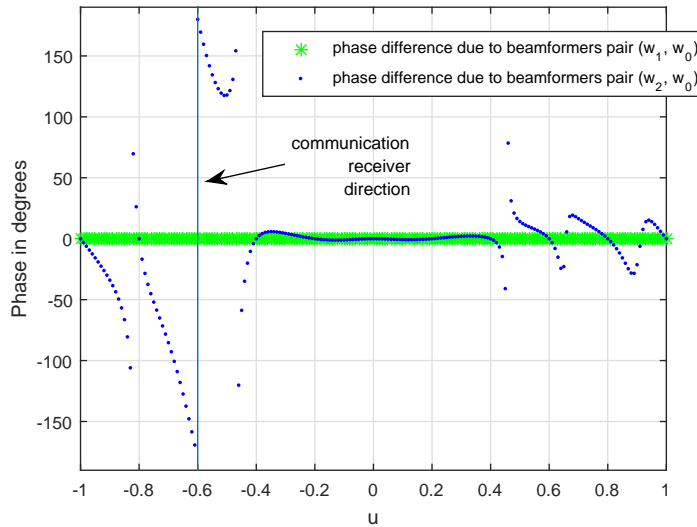
Figure 10.19: Phase difference of the beamformer pairs of Fig. 10.18 ($\mathbf{w}_1$,$\mathbf{w}_0$) and ($\mathbf{w}_2$,$\mathbf{w}_0$) in the u-space.

We propose a DBPSK signaling strategy that differs from the strategies for embedding sidelobe phase modulation existent in the DFRC literature so far. The DBPSK modulation is explained in 9.4.2, it can be summarized as: when bit "0" is triggered for transmission, the same beamformer as the last pulse is used and when bit "1" is triggered for transmission the other beamformer, different from the one used for the last pulse, is chosen. For the described example, Fig. 10.20 depicts the power pattern of the proposed beamformers, $\mathbf{w}_1$ and $\mathbf{w}_2$, that embed the DBPSK modulation towards $u_c = -0.6$ according to proposed Method 1.

Fig. 10.20 shows the given transmit output power profile in green and the two power patterns that correspond to the two beamformers generated using the proposed Method 1 with first derivative null constraint and $\alpha = 0.6$. We chose this value of α because it led to better mainlobe fit without crossing the permitted sidelobe level. The beampattern generated by $\mathbf{w}_2$ has a phase shift towards u_c of 180° in relation to the beampattern generated by $\mathbf{w}_1$ and vice versa. Both $\mathbf{w}_1$ and $\mathbf{w}_2$ try to match as close as possible the beampattern of the reference beamformer, $\mathbf{w}_o$, with a tighter adjustment at the mainlobe. We can notice that the mainbeam is closely matched by the two beamforming vectors and none of them lead to sidelobe levels higher than the permitted level. When α gets closer to 1, the sidelobes cross the permitted level in a few areas.

Fig. 10.21 shows the phase difference of the beamformer pair of Fig. 10.20 ($\mathbf{w}_2$,$\mathbf{w}_1$) in the u-space. We can note that towards $u_c = -0.6$ the phase difference between $\mathbf{w}_2$ and $\mathbf{w}_1$ is, as expected, of 180°.
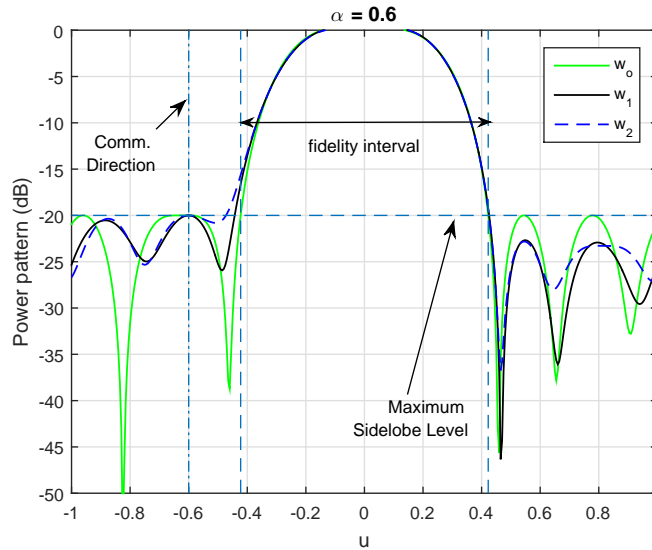
Figure 10.20: Power pattern of beamformers $\mathbf{w}_1$ and $\mathbf{w}_2$ that embed a DBPSK modulation towards $u_c = -0.6$ generated using the proposed Method 1 for $\alpha = 0.6$.
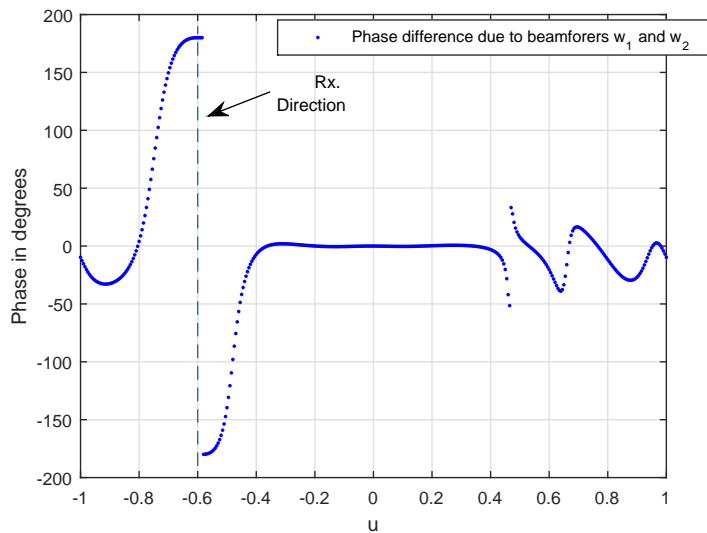
Figure 10.21: Phase difference of the beamformer pair of Fig. 10.20 $(\mathbf{w}_2, \mathbf{w}_1)$ in the u-space.

We can note from observing Figs. 10.20 and 10.21 that around $u = -0.6$ the beampatterns generate a small plateau at their specific communication constraints which keeps the phase difference stable within this plateau.

Fig. 10.22 depicts the behavior of the normalized rms error of the mainbeam $e_{\mathrm{MB}}(\alpha)$ vs. α and the total normalized rms error $e_{\mathrm{T}}(\alpha)$ vs. α due to beamformers $\mathbf{w}_1$ and $\mathbf{w}_2$. The behavior of the curves of $e_{\mathrm{MB}}(\alpha)$ and $e_{\mathrm{T}}(\alpha)$ seen in Fig. 10.22 is as expected. As α increases, the total error in the mainbeam decreases, and as we force the beamformer to fit tightly the mainbeam, the
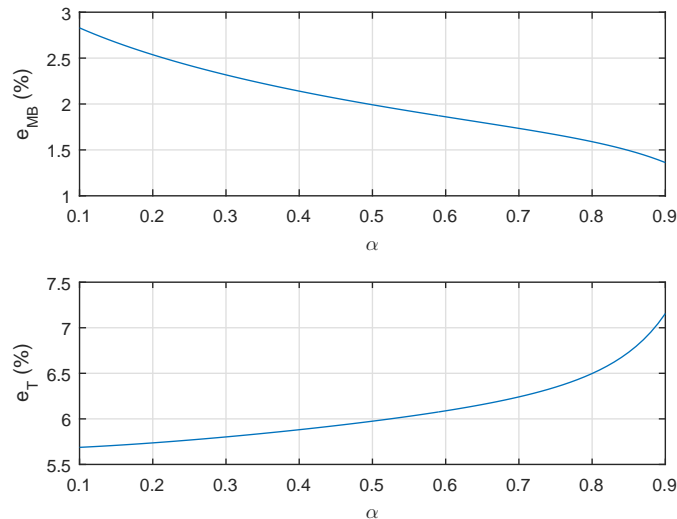
Figure 10.22: Mainbeam and total rms error vs. α due to beamformers $\mathbf{w}_1(\alpha)$ and $\mathbf{w}_2(\alpha)$ depicted in Fig. 10.20.
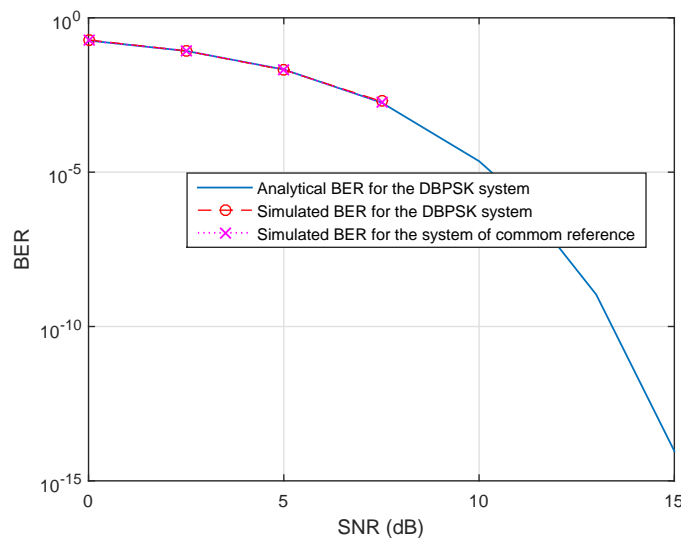
Figure 10.23: Simulated and analytical BER for a DBPSK system.

sidelobes get more erroneous, increasing the total error.

Fig. 10.23 depicts the BER for the proposed binary DPSK system, both analytical and simulated, and the simulated BER for the method of commom reference from the Villanova Center [4]. We can note from Fig. 10.23 that the simulated and analytical curves are in agreement and we can also note that, though the method of commom reference is more sophisticated, it achieves the same BER as the simple DBPSK signalling strategy proposed here for sidelobe phase modulation.
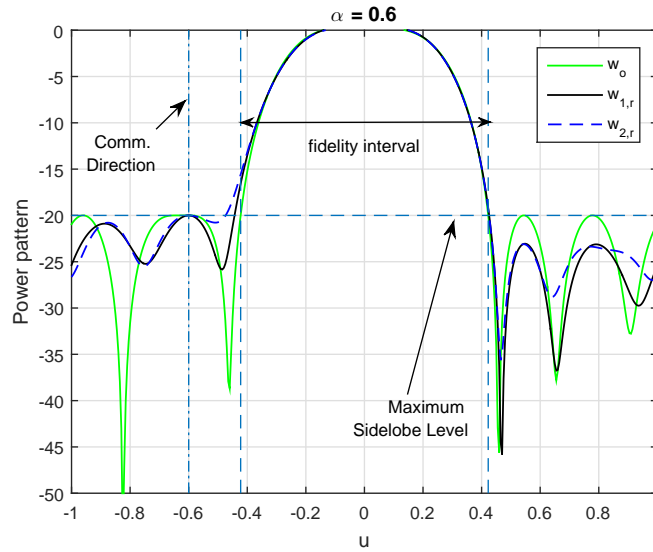
Figure 10.24: Power pattern of beamformers $\mathbf{w}_{1,r}$ and $\mathbf{w}_{2,r}$ that embed a binary DPSK constellation towards $u_c = -0.6$ generated using the recursive version of the proposed Method 1 for $\alpha = 0.6$.
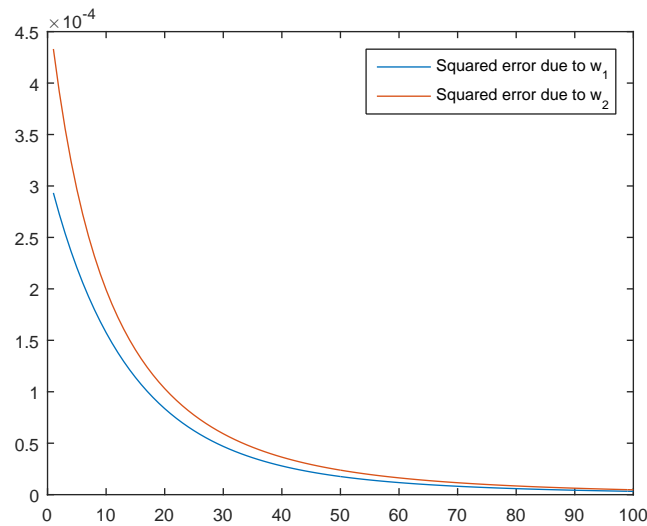
Figure 10.25: Squared error vs. number of iterations of the beamformers $\mathbf{w}_{1,r}$ and $\mathbf{w}_{2,r}$, depicted in Fig. 10.24, generated using the recursive version of the proposed Method 1 for $\alpha = 0.6$.

(a) Recursive Version of Method 1

Fig. 10.24 depicts the power pattern of the proposed beamformers, $\mathbf{w}_{1,r}$ and $\mathbf{w}_{2,r}$, that embed the binary DPSK modulation towards $u_c = -0.6$ according to the recursive version of the proposed Method 1 for 100 iterations. We can note that Figs. 10.24 and 10.20 look exactly the same. Fig. 10.25 depicts the squared error vs. number of iterations.
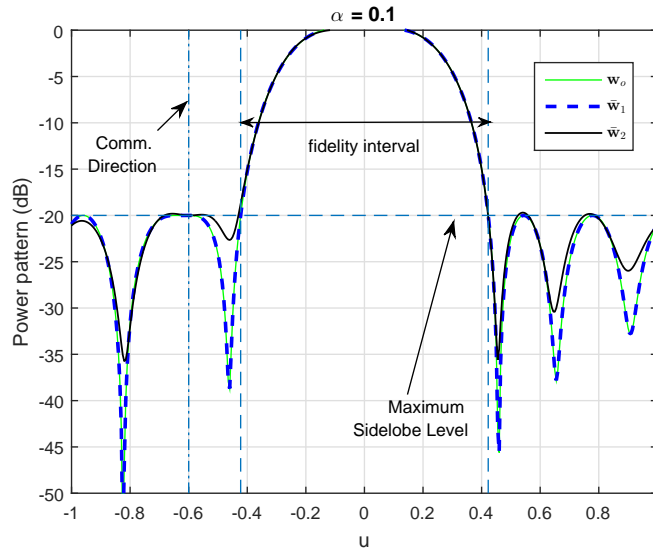
Figure 10.26: Beamformers that embed a binary DPSK constellation towards $u_c = -0.6$ using the proposed Method 1 for $\alpha = 0.1$ **without** the first derivative null constraint.

(b) Method 1 without the Derivative Constraint

Fig. 10.26 depicts the same example of Fig. 10.20 for the case **without** the first derivative null constraint and $\alpha = 0.1$. We can notice that the mainbeam is matched exactly by the two beamforming vectors, $\bar{\mathbf{w}}_2$ and $\bar{\mathbf{w}}_1$. We had to use a very small α so that none of beampatterns lead to sidelobe levels higher than the permitted level. Even though, the sidelobes are just in the limit, like the beampatterns generated by the method of common reference from the Villanova Center, [4], depicted in Fig. 10.18.

Fig. 10.27 shows the phase difference of the beamformer pair of Fig. 10.26 ($\bar{\mathbf{w}}_2$,$\bar{\mathbf{w}}_1$) in the u-space. We can note that towards $u_c = -0.6$ the phase difference between $\bar{\mathbf{w}}_2$ and $\bar{\mathbf{w}}_1$ is, as expected, of 180°.

Fig. 10.28 illustrates the behavior of the normalized rms error of the mainbeam vs. α and the total normalized rms error vs. α for the case **without** the first derivative null constraint due to beamformers $\bar{\mathbf{w}}_1$ and $\bar{\mathbf{w}}_2$.
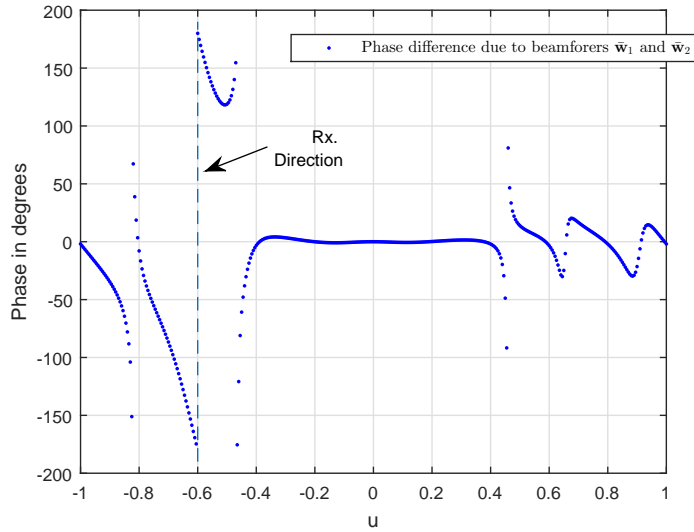
Figure 10.27: Phase difference of the beamformer pair of Fig. 10.26 ($\mathbf{w}_2,\mathbf{w}_1$) in the u-space.
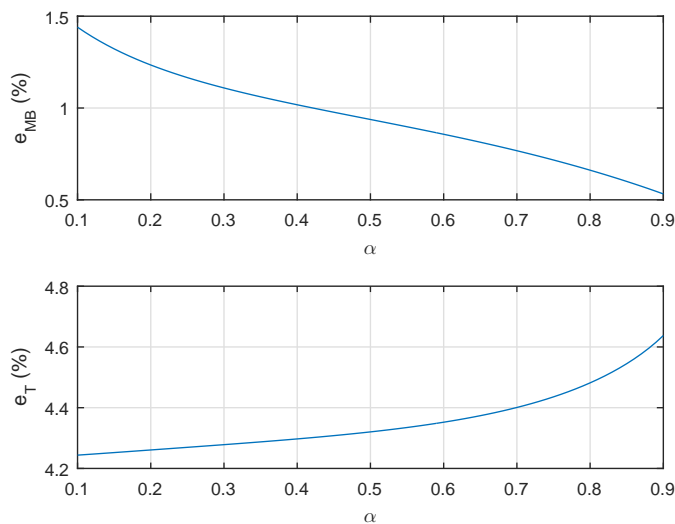
Figure 10.28: Mainbeam and total rms error vs. α for the case **without** the first derivative null constraint due to beamformers $\bar{\mathbf{w}}_1(\alpha)$ and $\bar{\mathbf{w}}_2(\alpha)$ depicted in Fig. 10.26.

(c) Recursive Version of Method 1 without the Derivative Constraint

Fig. 10.29 depicts the power pattern of the proposed beamformers, $\bar{\mathbf{w}}_{1,r}$ and $\bar{\mathbf{w}}_{2,r}$, that embed the binary DPSK modulation towards $u_c = -0.6$ according to the recursive version of the proposed Method 1 for 100 iterations. We can note that Figs. 10.29 and 10.26 look exactly the same.

Fig. 10.30 depicts the squared error, e_1 and e_2, due to the convergence of $\bar{\mathbf{w}}_{1,r}$ and $\bar{\mathbf{w}}_{2,r}$ respectively, vs. number of iterations.
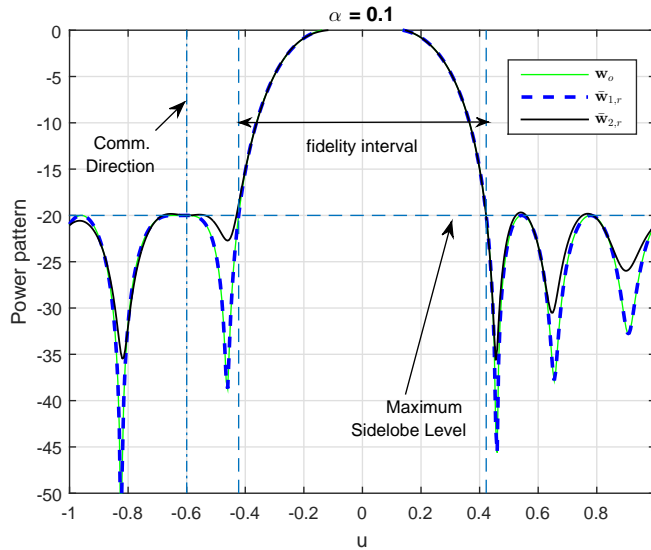
Figure 10.29: Power pattern of beamformers $\bar{\mathbf{w}}_{1,r}$ and $\bar{\mathbf{w}}_{2,r}$ that embed a binary DPSK constellation towards $u_c = -0.6$ generated using the recursive version of the proposed method 1 for $\alpha = 0.1$ for the case **without** the first derivative null constraint.
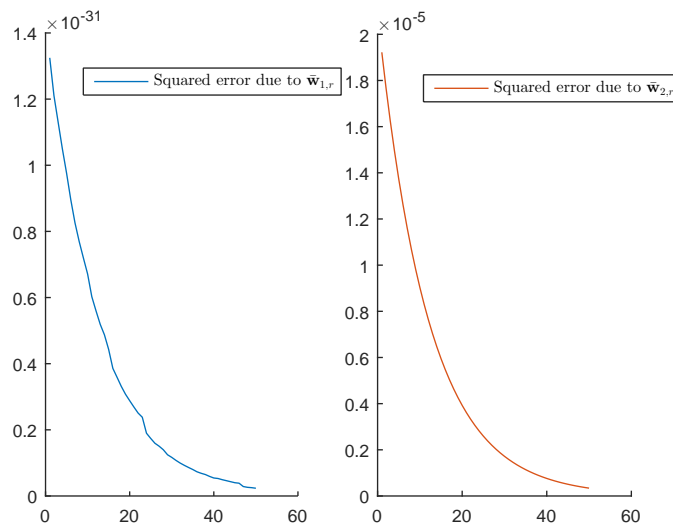
Figure 10.30: Squared error vs. number of iterations of the beamformers $\bar{\mathbf{w}}_{1,r}$ and $\bar{\mathbf{w}}_{2,r}$, depicted in Fig. 10.29, generated using the recursive version of the proposed Method 1 for $\alpha = 0.1$ for the case **without** the first derivative null constraint.

10.5 Example of the Proposed Method 2 for Sidelobe Phase Modulation

In this section we repeat the data of the example of Section 10.4 and we apply the Method 2, described in Section 9.3, for generating the beamformers that embed the DBPSK modulation. The power patterns of the beamformers generated using Method 2, $\mathbf{w}_{1,e}$ and $\mathbf{w}_{2,e}$, are depicted in Fig. 10.31 for $N_e = 5$, which is the number of eigenvalues that sum up 95% of the trace of $\mathbf{Q}$. Note
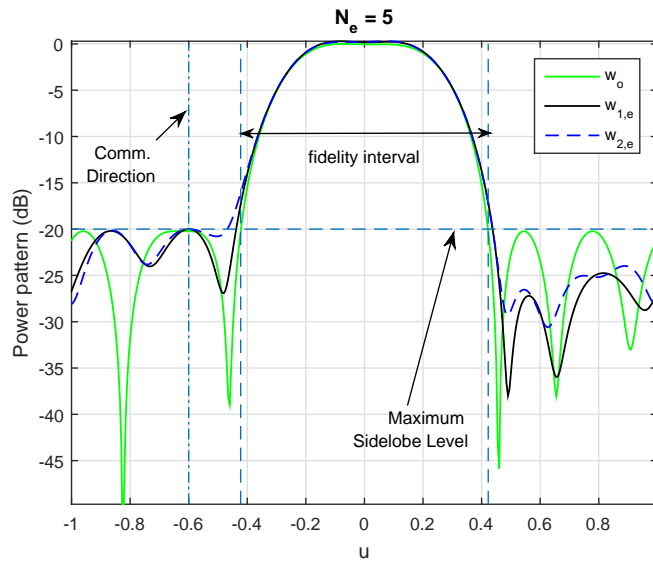
Figure 10.31: Power pattern of beamformers $\mathbf{w}_{1,e}$ and $\mathbf{w}_{2,e}$ that embed a binary DPSK constellation towards $u_c = -0.6$ generated using the proposed Method 2 for $N_e = 5$.
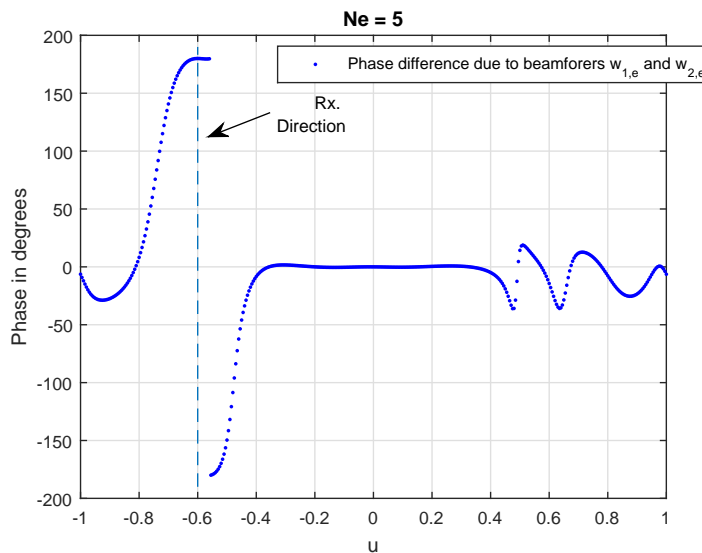
Figure 10.32: Phase difference of the beamformer pair of Fig. 10.31 $\left(\mathbf{w}_{2,e}, \mathbf{w}_{1,e}\right)$ in the u-space.

that as long as the mainbeam sector and the array remain the same, the number of eigenvalues that sum up 95% of the trace of $\mathbf{Q}$ is the same.

Fig. 10.32 shows the phase difference of the beamformer pair of Fig. 10.31 $\left(\mathbf{w}_{2,e}, \mathbf{w}_{1,e}\right)$ in the u-space. We can note that towards $u_c = -0.6$ the phase difference between $\mathbf{w}_2$ and $\mathbf{w}_1$ is, as expected, of 180°.

We can note from observing Figs. 10.31 and 10.32 that around $u = -0.6$ the beampatterns generate a small plateau at their specific communication constraints which keeps the phase difference stable within this plateau.
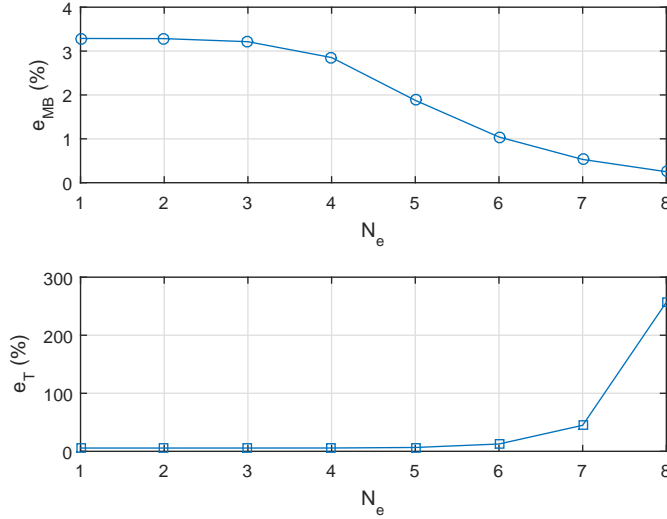
Figure 10.33: Mainbeam and total rms error vs. N_e due to beamformers $\mathbf{w}_{1,e}(N_e)$ and $\mathbf{w}_{2,e}(N_e)$ depicted in Fig. 10.31.

Fig. 10.33 illustrates the behavior of the normalized rms error of the mainbeam vs. N_e and the total normalized rms error vs. N_e due to beamformers $\mathbf{w}_{1,e}$ and $\mathbf{w}_{2,e}$.

The behavior of the curves of $e_{\mathrm{MB}}(N_e)$ and $e_{\mathrm{T}}(N_e)$ seen in Fig. 10.33 is as expected. We can compare N_e of Method 2 to α of Method 1. Similarly to α, as N_e increases, the total error in the mainbeam decreases, and as we force the beamformer to fit tightly the mainbeam, the sidelobes get more erroneous, increasing the total error.

Comparing the power patterns generated using Methods 1 and 2 in Figs. 10.20 and 10.31 respectively, we can note that they are very similar. The mainbeam and total errors for Method 1 and $\alpha = 0.6$ are of $e_{MB}(\alpha = 0.6) = 1.86\%$ and $e_T(\alpha = 0.6) = 6.09\%$ respectively, while for the Method 2 with $N_e = 5$ they are of $e_{MB}(N_e = 5) = 1.88\%$ and $e_T(N_e = 5) = 6.63\%$ respectively. The difference between the two methods is very small.

(a) Method 2 without the Derivative Constraint

Fig. 10.34 depicts the same example of Fig. 10.31 for the case **without** the first derivative null constraint and $N_e = 5$. The beamformers generated using the proposed Method 2 without the first derivative null constraint are denoted here by $\bar{\mathbf{w}}_{1,e}$ and $\bar{\mathbf{w}}_{2,e}$. We can notice that the original power pattern is matched exactly by the beamforming vector $\bar{\mathbf{w}}_{1,e}$, but beamforming weighting vector $\bar{\mathbf{w}}_{2,e}$ generated a small hump around $u = -0.5$ over the maximum permitted sidelobe level. Therefore we reduced the number of null eigenvectors to 3, $N_e = 3$, in order to reduce this hump. The power patterns
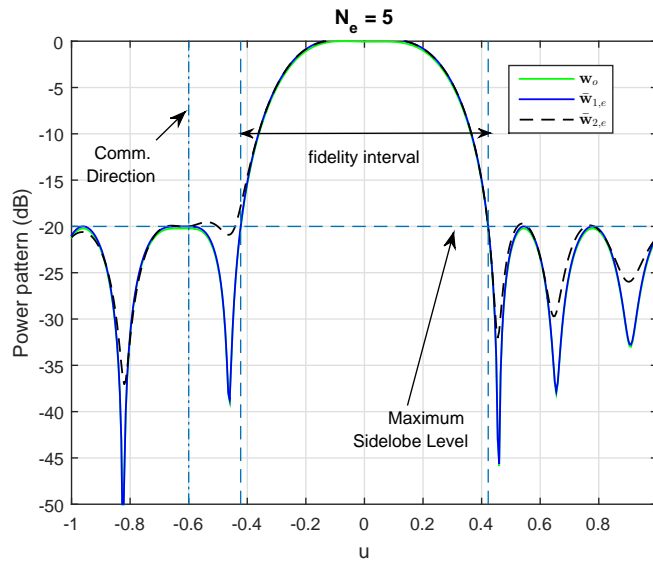
Figure 10.34: Beamformers, $\bar{\mathbf{w}}_{1,e}$ and $\bar{\mathbf{w}}_{2,e}$, that embed a binary DPSK constellation towards $u_c = -0.6$ using the proposed Method 2 for $N_e = 5$ **without** the first derivative null constraint.
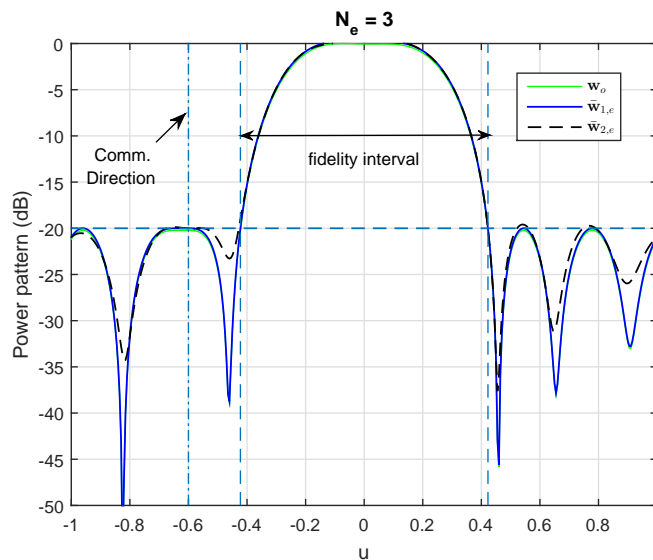
Figure 10.35: Beamformers, $\bar{\mathbf{w}}_{1,e}$ and $\bar{\mathbf{w}}_{2,e}$, that embed a binary DPSK constellation towards $u_c = -0.6$ using the proposed Method 2 for $N_e = 3$ **without** the first derivative null constraint.

using $N_e = 3$ are depicted in Fig. 10.35. Using $N_e = 3$, the beampatterns generated using Method 2 without the derivative constraint are very similar to the beampatterns obtained using Method 1 without the derivative constraint and $\alpha = 0.1$ and the beampatterns from the Villanova Center, [4], depicted in Fig. 10.18.

Fig. 10.36 shows the phase difference of the beamformer pair of Fig. 10.35 ($\bar{\mathbf{w}}_{2,e}, \bar{\mathbf{w}}_{1,e}$) in the u-space. We can note that towards $u_c = -0.6$ the phase difference between $\bar{\mathbf{w}}_{2,e}$ and $\bar{\mathbf{w}}_{1,e}$ is, as expected, of 180°.
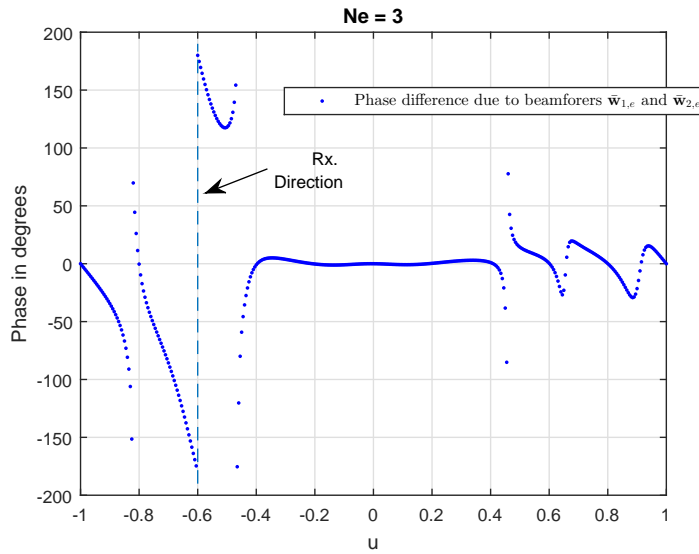
Figure 10.36: Phase difference of the beamformer pair of Fig. 10.35 ($\mathbf{w}_2,\mathbf{w}_1$) in the u-space.
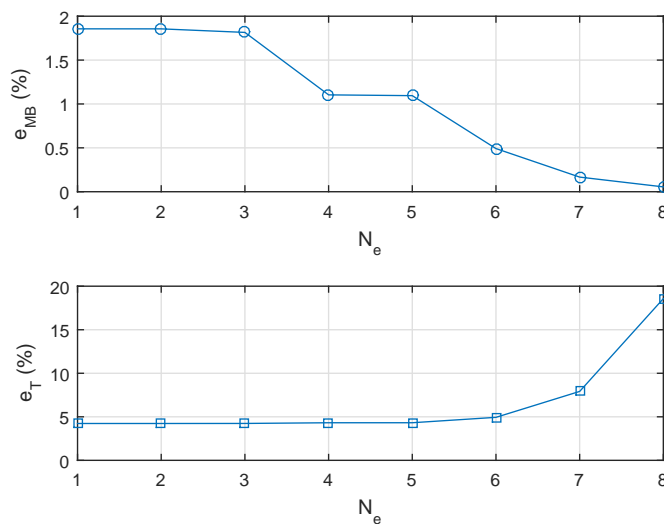
Figure 10.37: Mainbeam and total rms error vs. N_e for the case **without** the first derivative null constraint due to beamformers $\bar{\mathbf{w}}_{1,e}(N_e)$ and $\bar{\mathbf{w}}_{2,e}(N_e)$ depicted in Fig. 10.35.

Fig. 10.37 illustrates the behavior of the normalized rms error of the mainbeam vs. N_e and the total normalized rms error vs. N_e for the case **without** the first derivative null constraint due to beamformers $\bar{\mathbf{w}}_{1,e}$ and $\bar{\mathbf{w}}_{2,e}$.

Comparing the power patterns for the case **without** the first derivative null constraint generated using Methods 1 and 2 in Figs. 10.26 and 10.35 respectively, we can note that they differ minimally visually. The mainbeam and total errors for Method 1 and $\alpha = 0.1$ are of $e_{MB}(\alpha = 0.1) = 1.44\%$ and $e_T(\alpha = 0.1) = 4.25\%$ respectively, while for the Method 2 with $N_e = 3$ they are
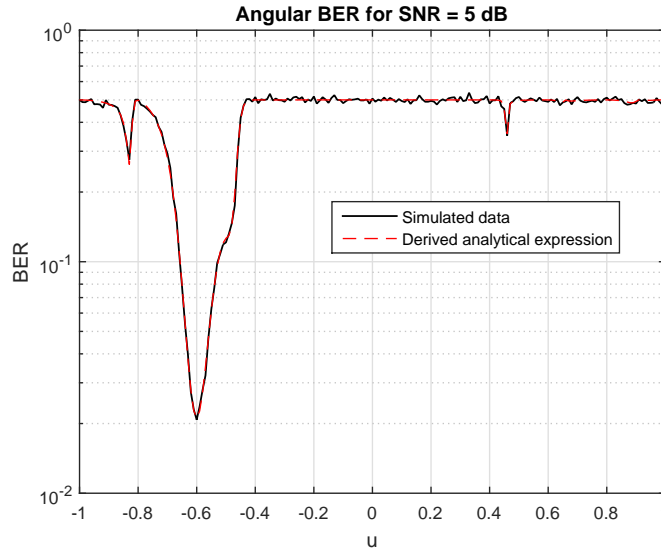
Figure 10.38: Analytical and simulated BER $\times$ u, for embedded DBPSK modulation at $u_c = -0.6$, for the proposed Method 1 without the derivative constraint for SNR = 5 dB.

of $e_{MB}(N_e = 3) = 1.82\%$ and $e_T(N_e = 3) = 4.22\%$ respectively. The difference between the two methods is indeed very small.

10.6 Robustness Analysis for the Proposed Sidelobe Phase Modulation Methods

In this section we will use the derived analytical expression for the DBPSK modulation when two arbitrary symbols are transmitted. We present Fig. 10.38 in order to attest that the derived expression in equation (9.91) is in agreement with the simulated data. Fig. 10.38 depicts the simulated and the analytical angular BER for the proposed DBPSK signaling strategy using the beamformers $\bar{\mathbf{w}}_1$ and $\bar{\mathbf{w}}_2$ of Fig. 10.26 for a SNR of 5 dB. We can note from Fig. 10.38 that the analytical expression is indeed in agreement with the simulated data, therefore we will use only the analytical expression for our proposed methods from now on.

Fig. 10.39 depicts the angular BER (more precisely the BER in u-space plane) of the proposed Method 1, with and without the derivative null constraint ($\alpha = 0.6$ and $\alpha = 0.1$ respectively), and the method of [4]. As the results of Method 1 and its recursive version are the same, assuming that convergence is achieved, we will depict only the results for Method 1 in its closed form. Fig. 10.40 depicts the angular BER of the proposed Method 2, with and without the derivative null constraint ($N_e = 5$ and $N_e = 3$ respectively), and the method of [4].

We can confirm by looking at Figs. 10.39 and 10.40 that the results of
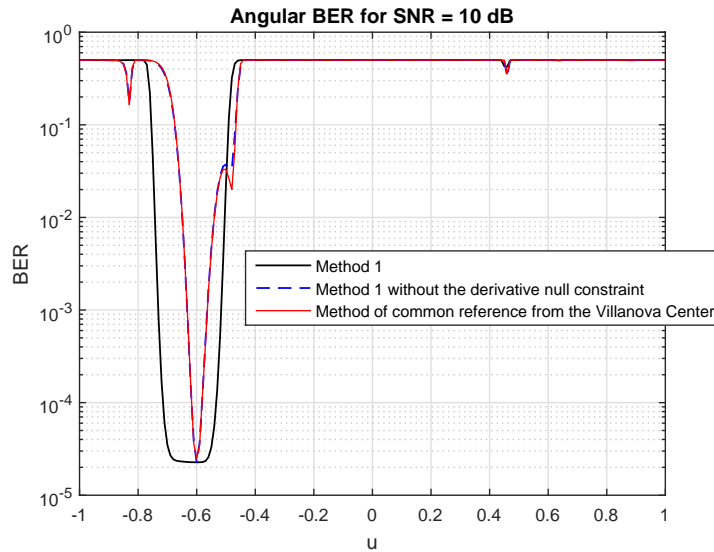
Figure 10.39: BER $\times$ u, for embedded DBPSK modulation at $u_c = -0.6$, for the proposed Method 1 with and without the derivative constraint and the method of [4] for SNR = 10 dB.
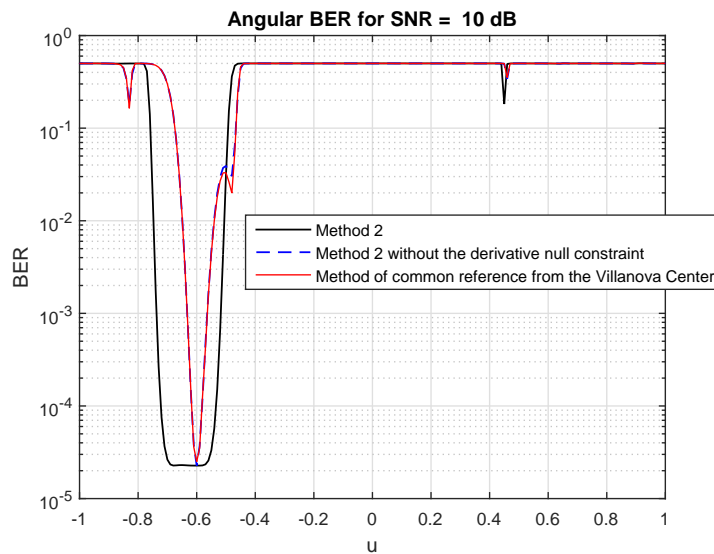
Figure 10.40: BER $\times$ u, for embedded DBPSK modulation at $u_c = -0.6$, for the proposed Method 2 with and without the derivative constraint and the method of [4] for SNR = 10 dB.

the proposed methods **without** the derivative null constraint and the method of [4] are very similar. The angular BER curve falls rapidly with a very narrow pit to the operational BER at the direction of the communication receiver. On the other hand, the outcome of the proposed methods with first derivative null constraint is a flat operational BER over a small region. This property makes the proposed techniques robust to small deviation errors on the preassigned direction, which is fundamental for the communication system
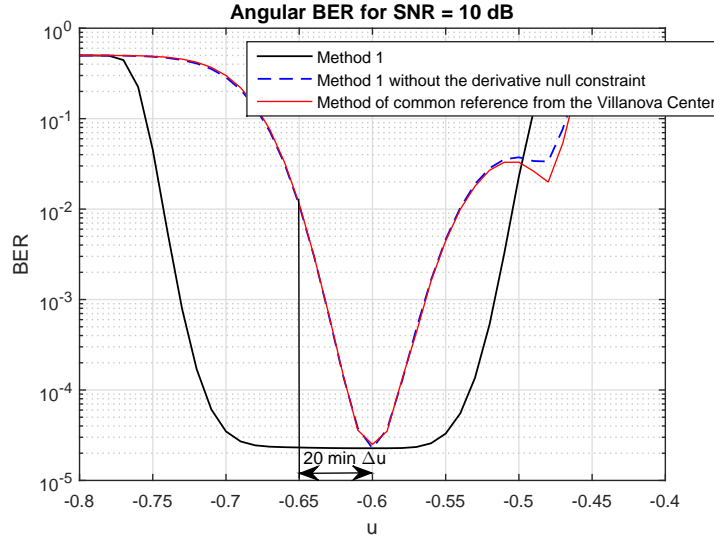
Figure 10.41: Zoom of the BER $\times$ u, for embedded DBPSK modulation at $u_c = -0.6$, for the proposed Method 1 with and without the derivative constraint and the method of [4] for SNR = 10 dB.

service, since unintentional small deviation errors in the relative positioning of the communication receiver and the radar is likely to happen.

Fig. 10.41 assumes the same data as the example in 10.3. Checking the angular BER in Fig. 10.39 we can see that the BER of the method of the Villanova Center would go from 2.5×10^{-5} to 0.01 in only 20 minutes. The BER of the proposed method, on the other side, goes from 2.5×10^{-5} to 2.31×10^{-5} in 20 minutes, which is a negligible performance degradation.

This BER dynamic is illustrated in a zoom of Fig. 10.39, Fig. 10.41.

10.7 Computational Complexity

Fig. 10.42 depicts a comparison of the total number of complex products and additions for the proposed Method 1, the recursive version of Method 1 and Method 2, given α and given N_e, according to Tables 9.1, 9.2 and 9.3 respectively.

The procedure of choosing N_e described in (9.73) has computational complexity of $N_e - 1 + M - 1$ complex additions and 1 complex product. On the other hand, in order to determine a good choice of α, one should discretise the α domain, which is the interval [0,1) into D samples and compute the total error for all the D possible beamforming filters. This procedure has computational complexity in the order of $O(DM^3)$. Though it seems high, there are efficient manners of computing a value of α which meets the error at the mainbeam requirement. Beside this, we have noticed that the error at the mainbeam is not the only important factor for choosing neither N_e nor α. It is important
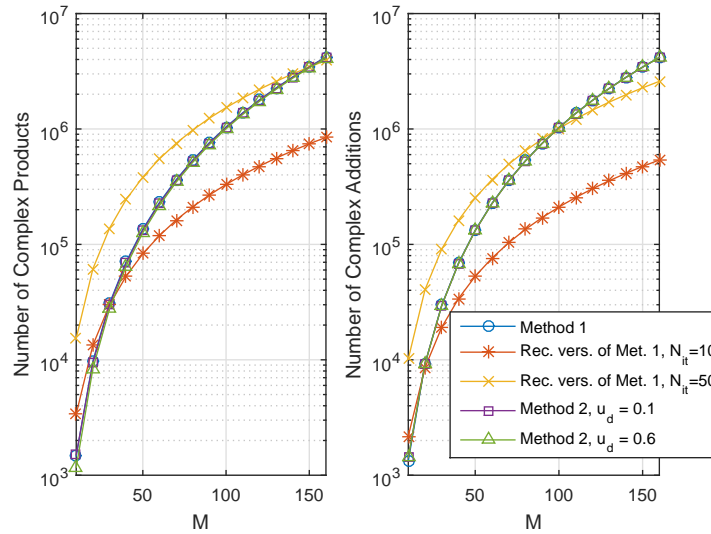
Figure 10.42: Comparison of the number of complex products and additions necessary for Method 1, recursive version of Method 1 and Method 2, given α and N_e.

to attest if the sidelobes are bellow the permitted level. Therefore, we won't consider the preprocessing step of choosing α nor N_e.

For Method 1 and its recursive version, the value of α doesn't change the number of operations, once it is chosen. On the other hand, the number of operations is dependent on N_e for Method 2. Therefore, for Method 2, we consider two different fidelity sectors, a wide one, of $u_d = 0.6$ and a narrow one of $u_d = 0.1$. We present two different fidelity sectors because the number of eigenvalues that sum up 95% of the trace of $\mathbf{Q}$ are different. Therefore, these two cases illustrate extreme cases. We used N_e as the number of eigenvalues that sum up 95% of the trace of $\mathbf{Q}$ for all different array sizes for both fidelity sectors. The values of N_e can be assessed from Fig. 9.7. For the recursive version of Method 1 we have considered two different number of iterations, $N_{it} = 10$ and $N_{it} = 50$, that is because the observed initial squared error is already very small. A metric based on the radar performance would be more appropriate for setting this value though.

We can see from Fig. 10.42 that the computational complexity of Methods 1 and 2, for both extreme cases of fidelity sector, given α and N_e, respectively, are very similar. The number of complex operations of the recursive version of Method 1 may be lower or higher depending on the number of iterations.

10.8 Clutter Analysis

A controversial topic within sidelobe modulation is the effect of sidelobe modulation in clutter mitigation techniques. It is said that sidelobe modulation

would cause Doppler spread, interfering in clutter mitigation methods. In this section we use the clutter expression normally used in clutter simulations derived in Section 3.2 and we extend it to the case where sidelobe modulation is used. Then we examine one clutter mitigation technique, namely, the space-time MVDR filter, and present simulation results for a few examples.

As explained in Section 3.2, the continuous field of clutter can be approximated by the superposition of a large number, N_c, of independent clutter sources that are uniformly distributed in azimuth about the radar. The location of the l, p-th clutter patch is described by its azimuth, ϕ_p, and range, R_l, (or elevation, θ_l). The corresponding spatial frequency is $\vartheta_{l,p} = \frac{d}{\lambda}\cos(\theta_l)\sin(\phi_p)$ [1].

The clutter amplitudes, $\alpha_{l,p}$, satisfy $\mathrm{E}\left[|\alpha_{l,p}|^2\right] = \sigma_n^2 \xi_{l,p}$, where σ_n^2 is the noise power per element and $\xi_{l,p}$ is the clutter to noise ratio (CNR). The CNR due to the l, p-th clutter patch can be obtained directly from the radar equation:

$$\xi_{l,p} = \frac{G_r G_t \lambda_c^2 |\bar{B}(\vartheta_{l,p})|^2 P_t \sigma_{l,p}}{(4\pi)^3 \sigma_n^2 L_s R_l^4}, \tag{10.8}$$

where G_t is the transmitter gain, G_r is the receiver gain, λ_c is the carrier frequency, P_t is the isotropically irradiated transmitted power, $\sigma_{l,p}$ is the (l, p)-th clutter patch cross section, R_l is the range of the (l, p)-th clutter patch, L_s is the system loss and $P_{l,p}$ is the power transmitted towards the l, p-th clutter patch which is dependent on its spatial frequency and $\bar{B}(\vartheta_{l,p})$ is the normalized beampattern towards $\vartheta_{l,p}$,

$$\bar{B}(\vartheta_{l,p}) = \frac{B(\vartheta_{l,p})}{B(\vartheta_{\max})}, \tag{10.9}$$

where $B(\vartheta_{\max})$ is the beampattern towards the direction of maximum.

In the case of SLL modulation, the transmit beamformer vector is chosen from a set of K possible beamformers at each pulse according to the communication symbols to be transmitted, which have uniform a priori probability distribution. It means that the amplitude $\alpha_{l,p}$ is a discrete random variable. Thus, for the case of sidelobe modulation the clutter to noise ratio relative to the (l, p)-th clutter patch is given by

$$\xi_{l,p} = \frac{G_r G_t \lambda_c^2 P_t \sigma_{l,p}}{K(4\pi)^3 \sigma_n^2 L_s R_l^4} \sum_{k=1}^{K} |\bar{B}_k(\vartheta_{l,p})|^2. \tag{10.10}$$

Assuming that returns from different clutter patches are uncorrelated,

$$\mathrm{E}\left\{\alpha_{l,p} \alpha_{i,j}^*\right\} = \sigma_n^2 \xi_{l,p} \delta_{l-i} \delta_{p-j}, \tag{10.11}$$

and assuming unambiguous range, i.e. only range R_l is contributing to the clutter, the clutter space-time covariance matrix defined in (3.51) is given by

[1]

$$\mathbf{R}_c = \mathrm{E}\left[\mathbf{c}[l]\mathbf{c}^H[l]\right] = \sigma_n^2 \sum_{p=1}^{N_c} \xi_{l,p}\mathbf{v}(\vartheta_{l,p}, f_{l,p})\mathbf{v}^H(\vartheta_{l,p}, f_{l,p}), \qquad (10.12)$$

where $\mathbf{v}(\vartheta_{l,p}, f_{l,p})$ is the space-time steering vector of the (l,p)-th clutter patch defined in (3.50).

We can note from (10.10) and (10.12) that the only difference in the clutter covariance matrix, R_c, when using sidelobe modulation, is that the clutter to noise ratio is, in fact, computed using the mean value of the various transmit beampatterns used. Therefore, if the clutter covariance matrix can be well estimated, we don't expect to have any degradation in clutter mitigation techniques that use the inverse of the covariance matrix, like the space-time MVDR method for example.

In order to illustrate this theoretical result, we will show some simulation results. In this analysis we consider that the radar platform is not moving relative to the clutter, $v_a = 0$ m/s, i.e, the clutter ridge, β is zero, so that the clutter is spread only in spatial frequency and not in the Doppler domain. We use this assumption because as the platform moves, the angular position of the communication receiver also varies. So, in order to assess realistic results, one should have to model the variation of the relative communication receiver direction with respect to the platform movement and change the beamformers consequently. This is dependent on the type of radar, as airborne radars are different from landbased radars for example.

In our simulations, we have used the beamformers of Fig. 10.2, repeated here in Fig. 10.43 with the addition of the mean beampattern. We adapted the coordinate system of the spatial frequency, ϑ, defined in Fig. 3.2 to be in agreement with the coordinate system adopted for the generation of the beamformers, therefore

$$\vartheta_{l,p} = \frac{d}{\lambda_c}\cos(\theta_l)\cos(\phi_p), \qquad (10.13)$$

where the array geometry and ϕ are as depicted in Fig. 2.4.

We simulated a radar with $K = 10$ elements displaced in a ULA separated by half of the carrier wavelength, which transmits $J = 18$ pulses per CPI with a pulse repetition frequency (PRF) of 300 Hz and operating frequency of $f_c = 450$ MHz. We modeled a ring of ground clutter distant 130 km from the radar using $N_c = 360$ clutter patches uniformly distributed in azimuth with a clutter cross section of $\sigma_{l,p} = 2.95 \times 10^3\ m^2$. The transmitter has a transmission power of $P_t = 200$ kW, gain of $G_t = 22$ dBi and the receiver has a receiver gain of $G_r = 10$ dBi, the system losses are of $L_s = 4$ dB and the noise power is of $\sigma_n^2 = 3 \times 10^{-14}$ W.
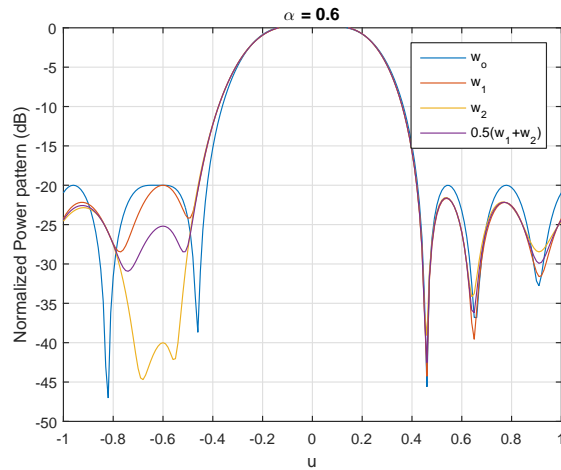
Figure 10.43: Beampatterns adopted for clutter analysis simulation.
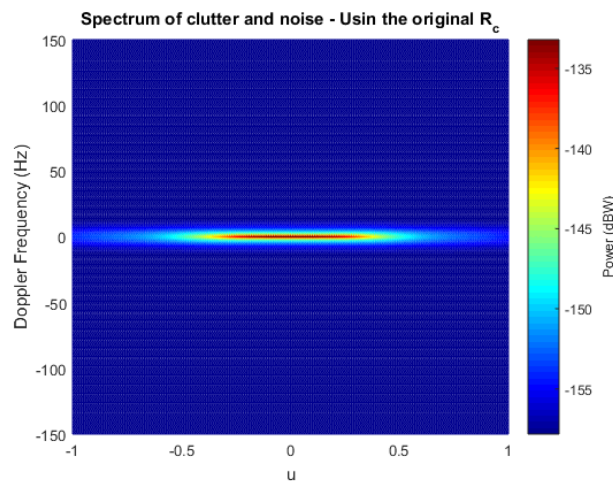
Figure 10.44: Original Capon spectrum of the clutter plus noise environment.

Fig. 10.44 depicts the Capon spectrum of the simulated scenario using the clutter covariance matrix generated using only the original beampattern depicted in blue ($\mathbf{w}_o$) in Fig. 10.43.

Fig. 10.45 depicts the Capon spectrum of the simulated scenario using the mean clutter covariance matrix according to the beampatterns depicted in Fig. 10.43 used for sidelobe modulation.

Fig. 10.46 depicts the cut of the Capon spectrum depicted in Figs 10.45 and 10.44 for $u = -0.6$, which is the direction of the communication receiver, where we expect the largest variation between the original beampattern and the mean beampattern.

Fig. 10.47 depicts the cut of the Capon spectrum depicted in Figs 10.45 and 10.44 for a fixed Doppler frequency of $f_D = 0$ Hz, which is the Doppler of the main clutter (where the clutter is more intense).

We can note from Figs. 10.44, 10.45, 10.46 and 10.47 that the phe-
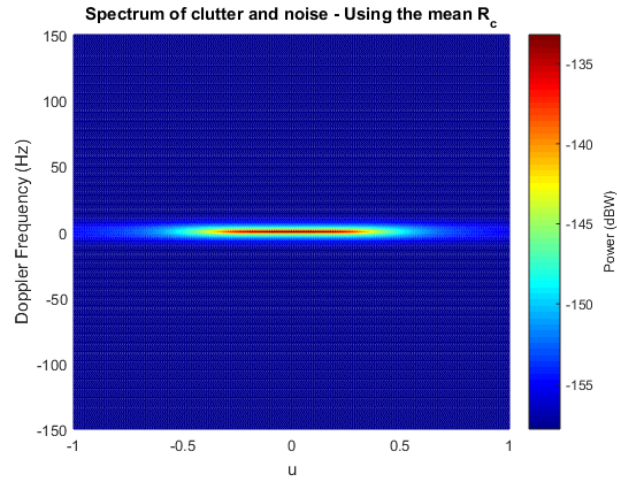
Figure 10.45: Capon spectrum of the clutter plus noise environment using sidelobe modulation.
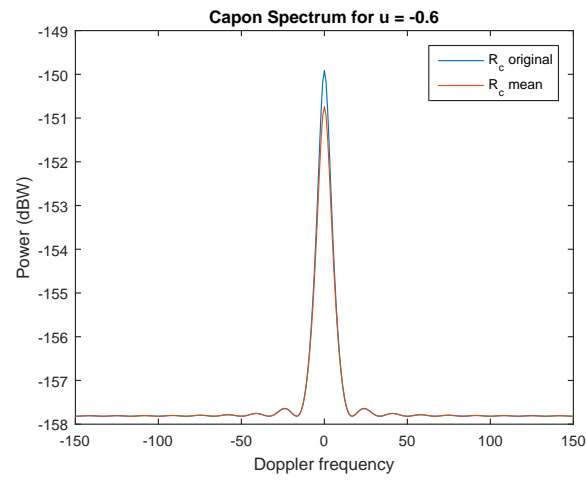
Figure 10.46: Cut of the Capon spectrum depicted in Figs 10.45 and 10.44 for $u = -0.6$.

nomenon of Doppler spread using the space-time MVDR filter is absent. The sidelobe modulation does not cause any degradation to the space-time MVDR filter.
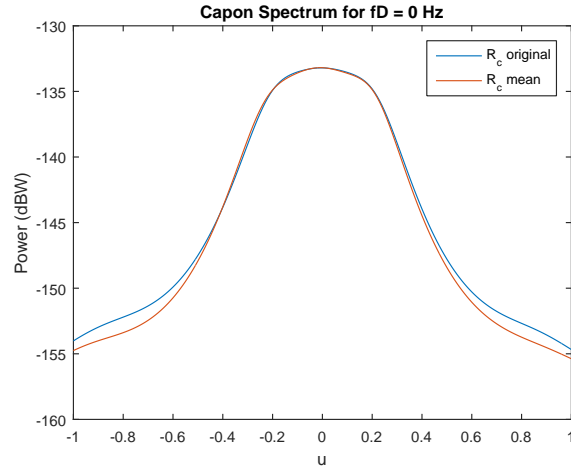
Figure 10.47: Cut of the Capon spectrum depicted in Figs 10.45 and 10.44 for $f_D = 0$ Hz.

10.9 Conclusion

We have proposed a different formulation of the dual-function radar-communications problem. This original formulation allowed us to develop new radar-embedded sidelobe modulation methods that have closed form expressions and are applicable to both amplitude and phase sidelobe modulation.

Our design uses a constrained optimization problem for generating transmit beampatterns, that match satisfactorily a given transmit profile (with high fidelity adjustment at the mainlobe), where each beampattern embeds a different symbol towards the communication receiver direction. In this thesis, we have also proposed an alternative way of dealing with the mainlobe adjustment requirement. The alternative proposed method is based on eigenvalue and point constraints.

Studying the DFRC topic, we have realized that the DFRC methods based in varying the transmit beampattern parameters in specific directions may provide operational bit error rates only towards that directions, what is interesting for secure communications purposes. This advantage, though, becomes a major disadvantage if the real receiver position doesn't match exactly the predefined one. This situation can easily arise if the communication receiver is moving relative to the radar. The methods proposed in the literature so far haven't addressed this important issue.

Therefore, we have proposed a modification of our problem formulation by adding a derivative null constraint. The proposed methods considering the derivative null constraint still have closed form expressions. The new constraint copes with this problem in a simple and yet effective manner. The derivative null constraint imposes the beampattern to sustain the symbol's complex

value over a small angular region, making the communication robust against small angular deviations. The addition of this other constraint does't lead to significant increase of the computational complexity and solves an important problem of the DFRC system.

In this thesis, we have also considered the important topic of adaptation in real-time applications when the communication receiver is moving relative to the radar. When we are dealing with dynamic scenarios, it is not feasible to keep solving, in real time, sophisticated optimization problems, or even convex problems by interior point techniques (as proposed in the DFRC literature so far). Therefore, we simplified our two proposed methods and derived low-complexity expressions for updating the beampatterns for following a moving communication receiver platform. The derivative null constraint itself already provides some flexibility in terms of update time, since the communication service is not so rapidly degraded with the movement. Thus, our proposed methods are well suited for online real-time processing.

We could also note that our simple, closed form solutions generates practically the same beampatterns, for both amplitude and phase modulation, as the methods of [5] and [4], which use interior point technique for computing the solutions to their problem formulation. The advantages of our proposed methods are that they have low-complexity closed form expressions which can be updated for following a moving communication platform with minimum computational burden. These advantages by their own are enough for preferring our proposed methods. But we go even further and face the robustness issue!

Referring to phase modulation, we proposed a new non-coherent signalling strategy within the DFRC context. In the literature so far, we can only find non-coherent phase modulation based on the simultaneous transmission of the symbol and the phase reference (multi-waveform Differential PSK-based methods). These methods require more sophisticated technology than the necessary to change only the transmit beampattern of only one array of sensors. To cope with this issue, we proposed a signaling strategy that is suitable for simpler radars, that have only one transmit array. We have also derived the analytical bit error rate expression for the proposed phase modulation signalling strategy when two arbitrary symbols are transmitted.

11
Conclusion

In this thesis, we presented our accomplished work in two main topics: reduced-rank beamforming and space-time processing and radar-embedded communications. This chapter summarizes our results and highlights possibilities of research directions.

Our work in rank reduced array signal processing produced interesting contributions. We have explored the application of the JIDS in two different areas: beamforming and space-time radar processing. The JIDS has never been tested within these contexts before and showed impressive results! By exploring the specificities of the beamforming environment, we were able to propose simplifications that led to a significant computational complexity reduction. A further work could be the investigation of the specificities of the space-time environment to see if it is possible to come up with simplifications for this application as well. There are still many open questions relative to the JIDS, like, for example, how to set the decimation factor F for a good tradeoff between complexity and performance and theoretical performance bounds as well.

Our work in the topic of DFRC sidelobe modulation has led to many contributions to the field. Those contributions are explained in Section 10.9. We summarize them here focusing on further researches possibilities:

– We have proposed two original robust radar-embedded sidelobe phase/amplitude modulation methods which have simple closed form equations.

– To the best of our knowledge, the need for robustness was not noticed by any other researcher in the field. We have not only alerted about this necessity as we have also proposed a simple and effective way of turning our methods robust against small angular errors in the relative position between the radar and the communication receiver.

– To the best of our knowledge, concerning the need of dealing with real-time issues, our work is the only one in the field that, besides pointing the potential dynamic characteristic of the DFRC application, effectively proposes a practical way for dealing with it. As our methods have

low-computational complexity closed form equations, we were able to derive practical update equations for pursuing a moving communication platform.

– We have also proposed a simple signalling strategy for sidelobe phase modulation and derived an analytical BER expression for it when two arbitrary symbols are transmitted, which is a common situation within the DFRC context.

– We have also started to work with the proposed recursive version of one of our proposed methods and we have noticed the potential of the stop criterium. A future work could be the investigation of a stop criterium that is directly related to the radar operation. A first action could be keeping the sidelobes bellow the maximum permitted level and also minimizing the mainbeam error. The feasibility of this suboptimal (in the mean squared sense) solution is an interesting topic, as it depends on the initial starting point.

– Another issue that offers a vast field of investigation is the analysis of the effects of sidelobe modulation in clutter mitigation techniques. We have presented the simple case where there is no relative movement and the clutter mitigation technique is the space-time MVDR filter. We have used the true mean covariance matrix in our experiments. Further works would involve the consideration of relative movement, simulations using estimated covariance matrices from different sample supports and also other clutter mitigation techniques such as Doppler filtering for example.

Finally, in this thesis we explained the accomplished studies and we pointed out directions for further researches in the area of array signal processing.

Bibliography

[1] J. Ward, "Space-time adaptive processing," Tech. Rep., MIT Lincoln Laboratory, 1994. (document), 3.2, 3.2, 3.3, 3.2, 3.2, 3.2, 3.3.2, 3.3.4, 4, 4, 6.3, 6.3, 6.3, 10.8, 10.8

[2] A. Hassanien, M. G. Amin, Y. D. Zhang, and F. Ahmad, "Dual-function radar-communications: Information embedding using sidelobe control and waveform diversity," *IEEE Transactions on Signal Processing*, vol. 64, no. 8, pp. 2168–2181, April 2016. (document), 7, 8.1, 8.1, 8.12

[3] A. Hassanien, M. G. Amin, Y. D. Zhang, and F. Ahmad, "Dual-function radar-communications using phase-rotational invariance," in *2015 23rd European Signal Processing Conference (EUSIPCO)*, Aug 2015, pp. 1346–1350. (document), 7, 8.2, 8.2.1, 8.13, 8.2.1, 8.2.1, 8.2.1, 8.25, 8.2.2, 8.2.2, 9.1

[4] A. Hassanien, M. G. Amin, Y. D. Zhang, F. Ahmad, and B. Himed, "Non-coherent PSK-based dual-function radar-communication systems," in *2016 IEEE Radar Conference*, May 2016, pp. 1–6. (document), 7, 8.2, 8.2.2, 8.2.2, 8.2.2, 8.26, 8.2.2, 8.2.2, 8.28, 8.2.2, 8.2.2, 9.1, 10.18, 10.4, 10.4, 10.4.2, 10.5.1, 10.6, 10.39, 10.40, 10.6, 10.41, 10.9

[5] A. Hassanien, M.G. Amin, Y.D. Zhang, and F. Ahmad, "A dual function radar-communications system using sidelobe control and waveform diversity," in *2015 IEEE Radar Conference*, May 2015, pp. 1260–1263. (document), 7, 8.1, 8.1, 8.1.2, 10.1, 10.1, 10.1.2, 10.2.1, 10.3, 10.15, 10.16, 10.3, 10.17, 10.9

[6] A. de Oliveira, R. Sampaio-Neto, J. M. Fortes, and F. Backx, "Interpolation-and-decimation-based dimensionality reduction applied to space-time processing," in *2016 IEEE Sensor Array and Multichannel Signal Processing Workshop*, July 2016, pp. 1–5. 1, 6

[7] A. de Oliveira, R. Sampaio-Neto, and J. M. Fortes, "Robust radar-embedded sidelobe level modulation using constrained optimization design," in *2016 IEEE Radar Conference*, May 2016. 1, 7, 9

[8] A. de Oliveira, R. Sampaio-Neto, and J. M. Fortes, "Low-Complexity robust Radar-Embedded sidelobe level modulation using linear constrained optimization design," in *2016 IEEE Sensor Array and Multichannel Signal Processing Workshop*, Rio de Janeiro, Brazil, July 2016. 1, 7, 9

[9] B. P. Lathi, *Modern Digital and Analog Communicatino Systems*, Oxford University Press, third edition, 1998. 2.1, 9.4, 9.4.2, 9.4.2

[10] H. L. VanTrees, *Optimum Array Processing*, 2002. 2.2, 4, 5, 5.1, 5.1, 9.2, 9.2, 9.3.1, 9.3.1

[11] W.L. Melvin, "A stap overview," *IEEE Aerospace and Electronic Systems Magazine*, vol. 19, no. 1, pp. 19–35, Jan 2004. 3, 3.2

[12] M. A. Richards, *Fundamentals of Radar Signal Processing*, McGraw Hill Education, second edition, 2014. 3.1, 3.2, 3.2, 3.2, 3.3.4, 4, 6.3, 7.1

[13] J. S. Goldstein and I. S. Reed, "Theory of partially adaptive radar," *IEEE Transactions on Aerospace and Electronic Systems*, vol. 33, no. 4, pp. 1309–1325, April 1997. 3.2, 4, 5, 5.4, 6.3

[14] L.E. Brennan and I.S. Reed, "Theory of adaptive radar," *IEEE Transactions on Aerospace and Electronic Systems*, vol. AES-9, no. 2, pp. 237–252, March 1973. 3.2, 3.2

[15] J. Capon, "High resolution frequency-wavenumber spectrum analysis," *Procedings of IEEE*, vol. 57, pp. 1408–1418, 1969. 3.3.1

[16] A. Papoulis and S. U. Pillai, *Probability, Random Variables and Stochastic Processes*, McGraw-Hill, New York, 4th ed. edition, 2001. 3.3.4, 3.3.4, 3.3.5

[17] E.J. Kelly, "An adaptive detection algorithm," *IEEE Transactions on Aerospace and Electronic Systems*, vol. AES-22, no. 2, pp. 115–127, March 1986. 3.3.5

[18] M. Rangaswamy, "An overview of space-time adaptive processing for radar," in *2003 IEEE Radar Conference*, Sept 2003, pp. 45–50. 4, 4

[19] O. L. Frost III, "An algorithm for linearly constrained adaptive array processing," *Proceedings of the IEEE*, vol. 60, no. 18, pp. 926–935, August 1972. 4, 5, 9.2.2, 9.2.2

[20] J. A. Apolinário Jr., M. L. R. de Campos, and C. P. Bernal O, "The constrained conjugate gradient algorithm," *IEEE Signal Processing Letters*, vol. 7, no. 12, pp. 351–354, Dec 2000. 4

[21] H. Hotelling, *Analysis of a Complex of Statistical Variables into Principal Components*, Baltimore, MD: Warwick and York, 1933. 4, 5, 5.4, 6.3

[22] A. Haimovich, "The eigencanceler: adaptive radar by eigenanalysis methods," *IEEE Transactions on Aerospace and Electronic Systems*, vol. 32, no. 2, pp. 532–542, Apr. 1996. 4, 5

[23] C. Lanczos, "Solution of systems of linear equations by minimized iterations," *Journal of Research of the National Bureau of Standards*, vol. 49, no. 1, pp. 33–53, Jul 1952. 4

[24] M. Joham and M. D. Zoltowski, "Interpretation of the multistage nested wiener filter in the Krylov subspace framework," Technical Report TR-ECE-00-51/TUM-LNS-TR-00-6, Purdue University/Munich University of Technology, [Online]. Available: http://cobweb.ecn.purdue.edu/ mikedz/research/msnwf tutorial.pdf, 2000. 4

[25] G. H. Golub and C. F. Van Loan, *Matrix Computations*, The Johns Hopkins Univ. Press, second edition, 1984. 4, 5.3.4

[26] W. E. Arnoldi, "The principle of minimized iterations in the solution of the matrix eigenvalue problem," *Quarterly of Applied Mathematics*, vol. 9, no. 1, pp. 17–29, Jan 1951. 4

[27] J. S. Goldstein, I. S. Reed, and L. L. Scharf, "A multistage representation of the Wiener filter based on orthogonal projections," *IEEE Transactions on Information Theory*, vol. 44, pp. 2943–2959, Nov. 1990. 4, 5, 5.3.4, 5.4, 6.3

[28] M. D. Zoltowski G. Dietl and M. Joham, "Recursive reduced-rank adaptive equalization for wireless communications," *Proceedings of SPIE*, vol. 4395, pp. 16–27, April 2001. 4, 5

[29] D. A. Pados and G. N. Karystinos, "An iterative algorithm for the computation of the mvdr filter," *IEEE Transactions on Signal Processing*, vol. 49, no. 2, pp. 290–300, Feb 2001. 4

[30] B. L. Mathews, L. Mili, and A. I. Zaghloul, "Auxiliary vector selection algorithms for adaptive beamforming," in *2005 IEEE Antennas and Propagation Society International Symposium*, July 2005, vol. 3A, pp. 271–274 vol. 3A. 4

[31] J. S. Goldstein, I. S. Reed, and P. A. Zulch, "Multistage partially adaptive STAP CFAR detection algorithm," *IEEE Transactions on Aerospace and Electronic Systems*, vol. 35, no. 2, pp. 645–661, April 1999. 4

[32] R. C. de Lamare and R. Sampaio-Neto, "Reduced-rank adaptive filtering based on joint iterative optimization of adaptive filters," *IEEE Signal Processing Letters*, vol. 14, no. 12, pp. 980–983, Dec 2007. 4

[33] L. Wang and R. C. de Lamare, "Low-complexity constrained adaptive reduced-rank beamforming algorithms," *IEEE Transactions on Aerospace and Electronic Systems*, vol. 49, no. 4, pp. 2114–2128, OCTOBER 2013. 4

[34] R. E. Crochiere and L. R. Rabiner, *Multirate Digital Signal Processing.*, Englewood Cliffs, NJ: Prentice-Hall, 1983. 4.1

[35] R. C. de Lamare and R. Sampaio-Neto, "Adaptive reduced-rank MMSE filtering with interpolated FIR filters and adaptive interpolators," *IEEE Signal Processing Letters*, vol. 12, no. 3, pp. 177–180, March 2005. 4.1

[36] R. C. de Lamare and R. Sampaio-Neto, "Reduced-rank interference suppression for DS-DCMA based on interpolated FIR filters," *IEEE Communications Letters*, vol. 9, no. 3, pp. 213–215, March 2005. 4.1

[37] R. C. de Lamare and R. Sampaio-Neto, "Adaptive interference suppression for DS-CDMA systems based on interpolated FIR filters with adaptive interpolators in multipath channels," *IEEE Transactions on Vehicular Technology*, vol. 56, no. 2, pp. 2457–2474, September 2007. 4.1

[38] R. C. de Lamare and R. Sampaio-Neto, "Adaptive reduced-rank processing based on joint and iterative interpolation, decimation, and filtering," *IEEE Transactions on Signal Processing*, vol. 57, no. 7, pp. 2503–2514, July 2009. 4.1

[39] A. de Oliveira, "Detecção de sinais em sistema de comunicações de banda ultra-larga," Master thesis, Pontifícia Universidade Católica do Rio de Janeiro, Rio de Janeiro, Brazil, 2010. 4.1, 5.3.2

[40] A. de Oliveira, R. Sampaio-Neto, and C. A. Medina, "Blind detection techniques for IEEE 802.15.4a communication system," in *2012 International Symposium on Wireless Communication Systems (ISWCS)*, Paris, France, August 2012, pp. 1064–1068. 4.1

[41] A. de Oliveira, R. Sampaio-Neto, and C. A. Medina, "Detecção de sinais em sistemas UWB baseados no padrão IEEE 802.15.4a," in *XXIX Simpósio Brasileiro de Telecomunicações*, Curitiba, Brazil, 2011. 4.1

[42] F. A. Sandoval and R. Sampaio-Neto, "Novos receptores com posto reduzido e sua aplicação em sistemas DS-CDMA," in *XXXI Simpósio Brasileiro de Telecomunicações*, Fortaleza, Brazil, 2013. 4.1, 5.3

[43] F. A. Sandoval, "Novos receptores com posto reduzido e suas aplicações em sistemas baseados em DS-CDMA," Master thesis, Pontifícia Universidade Católica do Rio de Janeiro, Rio de Janeiro, Brazil, 2013. 4.1

[44] H. Cox, R. M. Zeeskind, and M. H. Owen, "Robust adaptive beamforming," *IEEE Transactions on Acustics, Speech and Signal Processing*, vol. 35, no. 10, pp. 1365–1376, October 1987. 5, 5.1

[45] M. H. Er and A. Cantoni, "Derivative constraints for broad-band element space antenna array processors," *IEEE Transaction on Acoustics, Speech and Signal Processing*, vol. 31, pp. 1378–1393, December 1983. 5

[46] K. M. Buckley and L. J. Griffiths, "An adaptive generalized sidelobe canceller with derivative constraints," *IEEE Transaction on Antennas and Propagation*, vol. 34, no. 3, pp. 311–319, March 1986. 5

[47] R. Couillet, F. Pascal, and J. W. Silverstein, "A joint robust estimation and random matrix framework with application to array processing," in *2013 IEEE International Conference on Acoustics, Speech and Signal Processing*, May 2013, pp. 6561–6565. 5

[48] D. D. Feldman and L. H. Griffiths, "A projection approach for robust adaptive beamforming," *IEEE transaction on signal processing*, vol. 42, pp. 867–876, April 1994. 5

[49] A. B. Gershman, N. D. Sidiropoulos, S. Shahbazpahahi, M. Bengtsson, and B. Ottersten, "Convex optimization-based beamforming," *IEEE Signal Processing Magazine*, vol. 27, no. 3, pp. 62–75, May 2010. 5.1

[50] S. A. Vorobyov, A. B. Gershman, and Zhi-Quan Luo, "Robust adaptive beamforming using worst-case performance optimization: a solution to the signal mismatch problem," *IEEE Transactions on Signal Processing*, vol. 51, no. 2, pp. 313–324, Feb 2003. 5.4

[51] I.S. Reed, J.D. Mallett, and L.E. Brennan, "Rapid convergence rate in adaptive arrays," *IEEE Transactions on Aerospace and Electronic Systems*, vol. AES-10, no. 6, pp. 853–863, Nov 1974. 6.1

[52] B. D. Van Veen, "Eigenstructure based partially adaptive array design," *IEEE Transactions on Antennas and Propagation*, vol. 3, pp. 357–362, March 1988. 6.3

[53] J. S. Goldstein and I. S. Reed, "Reduced-rank adaptive filtering," *IEEE Transactions on Signal Processing*, vol. 45, no. 2, pp. 492–496, February 1997. 6.3

[54] J. S. Goldstein and I. S. Reed, "Subspace selection for partially adaptive sensor array processing," *IEEE Transactions on Aerospace and Electronic Systems*, vol. 33, no. 2, pp. 357–362, April 1997. 6.3

[55] [online], "http://spib.linse.ufsc.br/radar.html," 2013. 6.3

[56] H. Griffiths, S. Blunt, L. Cohen, and L. Savy, "Challenge problems in spectrum engineering and waveform diversity," in *2013 IEEE Radar Conference*, April 2013, pp. 1–5. 7

[57] C. Baylis, M. Fellows, L. Cohen, and R. J. Marks II, "Solving the spectrum crisis: Intelligent, reconfigurable microwave transmitter amplifiers for cognitive radar," *IEEE Microwave Magazine*, vol. 15, no. 5, pp. 94–107, July 2014. 7

[58] H. Griffiths, L. Cohen, S. Watts, E. Mokole, C. Baker, M. Wicks, and S. Blunt, "Radar spectrum engineering and management: Technical and regulatory issues," *Proceedings of the IEEE*, vol. 103, no. 1, pp. 85–102, Jan 2015. 7

[59] H. Deng and B. Himed, "Interference mitigation processing for spectrum-sharing between radar and wireless communications systems," *IEEE Transactions on Aerospace and Electronic Systems*, vol. 49, no. 3, pp. 1911–1919, July 2013. 7

[60] Z. Geng, H. Deng, and B. Himed, "Adaptive radar beamforming for interference mitigation in radar-wireless spectrum sharing," *IEEE Signal Processing Letters*, vol. 22, no. 4, pp. 484–488, April 2015. 7

[61] S. C. Surender, R. M. Narayanan, and C. R. Das, "Performance analysis of communications & amp; radar coexistence in a covert UWB OSA system," in *2010 IEEE Global Telecommunications Conference (GLOBECOM 2010)*, Dec 2010, pp. 1–5. 7

[62] D.W. Bliss, "Cooperative radar and communications signaling: The estimation and information theory odd couple," in *2014 IEEE Radar Conference*, May 2014, pp. 0050–0055. 7

[63] H. T. Hayvaci and B. Tavli, "Spectrum sharing in radar and wireless communication systems: A review," in *2014 International Conference on Electromagnetics in Advanced Applications (ICEAA)*, Aug 2014, pp. 810–813. 7

[64] F. Paisana, N. Marchetti, and L. A. DaSilva, "Radar, TV and cellular bands: Which spectrum access techniques for which bands?," *IEEE Communications Surveys Tutorials*, vol. 16, no. 3, pp. 1193–1220, Third 2014. 7

[65] J. R. Guerci, R. M. Guerci, A. Lackpour, and D. Moskowitz, "Joint design and operation of shared spectrum access for radar and communications," in *2015 IEEE Radar Conference*, May 2015, pp. 0761–0766. 7

[66] Kuan-Wen Huang, M. Bica, U. Mitra, and V. Koivunen, "Radar waveform design in spectrum sharing environment: Coexistence and cognition," in *2015 IEEE Radar Conference*, May 2015, pp. 1698–1703. 7

[67] G. Lellouch and H. Nikookar, "On the capability of a radar network to support communications," in *2007 14th IEEE Symposium on Communications and Vehicular Technology in the Benelux*, Nov 2007, pp. 1–5. 7

[68] S.D. Blunt, P. Yatham, and J. Stiles, "Intrapulse radar-embedded communications," *IEEE Transactions on Aerospace and Electronic Systems*, vol. 46, no. 3, pp. 1185–1200, July 2010. 7

[69] S. D. Blunt, M. R. Cook, and J. Stiles, "Embedding information into radar emissions via waveform implementation," in *2010 International Waveform Diversity and Design Conference (WDD)*, Aug 2010, pp. 000195–000199. 7

[70] D. Ciuonzo, A. de Maio, G. Foglia, and M. Piezzo, "Intrapulse radar-embedded communications via multiobjective optimization," *IEEE Transactions on Aerospace and Electronic Systems*, vol. 51, no. 4, pp. 2960–2974, Oct 2015. 7

[71] J. Euziere, R. Guinvarc'h, M. Lesturgie, B. Uguen, and R. Gillard, "Dual function radar communication time-modulated array," in *2014 International Radar Conference*, Oct 2014, pp. 1–4. 7, 8.1, 8.1.2

[72] J. Li and P. Stoica, *MIMO Radar Signal Processing*, Wiley, 2009. 7

[73] A. Khabbazibasmenj, A. Hassanien, and S. A. Vorobyov, *How many beamforming vectors generate the same beampattern?*, arXiv preprint, arXiv:1402.1682, 2014. 7, 8.2.1, 8.2.1

[74] S Boyd and L. Vandenberghe, *Convex Optimization*, Cambridge University Press, first edition, 2004. 8.1, 8.2.2, 9.2

[75] P. Forster and G. Vezzosi, "Application of spheroidal sequences to array processing," in *IEEE International Conference on Acoustics, Speech, and Signal Processing*, Apr 1987, vol. 12, pp. 2268–2271. 8.2.1

[76] D.H. Brandwood, "A complex gradient operator and its application in adaptive array theory," *IEE Proceedings of Communications, Radar and Signal Processing*, vol. 130, no. 1, pp. 11–16, February 1983. 9.2

A
Appendix

In this appendix we derive the analytical BER expression for the DBPSK modulation when two arbitrary symbols are transmitted.

The DBPSK receiver uses the following decision rule

$$\Re\{z[i]\} \gtrless_1^0 0, \tag{A.1}$$

where $z[i]$ is defined in (9.86)

$$z[i] = E_r|c_i(u)||c_{i-1}(u)|e^{j(\hat{\phi}_i - \hat{\phi}_{i-1})} + N[i].$$

The decision regions of the DBPSK case is illustrated in Fig. A.1.

One of two cases may happen if a bit "0" is transmitted, i.e. the null hypothesis, H_0, is true. First case, denoted $C_{0,0}$: $C_{0,0}$ implies that $c_i(u)$ and $c_{i-1}(u)$ in (9.86) are equal to C_0. Second case, denoted $C_{1,1}$: $C_{1,1}$ implies that $c_i(u)$ and $c_{i-1}(u)$ in (9.86) are equal to C_1. The probability of occurring an error given hypothesis H_0 is

$$P(e|H_0) = P(C_{0,0})P(e|H_0, C_{0,0}) + P(C_{1,1})P(e|H_0, C_{1,1}). \tag{A.2}$$

Assuming that $P(C_{0,0}) = P(C_{1,1}) = 1/2$ we have that

$$P(e|H_0) = \frac{1}{2}\left[P(e|H_0, C_{0,0}) + P(e|H_0, C_{1,1})\right]. \tag{A.3}$$

Considering the decision rule (A.1) we can rewrite (A.3) as

$$P(e|H_0) = \frac{1}{2}\left[P(\Re\{z[i]\} < 0|H_0, C_{0,0}) + P(\Re\{z[i]\} < 0|H_0, C_{1,1})\right]. \tag{A.4}$$

Given that a bit "1" is transmitted, i.e. the hypothesis H_1 is true, the probability of occurring an error is

$$\begin{aligned} P(e|H_1) &= \frac{1}{2}\left[P(e|H_1, C_{1,0}) + P(e|H_1, C_{0,1})\right], \tag{A.5} \\ &= \frac{1}{2}\left[P(\Re\{z[i]\} > 0|H_1, C_{1,0}) + P(\Re\{z[i]\} > 0|H_1, C_{0,1})\right], \tag{A.6} \end{aligned}$$

where case $C_{1,0}$ implies that $c_i(u) = C_1$ and $c_{i-1}(u) = C_0$ in (9.86) and case $C_{0,1}$ implies that $c_i(u) = C_0$ and $c_{i-1}(u) = C_1$ in (9.86).
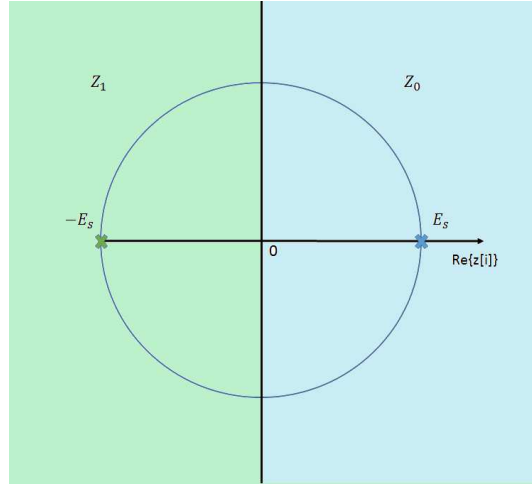
Figure A.1: Illustration of a DBPSK modulation and its decision regions.

The error probability is given by

$$P(e) = P(H_0)P(e|H_0) + P(H_1)P(e|H_1). \tag{A.7}$$

Since bits "0" and "1" are equiprobable we have

$$P(e) = \frac{1}{2}\left[P(e|H_0) + P(e|H_1)\right], \tag{A.8}$$

$$= \frac{1}{2}\left\{\frac{1}{2}\left[P(e|H_0,C_{0,0}) + P(e|H_0,C_{1,1})\right] + \frac{1}{2}\left[P(e|H_1,C_{1,0}) + P(e|H_1,C_{0,1})\right]\right\}. \tag{A.9}$$

Noting that

$$\Re\{r[i]r^*[i-1]\} = \left|\frac{r[i]+r[i-1]}{2}\right|^2 - \left|\frac{r[i]-r[i-1]}{2}\right|^2 \tag{A.10}$$

and defining

$$w_1 \triangleq \frac{r[i]+r[i-1]}{2} \quad \text{and} \tag{A.11}$$

$$w_2 \triangleq \frac{r[i]-r[i-1]}{2}, \tag{A.12}$$

thus, $\Re\{z[i]\} < 0 \Rightarrow |w_2| > |w_1|$ and $\Re\{z[i]\} > 0 \Rightarrow |w_1| > |w_2|$. Therefore

$$P(e|H_0,C_{0,0}) = P(|w_2| > |w_1||H_0,C_{0,0}), \tag{A.13}$$
$$P(e|H_0,C_{1,1}) = P(|w_2| > |w_1||H_0,C_{1,1}), \tag{A.14}$$
$$P(e|H_1,C_{1,0}) = P(|w_1| > |w_2||H_1,C_{1,0}), \tag{A.15}$$
$$P(e|H_1,C_{0,1}) = P(|w_1| > |w_2||H_1,C_{0,1}). \tag{A.16}$$

Let us observe (A.13). Note that

$$P(|w_2| > |w_1|| H_0, C_{0,0}) = \int_0^{+\infty} P(|w_2| > |w_1|, |w_1| = \alpha | H_0, C_{0,0}) \mathrm{d}\alpha, \qquad (A.17)$$

$$= \int_0^{+\infty} P(|w_2| > |w_1|| |w_1| = \alpha, H_0, C_{0,0}) p_{|w_1|| H_0, C_{0,0}}(\alpha) \mathrm{d}\alpha. \tag{A.18}$$

But as $P(|w_2| > |w_1|| H_0, C_{0,0})$ is conditionally independent of $|w_1|$ assuming any value, we can write (A.18) as

$$P(|w_2| > |w_1|| H_0, C_{0,0}) = \int_0^{+\infty} P(|w_2| > \alpha | H_0, C_{0,0}) p_{|w_1|| H_0, C_{0,0}}(\alpha) \mathrm{d}\alpha. \tag{A.19}$$

We can now write

$$P(|w_2| > |w_1|| H_0, C_{0,0}) = \int_0^{+\infty} \left(\int_\alpha^\infty p_{|w_2|| H_0, C_{0,0}}(x) \mathrm{d}x \right) p_{|w_1|| H_0, C_{0,0}}(\alpha) \mathrm{d}\alpha, \tag{A.20}$$

$$P(|w_2| > |w_1|| H_0, C_{1,1}) = \int_0^{+\infty} \left(\int_\alpha^\infty p_{|w_2|| H_0, C_{1,1}}(x) \mathrm{d}x \right) p_{|w_1|| H_0, C_{1,1}}(\alpha) \mathrm{d}\alpha, \tag{A.21}$$

$$P(|w_1| > |w_2|| H_1, C_{1,0}) = \int_0^{+\infty} \left(\int_\alpha^\infty p_{|w_1|| H_1, C_{1,0}}(x) \mathrm{d}x \right) p_{|w_2|| H_1, C_{1,0}}(\alpha) \mathrm{d}\alpha, \tag{A.22}$$

$$P(|w_1| > |w_2|| H_1, C_{0,1}) = \int_0^{+\infty} \left(\int_\alpha^\infty p_{|w_1|| H_1, C_{0,1}}(x) \mathrm{d}x \right) p_{|w_2|| H_1, C_{0,1}}(\alpha) \mathrm{d}\alpha. \tag{A.23}$$

But

$$w_1 = \frac{1}{2}(\sqrt{E_r}|c_i(u)|e^{j\hat\phi_i} + n_i + \sqrt{E_r}|c_{i-1}(u)|e^{j\hat\phi_{i-1}} + n_{i-1}), \qquad (A.24)$$

which is a complex Gaussian variable with mean $\mu_1 = \sqrt{E_r}(|c_i(u)|e^{j\hat\phi_i} + |c_{i-1}(u)|e^{j\hat\phi_{i-1}})/2$ and variance given by $\sigma_n^2/2 = N_0/2$, and

$$w_2 = \frac{1}{2}(\sqrt{E_r}|c_i(u)|e^{j\hat\phi_i} + n_i - \sqrt{E_r}|c_{i-1}(u)|e^{j\hat\phi_{i-1}} - n_{i-1}), \qquad (A.25)$$

which is a complex Gaussian variable with mean $\mu_2 = \sqrt{E_r}(|c_i(u)|e^{j\hat\phi_i} - |c_{i-1}(u)|e^{j\hat\phi_{i-1}})/2$ and variance given by $\sigma_n^2/2 = N_0/2$. The random variables w_1 and w_2 can be shown to be independent. If we write,

$$w_i = w_{i,R} + jw_{i,I}, \quad i = 1, 2, \tag{A.26}$$

then variables $w_{i,R}$ and $w_{i,I}$, $i = 1, 2$, have variance given by $\sigma_w^2 = \sigma_n^2/4 = N_0/4$.

Given H_0 and $C_{0,0}$, we have that $c_i(u) = c_{i-1}(u) = C_0$, thus $|\mu_1| = \sqrt{E_r}|C_0|$ and $|w_1|$ follows the Rician distribution,

$$p_{|w_1|\,|H_0,C_{0,0}}(x) = \frac{x}{\sigma_w^2}e^{-\frac{x^2+|\mu_1|^2}{2\sigma_w^2}}I_0\left(\frac{x|\mu_1|}{\sigma_w^2}\right), \quad x \geq 0, \qquad (A.27)$$

where $I_0(\cdot)$ is the modified Bessel function of the first kind and zero-th order, $|\mu_2| = 0$ and $|w_2|$ follows the Rayleigh distribution,

$$p_{|w_2|\,|H_0,C_{0,0}}(x) = \frac{x}{\sigma_w^2}e^{-\frac{x^2}{2\sigma_w^2}}, \quad x \geq 0. \qquad (A.28)$$

Given H_0 and $C_{1,1}$, we have that $c_i(u) = c_{i-1}(u) = C_1$, thus $|\mu_1| = \sqrt{E_r}|C_1|$ and $|w_1|$ follows the Rician distribution,

$$p_{|w_1|\,|H_0,C_{1,1}}(x) = \frac{x}{\sigma_w^2}e^{-\frac{x^2+|\mu_1|^2}{2\sigma_w^2}}I_0\left(\frac{x|\mu_1|}{\sigma_w^2}\right), \quad x \geq 0, \qquad (A.29)$$

$|\mu_2| = 0$ and $|w_2|$ follows the Rayleigh distribution, $p_{|w_2|\,|H_0,C_{1,1}}$,

$$p_{|w_2|\,|H_0,C_{1,1}}(x) = \frac{x}{\sigma_w^2}e^{-\frac{x^2}{2\sigma_w^2}}, \quad x \geq 0. \qquad (A.30)$$

Given H_1 and $C_{1,0}$, we have that $c_i(u) = C_1$ and $c_{i-1}(u) = C_0$, thus $|\mu_1| = \sqrt{E_r}|C_1 + C_0|/2$ and $|w_1|$ follows the Rician distribution,

$$p_{|w_1|\,|H_1,C_{1,0}}(x) = \frac{x}{\sigma_w^2}e^{-\frac{x^2+|\mu_1|^2}{2\sigma_w^2}}I_0\left(\frac{x|\mu_1|}{\sigma_w^2}\right), \quad x \geq 0, \qquad (A.31)$$

$|\mu_2| = \sqrt{E_r}|C_1 - C_0|/2$ and $|w_2|$ follows the Rician distribution,

$$p_{|w_2|\,|H_1,C_{1,0}}(x) = \frac{x}{\sigma_w^2}e^{-\frac{x^2+|\mu_2|^2}{2\sigma_w^2}}I_0\left(\frac{x|\mu_2|}{\sigma_w^2}\right), \quad x \geq 0. \qquad (A.32)$$

Given H_1 and $C_{0,1}$, we have that $c_i(u) = C_0$ and $c_{i-1}(u) = C_1$, thus $|\mu_1| = \sqrt{E_r}|C_0 + C_1|/2$ and $|w_1|$ follows the Rician distribution,

$$p_{|w_1|\,|H_1,C_{0,1}}(x) = \frac{x}{\sigma_w^2}e^{-\frac{x^2+|\mu_1|^2}{2\sigma_w^2}}I_0\left(\frac{x|\mu_1|}{\sigma_w^2}\right), \quad x \geq 0, \qquad (A.33)$$

$|\mu_2| = \sqrt{E_r}|C_0 - C_1|/2$ and $|w_2|$ follows the Rician distribution,

$$p_{|w_2|\,|H_1,C_{0,1}}(x) = \frac{x}{\sigma_w^2}e^{-\frac{x^2+|\mu_2|^2}{2\sigma_w^2}}I_0\left(\frac{x|\mu_2|}{\sigma_w^2}\right), \quad x \geq 0. \qquad (A.34)$$

Now we can compute the integrals in (A.20), (A.21), (A.22) and (A.23).

Substituting (A.29) and (A.30) into (A.20), we have that $P(e|H_0, C_{0,0})$ is given by

$$P(e|H_0, C_{0,0}) = \int_0^{+\infty}\left(\int_\alpha^\infty \frac{x}{\sigma_w^2}e^{-\frac{x^2}{2\sigma_w^2}}\,\mathrm{d}x\right)\frac{\alpha}{\sigma_w^2}e^{-\frac{\alpha^2+|\mu_1|^2}{2\sigma_w^2}}I_0\left(\frac{\alpha|\mu_1|}{\sigma_w^2}\right)\,\mathrm{d}\alpha. \quad (A.35)$$

Since

$$\int_{\alpha}^{\infty} \frac{x}{\sigma_w^2} e^{-\frac{x^2}{2\sigma_w^2}} \mathrm{d}x = e^{\frac{-\alpha^2}{2\sigma_w^2}}, \tag{A.36}$$

we obtain

$$P(e|H_0, C_{0,0}) = \int_0^{+\infty} \frac{\alpha}{\sigma_w^2} e^{-\frac{2\alpha^2+|\mu_1|^2}{2\sigma_w^2}} I_0\left(\frac{\alpha|\mu_1|}{\sigma_w^2}\right) \mathrm{d}\alpha. \tag{A.37}$$

If we substitute $u = \sqrt{2}\alpha$ and $\mathrm{d}u = \sqrt{2}\mathrm{d}\alpha$ into (A.37) we obtain

$$\begin{aligned}
P(e|H_0, C_{0,0}) &= \int_0^{+\infty} \frac{u}{\sqrt{2}\sigma_w^2} e^{-\frac{u^2+|\mu_1|^2}{2\sigma_w^2}} I_0\left(\frac{u|\mu_1|}{\sqrt{2}\sigma_w^2}\right) \mathrm{d}u, \tag{A.38} \\
&= \frac{e^{-\frac{|\mu_1|^2}{4\sigma_w^2}}}{2} \int_0^{+\infty} \frac{u}{\sigma_w^2} e^{-\frac{u^2+|\mu_1|^2/2}{2\sigma_w^2}} I_0\left(\frac{u|\mu_1|/\sqrt{2}}{\sigma_w^2}\right) \mathrm{d}u.
\end{aligned}$$
$$\tag{A.39}$$

Noting that we are integrating a Rician distribution from 0 to $+\infty$ in (A.39) the solution of (A.37) is given by

$$P(e|H_0, C_{0,0}) = \frac{1}{2} e^{-\frac{E_r|C_0|^2}{4\sigma_w^2}}. \tag{A.40}$$

Substituting (A.29) and (A.30) into (A.21), we have that $P(e|H_0, C_{1,1})$ is given by

$$P(e|H_0, C_{1,1}) = \int_0^{+\infty} \left(\int_{\alpha}^{\infty} \frac{x}{\sigma_w^2} e^{-\frac{x^2}{2\sigma_w^2}} \mathrm{d}x\right) \frac{\alpha}{\sigma_w^2} e^{-\frac{\alpha^2+|\mu_1|^2}{2\sigma_w^2}} I_0\left(\frac{\alpha|\mu_1|}{\sigma_w^2}\right) \mathrm{d}\alpha \tag{A.41}$$

The solution of (A.41) is equal to the solution of (A.35), except that $|\mu_1|^2$ for the case $C_{1,1}$ is given by $E_r|C_1|^2$. Therefore

$$P(e|H_0, C_{1,1}) = \frac{1}{2} e^{-\frac{E_r|C_1|^2}{4\sigma_w^2}}. \tag{A.42}$$

Substituting (A.31) and (A.32) into (A.22), we have that $P(e|H_1, C_{1,0})$ is given by

$$P(e|H_1, C_{1,0}) = \int_0^{+\infty} \left(\int_{\alpha}^{\infty} \frac{x}{\sigma_w^2} e^{-\frac{x^2+|\mu_1|^2}{2\sigma_w^2}} I_0\left(\frac{x|\mu_1|}{\sigma_w^2}\right) \mathrm{d}x\right) \frac{\alpha}{\sigma_w^2} e^{-\frac{\alpha^2+|\mu_2|^2}{2\sigma_w^2}} I_0\left(\frac{\alpha|\mu_2|}{\sigma_w^2}\right) \mathrm{d}\alpha$$
$$\tag{A.43}$$

Since the Marcum Q function of a and b, $Q_M(a, b)$, is defined as

$$Q_M(a, b) = \int_b^{+\infty} x e^{-\frac{x^2+a^2}{2}} I_0(ax) \mathrm{d}x, \tag{A.44}$$

equation (A.43) can be written as

$$P(e|H_1, C_{1,0}) = \int_0^{+\infty} Q_M\left(\frac{|\mu_1|}{\sigma_w}, \frac{\alpha}{\sigma_w}\right) \frac{\alpha}{\sigma_w^2} e^{-\frac{\alpha^2+|\mu_2|^2}{2\sigma_w^2}} I_0\left(\frac{\alpha|\mu_2|}{\sigma_w^2}\right) \mathrm{d}\alpha,$$
$$\tag{A.45}$$

Substituting the values of $|\mu_1|$ and $|\mu_2|$ for case $C_{1,0}$, which are $|\mu_1| = \sqrt{E_r}|C_1 + C_0|/2$ and $|\mu_2| = \sqrt{E_r}|C_1 - C_0|/2$, we have

$$P(e|H_1, C_{1,0}) =$$
$$\int_0^{+\infty} Q_M\left(\frac{\frac{\sqrt{E_r}|C_1+C_0|}{2}}{\sigma_w}, \frac{\alpha}{\sigma_w}\right) \frac{\alpha}{\sigma_w^2} e^{-\frac{\alpha^2 + \frac{E_r|C_1-C_0|^2}{4}}{2\sigma_w^2}} I_0\left(\alpha\frac{\frac{\sqrt{E_r}|C_1-C_0|}{2}}{\sigma_w^2}\right) \mathrm{d}\alpha.$$

$$(A.46)$$

Equation (A.46) is the analytical value of $P(e|H_1, C_{1,0})$, but the integral in (A.46) has to be computed numerically.

Substituting (A.33) and (A.34) into (A.23), we have that $P(e|H_1, C_{0,1})$ is given by

$$P(e|H_1, C_{0,1}) = \int_0^{+\infty} \left(\int_\alpha^\infty \frac{x}{\sigma_w^2} e^{-\frac{x^2 + |\mu_1|^2}{2\sigma_w^2}} I_0\left(\frac{x|\mu_1|}{\sigma_w^2}\right) \mathrm{d}x\right) \frac{\alpha}{\sigma_w^2} e^{-\frac{\alpha^2 + |\mu_2|^2}{2\sigma_w^2}} I_0\left(\frac{\alpha|\mu_2|}{\sigma_w^2}\right) \mathrm{d}\alpha$$
$$(A.47)$$

The solution of (A.47) is equal to the solution of (A.46), except for the values of $|\mu_1|$ and $|\mu_2|$, which are $|\mu_1| = \sqrt{E_r}|C_0 + C_1|/2$ and $|\mu_2| = \sqrt{E_r}|C_0 - C_1|/2$. But note that $|\mu_1|$ and $|\mu_2|$ given hypothesis H_1 and case $C_{0,1}$ are equal to the values of $|\mu_1|$ and $|\mu_2|$ given hypothesis H_1 and case $C_{1,0}$. Therefore

$$P(e|H_1, C_{0,1}) = P(e|H_1, C_{1,0}), \qquad (A.48)$$

which is given in (A.46).

Substituting (A.34), (A.42), (A.46) and (A.48) into (A.8), we have that the error probability, $P(e)$, is given by

$$P(e) = \frac{1}{8} e^{-\frac{E_r|C_0|^2}{4\sigma_w^2}} + \frac{1}{8} e^{-\frac{E_r|C_1|^2}{4\sigma_w^2}}$$
$$+\frac{1}{2}\int_0^{+\infty} Q_M\left(\frac{\frac{\sqrt{E_r}|C_1+C_0|}{2}}{\sigma_w}, \frac{\alpha}{\sigma_w}\right) \frac{\alpha}{\sigma_w^2} e^{-\frac{\alpha^2 + \frac{E_r|C_1-C_0|^2}{4}}{2\sigma_w^2}} I_0\left(\alpha\frac{\frac{\sqrt{E_r}|C_1-C_0|}{2}}{\sigma_w^2}\right) \mathrm{d}\alpha.$$

$$(A.49)$$